THE ROLE OF MAGNETIC FIELDS IN THE PRE-MAIN SEQUENCE EVOLUTION OF SOLAR TYPE STARS

By

Alicia N. Aarnio

Dissertation

Submitted to the Faculty of the

Graduate School of Vanderbilt University

in partial fulfillment of the requirements

for the degree of

DOCTOR OF PHILOSOPHY

in

PHYSICS

May, 2010
Nashville, Tennessee

Approved:

Keivan G. Stassun

J. Kelly Holley-Bockelmann

Andreas Berlind

David A. Weintraub

David J. Ernst

First and foremost, I would like to thank my advisor, Keivan Stassun, for supporting me throughout my graduate tenure. His encouragement and feedback were key in completing this work. I cannot emphasize enough the importance of the intellectual freedom of these five years, and how much being given room to work in my own way has shaped me as a scientist.

To the faculty at Vanderbilt University, my gratitude for their continued guidance. I appreciate the suggestions and comments given by my committee which served to strengthen this document. Thank you to David Weintraub, Kelly Holley-Bockelmann, Andreas Berlind, and David Ernst.

My sincerest appreciation goes to the National Science Foundation; much of this work was funded via NSF grant AST 0808072. I thank the Graduate School for continued support in the form of the travel and dissertation enhancement grants, which allowed for the presentation of this research as well as travel to meet with collaborators to add to the scientific impact of this work.

I am indebted to the many colleagues who have supported this research. In roughly chronological order, this distinguished group of scientists includes: Suzan Edwards, Edward Schmahl, Alycia Weinberger, Eric Mamajek, David James, Sean Matt, Scott Gregory, and Moira Jardine.

The graduate student body of Vanderbilt also has my appreciation for their continued encouragement and commiseration. A couple of sentences can't speak enough to the credit

of those going through this process with me, but to put it simply, the astronomy group grad students made it a little easier to drag myself to my cubicle every day.

I thank my family for patiently listening to explanations of how matter bends space-time involving tablecloths and oranges, or anything else I may or may not have rambled on about. Their support has been invaluable.

Finally, this thesis would not have been possible without the love and encouragement of my classmate, best friend, and husband, Ron.

To my parents, Jim and Ragena-
this would not have been possible
without your love, support,
and a lot of collective *sisu*.

TABLE OF CONTENTS

Page

LIST OF TABLES viii

LIST OF FIGURES ix

Chapter

I. EXECUTIVE SUMMARY 1

II. INTRODUCTION 5

- 2.1. Magnetic Fields in Star Formation 7
  - 2.1.1. Early Evolution of Solar Type Stars 7
  - 2.1.2. The Earliest Stages of Star Formation: Observations of Molecular Clouds 9
  - 2.1.3. Theoretical Models of Star Formation 11
- 2.2. Issues With the Current Stellar Evolution Paradigm 14
  - 2.2.1. Angular Momentum Evolution 14
  - 2.2.2. X-ray Production 19
  - 2.2.3. Magnetic Field Origin 22
    - 2.2.3.1. Fossil or Remnant 22
    - 2.2.3.2. Self-produced and Maintained 23
- 2.3. Stellar Magnetic Fields 24
  - 2.3.1. Field Strength and Topology 24
  - 2.3.2. Current Pre-Main Sequence Magnetic Field Models 27
  - 2.3.3. Solar Physics Cues 30

III. A SURVEY FOR A COEVAL, COMOVING GROUP ASSOCIATED WITH HD 141569 49

- 3.1. Stellar Associations 49
- 3.2. Characterizing An Association of Young Stars 51
  - 3.2.1. Target Selection 51
  - 3.2.2. Observations 52
  - 3.2.3. Reduction Procedure 53
- 3.3. Analysis 54
  - 3.3.1. Effective Temperatures 54
  - 3.3.2. Lithium Equivalent Width 56

3.3.3. Radial Velocity 58
3.3.4. Moving Cluster Parallaxes 59
3.4. Results 61
3.4.1. Distances, comovement probabilities, and membership . . . 61
3.4.2. Space Motions 63
3.4.3. H-R Diagram 64
3.4.4. Is HD 141569 Related to US? 66
3.5. Summary and Conclusions 68

IV. A SEARCH FOR STAR-DISK INTERACTION AMONG THE STRONGEST X-RAY FLARING STARS IN THE ORION NEBULA CLUSTER 82

4.1. Energetic X-ray Flares on Young Stars 83
4.2. Data 86
4.2.1. Study Sample, Loop Heights, and Stellar Data 86
4.2.2. Photometric Data 88
4.3. Preliminary Disk Diagnostics: Color Excess and Accretion Indicators 89
4.4. Synthetic Spectral Energy Distribution Models 96
4.5. Interpreting the Spectral Energy Distributions 101
4.5.1. SED Categorization Criteria 101
4.5.2. Example Cases 104
4.6. Results 106
4.7. Discussion and Conclusions 107

V. SOLAR FLARES AND CORONAL MASS EJECTIONS: A STATISTICALLY DETERMINED FLARE FLUX-CME MASS CORRELATION 122

5.1. Solar and Stellar Flares and CMEs 123
5.2. Archival Data 125
5.3. Determining Flare-CME Association 126
5.4. Results 128
5.4.1. CME Linear Speed and Flare Flux 130
5.4.2. CME Mass and Acceleration 131
5.4.3. CME Mass, Flare Flux 132
5.5. Conclusions and Discussion 134

VI. T TAURI ANGULAR MOMENTUM LOSS EXAMPLE CALCULATION . 147

6.1. Data and procedure 147
6.2. Results 152
6.3. Discussion 153

Appendix

A. STELLAR ASSOCIATION: SUPPLEMENTAL TABLES 160

B. UNIFORM COOLING LOOP MODEL 167

C. SPECTRAL ENERGY DISTRIBUTIONS 170

D. ANGULAR MOMENTUM LOSS: AN ORDER-OF-MAGNITUDE APPROXIMATION 199

LIST OF TABLES

Table Page

II.1. Astronomer Suitcase 32

III.1. Observing Log 70

III.2. Stellar Parameters 71

III.3. Effective Temperatures and Lithium Equivalent Widths 72

III.4. Kinematic Analysis of Membership Probability 73

III.5. Association Notes 81

IV.1. Stellar Parameters 111

IV.2. *Hubble* ACS and WFI Fluxes 112

IV.3. V, I, 2MASS, and *Spitzer* Fluxes 113

IV.4. Reliability of Near-IR Excess as Tracer of Inner Disk Edge 114

IV.5. Reliability of Near-UV Excess as Tracer of Inner Disk Edge 114

IV.6. Spectral Energy Distribution Result Summary 115

VI.1. Angular momentum loss parameters 150

A.1. Full Table III.1: Observing Log 161

A.2. Full Table III.2: Stellar Parameters 163

A.3. Full Table III.3: T_{eff} and Lithium Equivalent Widths 165

LIST OF FIGURES

Figure Page

2.1. Map of the Taurus Molecular Cloud 33

2.2. Star formation cartoon 34

2.3. Spectral energy distributions of different protostar classes, i=87° 35

2.4. Spectral energy distributions of different protostar classes, i=56° 36

2.5. Spectral energy distributions of different protostar classes, i=18° 37

2.6. Star-disk interaction schematic 38

2.7. Angular momentum loss estimate, COUP 1410 39

2.8. Rotation-activity relationship, < 10 Myr stars 40

2.9. Rotation periods for stars in the ONC 41

2.10. Rotation activity relationship, < 30 Myr stars 42

2.11. Bias in rotation-activity measurements 43

2.12. Zeeman-Doppler imaging of AB Doradus 44

2.13. Doppler imaging schematic 45

2.14. Effect of coronal temperature on X-ray emission measure (AB Dor) 46

2.15. Effect of coronal density on X-ray emission measure (AB Dor) 47

2.16. Modeled structure of disk-constrained magnetic field 48

3.1. Galactic coordinate map of HD 141569 and surrounding area 74

3.2. Color-T_{eff} relationship of sample stars 75

3.3. Near-infrared color-color diagram 76

3.4. Li I EW measurements: identifying young stars 77

3.5. Youthful stars in the immediate area of HD 141569 78
3.6. Radial velocities of sample stars 79
3.7. H-R diagram 80

4.1. SED of COUP 262: new A_v measurements needed 116
4.2. Effects of surface gravity on excess measurement 117
4.3. SED of COUP 1410 118
4.4. SED of COUP 141 119
4.5. SED of COUP 720 120
4.6. SED of COUP 997 121

5.1. LASCO CME database summary 135
5.2. GOES flare database summary 136
5.3. Flare-CME time offset 137
5.4. Comparison of flare-CME time offsets using flare start, peak, and end times 138
5.5. Angular separation of flares and CMEs 139
5.6. Illustration of CME sample narrowing with each constraint applied 140
5.7. CME linear speeds 141
5.8. CME accelerations 142
5.9. CME mass and acceleration 143
5.10. CME mass and flare flux 144
5.11. Quantifying the relationship between CME mass and flare flux 145
5.12. CME mass-flare flux relationship, single linear fit 146
5.13. CME mass-flare flux relationship, broken linear fit 146

6.1. Angular momentum loss calculation guide 147
6.2. Solar CME mass/flare flux relationship converted to CME mass/flare energy 155
6.3. Stellar CME mass/flare energy distribution 156
6.4. Stellar CME frequency over 1 Myr 157
6.5. Central position angles of flare-associated CMEs 158
6.6. Central position angles of flare-associated CMEs modulo 90°: $\sin(i)$ factors 159

C.1. SED of COUP 7 171
C.2. SED of COUP 28 172
C.3. SED of COUP 43 173
C.4. SED of COUP 90 174
C.5. SED of COUP 223 175
C.6. SED of COUP 262 176
C.7. SED of COUP 332 177
C.8. SED of COUP 342 178
C.9. SED of COUP 454 179
C.10. SED of COUP 597 180
C.11. SED of COUP 649 181
C.12. SED of COUP 669 182
C.13. SED of COUP 752 183
C.14. SED of COUP 848 184
C.15. SED of COUP 891 185
C.16. SED of COUP 915 186
C.17. SED of COUP 960 187

C.18. SED of COUP 971 188

C.19. SED of COUP 976 189

C.20. SED of COUP 1040 190

C.21. SED of COUP 1083 191

C.22. SED of COUP 1114 192

C.23. SED of COUP 1246 193

C.24. SED of COUP 1343 194

C.25. SED of COUP 1384 195

C.26. SED of COUP 1443 196

C.27. SED of COUP 1568 197

C.28. SED of COUP 1608 198

CHAPTER I

EXECUTIVE SUMMARY

T Tauri stars, being pre-main sequence and solar mass, tell us what our Sun was like when it was very young. T Tauri stars and their protoplanetary disks are ideal astrophysical laboratories for studying the solar system when planets were forming. At the same time, there is no astrophysical laboratory like the present-day Sun for studying in detail the microphysics that occurs in a star: this microphysics is key to understanding early stellar evolution. Specifically, a goal of this work is to understand the role of large-scale structures in stellar magnetic fields. Do these structures facilitate star-disk interaction? Do they, in a process first examined by us here, serve a different purpose and shed stellar angular momentum? We begin with a general overview of star formation and stellar evolution, focusing on the role of magnetic fields in these processes. Under the broad aegis of star formation and evolution, the remainder of this work aims to methodically explore stellar association, star-disk interaction, and a new pre-main sequence angular momentum loss mechanism.

In Chapter 3, we present results of a search for a young stellar moving group associated with the star HD 141569, a nearby, isolated Herbig AeBe primary member of a 5±3 Myr-old triple star system on the outskirts of the Sco-Cen complex (Aarnio et al., 2008). The youth of these objects makes them useful for studies of circumstellar disks and stellar evolution. We perform a spectroscopic survey of the immediate area around the HD 141569 trio and find

$\sim$20 apparently young ($\lesssim$30 Myr) stars which share common proper motions. Unexpectedly, however, these young stars are not physically close to the system; they are within 30° but on the outskirts of the selected field. In fact these stars are closer to the nearest known association complex, Scorpius-Centaurus. To ascertain which association these stars may belong to, we compare the space motions in proper motion as well as velocity space, deriving moving cluster parallaxes in order to assess the stars' galactic UVW space motions. Most of the stars identified by us as young are comoving with Upper Scorpius and Upper Centaurus Lupus. Surprisingly, if we trace the motion of the HD 141569 system back in time, we find that 5Myr ago, HD 141569 apparently formed in isolation, over tens of parsecs away from known star forming regions. This discovery either indicates there may be an as yet undiscovered star forming region in this area of the Southern Hemisphere, or it challenges the currently held paradigm of star formation.

Concurrently, the Chandra Orion Ultradeep Project was observing hundreds of young, low-mass stars undergoing highly energetic X-ray flares in a better known group of young stars, the Orion Nebula Cluster. Chapter 4 focuses on a subset of these observations, the stars which exhibited the most powerful flares, which are several orders of magnitude more energetic than the most powerful X class solar flares observed. The flares of this sample of 32 T Tauri stars were analyzed with solar-calibrated models in order to ascertain the size scale of the magnetic field confining the X-ray emitting plasma. The results were provocative: magnetic loops tens of stellar radii in size, potentially extending from the stellar surface far enough to intersect a circumstellar disk. To determine whether this is indeed happening, in

Chapter 4 we present efforts to assess the location of inner disk edges in this sample (Aarnio *et al.* 2010, *submitted*). By constructing spectral energy distributions, we are able to fit the photometry to star+disk radiative transfer models to locate the inner edge of a dust disk, and compare this to the observed magnetic loop sizes. In ∼60% of the cases, we find either no disk for the magnetic loop to intersect, or the dust disk is truncated far from the loop.

We used flare magnetic loops as a proxy for the extent of the stellar magnetosphere, and this may yield a bias. From another perspective, however, if these large scale structures are not driving star-disk interaction, it is unclear what other role they play. To address this, we look again to solar physics. Being our closest star, the Sun provides observational advantages for obtaining high spatial and temporal resolution, multi-wavelength data. In Chapter 5, we utilize long-term observations of the Sun documenting flares, coronal mass ejections (CMEs), and their properties in an effort to assess the correlation of flare and CME properties. Calibrating these relationships, it is then possible to apply them to young stars, observing a stars' X-ray flux and relating that to a fundamental but unobservable process. The ultimate goal then is to determine statistically a stellar mass-loss rate via large-scale coronal mass ejections. Potentially, if solar flares and CMEs are associated phenomena, stellar flares that are orders of magnitude more energetic than those on the Sun could be associated with stellar CMEs which shed substantial mass (Aarnio et al., 2007).

Using extensive solar CME and flare databases from LASCO and GOES, we correlate X-ray flare and CME occurrence from 1996 to 2006 (Chapter V). The study compares ∼7000 CMEs and ∼12000 flares, requiring the events to be roughly cospatial and cotemporal. The final sample of associated flares and CMEs consists of 826 event pairs, the largest study of this nature to date. With such high number statistics, we discover that the flare fluxes and CME masses are indeed correlated. The correlation holds over approximately 3 dex in flare flux, with CME mass increasing by an order of magnitude over this range.

In summary, we begin with a broad focus on a group of young stars, then examine more closely the interaction of young stars with their disks via their magnetic fields, and then launch a detailed look at other ways in which the field can affect stellar evolution. In searching for a group of young stars, we find the surprising result that the particular young trio of stars in question apparently formed separately from any known association or star forming region in the vicinity. Turning then to a well-studied group of million year old stars, the Orion Nebula Cluster, we seek to determine whether a group of young stars' magnetospheres are linked to circumstellar disks. In the majority of cases, we found that large-scale loops did not intersect disk material. Hence, we are left with the puzzle of how such large structures then could affect stellar evolution if not via star-disk interaction. We invoke solar physics to relate solar flare flux to CME mass. With this solar calibrated relationship, we construct a stellar CME mass loss rate (Chapter VI), approaching angular momentum evolution in the pre-main sequence from a novel angle.

CHAPTER II

INTRODUCTION

Among the most fundamental of physical processes, magnetic fields play manifold complex roles in governing stellar birth and evolution. In spite of the theoretical importance of this fundamental physical property, the origins, generation, and effects of stellar magnetic fields are not well understood. The very magnetic fields which influence so much of a star's life cause changes which in return affect the evolution of the field structure itself, yet the precise nature of this complex feedback remains to be elucidated.

From an observational perspective, the gas-enshrouded state of an embedded protostar makes the most fundamental stellar properties extremely difficult to directly measure. Once rid of its obscuring envelope, the young T Tauri star is itself inherently faint and possesses a highly structured, many-featured spectrum which again makes measurements of parameters such as magnetic field strength difficult to obtain. To further complicate matters, the faintness of these objects frequently places them below the detectable limits of surveys. Specifically detrimental to our understanding of T Tauri stars, trigonometric parallax surveys do not include many young stars, so many of their distances are poorly constrained.

Observational efforts to measure T Tauri stars' magnetic fields have made substantial progress in the past 20 years. Higher resolution spectra and clever utilization of Zeeman broadening have enabled higher accuracy surface field strength measurements. Multiwavelength approaches have allowed for field structure determinations at multiple stellar atmosphere scale heights, thus constraining magnetic field models. Innovations largely based on solar X-ray observations have served to push our understanding of stellar magnetic fields forward.

For theorists, modeling pre-main sequence evolution is made challenging by the coupling of fluid dynamics and electrodynamics; indeed, magnetohydrodynamical simulations are difficult to set up, computationally expensive to run, and may not be benchmarked with physically appropriate initial conditions. In spite of these obstacles, present models reveal intricate magnetic field structure and are able to accurately reproduce observed coronal properties (Jardine et al., 2002).

Solar-mass stellar evolution is of the utmost importance in astrophysics. For example, its understanding could provide insight into the nature of planetary systems and their formation (Miura & Nakamoto, 2007). Stellar evolution plays a major role in galactic enrichment and evolution (c.f., Christlein & Zabludoff, 2005; Pelupessy & Papadopoulos, 2009, and references therein). As is the case with all research, fundamental physics learned in this context could be applied to other phenomena. For these reasons, it is imperative that we understand how stars form; it is clear that magnetic fields play a pivotal role in the process (McKee & Ostriker, 2007).

2.1 Magnetic Fields in Star Formation

Understanding star formation requires physics on scales from the subatomic to the extragalactic (Kereš et al., 2005). Based on the microphysics of plasma distributions, the properties of a star forming in a given region could be predicted. For multiple protostellar cores in a molecular cloud, a stellar initial mass function (IMF) could then be derived from first principles. Understanding star formation rates and histories can further push our understanding of the structure and evolution of galaxies. As put in an annual review by McKee & Ostriker (2007):

> Stars are the "atoms" of the universe ... By transforming gas into stars, star formation determines the structure and evolution of galaxies. By tapping the nuclear energy in the gas left over from the Big Bang, it determines the luminosity of galaxies and, quite possibly, leads to reionization of the Universe.

Furthermore, in a more localized region of interest, stellar life and death produce the elements which make up the small bodies in our own planetary system as well as others yet to be discovered.

2.1.1 Early Evolution of Solar Type Stars

In a purely heuristic view of star formation, a relatively cool, dense cloud of molecular gas experiences perturbations and instabilities that create overdense regions (aptly named "dense cores", see Fig. 2.2 for an illustration) that then self gravitate and collapse. While intuitive and somewhat satisfying, many fascinating underlying processes are lost in this description.

A solely gravitational collapse scenario is overly simplistic, and magnetic fields must be included when modeling star formation. It has been found that star forming regions can be well described using turbulent flow models of fluid dynamics; indeed, inclusion of turbulence was an important moment in theoretical astrophysics (McKee & Ostriker, 2007). Magnetohydrodynamic (MHD) treatment is necessary as the presence of a magnetic field will introduce preferential directionality into the system. When strong enough, the magnetic field exerts a force on charged species in a plasma, which effectively couples the Lorentz force law with fluid dynamics equations, and this coupling is the cause of directional preference in the MHD description. Within this interplay of magnetic fields and mass, star formation occurs.

For solar-mass star formation, four specific protostellar phases are identifiable via spectral energy distribution (SED) analysis. Specific classes are assigned based upon the near-infrared slope of the observed SED; these classes describe the evolutionary phase of the object using the ratio of the observed stellar and circumstellar flux. A Class 0 object is a protostar fully embedded in natal material, its optical and higher energy emission almost entirely extinguished. At Class I, the protostar's optical emission begins to approach the intensity of infrared emission, and the trend continues through classes II and III. Class III stars are often called "naked," as their SEDs reflect solely stellar photospheric emission. For an illustration of these classes and the effect of system inclination on the observed spectral energy distribution, see Figs. 2.3, 2.4 and 2.5. These figures are the result of models created by Whitney et al. (2003b,a) (see §1.3 below). As these plots show, the inclination angle greatly affects the surface area over which we observe the radiated flux; as a result, the information gathered on disk geometry (such as dust truncation radius) could be limited.

Once a low-mass protostar sheds enough of its outer envelope to become optically visible, it is dubbed a T Tauri star (TTS), after the prototypical object of this class, T Tauri. By this definition, TTS occupy the Class II-III regime, with some shown to possess circumstellar disks and others lacking. TTS are thought to evolve from so-called “classical T Tauri Stars” (cTTS) into “weak-lined T Tauri Stars” (wTTS); these phases are representative of classes II and III, respectively, in the SED based classification scheme. The designation of cTTS or wTTS is based primarily on optical wavelength spectral signatures, particularly emission lines such as Hα and Ca 2 associated with accretion of circumstellar disk material. If a canonical evolution scenario from cTTS to wTTS is adopted (Bertout et al., 2007), it could then be possible, to add further weight to this view, use warm circumstellar dust presence as an additional discriminating criterion. Observations in other wavelength regimes also show dissimilarities in cTTS and wTTS; most importantly to magnetic field activity, their X-ray properties are distinct (see § 2.2).

2.1.2 The Earliest Stages of Star Formation: Observations of Molecular Clouds

Star formation occurs in molecular clouds, and understanding a cloud’s fundamental physical attributes sets the initial conditions for any stellar evolution paradigm. An image of a well-studied molecular cloud that is known to host star formation is shown in Fig. 2.1; the grayscale portion of the image was made from A_V, or Johnson V band wavelength extinction, while the overlaid contours indicate CO emission. Molecular cloud masses are measured via the $J = 1 - 0$ ro-vibrational transition of ^{12}CO or ^{13}CO. Depending upon the extent of the cloud structure, clouds can range from 30 $M_{\odot}$ for an individual cloud to 10^4–10^5 $M_{\odot}$ for complexes and fittingly named Giant Molecular Clouds (Stahler & Palla, 2005).

Magnetic field measurements of molecular clouds are particularly difficult to make, and the existing measurements using Zeeman splitting are of lower density regions which may not necessarily host star formation. Polarization of background starlight can be used to measure the direction of the magnetic field, but this is only an option with less dense clouds. Submillimeter polarization measurements have been performed on dense cores themselves, which are likely heated by a forming protostar within; these measurements reveal a falloff in polarization toward the center of the core (Stahler & Palla, 2005). The drop in polarization could be attributed to an increased optical depth due to geometric properties or it may also be caused by the last phases before core collapse accelerates: as the field lines are diffused outward and magnetic support is removed from the central core region, the polarization measure would most certainly decrease. The best field strength measurements were in Perseus B1; Zeeman splitting of OH yielded fields ~10 μG throughout, with the strength increasing by a factor of a few in the most compact region[1], likely a dense core (Stahler & Palla, 2005).

Spatial mapping of CO has been used to demonstrate the ages of molecular clouds based upon their structure; largely unperturbed structures would indicate a lifetime shorter than a Galactic rotation period. Even this, the earliest stage of star formation, remains poorly

---

[1] For comparison, the mean magnetic field of the Sun is ±1 G (see Table II.1 for additional magnetic field quantitative comparisons).

constrained and under debate. The age of molecular clouds is hugely important in determining the effects of turbulence versus ambipolar diffusion in the star formation process (Mouschovias et al., 2006). If these clouds are indeed short-lived objects, the ambipolar diffusion timescale is far too long for the effect to be relevant.

To constrain star formation models, the mass distribution within molecular clouds must be well measured to define an initial mass function. The velocity distribution of circumprotostellar material and the radiative flux of this material can also provide insight to the nature of accretion processes. Spectral energy distributions can assist in determining protostellar structure, but degeneracies are introduced due to inclination angles and phenomena such as jets, which can create an apparently flattened disk structure about a Class 0 source which would otherwise have remained embedded (McKee & Ostriker, 2007).

2.1.3 Theoretical Models of Star Formation

In the most general of terms, the greatest problems addressed by stellar evolution models are rooted in what protostellar cores undergo to take them from regions of lower than typical interstellar medium magnetic flux and density to many orders of magnitude greater.

As described in McKee & Ostriker (2007), in determining the competing roles of magnetic fields and gravitational interactions, the molecular cloud mass and the magnetic critical mass must be compared. The magnetic critical mass is based upon a magnetostatic equilibrium condition (equating magnetic energy and gravitational energy) and is defined as follows:

$$M_\Phi \equiv c_\Phi \frac{\Phi}{\sqrt{G}} \tag{2.1}$$

where Φ is the magnetic flux threading through the cloud, while c_Φ is a constant describing the mass and magnetic flux densities within the cloud. c_Φ is determined on a cloud-by-cloud basis via submillimeter mass estimates and polarimetric measurements of magnetic flux density. A cloud is considered subcritical when $M_\Phi > M$. In this scenario, gravitational collapse is not possible because the magnetic field provides a counteracting, supporting force. The opposite of this is a supercritical state wherein $M > M_\Phi$; the magnetic field in this regime cannot prevent gravitational collapse. The cloud mass changes due to material flowing along field lines, and M_Φ can change due to ambipolar diffusion; the complex interplay of these states give rise to conditions ripe for star formation. For example, models show that a cloud begins in a subcritical state, undergoes ambipolar diffusion, and when the central region of the dense core becomes supercritical, gravitational collapse begins to occur and accelerate.

As mentioned previously, the velocity distribution about dense cores can be used to describe the accretion of material onto a collapsing protostar. Because a molecular cloud is considered turbulent, the velocity distribution of the cloud is greatly varying from one spatial point to the next; the consequences of this on accretion are density and velocity fluctuations, which could potentially be observed in the later phases of accretion. During this phase of star formation, in the Bondi-Hoyle accretion model[2], the local magnetic field

---

[2] Bondi accretion describes material accreting onto a point mass (Bondi, 1952), Hoyle had previously

is essentially negligible (McKee & Ostriker, 2007) and can be corrected for with a simple velocity approximation. Once a net rotation is established by the central core, it begins to influence the surrounding material and a general flattening of a disk perpendicular to the rotation axis begins to occur. As the collapse progresses and more of the available material within a specific radius is accreted, the protostar emerges from its envelope and can be classified by the schemes described in § 1. The amount of material available in this accretion reservoir is defined by a spherical shell of radius R_{BH}; the Bondi-Hoyle radius depends on the core mass and its motion through the molecular cloud:

$$R_{BH} \sim \frac{m_{core}}{c_s^2 + v_0^2} \tag{2.3}$$

where c_s is the cloud's sound speed and v_0 is the star's speed (McKee & Ostriker, 2007): for higher velocity objects, the available accretion reservoir shrinks.

The presence of a circumstellar disk is an interesting property of pre-main sequence objects as the disks are potential planetary system progenitors. Disks also influence the accretion history – and potentially the rotational evolution – of the hosting central star (see §2.1). Beyond the initial collapse and protostellar phases, models of energy transport from star to disk have been developed (Whitney et al., 2003a,b); these models reproduce the spectral energy distribution observed for young stellar objects of varying mass and envelope

---

generalized the process for a moving mass (Hoyle & Lyttleton, 1941):

$$\frac{dM}{dt} = \frac{4\pi G^2 M}{c_s^3} \tag{2.2}$$

enshroudment. In the following sections we discuss possible star-disk interactions in which the truncation radius of disk material could be a critical parameter. For these models, the radiative transfer codes can help determine where material is located when input with near infrared photometry.

2.2 Issues With the Current Stellar Evolution Paradigm

2.2.1 Angular Momentum Evolution

Rotation period measurements of young stars reveal that angular momentum is not conserved in the pre-main sequence phase of evolution. A simplistic model of a contracting solid body that conserves angular momentum requires an increasing rotational velocity with decreasing radius. As solar-type stars contract onto the main sequence, however, we observe them to lose an order of magnitude or more angular momentum, resulting in longer rotation periods than expected. At present, two basic scenarios are under investigation to resolve this apparent discrepancy: star-disk interaction mediated by the stellar magnetosphere, and stellar wind loss mechanisms. Fig. 2.6 is an illustration of the stellar environs with these processes depicted.

In the star-disk interaction regime, disk locking as an angular momentum loss mechanism was first presented in the 1990's (cf. Koenigl, 1991; Collier Cameron & Campbell, 1993; Shu et al., 1994; Ostriker & Shu, 1995). In a disk-locked system, the TTS's magnetosphere truncates disk material at the Keplerian corotation radius and, potentially, field lines thread through disk material. Until dissipation of the circumstellar disk, transfer of angular momentum and material could occur via this interaction.

Observational attempts to test disk-locking consist mainly of large scale young cluster/association photometric surveys aimed at correlating rotation period and disk signatures such as accretion (Edwards et al., 1993) or near-mid ($\sim 10\mu$m) infrared excess (cf. Stassun et al., 2001; Rebull, 2001; Herbst et al., 2002) . If disk locking is effective, the expectation is that slower rotating stars will be found with circumstellar dust material that could couple to a magnetosphere and transfer angular momentum from star to disk via magnetic field lines' interaction with charged disk particles. Models of disk torque show that differential rotation opens field lines (Matt & Balick, 2004), thereby eliminating this drag as a source of substantial angular momentum depletion. Furthermore, with ongoing accretion and an assumed strong coupling between star and disk, the overall field topology is influenced such that an even weaker torque occurs (Matt & Pudritz, 2005b). An additional issue with disk locking lies in the understanding that disks are turbulent, which makes them poor conductors. This would imply that field lines anchoring to the disk would be inefficient at best, and entirely ineffective for torquing and angular momentum transfer at worst. A problem also not addressed by these methods is the presence of gas; slow rotators that at first appear to be diskless could well possess gaseous disks, invisible to near IR photometric measurements yet able to interact with the star.

Stellar winds and magnetic braking constitute another potential sink for stellar angular momentum. As described in Tayler (1997), magnetic braking occurs as material with velocity greater than stellar escape velocity travels along open magnetic field lines; when corotating at the stellar surface, the angular momentum per unit mass of a "plasma packet" is ΩR_{star}, but as the packet moves outward along the field line, the kinetic energy density of material increases as the magnetic field energy density decreases. By definition, at the Alfvén surface, the two energy densities are equal, and the angular momentum per unit mass has now increased to $\Omega R_{Alfv\acute{e}n}$: this increase means that angular momentum from the star is now contained in the angular momentum of the plasma packet! In this manner, stellar angular momentum can be shed via mass loss. The first calculations of wind-based angular momentum loss were performed by Weber & Davis (1967); the authors found that the effective lever arm for the torque applied to the Sun by the wind extends out to 15−50 $R_{\odot}$. Magnetic braking calculations were then applied to late-type stars by Mestel & Spruit (1987).

Stellar winds could well be an effective way of shedding angular momentum if they are able to rid the central star of mass at a substantial rate. The first work to conclusively show that magnetic braking could indeed describe the rotational evolution of stars was done by Schatzman (1962) on A stars. The author applied a Parker (1955) dynamo scenario to model the pre-main sequence magnetic field and determine mass loss via winds in a non-contracting system, and contraction is applied afterward. This work is fundamental to the development of stellar wind models and serves as the basis for the models which follow. Kawaler (1988) showed using a steady-state wind loss model that the stellar wind could indeed effectively spin a star down over the pre-main sequence phase, however, this analysis fell out of favor in the TTS regime in the years following its publication, due partially to the assumption of a field far weaker than observed four years later (Basri et al., 1992). Kawaler also assumed a purely radial field and a field strength directly proportional to the rotation rate, which has not, to date, been proven, and due to the fully convective nature of TTS, a dynamo driven field cannot be assumed. Despite these critical departures from key T Tauri properties, the idea of a stellar wind shedding angular momentum is valid.

Approaching the problem 20 years later from a different angle, Matt & Pudritz (2007) begin by noting that in order to account for the angular momentum losses observed, the wind angular momentum loss rate would have to be ∼10% of the accretion rate, or $\sim 10^{-9}$ $M_\odot$ yr^{-1} (Matt & Pudritz, 2005a). Using a scaled-up solar coronal wind model, Matt & Pudritz (2007) compute a pressure driven wind's ability to shed angular momentum and find that this mechanism could indeed counteract the angular momentum gained via accretion. The authors note, however, an important caveat to this calculation: in order for the wind to effectively radiate energy away from the star, the gas must remain hot for the duration of its acceleration away from the star. Unfortunately, if the gas were in local thermodynamic equilibrium (LTE), cooling would occur more quickly, which suggests that something must be heating the gas. Matt & Pudritz (2007) suggest accretion itself is providing this energy. In spite of some theoretical setbacks, stellar winds remain a compelling contributor to angular momentum loss.

The idea of periodic mass and thereby angular momentum loss events has recently come back into consideration. High-cadence, long temporal baseline X-ray data (e.g. COUP, XEST: Getman et al., 2005a; Audard et al., 2007) reveal that periodic, energetic flaring events which occur with regular frequency in young stars. These flares appear to be similar to solar flares, but are orders of magnitude more energetic and are larger in physical size. An analysis based on solar events (Reale et al., 1997) was applied to the most energetic events of the COUP sample (Favata et al., 2005), and the confining magnetic loop structures were found to be several stellar radii in length from footpoint to footpoint. Recently presented work (Aarnio et al., 2007), based upon the Favata et al. (2005) sample, models the angular momentum shed via periodic, large-scale eruptive flares. As can be seen in Fig. 2.7 for the star COUP 1410, given a physically realistic flaring event rate, substantial angular momentum can be shed in the pre-main sequence lifetime of a low mass star via this mechanism (∼20%). Future work will apply an event-rate energy distribution as a function of mass to the COUP "superflaring" objects. This will determine if integrating events of varying magnitude can account for the total angular momentum loss observed in pre-main sequence stars (see Chapter VI for an outline of this calculation) .

The present understanding of star-disk interaction is heavily debated, with contradictory results based on interpretations of circumstantial evidence. Although the observational campaigns appear robust, to date, no contemporaneous stellar magnetic field, rotation period, and circumstellar disk measurements have been made that could unambiguously probe a star-disk connection and subsequent interaction. More likely than not, multiple factors contribute to the observed leeching of stellar angular momentum, and these factors should be simultaneously considered. Observationally, these factors could be disentangled by simultaneously obtaining the following information for a substantial ($N \gtrsim 100$) sample size:

1. Circumstellar dust structure. Obtained by deconvolving spectral energy distributions. Requires optical and near-mid infrared photometry;
2. Circumstellar gas content. Requires detection of molecular gas emission via near-mid infrared spectroscopy (cf. Weintraub et al., 2000);
3. Magnetic field topology. Requires surface Zeeman-Doppler imaging, extrapolated to the stellar corona (Jardine et al., 2002; Hussain et al., 2007);
4. Magnetic activity. Requires X-ray light curves to measure quiescent emission levels as well as periodic reconnection event energies and event frequencies (Albacete Colombo et al., 2007).

2.2.2 X-ray Production

Even in quiescence, T Tauri stars produce several orders of magnitude more X-rays than the present-day Sun. While spectroscopic indicators of accretion distinguish cTTS and wTTS, both are X-ray detected. X-ray emission from young, low mass stars is generally attributed to their hot, magnetic coronae; with temperatures in excess of 10^6 K (Güdel, 2004), optically thin thermal bremsstrahlung is observed in T Tauri X-ray spectra. Understanding the origin of such high coronal temperature has long been solar physicists' goal; presently, coronal heating is attributed to magnetic heating mechanisms such as micro/nanoflaring and resistive heating. X-rays can be produced in stellar coronae which are considered to be in a state of collisional equilibrium. As described in Paerels & Kahn (2003), in an optically thin plasma of low density, excitation occurs as a result of collision, and deexcitation is spontaneous. Because the interaction is collisional, the observed flux is dependent on the number density in a given energy level population. The two-body nature means any flux goes as n_e^2 dV: this parameter, commonly used in X-ray astronomy, is known as the emission measure.

Magnetic reconnection events occur with regular frequency, and these produce emission via two mechanisms. Synchrotron is produced by acceleration of plasma near the reconnection site, either via field line motions or shocks, and turbulence creates cyclotron/synchrotron emission. The heated plasma evaporating into the post-flare confining loop structure produces soft X-ray bremsstrahlung. Quiescent emission, therefore, should consist of mainly soft X-ray emission due to bremsstrahlung ($\leq$10 keV), and hard X-rays ($\geq$10 keV) from reconnection events should occasionally punctuate the continuum level emission. A two temperature plasma is generally used to model T Tauri coronae; the hard X-ray component has a T_x= 15-30 MK while the soft component has a T_x= 2-5 MK (Feigelson & Montmerle, 1999).

Some X-ray observations of star forming regions indicate that cTTS are more highly variable and ~2 times less X-ray luminous than their non-accreting counterparts, wTTS (Preibisch et al., 2005). Their difference in age and thereby evolutionary status (Bertout et al., 2007) does not appear to be the source of this X-ray emission difference. Recent modeling work has shown that dense gas within the accretion columns of cTTS strongly absorbs coronal X-ray emission (Gregory et al., 2007). To determine this result, magnetic field surface mapping is employed to extrapolate and determine the field structure of stellar coronae (see §3.1), and radiative transfer code models X-ray production and the resulting photons' travel through an accretion-column riddled corona.

On the main sequence, a rotation-activity relation is well defined (e.g. Pallavicini et al., 1981; Randich, 2000). In Fig. 2.8, the main-sequence relationship between $\frac{L_X}{L_{bol}}$ and Rossby number (ration of rotation period to convective turnover timescale) is shown, while Figs. 2.9 shows the same relationship as measured for a <10 Myr old population. The main issue raised in comparing these relationships is the apparent lack of data for pre-main sequence stars in the higher Rossby number regime. Does a physical explanation account for these "missing" data, or is it a selection effect? Stassun et al. (2004a) show there exists a dearth of rotation period measurements of for less X-ray active young stars (Fig. 2.11) and conclude that the underrepresented population here consists of cTTS, which are thought to be less X-ray luminous than wTTS. This would indicate that for the youngest PMS stars, a rotation-activity relationship has yet to be defined. Unfortunately, it remains unclear how separating cTTS from wTTS in the rotation-activity plot would give any indication of this bias, as high starspot filling factors could also lower the number of wTTS for which rotation periods could be measured. In addition to a potential observational selection effect, there may be a physical selection effect due to the nature of the objects observed; for stars still contracting onto the main sequence and developing a radiative core, the size of the convection zone is changing, which would thereby alter the Rossby number. It is also unclear how contraction affects the rotation period, another factor upon which the Rossby number depends. It is herein that multiple gaps in the understanding of star formation intersect: stellar angular momentum, activity, and magnetic field structure are intimately related in ways which remain to be fully revealed. We seek to clarify stellar angular momentum here (see Chapters IV, VI)

2.2.3 Magnetic Field Origin

While the physical mechanisms producing X-ray emission in a magnetic field laced plasma can be deduced, it is a far more difficult task to determine what produced the field. Either the magnetic field is a remnant of a primordial field, or it is generated by the star itself.

2.2.3.1 Fossil or Remnant

It has been proposed that a relic field remains toward the stellar core in main sequence stars. This field then migrates outward via flux tube buoyancy; simulations have recently shown, however, that in the presence of convection, flux tubes can at times be suppressed, and thus the observed field strengths cannot be reproduced (Schrijver & Zwaan, 2000). In the stable region beneath the convective zone, field strengths of up to 10^4 G can be maintained over long timescales (Parker, 1975). While the primordial entrapment mechanism remains unknown, based on solar analogy, there indeed exists a stable location for this field to be stored. As (Parker, 1975) points out, the solar dynamo can account for the magnetic flux inferred from observations, but for cases of stars with fields >100 G, may require additional magnetic flux.

2.2.3.2 Self-produced and Maintained

An $\alpha - \Omega$ type dynamo mechanism is the method of magnetic field generation in our Sun (Parker, 1955); this mechanism is characterized by differential rotation in the upper layers of the Sun and large scale velocity shear where the base of the convective zone meets the radiative zone. The terms α and Ω describe processes which convert toroidal field to poloidal, and polodial to toroidal, respectively. For TTS, X-ray production via a scaled-up solar coronal model reproduces the observed quiescent X-ray emission (Telleschi et al., 2007), but because TTS are unlikely to generate fields via a solar-type α-Ω dynamo, it's surprising that the description works so well. Chabrier & Baraffe (1997) show that in the pre-main sequence phase, up until $\sim 10^7$ years, a cool, low-mass star will be fully convective. Early work has shown convection always drives a turbulent dynamo; Schrijver & Zwaan (2000) argue that across spectral types, the transition from solar type boundary-layer driven dynamos and turbulent dynamos must be smooth. Therefore perhaps to make this transition smooth a third type of dynamo is possible in which both differential rotation and turbulent motions occur deep within the star. Recent modeling results for 0.3 $M_\odot$ dwarfs posit that despite a fully convective interior, regions remain (i.e., the tachocline, the boundary between the radiative and convective zones) in which there is some velocity shear between upper differentially rotating layers and lower, solid-body rotating layers (Browning & Basri, 2007). It remains entirely unclear observationally whether this is indeed the case; results published for the M4 dwarf V374 Peg show that it appears there is some relationship between the small differential rotation and the time evolution of the magnetic field structure (Morin et al., 2008), but the nature of this relationship is entirely uncertain.

2.3 Stellar Magnetic Fields

Magnetic fields are known to play a key role in the stellar evolution process, but the magnitude of that role mostly remains to be determined. It is essential, therefore, that research move in the direction of characterizing stellar magnetic fields across a range of ages in the pre-main sequence as well as the main sequence; it is only in this manner that we may understand the evolution of these complex structures and mechanisms and place them into context with other observations.

Since the 1980s, indicators of magnetic field activity have been observed in young stellar objects (YSOs) and YSO systems. These indicators include photometrically detectable starspots, keV and MeV particle emission in the wake of field line reconnection events, Zeeman effects in optical and UV spectra, and nonthermal radio continuum flares (Feigelson & Montmerle, 1999). High energy processes which are currently monitored on the Sun with phenomenal temporal and spatial resolution are observed in YSOs as well, and models of young stars' magnetic activity can be, with great care and no small amount of difficulty, created based on tracers of activity and analogy to the solar case (for example, see the work of Haisch et al., 1995; Reale et al., 1997; Peres et al., 2001).

2.3.1 Field Strength and Topology

In TTS, measurements of magnetic field strengths are difficult to make, in part because:

1. Late type (cool, low-mass) stars are inherently faint;
2. Late type stars have a plethora of absorption features which can crowd nearby lines and blend;
3. Multiple sources of broadening (e.g., rotational, pressure) cause ambiguity in discerning Zeeman signatures;
4. A major factor in mapping the magnetic field structure is knowing the star's rotation period: in late type stars, irregular starspot patterns as well as high filling factors can make a rotation period very difficult to measure.

In spite of these challenges, Zeeman splitting is indeed observed, albeit somewhat indirectly: superimposed Zeeman split features and rest wavelength absorption features result in a net broadened line. Synthetic spectra are compared to observations to determine the magnetic field strength responsible for the observed broadening. Unfortunately, this is very difficult to do, especially in cases where rotational broadening is also a factor. The first measurements of surface magnetic field strength upper limits were made using Zeeman broadened Fe I lines. For example, the resulting upper limit for the star TAP 35 was ∼1.5 kG (Basri et al., 1992). A later enhancement of this method was the exploitation of the Zeeman effect's wavelength dependence, which causes more pronounced splitting of redward wavelengths. To gauge this effect, Ti I at 2.2μm is frequently used (Johns-Krull et al., 1999). As model atmospheres and abundance measurements improve, constraints on surface field strength measurements become more accurate.

Presently it is understood that at the stellar surface, higher order magnetic moments tend to dominate magnetic field structure and strength, while farther from the star, a weaker, predominantely dipole field exists. From spectropolarimetry, polarization measurements can be taken which describe the direction of the magnetic field (cf., Daou et al., 2006, for a detailed demonstration of this technique). To obtain spatial information helpful in determining where the feature is located on the surface, time-series spectra are necessary, as well as knowledge of the stellar rotation period. Polarization measures in concert with Zeeman-Doppler imaging results can provide a map of magnetic field topology at the stellar surface, where magnetic field strengths and directions are defined as functions of spatial coordinates (for an example, see Fig. 2.12).

The above methods for determining magnetic field structure involve very direct measurements; periodic X-ray flaring events can be utilized to probe magnetic field structure. Via comparison with solar flare models, time-series X-ray photometry can provide emission measures and decay timescales which reveal magnetic loop sizes (see §3.3). The modeling of these flaring loop parameters was performed based solely on thermodynamic and electrodynamic principles, but was then benchmarked using solar observations (Reale et al., 1997). The fundamental physics is sound, but the assumptions which must be taken with care include the aspect ratio of the loop (the ratio of length to loop radius) as well as the principle assumption that heating is impulsive and no additional energy is added during the decay of the initial flare.

2.3.2 Current Pre-Main Sequence Magnetic Field Models

Surface map field extrapolation techniques are currently at the forefront of magnetic field structure modeling in pre-main sequence stars. Zeeman-Doppler imaging is presently the best way to determine surface field strength and orientation. The technique uses time series, circularly polarized spectra to obtain field strengths due to Zeeman broadening of lines and field orientation measures from the Stokes polarization parameters. Spatial orientation informationc san be determined from the Doppler shifts of the line centers and some knowledge of the object's differential surface rotation. An example of the technique as applied to the nearby star AB Doradus (AB Dor) is shown in Fig. 2.12 from Hussain et al. (2007). At a distance of 40 pc and an age of $\sim$30 Myr, AB Dor is particularly interesting because it is still quite active and just approaching the main sequence. The first panel of Fig. 2.12 is a star spot map, created by time series spectral analysis. A cartoon illustration of how Doppler imaging works is shown (Fig. 2.13). By analyzing starspots' characteristic narrow-line filling of absorption features, the spatial distribution of spots can be determined, as well as an intensity change associated with each spot.

Similarly, Zeeman-Doppler imaging uses circularly polarized time-series spectra to map surface magnetic field directions and strengths. Stokes V spectra are made by taking the difference of right and left circularly polarized (RCP and LCP) spectra. The Stokes V parameter is sensitive to field orientation, and the result is that the amplitudes of spectral features will be modulated depending upon field orientation. In the presence of a radial field, the RCP and LCP features will have the same intensity, whereas an azimuthal field causes asymmetric modulation of intensity. This effect can be directly seen in the symmetry or asymmetry of Stokes V spectral features. This yields the field direction, while simultaneously, the broadening of spectral lines due to the superposition of Zeeman split features can give the magnitude of the field. The middle and lower panels of Fig. 2.12 show spatial mapping of radial and azimuthal fields respectively, and the images are scaled to field strengths of ± 1300 G (in blue and red). The spatial scale was recovered using Doppler shifts to determine projection.

Combining some simple assumptions regarding the field's behavior with scale height and coronal density models, the surface field can then be extrapolated up into the corona (for a review of this method, see Jardine et al., 2002) and known, observed quantities can be compared to the model. From X-ray spectra, coronal number densities and temperatures can be derived (recall a two-temperature model effectively fits the X-ray regime from soft to hard X-rays). Since flux is proportional to the integrated emission measure, we observe the emission measure integrated over the volume of the corona visible to our detector. With spatial information of the magnetic field confining the emitting plasma, however, the emission measure can be shown as a function of spatial coordinates. The observed flux, then, is the integral of all the emission measure we can "see;" Figs. 2.14 and 2.15 show exactly this, with coronal temperature and number density varied. X-ray flux is observed to be modulated at the stellar rotation period in young stars (Flaccomio et al., 2005), and these maps show precisely why: localized X-ray "hot spots," the emission measures of which depend upon density and temperature. As a star rotates, regions of varying emission measure enter and exit the field of view, and the integrated emission measure changes depending on the filling factor of these hot loops.

In some cases, like the one illustrated in Fig. 2.14, the temperature effectively raises the magnetic field loops (which contain X-ray emitting plasma), and this decreases rotational modulation as much of the plasma is visible over an entire rotation period. Fig. 2.15 shows that a higher number density corona results in field lines being forced open (the kinetic energy density of the plasma is greater than the magnetic field energy density), thereby limiting the volume of magnetic confining structures and creating a more spatially compact coronal structure. Thus, in spite of a density change of two orders of magnitude, the decrease in volume makes the magnitude of emission measure only increase by a factor of $\sim$2.

The previously mentioned study conducted on AB Dor (Hussain et al., 2007) couples surface field topology indicators with coronal activity measurements to produce models consistent with observations of quiescent post-TTS coronae. The importance of this work lies in two layers of boundary conditions which tightly constrain the modeled magnetic field structure. Interestingly, the addition of the coronal constraint shows that in order for the modeled emission measure to match the observational data, the polarity of the field in the obscured (due to 60° inclination) southern hemisphere of AB Dor must be the same as the visible hemisphere; this is not as observed on the Sun.

2.3.3 Solar Physics Cues

Our Sun provides us with exquisite, high resolution data with which we have already made leaps and bounds of progress toward understanding the nature of stellar magnetic fields. Although we lack similar high resolution data for other stars, efforts have been made in a multitude of arenas to apply solar physics principles to a range of spectral types and ages. Caution must always be used in these applications, but frequently, applying solar insights have been hugely rewarding.

An instrument on the SOlar and Heliospheric Observatory (SOHO) satellite, the Extreme ultraviolet Imaging Telescope (EIT), is sensitive to solar ultraviolet radiation. The instrument probes a region of the solar corona ranging in temperature from 80 kK to 2.5 MK. UV radiation probes a layer of a star's atmosphere, the $\sim 10^5$ K plasma of the transition region, that is between the optically visible photosphere and the X-ray detected corona. Gómez de Castro (2002) took ultraviolet spectroscopic observations of AB Dor and was able to measure the infall velocity of material based upon redward Doppler shifts of spectral lines. The author derived a free fall time based upon the scale height of the emission ($\sim$30,000 km), and found that it was consistent with the decay time of the UV flare. This type of measurement can constrain the coronal structure of emitting plasma.

In optical wavelengths, sunspot observations have lead to the inference of starspots. On the Sun, a spot is created when the magnetic field in a region is overly dense, thereby inhibiting convection there and creating a localized cooler spot. Variations in stellar light curves attributed to these spots allow for the measurement of yield rotation periods. Filling factor estimates based upon the net reduction of stellar flux due to spots can be used as a proxy for magnetic activity; a higher filling factor signifies high spot activity and therefore a high level of magnetic activity.

The occurrence of reconnection events on the Sun has been used to benchmark relationships between X-ray flare decay slopes and the magnetic field structure confining the emitting plasma. After a magnetic reconnection event occurs, heated plasma evaporates from the chromosphere into the confining loop, where it cools by emitting soft X-rays (Priest & Forbes, 2002). Both the X-ray decay time and its slope in density-temperature space can be related to the loop size (Reale et al., 1997). This method was developed using numerical hydrodynamic simulations and then calibrated using solar data for which spatially resolved imaging confirmed loop length scales predicted by the model.

Based upon the solar example, models have reproduced stellar observations well. As progress continues to be made in ascertaining stellar magnetic field structure, we further our understanding of the stellar evolution process and the fundamental physics which govern it.

Table II.1. Astronomer Suitcase

Physical Parameter	Solar Value	Typical T Tauri Value	T Tauri Value Reference
T_{eff}	5,777 K	3,700−6,000	Kenyon & Hartmann (1995)
Age	4.5-4.7×10^9 yr	$<10^7$ yr	Feigelson & Montmerle (1999)
Mass	1 $M_\odot$	∼0.2−2 $M_\odot$	Feigelson & Montmerle (1999)
Radius	1 $R_\odot$	∼2−3 $R_\odot$	Feigelson & Montmerle (1999)
Spectral Type	G2 V	G−M1 V	Cox (2000)
B	±1 G$^{(1a)}$ / 2−4 kG $^{(1b)}$	12±35G$^{(1c)}$ / ∼2.4kG$^{(1d)}$	T Tauri (Daou et al., 2006)
Mass Loss Rate	10^{-14} $M_\odot yr^{-1}$	∼$10^{-7} M_\odot yr^{-1}$	Feigelson & Montmerle (1999)
Rotation Period	∼25 d	1−20 d	Cox (2000)
L_X	10^{20}−10^{23} erg s^{-1} $^{(2)}$	$10^{28.5}$−10^{31} erg s^{-1}	Feigelson & Montmerle (1999)
Hα	In absorption	± 1 Å	(3)

Note. — Unless otherwise noted, all solar constants obtained from Cox (2000).

[1a] Mean peak magnetic field.

[1b] Within a sunspot umbra.

[1c] Mean longitudinal field.

[1d] Mean field on surface, from Zeeman broadening seen in unpolarized spectra.

[2] X-ray luminosity of typical flares for E>20 keV.

[3] cTTS are seen to have Hα in emission due to accretion, wTTS generally have Hα in absorption (see Edwards et al., 1994; Kurosawa et al., 2006, for observations and models, respectively).

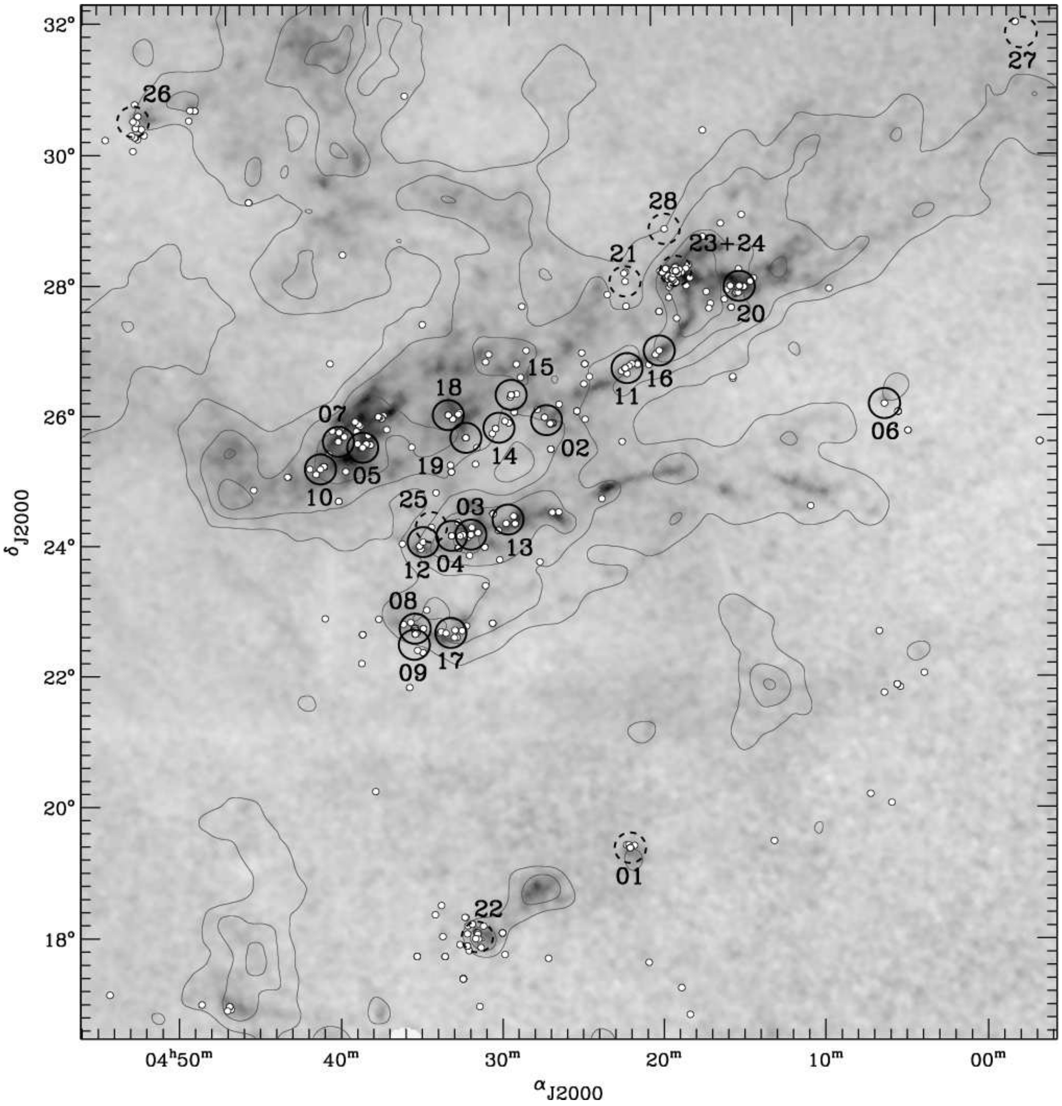

Figure 2.1: A map of the Taurus molecular cloud (Güdel et al., 2007). Grayscale indicates visual band extinction, A_V, (from Dobashi et al., 2005), and contours represent CO emission. Each numbered circle is an *XMM-Newton* Taurus XEST survey field.

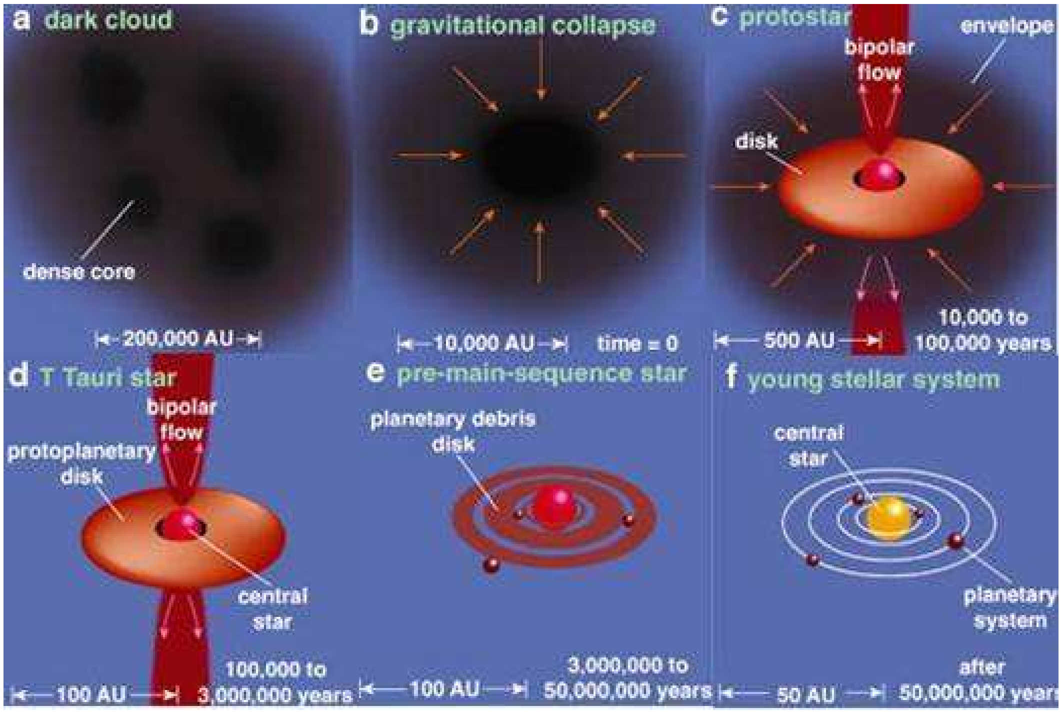

Figure 2.2: A cartoon representation of the current low-mass star formation paradigm. This work is specifically targeting the T Tauri phase of evolution, shown in panel d. Graphic from Spitzer Science Center.

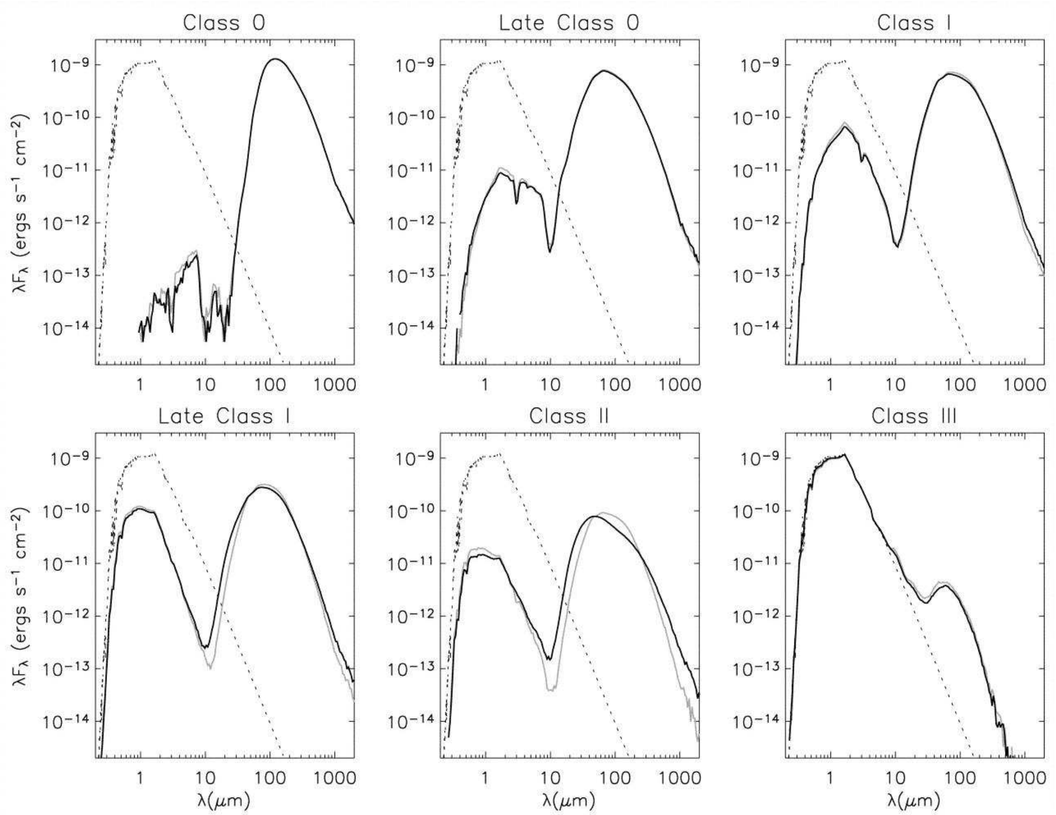

Figure 2.3: Monte-Carlo radiative transfer modeled spectral energy distributions (SEDs) are shown here as viewed from an almost completely face-on inclination angle of 87°. These models were generated with the T Tauri Star Radiative Equilibrium (TTSRE) code of Whitney et al. (2003a). For comparison, in each panel a stellar black body function is shown (dotted line), emphasizing how disk presence affects the SED.

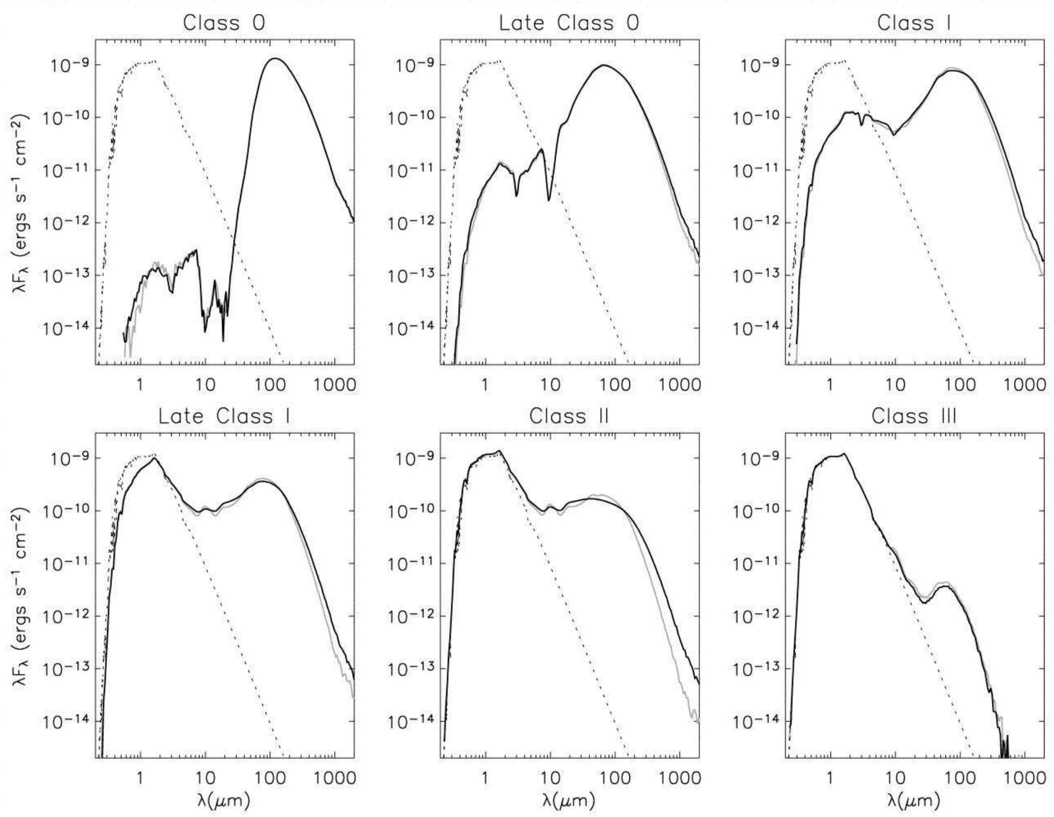

Figure 2.4: As in Fig. 2.3, model SEDs for the protostellar classes. An inclination angle of 56°is shown here (Whitney et al., 2003a).

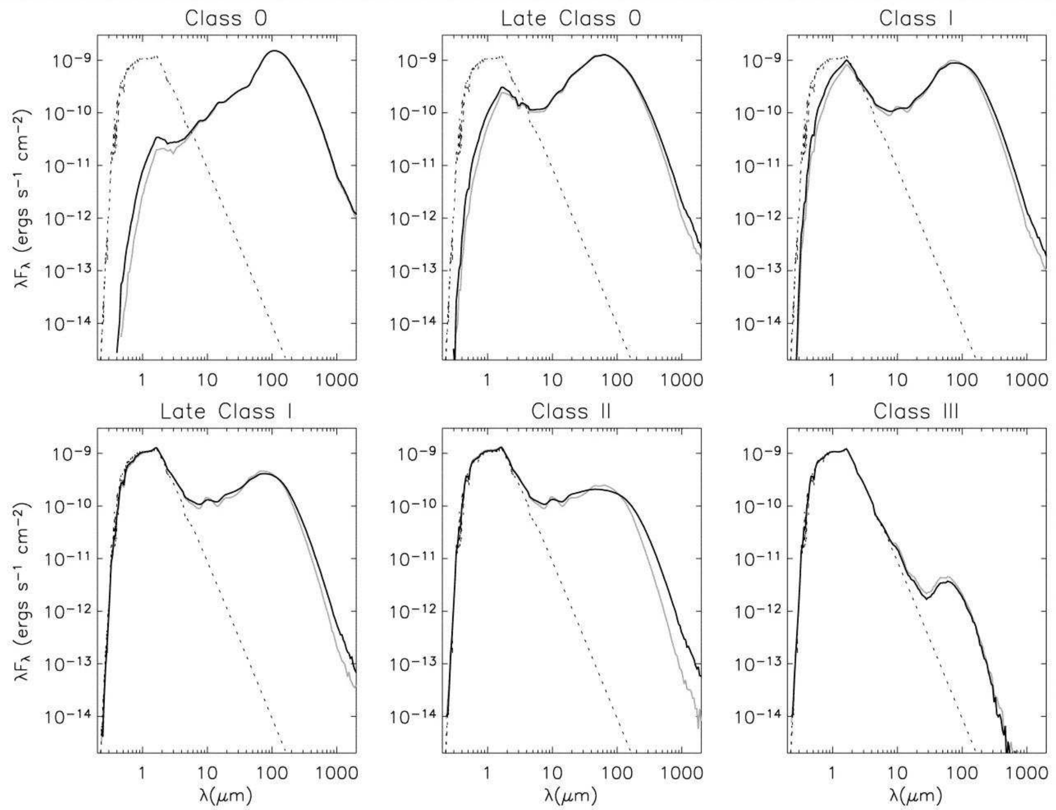

Figure 2.5: As in Figs. 1 and 2, spectral energy distributions for protostellar classes I-III. An almost pole-on inclination angle of 18 degrees is shown here (Whitney et al., 2003a).

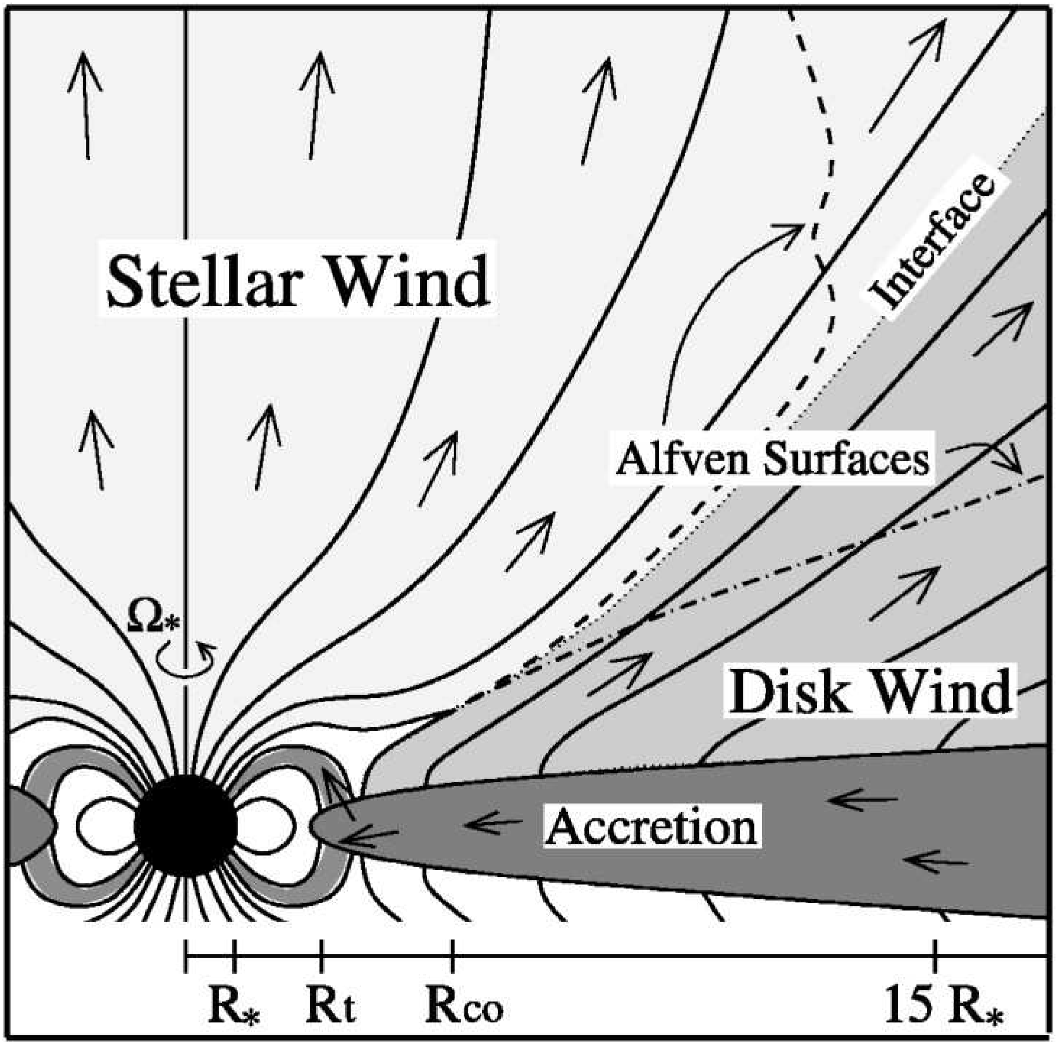

Figure 2.6: Schematic of an interacting star-disk system (Matt & Pudritz, 2005a). In this illustration, the stellar magnetosphere is connected to the inner edge of the disk, regulating angular momentum and material transport. The Alfvén surfaces represent places where star or disk wind pressures balance the ram pressure of infalling material.

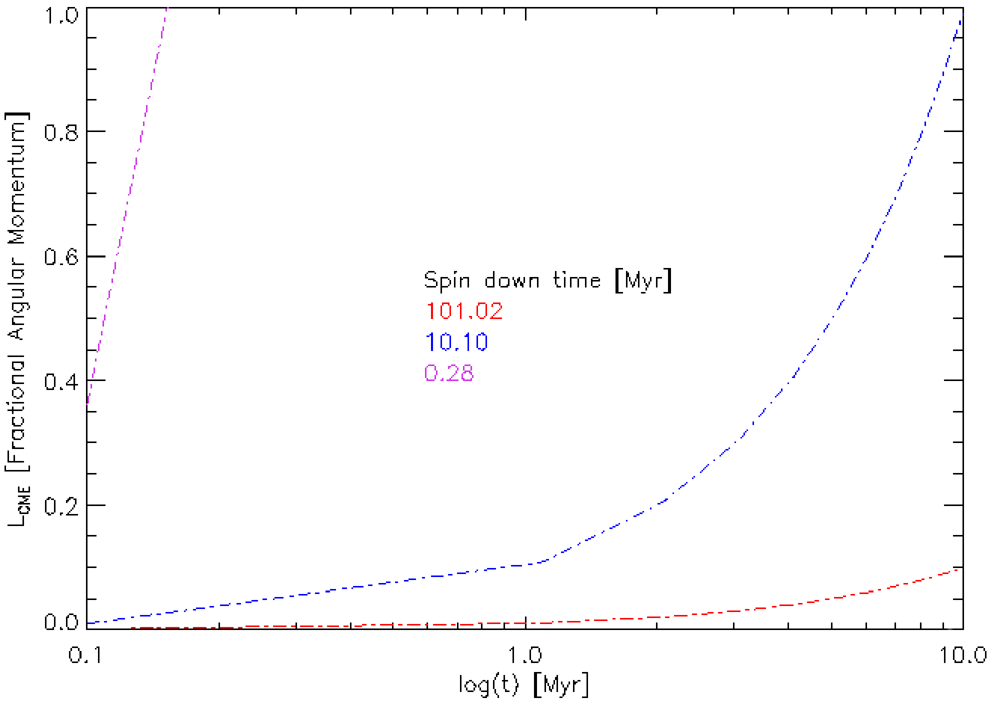

Figure 2.7: COUP 1410 is a young star observed by the Chandra Orion Ultradeep Project, a ~13 day long X-ray imaging campaign in the Orion Nebula Cluster. Favata et al. (2005) derived a flaring loop length of multiple stellar radii. Using the number density and an assumption of 1:1 loop mass:mass loss ratio, Aarnio et al. (2007) derive angular momentum loss via repeated events of this magnitude. The red line represents an event rate of 1 per year, blue 10 per year, and purple is the unrealistic case of one flare per day. In Chapter V, we begin work to apply a realistic event rate and mass loss distribution including flares of varying magnitudes and frequency; the anticipated result is a spin down time between 10 and 100 Myr.

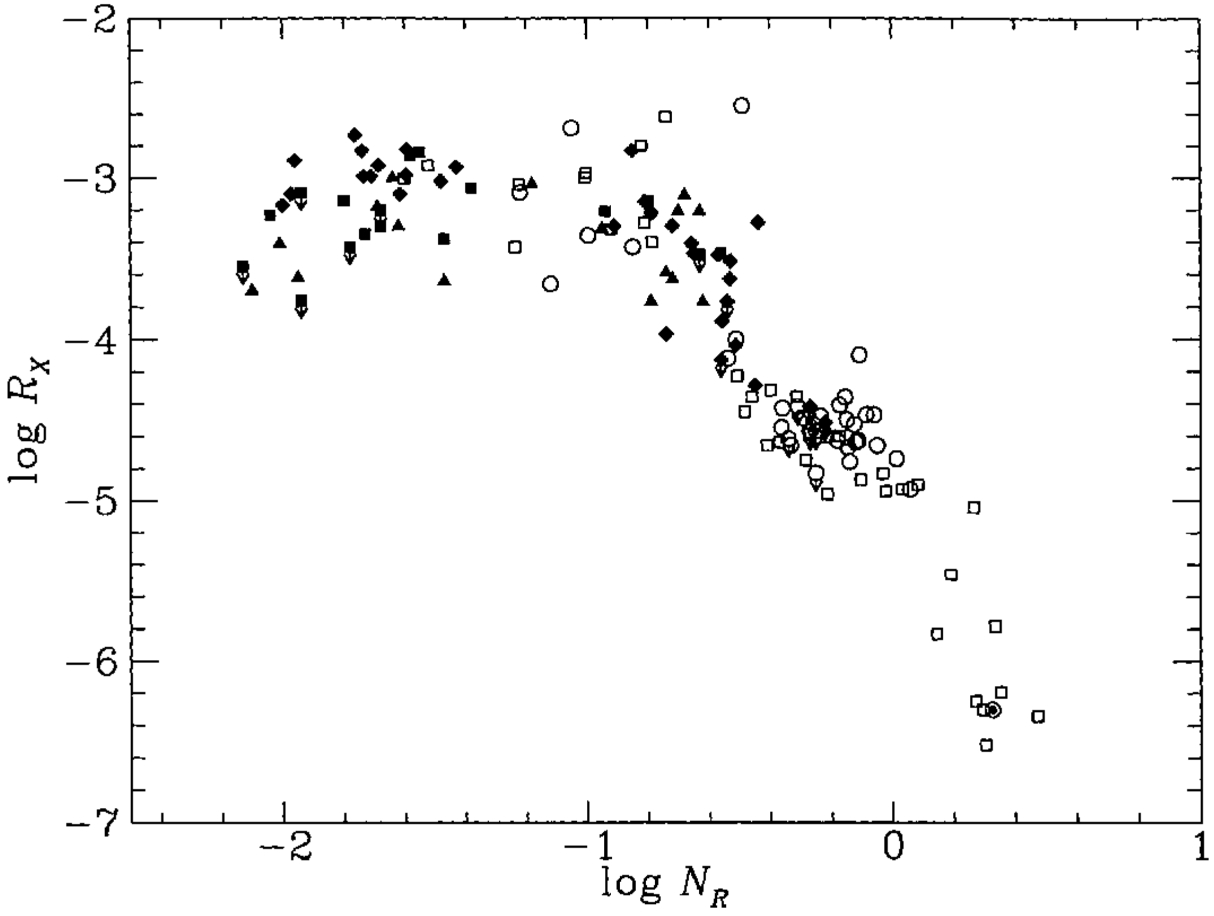

Figure 2.8: In this figure, Jeffries (1999) demonstrates the empirically determined activity-rotation relationship. This relationship demonstrates that stellar rotation and X-ray activity are correlated. R_X is the ratio of X-ray luminosity (L_X) to total, or bolometric, luminosity (L_{bol}) and N_R is the Rossby number, also denoted R_O. The Rossby number is defined as $R_O \equiv \frac{P}{\tau_c}$, where P is the stellar rotation period and τ_c is the convective turnover time for that star. Points in the plot represent late type stars (F5-M5) from the following clusters: IC 2391− filled triangles, α Per− filled squares, Pleiades− filled diamonds, Hyades− open circles, field stars− open squares.

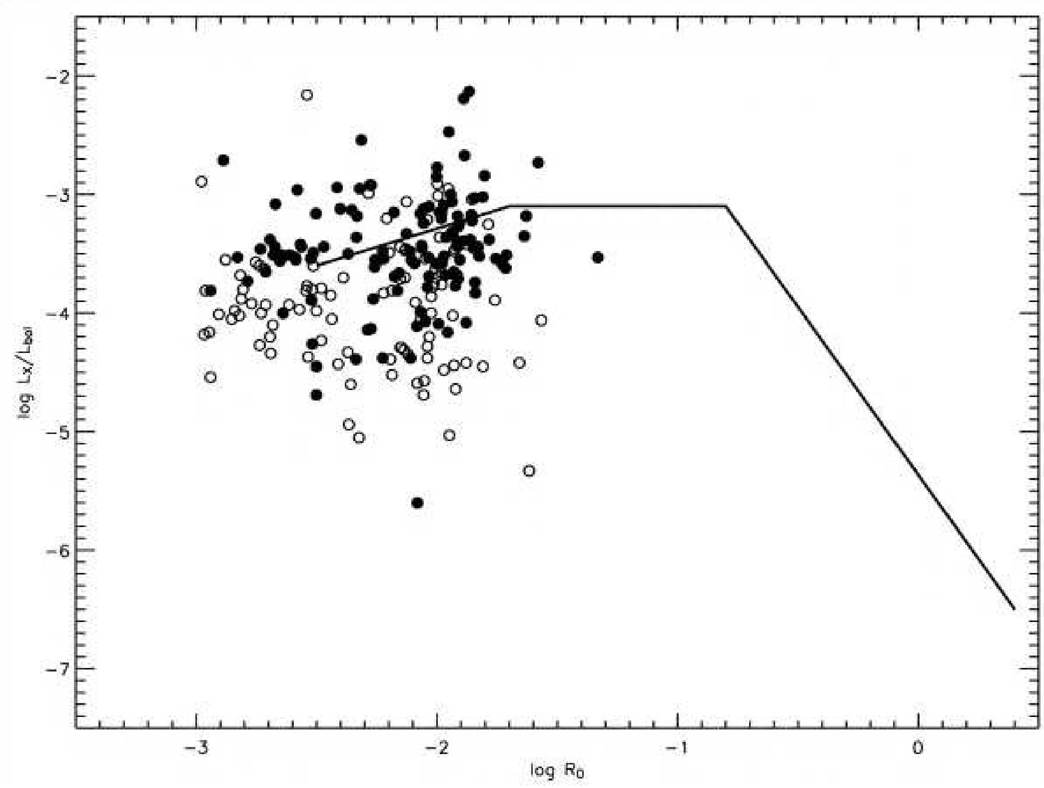

Figure 2.9: Rotation periods of PMS stars in the Orion Nebula Cluster (ages < 10 Myr) (Stassun et al., 2004a). As in the previous figure, the rotation-activity relationship for main-sequence stars is plotted as a solid line. Open circles are targets from Stassun et al. (2004a), filled circles are from Feigelson et al. (2002). There is a distinct dearth of points toward higher Rossby number; this could potentially be explained as an observational bias (cf., Stassun et al., 2004a, also see §2.2 for a description of cTTS versus wTTS X-ray emission)

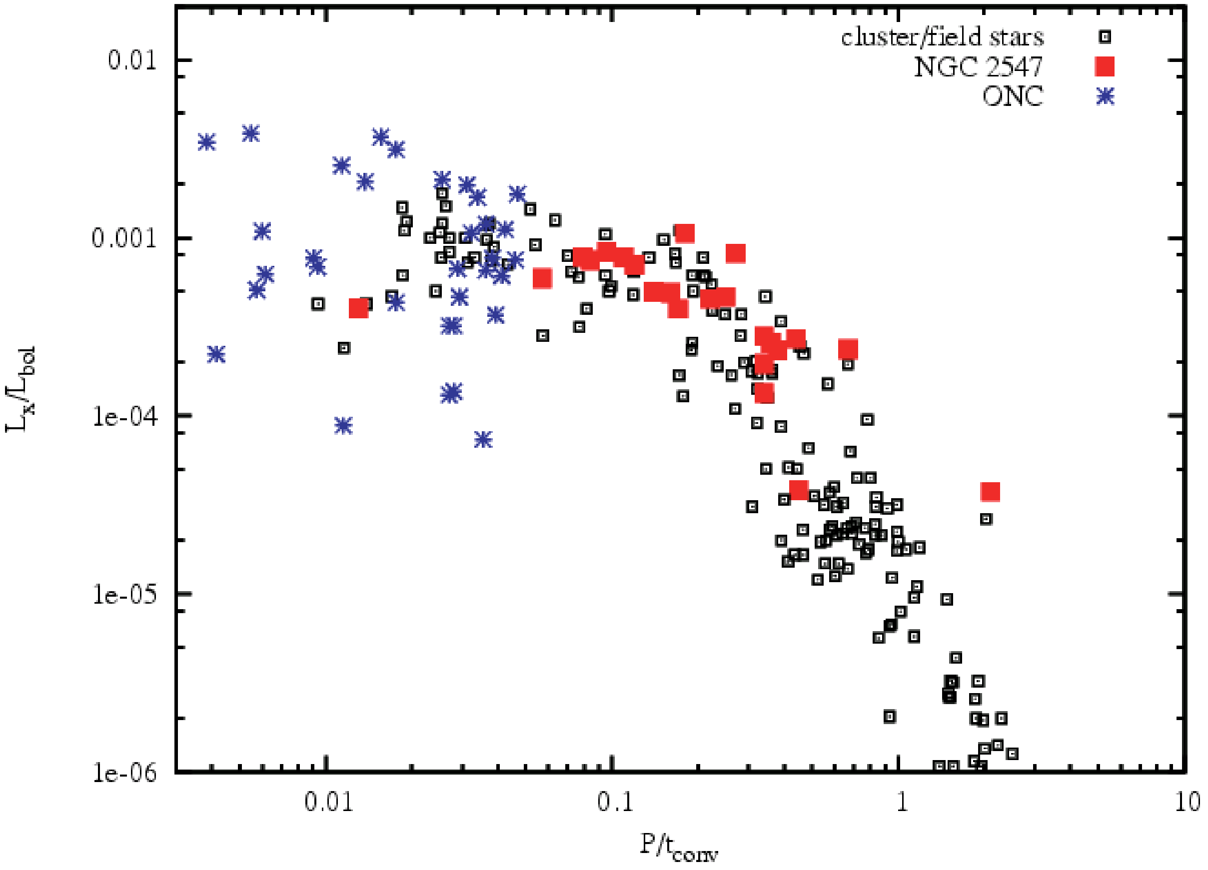

Figure 2.10: Similar to Fig. 2.8, this plot includes the ONC and a 30 Myr old cluster, NGC 2547 (Jeffries et al., 2006). The axes have different units and labels, but are the same as Fig. 2.8: $R_X \equiv L_X/L_{bol}$, and the Rossby number, $R_O \equiv P/t_{conv}$ (where t_{conv} is equivalent to τ_c. At 30 Myr, a time when low mass stars are approaching the zero age main sequence, the beginnings of a radiative core should be forming. This figure could be interpreted as an evolutionary progression from lower to higher Rossby number with age. This relationship, however, is quite complicated and includes the stellar rotation period. Pre-main sequence rotation evolution is not well understood. The process also is certainly a function of mass, which is frequently a model dependent parameter, these models are not yet well constrained, as only a few dynamical masses determined from low-mass eclipsing binary systems exist.

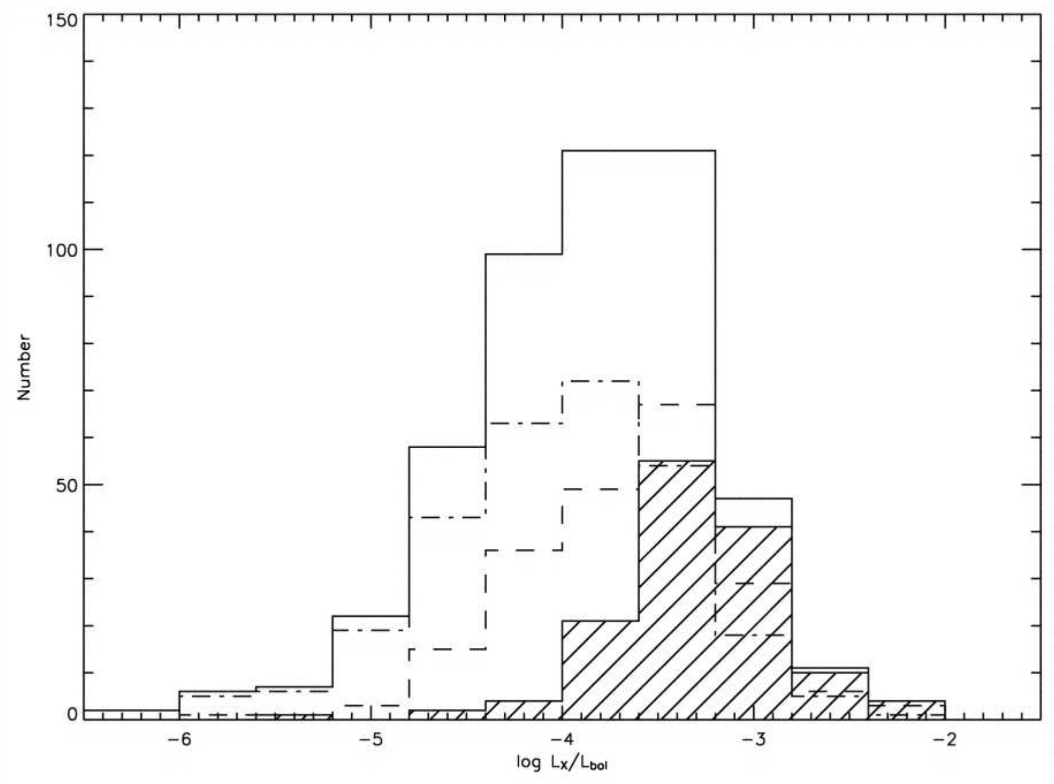

Figure 2.11: A histogram illustrating selection effects present in X-ray activity and rotation period measurements. The dashed distribution indicates stars with periods measured by Feigelson et al. (2002). The hatched bins represent where period measurements were made by Stassun et al. (2004a). The solid lined distribution accounts for all starts in the ONC which are bright enough to use optical photometry to measure rotation periods; this distribution includes both stars that do and do not have measured rotation periods. Finally, the dot-dashed distribution indicates stars lacking measured rotation periods. There is a clear bias in that rotation period measurements for X-ray bright sources are more complete; this means cTTS have been systematically excluded, and thus a rotation-period relation for <5 Myr is undefined.

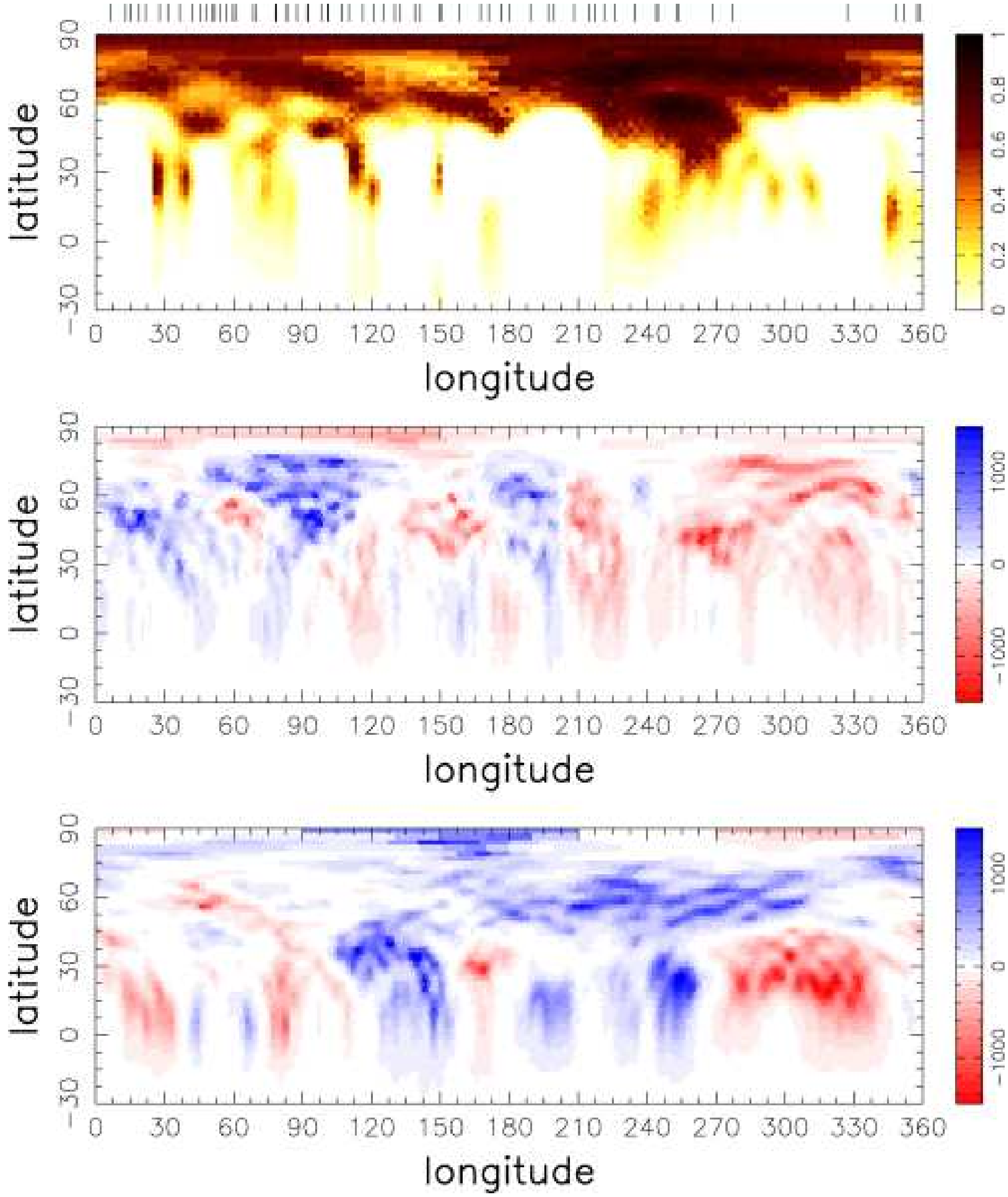

Figure 2.12: Zeeman-Doppler images of AB Dor by Hussain et al. (2007). The upper panel is a spot map, with black indicating starspot presence and white bare photosphere. The middle and bottom panels map the radial and azimuthal fields respectively; blue and red indicate ±1300 G. These data were taken in 2002, and well represent AB Dor's characteristic field structure. AB Dor is observed at an inclination of 60°, and thus coverage is limited to -30° latitude and above. At a very close distance of 40 pc, AB Dor is an ideal candidate for studies such as this.

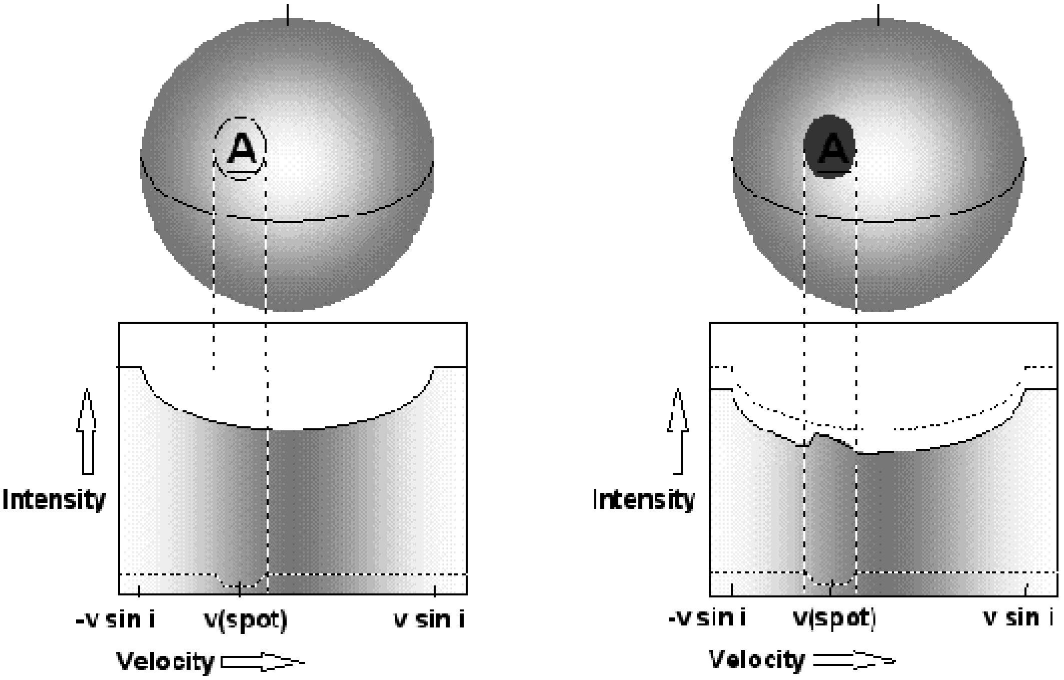

Figure 2.13: This cartoon illustrates how Doppler imaging works. When a spot crosses the stellar surface at a given latitude, there is a net decrease in continuum flux observed, but a contribution remains in every absorption feature that is Doppler shifted by an amount dependent on the spot's latitude. By taking time-series spectra, the motion and location of spots can be determined by modeling these contributions to the stellar absorption lines. Image by A. Collier Cameron.

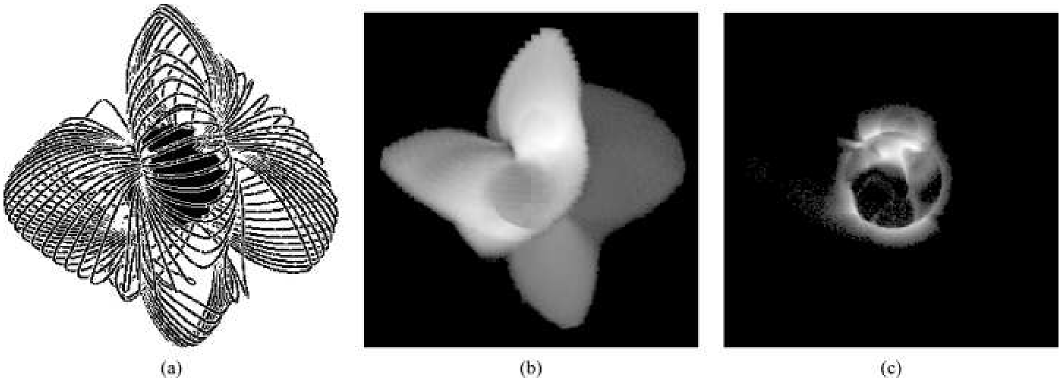

Figure 2.14: This model of the star AB Dor from Jardine et al. (2002) illustrates the effect of temperature on coronal X-ray emission measure. The left figure is the large-scale magnetic field extrapolated from surface Zeeman-Doppler imaging. In the middle, an emission measure image is shown, generated using a temperature of 10^7 K and an emission measure weighted density of $4{\times}10^8$ cm^{-3}. The right panel is also an emission measure image, but a temperature of 10^6 K and a corresponding emission measure weighted coronal density of $2{\times}10^8$ cm^{-1} was used. The emission measure may be raised by the change in structure density and scale height that results from temperature alteration; effectively, higher temperatures "puff out" the plasma confining magnetic loops while maintaining a higher density within the upper reaches of the loops. Denser material is thus lifted to radii which remain visible over multiple rotation periods and continually contribute to the overall emission measure.

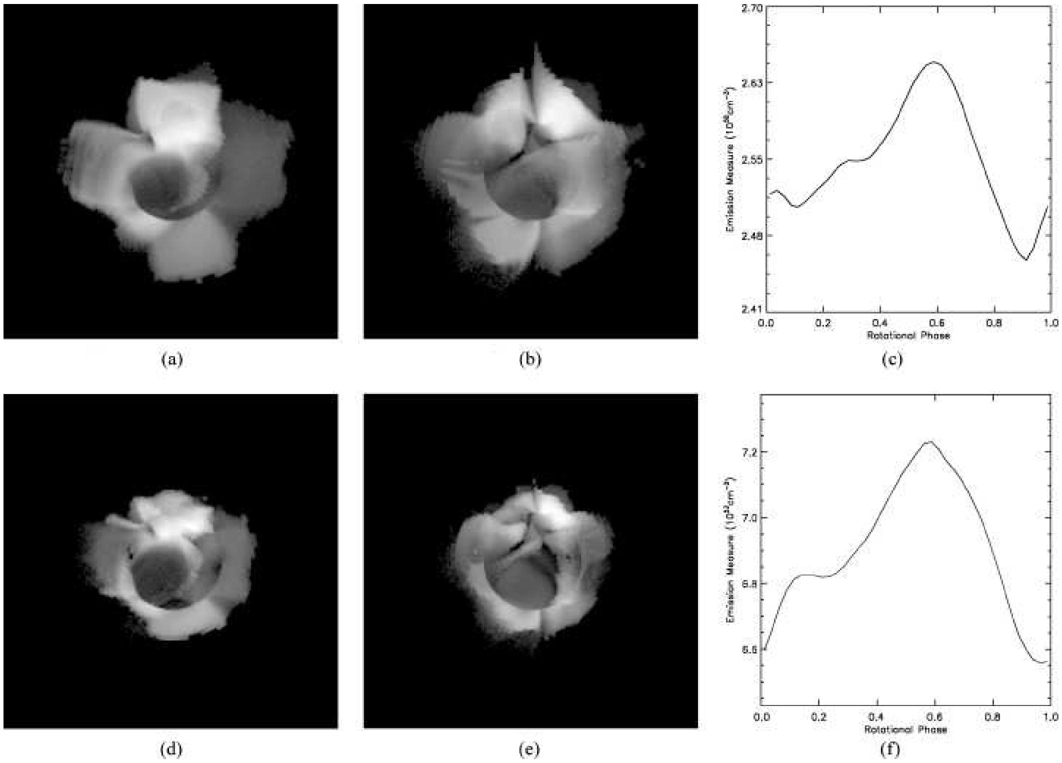

(a) (b) (c)

(d) (e) (f)

Figure 2.15: In this figure, Jardine et al. (2002) illustrate how changes to coronal number density affect the observed emission measure from X-ray spectra. The star in question is again AB Dor, and the field structure used is that of Fig. 2.14. The temperature used is 10^7 K; the top row of images were generated with an emission measure weighted density of 4×10^8 cm^{-3}, and the bottom row used models with $n_e = 1.5\times10^{10}$ cm^{-3}. It is unsurprising, knowing that emission measure $\sim n_e^2$, that the magnitude of the emission measure increases as n_e increases. The resulting more compact coronal structure in the cooler temperature case is attributed to the rise in plasma pressure forcing magnetic field lines open, thereby resulting in the reduction of the emitting volume of the corona.

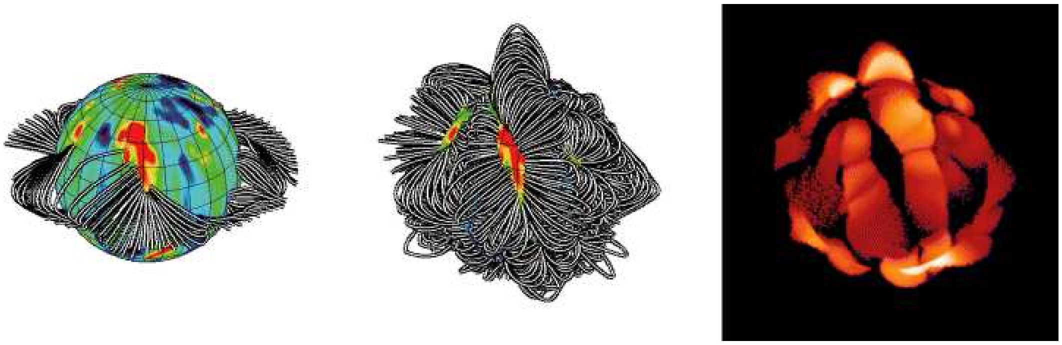

Figure 2.16: Magnetic field topology of a T Tauri star whose disk confines coronal structure (Jardine et al., 2006). Known stellar parameters used for modeling were the mass, 0.15 $M_\odot$, radius, 4.02 $R_\odot$, and a rotation period of 17.91 days. The coronal extent would, at most, be 1.58 $R_{\mathrm{corotation}}$. The left panel shows field lines that are available for accreting disk material. Field lines that are closed and could confine X-ray emitting gas are plotted in the middle panel. To the right, an X-ray emission image is shown; the X-ray flux clearly illuminates the field line structure, which is consistent with solar observations.

CHAPTER III

A SURVEY FOR A COEVAL, COMOVING GROUP ASSOCIATED WITH HD 141569

3.1 Stellar Associations

The HD 141569 stellar system initially garnered the interest of Rossiter (1943) as a potential triple star system. The existence of this group was confirmed over half a century later when Weinberger et al. (2000) showed that the stars' position angles relative to one another had not changed since Rossiter's 1938 observations, thus confirming common proper motions. They also noted that all three stars are consistent with being the same age, indicating a comoving and coeval system. This triumvirate is particularly interesting because all components are quite young; the age of the system was found to be 5±3 Myr (Weinberger et al., 2000), and recently the A star's age was constrained using surface gravities and effective temperatures to be ∼4.7 Myr (Merín et al., 2004). HD 141569 itself is near enough to resolve its large, dusty disk, and near-infrared signatures indicate perturbations to the disk's structure which could be explained by planet formation (Weinberger et al., 1999). Were a coherent group present, it would therefore be distinctly possible to similarly observe additional young, disk-bearing stars. Furthermore, surveying a coeval sample at this distance would be useful for determining disk frequency and mechanisms by which they arise and evolve.

In some cases, seemingly isolated young stars have later been found to have an entourage of other low-mass young stars which constitute a stellar association (e.g. HD 104237, HR 4796, β Pictoris; cf. Mamajek et al., 2002; Li, 2005). The lower mass members of these associations have been useful for estimating the age of the massive star in question, as often the massive star is on the main sequence and the uncertainty in its Hertzsprung-Russell diagram (hereafter HRD or H-R diagram, §3.4.3), position is substantial enough to impede an isochronal age estimate. Any additional association members should be identifiable by their similar space motions. The youth of these objects makes them useful for studies of circumstellar disks and stellar evolution. In this region of sky rich with already identified associations such as ρ Ophiucus, Upper Scorpius (US) and Upper Centaurus Lupus (UCL), placing an "HD 141569 Association" into context with surrounding moving groups could aid in understanding the star formation histories in giant molecular clouds.

So motivated, in this work we seek to identify a sample of stars associated with HD 141569. Previous studies (e.g. Mamajek et al., 2002; Li, 2005) have shown that catalog searches based on X-ray activity, proper motions, and distance criteria can yield new members of associations. Here we also identify candidate members with a catalog search for X-ray active stars in the vicinity of HD 141569 possessing proper motions consistent with HD 141569 (§3.2.1). From new spectroscopic observations (§3.2.2), in §3.3 we identify a subset of 21 stars which we claim as youthful using Li I equivalent widths; furthermore, we also note the presence of Hα emission as an interesting quantity usually indicative of chromospheric activity. Lacking direct distance measurements for these stars, we derive distances using a modified version of the traditional moving cluster parallax method (de Bruijne, 1999; de

Zeeuw et al., 1999; Mamajek, 2005), with which we further determine the probability that the sample stars are comoving with HD 141569 (§3.3.4).

Placing these stars on a H-R diagram, we find that the stars' distances—and hence ages—are most consistent with their strong lithium abundances when we derive their moving cluster parallaxes assuming comovement with US or UCL associations of young stars. In §3.5 we summarize our study and present thirteen newly identified Sco-Cen members.

3.2 Characterizing An Association of Young Stars

3.2.1 Target Selection

Potential targets for observation were found by two catalog queries for stellar properties indicative of youth and comovement with HD 141569. In the first search, 10 stars were found through a query of the *Hipparcos* catalog (Perryman & ESA, 1997) for objects within 10° of HD 141569 with similar distances (99±8pc, as reported in Perryman & ESA, 1997) and proper motions. Eight objects from the *ROSAT* Faint Source Catalog (Voges et al., 2000) supplemented this sample, as previous low-resolution spectroscopic observations (A. Weinberger, unpublished data) showed evidence for spectroscopic signatures indicative of youth. A second search was performed in which the *ROSAT* Bright Source Catalog (Voges et al., 1999) was probed for X-ray sources within a 30° radius of HD 141569. Of the 1,114 resulting targets, ∼400 sources had Tycho-2 (Høg et al., 2000) catalogued proper motions. We required proper motions to be within ±15 and ±20 mas yr^{-1} in RA and Dec of HD 141569's proper motion, respectively, based on the range of proper motions observed in the widely dispersed and similarly aged TW Hydrae Association (Zuckerman et al., 2001; Webb et al., 1999). Finally, we required that the *ROSAT* sources not be extended and that they be cospatial with the Tycho coordinates. This procedure resulted in ∼70 objects desirable for further study to establish youth and space motions. A map of the observed sample is shown in Fig. 3.1; members of other nearby associations are also shown for added context and perspective.

3.2.2 Observations

Forty-nine stars of our input catalog were observed spectroscopically over the course of three observing runs in order to measure spectral types, radial velocities, and Li I and Hα equivalent widths. Four targets were found to be close visual binaries so their companions were observed as well; of these four, two were determined to be background objects on the basis of apparent magnitudes and spectral type in comparison to the primary and are thus not discussed further. An observing log of the 51 stars (49 targets + 2 visual companions) which form our final sample for this work is presented in Table III.1. Photometry, proper motions, and parallax measurements from the literature are documented in Table III.2.

On 2001 June 18 (UT), the ten *Hipparcos* selected targets and five FSC targets were observed using the Hamilton Echelle Spectrometer at Lick Observatory. The Hamilton echelle covers a wavelength range of ∼3,500-10,000 Å with a resultant resolving power of 60,000 at 6,000 Å when using a slit width of $1\farcs2$. During April 2002, a further 36 target stars of the second catalog search were observed using the echelle spectrograph on the Irénée du Pont telescope at Las Campanas Observatory. The du Pont spectrograph observes a wavelength range of ∼3,700-9,800 Å with a resolving power of 40,000 at a slit width of $0.75''$. On both observing runs, comparison arc spectra were taken to establish a pixel to wavelength calibration. At LCO, thorium-argon lamp spectra were taken between each object exposure because the spectrograph is situated at the Cassegrain focus, whereas the Coudé-fed Hamilton echelle required less frequent arc calibration, with arc spectra taken at the beginning and end of each night.

3.2.3 Reduction Procedure

The echelle data were reduced using IRAF[1] to perform standard spectral reduction procedures. Instrumental effects were accounted for via measurement of bias level and read noise, variations in pixel-to-pixel CCD response were removed in the flat fielding process, and dead columns were identified (which then prevented measurement of the Hα 6563 Å line). A basic reduction process was then followed to locate and extract the echelle orders as well as remove scattered light. The thorium-argon arcs were similarly extracted, their features identified so as to wavelength calibrate the object spectra.

---

[1] Image Reduction and Analysis Facility, IRAF, is distributed by the National Optical Astronomy Observatories, which are operated by the Association of Universities for Research in Astronomy, Inc., under cooperative agreement with the National Science Foundation.

3.3 Analysis

We aim to identify the subset of our sample which shows evidence for youth consistent with membership to a young, ∼5 Myr-old association. Additionally, we wish to assess kinematic properties and test for comovement. To these ends, from the literature, we obtain effective temperatures, infrared photometry, and proper motions. From the spectra, we measure Li I equivalent widths and radial velocities. Utilizing these data, we estimate ages and select a high lithium, and therefore presumably youthful sample, and we test for kinematic similarity against the velocity models of nearby, young moving groups (Sec. 3.4.2).

3.3.1 Effective Temperatures

Spectral types for the majority of the stars in our sample are reported in the literature (Houk, 1982; Houk & Smith-Moore, 1988; Houk & Swift, 1999; Torres et al., 2006). These are converted to $T_{\rm eff}$ using the main-sequence spectral type–$T_{\rm eff}$ relationship of Kenyon & Hartmann (1995). We supplement these with spectral types determined from low-resolution spectra obtained with the Lick KAST spectrograph (A. Weinberger, unpublished data) as well as $T_{\rm eff}$ determined from the Fe I to Sc I line ratio (cf. Stassun et al., 2004b; Steffen et al., 2001) observed in our high-resolution spectra (§3.2.2). The line ratios measured for our spectral type standards are in good agreement with the calibration of Basri & Batalha (1990); we thus adopt their line ratio-spectral type scale in assigning types to our sample. In some cases, primarily for more massive stars, the Fe I and Sc I lines were not present or could not be measured with confidence above the noise level. $T_{\rm eff}$ values are summarized in

Table III.3. Where multiple $T_{\rm eff}$ values are available, they generally show good consistency with one another to within $\sim$ 300 K (corresponding to $\sim$ 2 spectral subclasses). For our final set of effective temperatures, we adopt literature spectral types where available, line ratio spectral types if not. For one object, HD 157310B, neither was available, and thus we interpolated its 2MASS (2 Micron All Sky Survey, Skrutskie et al., 2006) $(H - K_s)$ color over the effective temperature-color relationship of Kenyon & Hartmann (1995). The set of adopted temperatures is reported in the final column of Table III.3.

In Fig. 3.2 we show these effective temperatures as a function of the objects' observed 2MASS $(H - K_s)$ colors; also plotted is the $T_{\rm eff} - (H - K_s)$ relationship from Kenyon & Hartmann (1995). For comparison, the standard stars observed (Table III.1) are also shown in this parameter space. The observed $(H - K_s)$ colors follow the expected relationship with $T_{\rm eff}$ with a scatter of $\sim$ 300 K, consistent with the scatter in $T_{\rm eff}$ from spectral types above. This indicates that our sample in general suffers relatively little extinction. Indeed, radio survey column-density measurements (Kalberla et al., 2005) in the direction of our targets indicate that $E(H - K_s)$ reddening toward our sample should be $\lesssim 0.1$ mag. Via comparison with expected intrinsic $(H - K_s)$ for a star of given effective temperature, we derive K_s band extinction values, A_{Ks}, and deredden the sample accordingly. $(H - K_s)$ colors are plotted in Fig. 3.3; lines illustrate dereddening by connecting colors before and after dereddening. Also displayed for comparison are the dwarf sequence from Bessell & Brett (1988) as well as reddening vectors assuming the standard ratio of total-to-selective extinction $R_V = 3.12$. For visual clarity, we only display the 21 targets identified as lithium rich (§3.3.2). The

K_s-band extinction corresponding to the applied dereddenings is in all cases $A_{Ks} < 0.15$ mag, with the exceptions of 2MASS J17215666-2010498 and TYC 6191-0552-1 (objects #19 and #2 in the data tables) for which $A_{Ks} = 0.33$ mag and $A_{Ks} = 0.16$ mag, respectively. We have checked *Spitzer* 24 μm data (A. Weinberger, private communication) and find that while most of the high lithium sample lacks 24 μm excess, 2MASS J17215666-2010498 has a substantial excess. TYC 6191-0552-1 was analyzed by Meyer et al. (2008) and was found to have moderate 24 μm excess. For both objects, the apparent excess in the H and K_S bands, in concert with 24 μm excess, confirms disk presence and thus we cannot and do not apply a standard interstellar dereddening law.

3.3.2 Lithium Equivalent Width

We measured the equivalent width (EW) of the λ6707 line of Li I from our spectra using the IRAF routine *Splot*. For each star, EW measurements were obtained by both directly integrating the flux in the line and by calculating the area of a best-fitting Gaussian. Our measured EW values include contributions from the small Fe I+CN blended line at 6707.44Å, leading to measured Li I EWs that are representative of a slightly (10-20 mÅ) over-estimated photospheric Li presence. For instance, Soderblom et al. (1993) report that this Fe/CN line blend has an EW = [20(B-V)$_0$-3]mÅ for main sequence solar-type stars. We correct for contamination following this prescription and find the median value for the sample is 10 mÅ; we report in Table III.3 the Li I EWs for each target via both measurement methods as well as the Fe line blend contribution. For all targets, the RMS of the difference between the

EWs determined using both methods is 18.4 mÅ. With the aim of conservatively selecting a sample, we use the lower of the two measured values; these are plotted in Fig. 3.4.

To identify the young stars in the sample, Li I EWs were compared to the upper envelope of EWs as a function of $T_{\rm eff}$ reported in the literature for the $\sim$ 30 Myr-old clusters IC 2602 and IC 2391 (Randich et al., 1997, 2001, our Fig. 3.4). Twelve stars are found to have Li I EWs above this envelope, which is compelling evidence of youth. In what follows we refer to these 12 stars as the "high Li" sample.

Also of interest, the Hα profiles of several objects are in emission in our spectra and some possess double-peaked profiles. Another 6 stars show elevated lithium levels ($\gtrsim$ 200 mÅ but are below the threshold shown in Fig. 3.4), placing them in the upper envelope of the IC 2602 and IC 2391 loci. An additional two stars have temperatures greater than 7,500 K and equivalent widths above the locus; although these are potentially older stars which simply lack deep enough convective zones to deplete primordial lithium abundances, we include them in the analyses for completeness. We also include star #13 in this group, as it is in a double system separated by $\sim 1''\!.2$ while the seeing that night was $\sim 1'\!.5$, making Li line filling likely. In Fig. 3.4, this star is plotted with its measured equivalent width doubled (denoted "13b") to demonstrate which sample group it would potentially belong to. In what follows, we refer to these nine stars as the "moderate Li" sample, two of which show double-peaked Hα in emission (Table III.3).

These 21 stars, which are the most likely in our sample to be of comparable age to HD 141569, will be the focus of the remainder of our analyses. For ease in tracking these stars through our analysis, they are labeled with a running numerical identifier in the data tables and figures, and all EW and line profile information is reported in Table III.3.

3.3.3 Radial Velocity

Heliocentric radial velocities were obtained using the IRAF task *fxcor* to cross correlate each target spectrum against the radial-velocity standard star of closest spectral type (Table III.1). Four echelle orders spanning the wavelength ranges 6025-6150Å, 6150-6275Å, 6625-6750Å, and 5120-5220Å were employed, as they contain many deep metallic lines and little or no telluric contamination. In Table III.4 we report the mean radial velocities from the four orders.

To determine the extent to which our radial-velocity measurements may be affected by the $v \sin i$ and signal-to-noise (S/N) of our target spectra, we performed a Monte Carlo simulation in which a narrow-lined, high S/N standard star spectrum was randomly degraded one hundred times. This process created artificially noisy spectra at S/N levels of 10–100, well representing the full range of S/N found in our sample. Each degraded spectrum was artificially broadened and cross-correlated against its original high S/N spectrum. These degraded spectra were furthermore cross-correlated against the other standard stars to assess the effects of spectral-type mismatch on the resulting radial velocities. We find that these effects are negligible (i.e., affecting the resulting radial velocities by $\lesssim 1$ km s^{-1}), unless $v \sin i > 70$ km s^{-1} or S/N < 30. As all of our target spectra have S/N > 30, only very fast rotators are potentially affected (by up to 2.3 km s^{-1} for $v \sin i = 100$ km s^{-1}). Measured $v \sin i$ and radial velocity values are documented in Table III.4. In addition to these effects, we note that on an aperture-to-aperture basis, errors in wavelength calibration could affect the measured radial velocity; this can be quantified as the standard deviation of the mean radial velocity measured from the four selected apertures. The final radial-velocity uncertainties quoted in Table III.4 are the quadrature sum of the internal uncertainty (the standard deviation of the four spectral orders used) and the uncertainty arising from rotational broadening.

3.3.4 Moving Cluster Parallaxes

With observed proper motions and measured radial velocities for the 21 "high" and "moderate" lithium stars, a kinematic picture of the sample is almost complete. Tycho-2 proper motions were used for consistency throughout (Table III.2), the only exception being one of the two close visual binary companions, HD 157310B, for which only UCAC2 (Zacharias et al., 2004) proper motions were available. Proper motion data are not available for the other close companion, 2MASS J17215666-2010498; in what follows, we assume common proper motion with its primary star, TYC 6242-0104-1. *Hipparcos* parallaxes are unavailable for the high lithium stars, thus a moving cluster parallax method (de Bruijne, 1999) provides a means for determining their parallaxes and hence their distances. With distances, it can be tested then whether these objects are consistent with being members of a coherent moving group.

Our procedure is rooted in the derivation of de Bruijne (1999, see their §2 and references therein). The process is executed assuming a velocity vector, and hence a convergent point, for the moving group to which we are testing membership. In analyzing the spatial distribution of the 21 stars of our youthful sample, we note they are all in closer proximity to US and UCL than HD 141569 (see Fig. 3.5). The youthful sample is highly spatially separated from HD 141569, and these separations indicate two kinematic issues. First, it is unlikely for objects with such large separations to be comoving. Second, had these stars indeed formed together, large initial velocities (∼6 km s^{-1}, inconsistent with the observed 1-2 km s^{-1} velocity dispersions of young associations) would be required to bring about the separations presently observed after ∼5 Myr of motion. As it is unlikely these objects are associated with HD 141569, we require estimates of the mean velocity vectors for US and UCL. The velocity vector for US is adopted from Mamajek (2008): $UVW = [-5.2, -16.6, -7.3]$ km s^{-1}. This vector incorporates a mean radial velocity for 120 US members, an improvement over prior velocity vectors which solely rely upon proper motion and parallax information. For UCL, the velocity model used for comparison is derived from the median position, proper motion, and radial velocities of UCL members (de Zeeuw et al., 1999); $UVW = [-5.4, -19.7, -4.4]$ km s^{-1}. We calculate these UVW vectors for US and UCL to precisions of $\sim \pm 0.3$ and $\sim \pm 0.4$ km/s respectively, but note there exist discrepancies between UVW vectors derived by various authors.[2] The reason for the systematic differences between published convergent points and velocity vectors for the OB subgroups is not completely clear. The leading candidates for these systematic differences are unaccounted-for expansion of the subgroups

---

[2] For example, Madsen et al. (2002) calculate for US $UVW = [-0.9, -16.9, -5.3]$ km s^{-1}. de Bruijne et al. (2001) cite $UVW = [4.1, -17.9, -3.7]$ km s^{-1} (with model-observation discrepancy parameter "g" set to equal nine) while de Zeeuw et al. (1999) report $UVW = [0.0, -16.1, -4.6]$ km s^{-1}.

and the probable presence of unresolved spatial and kinematic substructure within the subgroups. For robustness, we include all available radial velocity measurements in derivation of UVW vectors.

For each of the 21 stars in our "high lithium" and "moderate lithium" samples, we derive moving cluster parallaxes using the HD 141569 and US velocity vectors (Table III.4). The formalism for this is:

$$\varpi = \frac{A\mu_{\upsilon}}{\upsilon \sin(\lambda)} \tag{3.1}$$

where ϖ is the parallax, A is 4.74 km yr s^{-1} (1 AU in convenient units of km times the ratio of one Julian Year in s), μ_{υ} is the parallel component of proper motion (proper motion in the direction of the convergent point), υ is the velocity of the group in km s^{-1}, and λ is the angular separation between the star and the convergent point (formula 1, Mamajek, 2005). An additionally useful parameter, the comovement probability, can also be calculated. Comovement probability is defined as $1-P_{\perp}$, where $P_{\perp}$ is the likelihood that the star's proper motion is entirely perpendicular to the direction of the convergent point; the projection of proper motion in this direction is denoted μ_{τ}, and a μ_{τ} close to 0 is indicative of comovement.

3.4 Results

3.4.1 Distances, comovement probabilities, and membership

The spatial proximity of our youthful sample stars to US and UCL (Fig. 3.5) suggests that these objects are not likely related kinematically to the farther away HD 141569 system. It is important to stress at this juncture that derived comovement probabilities are not absolute probabilities per se; their derivation depends directly on the velocity model assumed *a priori*. We do know with high confidence that the stars in our sample are young (by virtue of their high Li abundances) and that they are moreover in projected proximity to other stars known to be young, nearby, and comoving (Fig. 3.1). Thus there is a strong “prior” favoring the velocity models that we have chosen to test. Still, the comovement probabilities reported in Table III.4 should be regarded as measures of *consistency* with the assumed velocity models, not proof of membership. We therefore adopt the very simple criterion of spatial proximity to a group in application of velocity modeling, and report the resulting distances and comovement probabilities for objects when tested against the velocity vectors of US and UCL. Parallax distances and comovement probabilities calculated as previously described (§3.3.4) are reported in Table III.4.

Based on two simple criteria, youth determined via measurement of the $\lambda6707$ line and spatial position, objects 2, 6, 7, 8, 9, 11, 13, 15, and 21 lie within the US “box” as defined by de Zeeuw et al. (1999). Similarly, stars 4, 5, 14, 17, and 20 appear to be UCL members. These “spatial matches” are summarized in column 3 of Table III.5. Due to the similarities of velocity vectors in the Ophiucus-Sco-Cen region, it is unsurprising that in some cases, objects we deem US or UCL members have higher comovement probabilities when tested against the velocity vector of the other group. Factors which create blurring of kinematic boundaries include internal velocity dispersions inherent to a given moving group and observational uncertainties which then propagate into the convergent point solution. We thus take (ℓ, b) position as the strongest indicator of group membership and then examine comovement probabilities as a supplement. Outside of the US box, stars 3, 12, and 18 have high comovement probabilities with US. We would present 12 and 18 with some caution as US members, as they are within a few degrees of the most extended, already known US members.

Object 3 is almost ten degrees away from the southernmost US stars and thus its association with US is also dubious. For these three objects, we tentatively suggest US membership and denote their membership in Table III.5 as “US?” In two cases we note objects with low comovement probabilities with their spatially matched groups: objects 1 and 19 do not have velocities consistent with US and are spatially inconsistent with being UCL members. Object 15, while spatially coincident with US, has low enough comovement probability to be suspect. Finally, stars 10 and 16 have high comovement probabilities with US, but appear to be too far away in (ℓ, b) space to be considered part of US. These remaining five objects we also classify as being of “indeterminate” membership. In summary, the total number of new US members presented here is eight, and five new members of UCL are also identified.

3.4.2 Space Motions

To illustrate kinematic association in a familiar way, we could use the transformation matrices of Johnson & Soderblom (1987) to calculate UVW space motions for the sample stars. UVW motions, however, depend on distance, a quantity we have obtained via assumption of comovement with a given UVW vector. The resulting UVW plot is thus degenerate and does not provide additional criteria by which we can further examine association.

As an additional check on the application of each velocity model, given an assumed velocity vector, radial velocities for each object can be predicted based on their proper motions and positions. We find consistency between the predicted radial velocities and those measured when comparing measured radial velocity to predicted radial velocity for whichever velocity model we would naïvely expect given simple spatial proximity to a given moving group. Illustrating the radial velocity structure of the sample in context with nearby groups can be a measurement-based, assumption-free way of analyzing space motions. In the selection criteria, we constrained proper motions to agree with those of HD 141569 within a wide range of values that includes proper motions generally observed in US. Measured radial velocities and projected radial velocities for the US velocity vector are plotted as a function of galactic longitude in Fig. 3.6. Most notably, the entire "high Li" sample agrees well with the predicted radial velocities of US within $\sim$2-3σ. The farthest outlying points are from the "moderate Li" sample.

3.4.3 H-R Diagram

In Fig. 3.7 we show the placement of the sample stars on three H-R diagrams to illustrate shifts in M_{Ks} magnitude due to changes in distance. Absolute magnitudes were calculated from the observed 2MASS K_S magnitudes (Table III.2) and one of three distances. Uncertainties in M_{Ks} are the propagated errors of the 2MASS photometry together with the formal errors in distance. The uncertainty in $T_{\rm eff}$ is taken to be two spectral subtypes (see §3.3.1). To derive ages for our sample stars, we also show the pre-main-sequence (PMS) evolutionary tracks of Baraffe et al. (1998) and D'Antona & Mazzitelli (1997).

In the upper panel, we illustrate placement of the sample on the HRD when we apply the distance to the HD 141569 system to every individual object. The isochronal ages inferred for most stars in our sample using the HD 141569 mean distance are in general older ($\sim$ 30–100 Myr) than what would be expected for the stars based on their lithium abundances and comovement with the HD 141569 system (age 5 ± 3 Myr). In concert with the lack of spatial proximity, we further rule out the potential for a coeval, coherent moving group near HD 141569.

In contrast, the inferred ages using the US mean distance ($\sim$145pc, effectively equivalent that of UCL, $\sim$142pc) are entirely consistent with the expectation of $\lesssim$30 Myr as imposed by the Li EW measurements. All stars appear on or above the 30 Myr isochrone, save objects #10 and #16, which, despite their high comovement probabilities with US, do not appear to be in close enough spatial proximity to be members of that moving group. In the third H-R diagram, applied distances are determined by the velocity model, US or UCL, that provides the highest comovement probability with a given object. This particular representation is not only mostly consistent with the age range expected from Li I presence, it also "correctly" places the higher mass objects closer to the ZAMS; particularly, objects 10, 16, and 17 have derived distances which make them appear to be ZAMS stars rather than anomalous objects far above or below the theoretical isochrones.

Scatter in an HRD generally can be attributed to many factors; the radial extent of a young association (Mamajek, 2005, e.g., TW Hydra $\sim$55pc), observational errors, or even the choice of evolutionary tracks can generate shifts and enhance spread in the isochronal age of a sample expected to be coeval. Using the D'Antona & Mazzitelli (1997) evolutionary models, our sample stars all appear to have isochronal ages $\lesssim$10 Myr. In general, these tracks appear shifted by $\sim$400 K to higher temperatures with respect to the Baraffe et al. (1998) tracks. For an illustration of these track-based discrepancies, see Simon et al. (2000). In spite of obstacles posed by apparently discrepant H-R diagrams, we can say with confidence based on Li I presence that these objects are indeed young, $\lesssim$30 Myr. The H-R diagram, when applying high comovement probability derived distances, provides a higher degree of confidence in adopting these distances, as the ages are indeed as expected from Li measurements.

3.4.4 Is HD 141569 Related to US?

HD 141569 is an apparently isolated system located within tens of degrees (and parsecs) of known sites of recent (<5 Myr) and ongoing star formation, all apparently associated with the Sco-Cen star forming complex (d = 100-200 pc; Preibisch & Mamajek, 2008, in press), which appears contiguous with the Aquila Rift regions (Dame et al., 1987, $\ell \simeq 30°$). The velocity of HD 141569 appears to agree with the projected velocity model of US (see Fig. 3.6, but we can rule out the possibility of HD 141569 originating or being kinematically associated with US. The hypothesis that HD 141569 could have been ejected at high velocity from a known high density stellar nursery can be strongly discounted on two grounds. First, HD 141569 has two low-mass companions at wide separation ($\sim$10^3 AU, with likely orbital motion of $\sim$1 km s^{-1}). A velocity kick of >2-3 km s^{-1} to either A or B+C would have likely disintegrated the system. A low velocity ejection ($<$2-3 km s^{-1}) would have placed the birth site within $<$10-15 pc ($<$5°-7°), but no such known young clusters or molecular clouds appear there.

Position and velocity information for these nearby groups was entered into an orbit code which employs the epicyclic approximation a two-dimensional model (potential dependent on radius and height out of the galactic plane) of orbits in an axisymmetric potential. The separations between these groups and HD 141569 were evaluated during the past 10 Myr; combined distance and velocity vector uncertainties result in $<$15 pc uncertainties over this time frame. Presently, HD 141569 is $\sim$55 pc away from the center of US, and was only slightly closer at its minimum separation of $\sim$53 pc ($\sim$2.7 Myr ago). In UVW, the only substantial difference is in the W component of velocity: while US has negligible vertical motion with respect to the Local Standard of Rest (Mamajek, 2008), HD 141569 is moving northward out of the disk at $\sim$5 km s^{-1}. This anomalous W component of motion is discrepant with any known molecular cloud or star forming region near HD 141569. Further, given the kinematic data and the isochronal age of HD 141569 ($\sim$4-5 Myr), it appears that HD 141569 *could not have formed from any of the known sites of recent star-formation in its vicinity.* The list of excluded birth-sites includes US, UCL, Lower Centaurus Crux (LCC), and the Ophiuchus, Corona Australis, and Lupus clouds.

Combining the kinematic, position, and age data, we conclude that the HD 141569 triple system likely formed in isolation or with a small entourage of companions in a cloud. It appears to have formed $\sim$25 pc closer to the Galactic plane than its present position, and its anomalously large W velocity component has carried it to its modern high latitude position ($b \simeq +37°$, ~90 pc above the Galactic plane).

3.5 Summary and Conclusions

We have identified a group of 21 PMS stars within 30° of HD 141569 on the basis of strong Li I absorption and, in 9 of those 21 cases, Hα in emission. These stars were selected through a joint catalog search for X-ray sources with spatial and proper-motion characteristics similar to those of HD 141569, a B9.5Ve star at 116 pc that harbors a circumstellar disk and for which two low-mass companions had previously been identified (Weinberger et al., 2000). For these 21 stars, we have applied a moving cluster parallax technique to proper-motion data from the literature.

Table III.5 outlines our final membership assessments: we present eight potential new members of US and five new potential members of UCL. These stars possess lithium presence consistent with youth and furthermore appear youthful on the H-R diagram. Primarily we utilize spatial position as the principal criterion for determining membership and supplement that with comovement probabilities from the moving cluster parallax derivation. Additionally, we examine the motion of the HD 141569 system away from the galactic midplane over its lifetime. The system, surprisingly, appears to have formed in isolation, well outside of presently known star forming regions and molecular clouds. Future work to confirm this could include an N-body model of the triple star system, assessing the probability that the HD 141569 could have been kicked out of a nearby star-forming region by a multi-body interaction.

Table III.1. Observing Log

Object Name	Right Ascension [J2000]	Declination [J2000]	Observation Time [UT]	Integration Time [s]	S/N$^{(1)}$	Comment(s)
2001-06-18 : UCO / Lick						
Alpha Boo	14:15:39.67	+19:10:56.7	04:17:13.0	1	200	K2III v_r Standard
HD 137396	15:26:05.91	-11:41:55.7	04:28:35.0	720	127	···
RHS 48	15:23:46.0	-00:44:25	04:52:38.0	1500	158	···
HD 138969	15:35:47.41	-12:51:32.9	05:25:23.0	720	105	···
HD 140574	15:44:26.30	-03:50:18.5	05:45:22.0	720	132	···

Note. — This table is accessible in full in A.

[1] Approximated using *Splot* at ∼6500Åand ∼6700Å.

[2] Suspected spectroscopic binary based upon broadened troughs of spectral features.

Table III.2. Stellar Parameters

Plot ID	Object Name	$J^{(1)}$	$H^{(1)}$	$K_s{}^{(1)}$	$\mu_\alpha{}^{(2)}$ [mas yr^{-1}]	$\mu_\delta{}^{(2)}$ [mas yr^{-1}]	Parallax$^{(3)}$ [mas]
A	HD 141569	6.872±0.027	6.861±0.040	6.281±0.026	-18.3±1.1	-20.5±1.1	8.63±0.59
1	TYC 6242-0104-1	9.963±0.027	9.305±0.026	9.151±0.024	-11.7±3.6	-13.7±4.0	···
2	TYC 6191-0552	9.261±0.022	8.535±0.042	8.325±0.024	-15.0±3.3	-20.2±3.7	···
3	TYC 6234-1287-1	8.659±0.025	8.012±0.024	7.829±0.020	-10.1±2.6	-39.0±2.7	···
4	TYC 7312-0236-1	9.601±0.024	9.079±0.024	8.919±0.019	-20.5±3.3	-20.5±3.2	···
5	TYC 7327-0689-1	9.300±0.024	8.755±0.036	8.563±0.019	-19.7±3.2	-27.5±3.1	···
6	TYC 6781-0415-1	7.974±0.030	7.367±0.033	7.241±0.024	-19.5±2.7	-30.1±2.4	···
7	TYC 6803-0897-1	9.275±0.024	8.743±0.049	8.648±0.025	-15.6±2.5	-28.6±2.5	···
8	TYC 6214-2384-1	9.230±0.019	8.659±0.036	8.509±0.019	-18.7±3.5	-26.2±3.8	···
9	TYC 6806-0888-1	9.216±0.025	8.785±0.027	8.659±0.026	-13.4±3.0	-27.5±2.7	···
10	BD +04 3405B	9.759±0.022	9.413±0.031	9.262±0.019	-5.3±1.5*	-14.9±1.8*	···
11	HD 144713	7.847±0.021	7.538±0.034	7.431±0.020	-11.7±1.7	-20.7±1.6	···
12	HD 153439	8.073±0.020	7.852±0.049	7.729±0.047	-6.7±1.6	-28.6±1.6	···
13	HD 148396	8.420±0.023	8.095±0.019	8.100±0.020	-6.9±2.4	-15.4±2.4	···
14	TYC 7334-0429-1	9.168±0.018	8.690±0.049	8.565±0.021	-17.5±2.2	-25.5±2.2	···
15	TYC 6817-1757-1	8.815±0.021	8.350±0.042	8.179±0.031	-10.1±2.8	-7.4±2.5	···
16	HD 157310	9.160±0.022	9.088±0.047	9.006±0.021	-5.4±1.5	-12.0±1.5	···
17	HD 142016	6.785±0.020	6.707±0.034	6.622±0.018	-26.4±1.2	-38.8±1.3	···
18	CD -25 11942	8.099±0.020	7.661±0.029	7.525±0.038	-9.8±2.0	-28.2±1.8	···
19	2MASS J17215666-2010498	8.150±0.023	7.187±0.047	6.840±0.023	···	···	···
20	TYC 6790-1227-1	9.212±0.023	8.719±0.026	8.624±0.023	-20.4±2.8	-26.0±2.3	···
21	TYC 7346-1182-1	9.018±0.027	8.663±0.053	8.530±0.019	-14.3±2.3	-27.0±2.2	···

Note. — This table is accessible in full in A. For star #19, we adopt proper motions of its companion, #1.

[1] From 2MASS Catalog.

[2] Tycho-2 proper motions.

[3] Hipparcos parallaxes.

*Proper motions from UCAC2.

Table III.3: Effective Temperatures and Lithium Equivalent Widths

Plot ID	Object Name	Li I EW [mÅ] Integ.	Li I EW [mÅ] GFit	Ctmn. [mÅ]	Hα Flag[1]	Spectral Type	Type Source[2]	T_{eff} [K]	λ6200/λ6210 Line Ratio	Spectral Type	T_{eff} [K]	Adopted T_{eff} [K]
1	TYC 6242-0104-1	491	487	25	e*	K5 Ve	2	4350	1.07	K5	4350	4350
2	TYC 6191-0552	481	492	15	e*	K2	1	4900	1.91	K2	4900	4900
3	TYC 6234-1287-1	464	452	18	e*	K4 Ve	2	4590	2.65	K1.5	4990	4590
4	TYC 7312-0236-1	434	433	15	e*	K2 Ve	2	4900	2.30	K2	4900	4900
5	TYC 7327-0689-1	416	414	15	e*	K2 Ve	2	4900	2.52	K2	4900	4900
6	TYC 6781-0415-1	409	426	13	e*	G9 IVe	2	5410	4.69	G9.5	5330	5410
7	TYC 6803-0897-1	408	413	14	a	···	···	···	3.62	K0.5	5165	5165
8	TYC 6214-2384-1	397	398	14	a	K1 IV	2	5080	2.48	K2	4900	5080
9	TYC 6806-0888-1	320	345	12	a	G8 IV	2	5520	11.3	G3	5830	5520
10	BD +04 3405B	233	242	5	a	···	···	···	‡	···	···	6600*
11	HD 144713	164	193	5	a	F4	5	6590	‡	···	···	6590
12	HD 153439	180	198	5	a	F5 V	3	6440	‡	···	···	6440
13	HD 148396	197	216	14	a	K1/2 + F	3	5080	8.09	G8.5	5465	5080
14	TYC 7334-0429-1	368	378	15	a	K2e	2	4900	3.99	K0	5250	4900
15	TYC 6817-1757-1	274	244	13	e*	K0 Ve	2	5250	6.03	G9	5410	5250
16	HD 157310	52	76	1	a	A7 II/III	5	7850	‡	···	···	7850
17	HD 142016	20	57	0	a	A4 IV/V	3	8460	‡	···	···	8460
18	CD -25 11942	307	324	13	a	K0 IV	2	5250	8.72	G8.5	···	5250
19	2MASS J17215666-2010498	223	226	20	e*	···	···	···	0.58	K7.5	4060	4060
20	TYC 6790-1227-1	324	344	13	a	G9 IV	2	5410	4.53	G9.5	5330	5410
21	TYC 7346-1182-1	256	262	12	a	G8 V	2	5520	5.94	G9	5410	5520

---

[0] Note- This table is accessible in full in A. We report here two Li λ6707 measurements- "Integ." in column 3 refers to direct integration over the line profile, and "Gfit" in column 4 indicates the result of fitting a Gaussian to the absorption feature. In column 5, we also report contamination (denoted "Ctmn.") of the Li I line; see § 3.3.2 for description of its derivation. † Blended line; result indicates Gaussian feature fit to Li I in deblending. ‡ denotes cases in which the line ratio could not be measured from the spectrum either due to extreme rotational broadening or the lack of presence of either or both lines in question. * Effective temperature determined via interpolation of dereddened $H - K$ color over the color-effective temperature relationship of Kenyon & Hartmann (1995), see Fig. 3.2.

[1] Indicator flags are defined as follows: Absorption, a; core filling observed, c; double peaked emission, e*; P-Cygni like feature, p; emission with overlaid absorption, o.

[2] Spectral types drawn from the following sources: typed by A.J. Weinberger using KAST low-resolution spectrograph, 1; Torres et al. (SACY, 2006), 2; Michigan spectral atlas (Houk, 1982; Houk & Smith-Moore, 1988; Houk & Swift, 1999), 3, 4, and 5, respectively; HD Catalog spectral type, 6.

Table III.4: Kinematic Analysis of Membership Probability

Plot ID	Object Name	$V sini$ [km s^{-1}]	Measured v$_r$ [km s^{-1}]	Predicted v$_r$ [km s^{-1}]	μ_τ [mas yr^{-1}]	Comovement Probability	Distance [pc]	Predicted v$_r$ [km s^{-1}]	μ_τ [mas yr^{-1}]	Comovement Probability	Distance [pc]
				US Velocity Model				UCL Velocity Model			
A	HD 141569	· · ·	-6±5	-9.4	-4.9 ± 1.1	15.5	127 ± 11	-8.1	-0.7 ± 1.1	95.4	148 ± 11
1	TYC 6242-0104-1	14	-7.5±1.9	-7.5	-8.4± 3.6	9.0	228 ± 59	-7.5	-5.1± 3.7	41.7	238 ± 56
2	TYC 6191-0552-1	<10	3.3±3.0	-6.1	-4.2± 3.4	56.4	151 ± 25	-4.7	0.0 ± 3.4	100.0	171 ± 26
3	TYC 6234-1287-1	22	-5.8±1.9	-8.7	-1.7± 2.6	92.0	87 ± 9	-8.8	6.5 ± 2.6	22.7	101 ± 9
4	TYC 7312-0236-1	24	4.7±1.7	-0.7	-6.3± 3.3	26.2	140 ± 19	1.4	-1.8 ± 3.3	88.7	152 ± 20
5	TYC 7327-0689-1	16	-0.7±1.7	-1.8	-4.0± 3.2	61.3	118 ± 14	0.0	1.6 ± 3.2	91.8	130 ± 15
6	TYC 6781-0415-1	29	-3.0±2.1	-3.4	-2.6± 2.6	77.8	109 ± 11	-1.7	3.1 ± 2.6	65.8	123 ± 12
7	TYC 6803-0897-1	22	-4.2±1.9	-4.3	-4.3± 2.5	46.8	120 ± 13	-3.3	1.5 ± 2.5	89.3	134 ± 13
8	TYC 6214-2384-1	15	-3.3±1.4	-5.5	-6.8± 3.5	27.8	121 ± 17	-4.4	-1.2 ± 3.6	95.6	134 ± 18
9	TYC 6806-0888-1	43	-2.2±1.8	-3.7	-2.2± 3.0	84.6	127 ± 15	-2.7	3.3 ± 2.9	64.6	144 ± 16
10	BD +04 3405B‡	39	-14.1±2.2	-13.9	-0.6± 1.5	96.2	169 ± 23	-14.3	3.3 ± 1.6	29.2	207 ± 27
11	HD 144713	>70	0.6±4.4	-4.4	-1.9± 1.7	72.7	163 ± 16	-3.1	2.1 ± 1.7	64.0	184 ± 17
12	HD 153439	56	-4.3±1.6	-5.0	1.4± 1.6	88.3	130 ± 12	-4.5	6.8 ± 1.6	2.0	151 ± 13
13	HD 148396	36	-0.2±2.1	-3.4	-0.9± 2.4	94.4	231 ± 37	-2.4	2.1 ± 2.4	72.6	261 ± 41
14	TYC 7334-0429-1	27	-4.3±1.5	-2.2	-5.2± 2.2	25.3	129 ± 13	-0.8	0.1 ± 2.2	99.9	142 ± 14
15	TYC 6817-1757-1	11	8.4±1.9	-4.8	-7.4± 2.8	3.8	379 ± 99	-4.1	-5.4 ± 2.7	16.5	382 ± 90
16	HD 157310	>70	-22.4±2.3†	-13.9	-1.6± 1.5	74.1	204 ± 28	-14.3	1.7 ± 1.5	67.7	245 ± 32
17	HD 142016	· · ·	-17.8±2.3†	-2.3	-6.2± 1.2	22.6	85 ± 7	-0.7	1.7 ± 1.2	87.3	94 ± 6
18	CD-25 11942	53	-6.5±1.5	-5.7	-2.1± 2.0	78.0	127 ± 12	-5.4	3.6 ± 2.0	43.4	144 ± 13
19	2MASS J17215666-2010498	<10	-7.3±1.9	-7.5	-8.4± 3.6	9.0	228 ± 59	-7.5	-5.1 ± 3.7	41.7	238 ± 56
20	TYC 6790-1227-1	33	2.0±2.0	-2.6	-6.1± 2.7	23.7	121 ± 13	-1.0	-0.7 ± 2.6	98.1	133 ± 13
21	TYC 7346-1182-1	28	3.7±1.7	-3.6	-4.8± 2.3	31.8	129 ± 13	-2.8	0.7 ± 2.3	97.1	143 ± 14

---

[0] Note- †Very broadened, featureless spectra. Radial velocity derived via centroid measurement of the Hα line. Uncertainty reflects an assumed centroid measurement error of 0.05Å. For a full discussion of error analysis, see § 3.3.3.

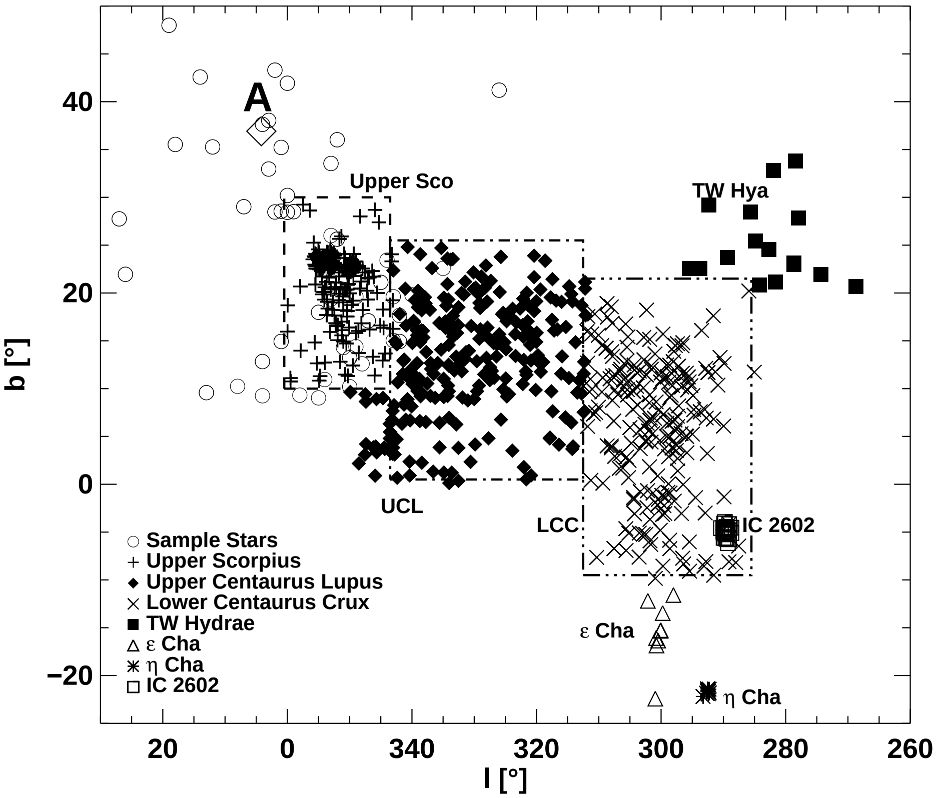

Figure 3.1: A galactic coordinate map of HD 141569 and nearby associations is presented. Open circles indicate our sample stars, while dashed boxes indicate regions studied by de Zeeuw et al. (1999). Details of objects plotted herein are to be found in the following papers: US (Preibisch et al., 2002), UCL and LCC (Mamajek et al., 2002; de Zeeuw et al., 1999), TW Hya (Mamajek, 2005), η and ϵ Cha (Zuckerman & Song, 2004; Zuckerman et al., 2001) and IC 2602 (Robichon et al., 1999). In all subsequent plots, the letter A denotes the position of HD 141569.

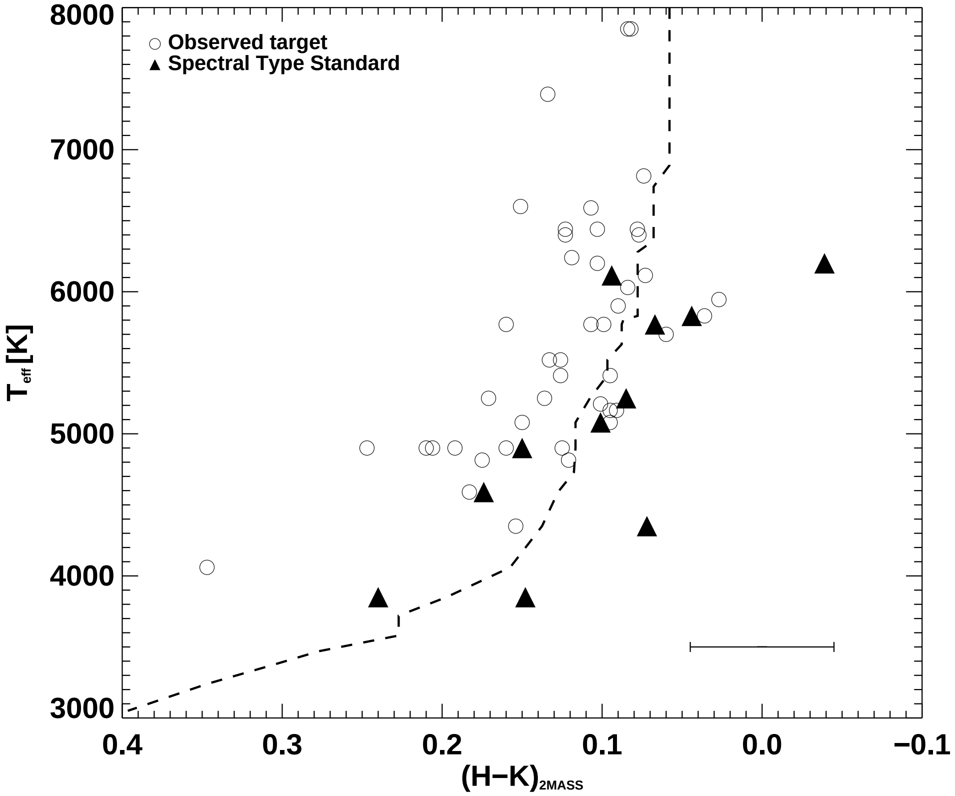

Figure 3.2: Color-T_{eff} relationship from Kenyon & Hartmann (1995) for 2MASS $(H - K)$ colors. The dashed line represents the main-sequence relationship as defined in Kenyon & Hartmann (1995). Open circles represent literature spectral types for our sample as reported in column 6 of Table III.3. Filled triangles represent literature spectral types for the standard stars observed by us (Table III.1).

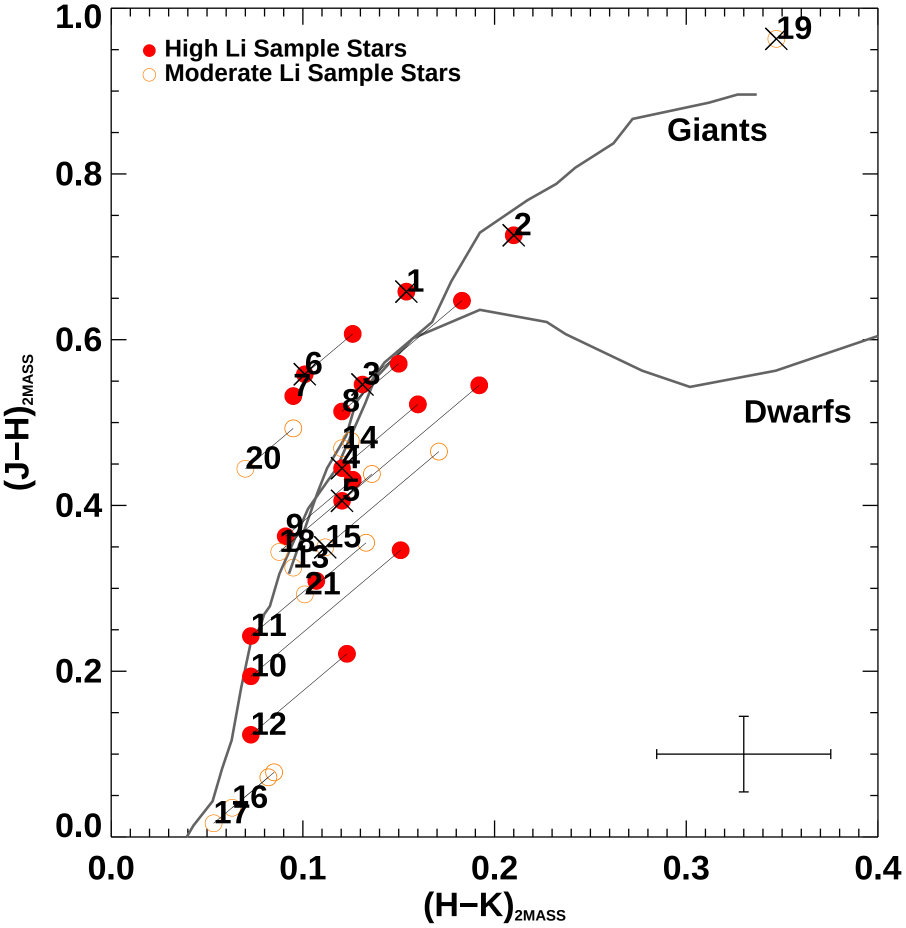

Figure 3.3: Near-infrared JHK colors from 2MASS. For visual clarity, we display here only the 21 stars that we identify as lithium rich (see §3.3.2 and Fig. 3.4). Solid lines represent the dwarf and giant sequences from Bessell (1991) and Bessell & Brett (1988). Dereddened objects are plotted with observed and dereddened colors connected by a thin, solid line parallel to a reddening vector defined by $\frac{E_{(J-H)}}{E_{(H-K)}} = 1.95$ (Bessell & Brett, 1988). Numbers next to the points are provided for ease in identifying the objects in the data tables. Stars with Hα in emission are indicated with an X over the point.

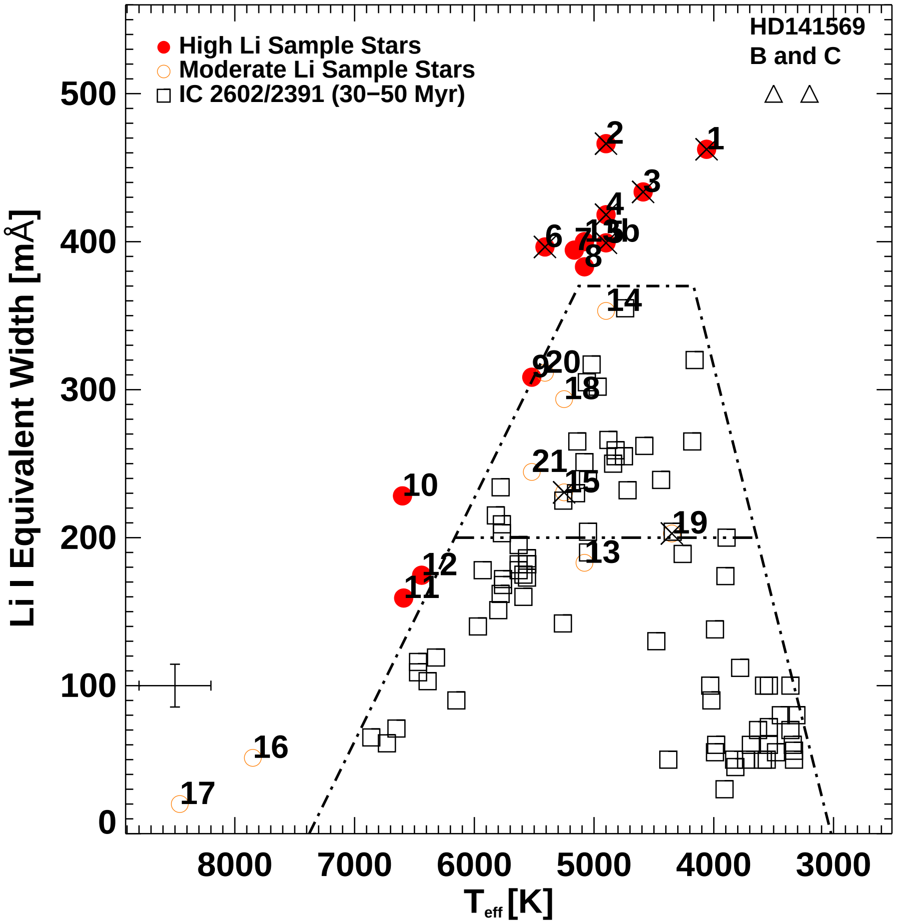

Figure 3.4: Using Li I EW measurements to identify young stars in our sample. Fe contamination corrected Li I EW as a function of T$_{\rm eff}$, plotted with the IC 2602/IC 2391 data from Randich et al. (1997, 2001). Stars possessing enough lithium to be above the selection threshold are likely to be pre–main-sequence, and are designated the “high Li” sample. Stars below the threshold but above the horizontal line at 200mÅ constitute the “moderate Li” sample; these stars have Li EWs in the upper envelope of the IC2602/IC2391 locus. We include objects 16 and 17 in the moderate sample to be conservative, potentially erring on the side of inclusion, as Li I is not a good age indicator in higher mass stars. Numbers next to the points are provided for ease in identifying the objects in the data tables. In two cases we show both the measured EW as well as the doubled value (indicated by a “b” after the number identifier), these objects may be suffering Li line filling (see §3.2). Stars showing Hα in emission are indicated with an X over the point.

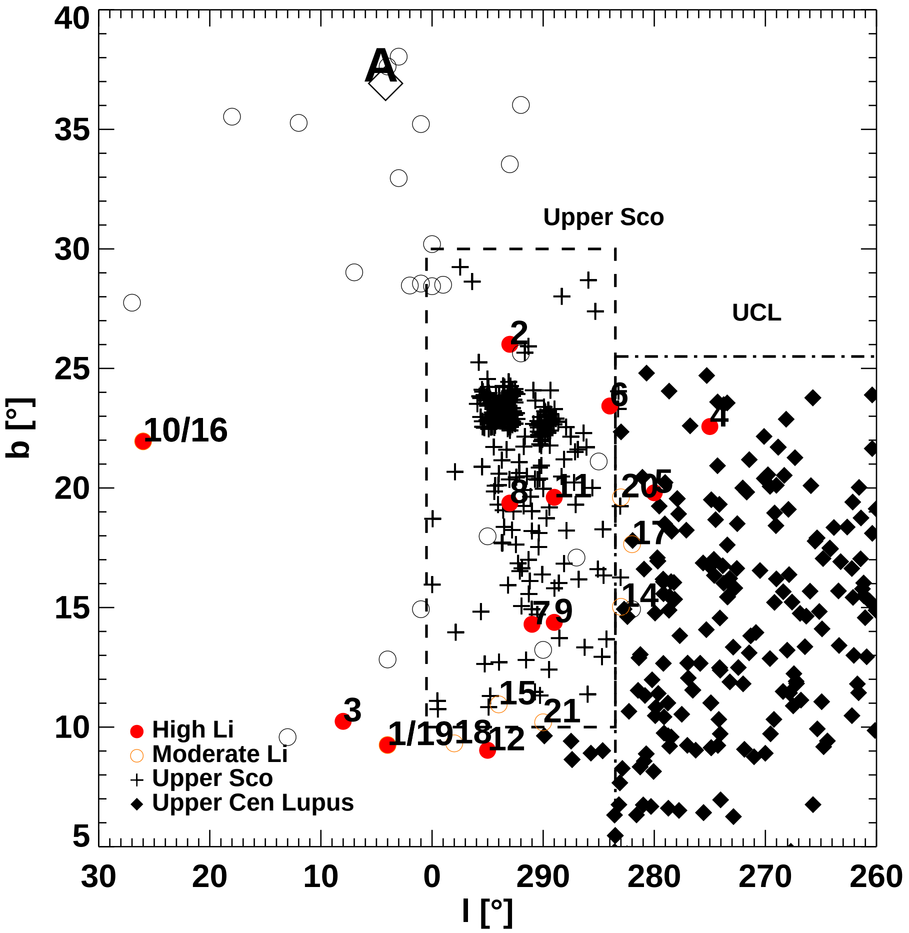

Figure 3.5: A cropped area about HD 141569 spatially plotted with high and moderate lithium sample. Symbols are defined as in Fig. 3.1.

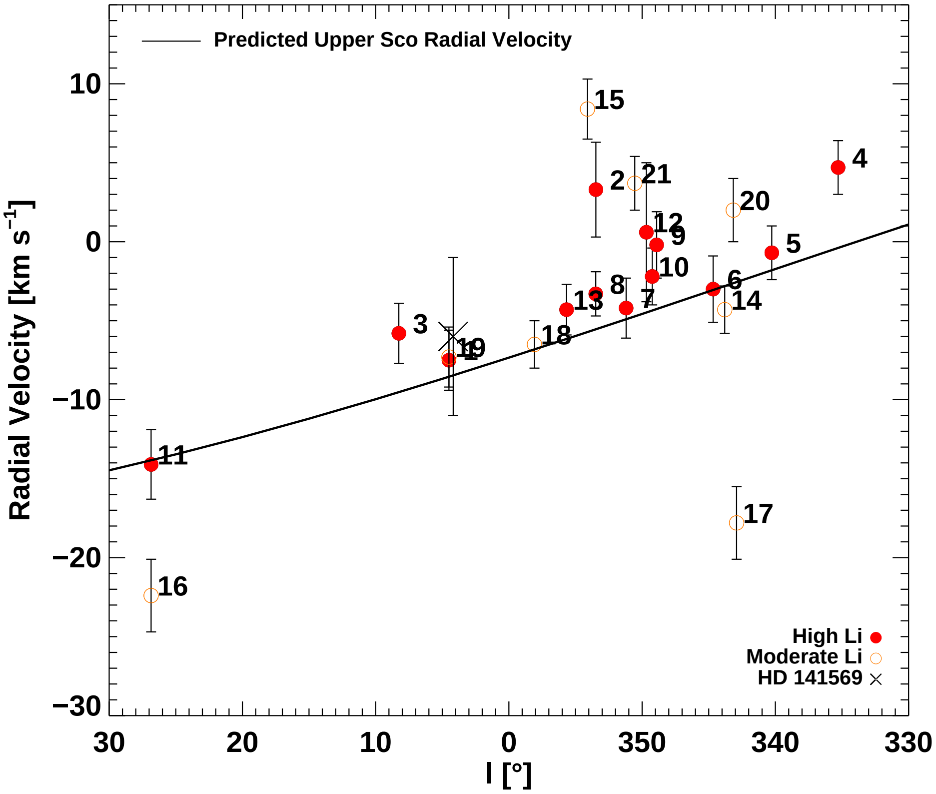

Figure 3.6: Radial velocities for the lithium selected sample plotted as a function of galactic longitude. For comparison, the radial velocities predicted from the US velocity vector at a galactic latitude of +20° are projected in galactic longitude. Shown are 1σ uncertainties; all high lithium stars are consistent in radial velocity space with US within 3σ.

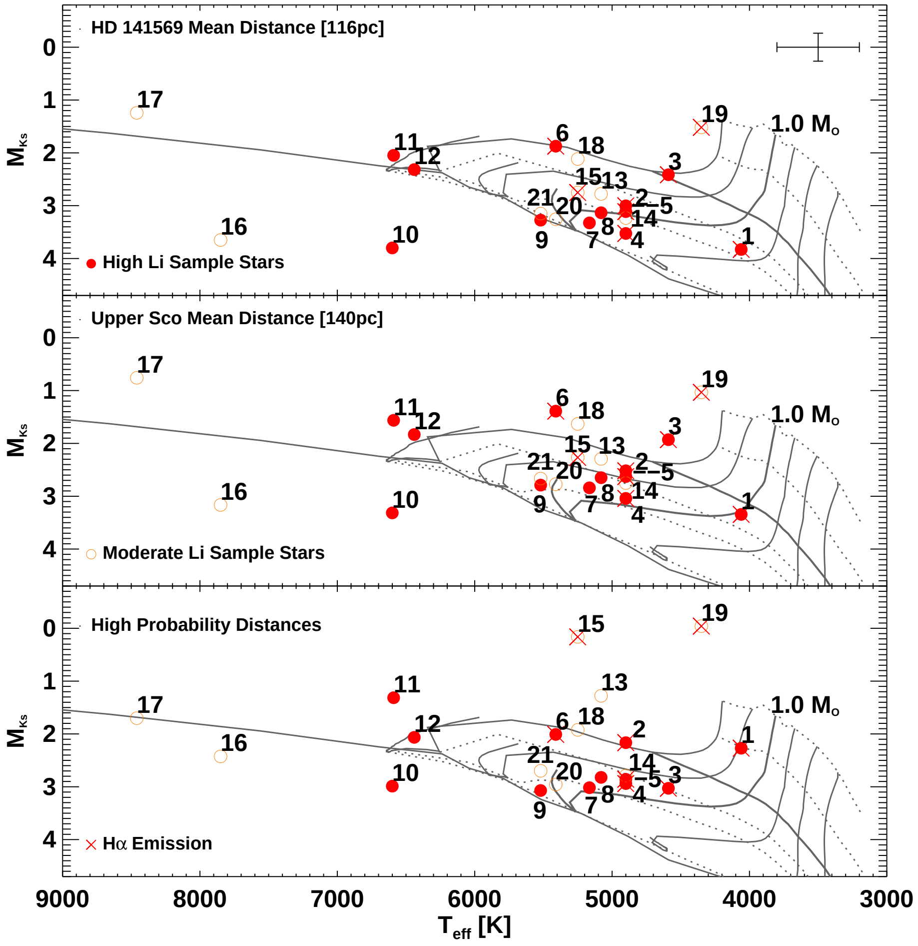

Figure 3.7: H-R Diagram for sample stars with the pre-main-sequence tracks of Baraffe et al. (1998) overplotted. Isochrones shown are (from top to bottom) 1, 3, 10, 20, 30, and 100 Myr. Also shown is the 100 Myr isochrone of D'Antona & Mazzitelli (1997) extending to higher masses. This isochrone and the 10 Myr isochrone are highlighted for reference. The upper panel shows the stars using M_{Ks} derived using the distance to HD 141569 from the second *Hipparcos* data release, 116±8 pc (van Leeuwen, 2007). In the middle panel, we apply the mean distance to US, 145±2 pc (de Zeeuw et al., 1999). The lower panel was generated using distances derived from the US velocity model (see text). The sample's isochronal age appears consistent with the high lithium abundances which indicate ages $\lesssim$30 Myr (see Fig. 3.4).

Table III.5. Association Notes

Plot ID	Object Name	Spatial Match	Velocity Model / Probability	US/UCL V_r Prediction	Determined Membership
1	TYC 6242-0104-1	?	US / 9%	$1\sigma/1\sigma$	I
2	TYC 6191-0552	US	US / 56%	no/3σ	US
3	TYC 6234-1287-1	?	US / 92%	$2\sigma/2\sigma$	US?
4	TYC 7312-0236-1	UCL	UCL / 89%	no/2σ	UCL
5	TYC 7327-0689-1	UCL	UCL / 92%	$1\sigma/1\sigma$	UCL
6	TYC 6781-0415-1	US	US / 78%	$1\sigma/1\sigma$	US
7	TYC 6803-0897-1	US	US / 47%	$1\sigma/1\sigma$	US
8	TYC 6214-2384-1	US	US / 28%	$2\sigma/1\sigma$	US
9	TYC 6806-0888-1	US	US / 85%	$1\sigma/1\sigma$	US
10	BD +04 3405B	?	US / 96%	$1\sigma/1\sigma$	I
11	HD 144713	US	US / 73%	$2\sigma/1\sigma$	US
12	HD 153439	?	US / 88%	$1\sigma/1\sigma$	US?
13	HD 148396	US	US / 94%	$2\sigma/2\sigma$	US
14	TYC 7334-0429-1	UCL	UCL / 100%	$2\sigma/3\sigma$	UCL
15	TYC 6817-1757-1	US	US / 4%	no/no	I
16	HD 157310	?	US / 78%	no/no	I
17	HD 142016	UCL	UCL / 87%	no/no	UCL
18	CD-25 11942	?	US / 78%	$2\sigma/2\sigma$	US?
19	2MASS J17215666-2010498	?	US / 9%	$1\sigma/1\sigma$	I
20	TYC 6790-1227-1	UCL	UCL / 98%	$3\sigma/2\sigma$	UCL
21	TYC 7346-1182-1	US	US / 32%	no/no	US

Note. — In column three, we note with which moving group each object is spatially consistent. Column four summarizes the results of velocity vector modeling and shows the vector with which each object had the highest comovement probability. In column five, we report the models which predicted radial velocities within 2σ of our measured values, and in the rightmost column we comment on membership; I denotes "indeterminate". See text (§ 3.5) for further discussion of our final membership determinations.

CHAPTER IV

A SEARCH FOR STAR-DISK INTERACTION AMONG THE STRONGEST X-RAY FLARING STARS IN THE ORION NEBULA CLUSTER

The Chandra Orion Ultradeep Project observed hundreds of young, low-mass stars undergoing highly energetic X-ray flare events. The 32 most powerful cases have been modeled by Favata et al. (2005) with the result that the magnetic structures responsible for these flares can be many stellar radii in extent. In this paper, we model the observed spectral energy distributions of these 32 stars in order to determine, in detail for each star, whether there is circumstellar disk material situated in sufficient proximity to the stellar surface for interaction with the observed large magnetic loops. Our spectral energy distributions span the wavelength range 0.3–8 μm (plus 24 μm for some stars), allowing us to constrain the presence of dusty circumstellar material out to $\gtrsim 10$ AU from the stellar surface in most cases. For 24 of the 32 stars in our sample the available data are sufficient to strongly constrain the location of the inner edge of the dusty disks. Six of these (25%) have spectral energy distributions consistent with inner disks within reach of the observed magnetic loops. Another four stars may have gas disks interior to the dust disk and extending within reach of the magnetic loops, but we cannot confirm this with the available data. The remaining 14 stars (58%) appear to have no significant disk material within reach of the large flaring loops. Thus, up to $\sim 40\%$ of the sample stars exhibit energetic X-ray flares that possibly arise from a magnetic star-disk interaction, and the remainder are evidently associated with extremely large, free-standing magnetic loops anchored only to the stellar surface.

4.1 Energetic X-ray Flares on Young Stars

The recent large X-ray surveys of the Orion and Taurus star-forming regions performed by *Chandra* and *XMM* (i.e., COUP, XEST: Getman et al., 2005a; Audard et al., 2007) provide an unparalleled opportunity to study the magnetic activity of young, low-mass stars. These deep observations spanning long temporal baselines (e.g., the COUP X-ray light curves span 13 days with near-continuous time coverage) reveal that low-mass pre-main-sequence (PMS) stars possess X-ray luminosities 3–4 magnitudes greater than that of the present-day Sun and exhibit extremely energetic flaring events with high frequency.

Detailed analyses of these flares reveal that they are similar to solar flares, but are orders of magnitude more energetic and larger in physical size. In particular, Favata et al. (2005) subjected the 32 most energetic flares observed by COUP to analysis via a standard uniform cooling loop model (Reale et al., 1997; Sylwester et al., 1993; Priest & Forbes, 2002; Favata & Micela, 2003), with which they derived the properties of the magnetic coronal loops that participate in the flare events. They found that these magnetic loops were extremely large—extending tens of stellar radii in some cases—much larger than ever observed on older stars. Such large-scale flares could have important ramifications for a number of issues, such as the shedding of stellar angular momentum and mass, powering of outflows, and ionization/dissipation of circumstellar disks.

Magnetic loops with sizes on the order of ~ 10 stellar radii have long been postulated as part of magnetospheric accretion scenarios. In this paradigm, a large-scale stellar magnetic field threads the inner edge of a circumstellar disk, channeling accretion from disk to star (e.g. Camenzind, 1990; Koenigl, 1991; Shu et al., 1994; Hartmann, 1994; Hayashi et al., 1996). Indeed, Favata et al. (2005) speculated that the large magnetic loops observed in the COUP sample may be facilitating this type of magnetic star-disk interaction, in part because they argued that such large loops would likely be unable to remain stable if anchored only to the stellar surface. However, in 2005, most of the 32 COUP sources studied by Favata et al. (2005) lacked sufficient photometric data to characterize the optical-infrared (IR) spectral energy distributions, so they could not confirm the presence of inner disks to which the observed magnetic loops might link.

Thus, there is still an outstanding question as to whether stellar coronal activity in these stars alone can drive such energetic flare events, or whether the energy (or at least the trigger) derives from a star-disk interaction. While the latter requires magnetic loops large enough to reach the inner edge of the disk, several theoretical studies (e.g., Ostriker & Shu, 1995; Uzdensky et al., 2002; Matt & Pudritz, 2005b, and references therein) have shown that the presence of a disk truncates the stellar magnetosphere so that closed magnetic loops extend not much further than the inner edge of the disk. Thus, if these flares are powered by the star-disk interaction, one would expect the size of the flaring loops to approximately coincide with the location of the disk inner edge. On the other hand, if the energetic flares are purely a stellar phenomenon, the largest loop sizes may only be exhibited by stars that lack disk material close to the star. To address this question, it will therefore be useful to be able to determine the proximity of disk material to the furthest extent of the flaring magnetic loops exhibited by the sample analyzed in this work.

Near- and mid-IR colors can be used as a crude tracer of close-in circumstellar material. Getman et al. (2008b) have used *Spitzer* IR colors to distinguish Class II and Class III objects (i.e., stars with dusty disks and naked T Tauri stars, respectively) among 161 flaring COUP stars. Interestingly, they found evidence that whereas the largest flaring loops tended to be associated with Class III objects, the Class II sources in their sample were more likely to possess relatively small magnetic loops. The IR colors alone do not provide a quantitative measure of the location of the inner disk edge, but Getman et al. (2008b) suggest that the magnetic loops may be confined by the disk to be within the disk co-rotation radius (the radius at which disk material, if present, orbits the star with angular velocity equal to the star's angular velocity). This suggestion is important, as the disk co-rotation radius is the point specifically at which some magnetospheric accretion theories predict magnetic star-disk interaction to occur. It is desirable, therefore, to establish the relationship between circumstellar disks and the very large magnetic loops observed by COUP more quantitatively than IR colors alone permit.

In this work, we present detailed spectral energy distributions (SEDs) for each of the 32 most powerful X-ray flaring COUP sources at wavelengths 0.34–8 μm, plus upper limits at 24 μm (§4.2). In §4.3 we present near-infrared color excesses for the sample as a basic tracer of close-in circumstellar disks. Next we compare in detail the full observed SEDs against synthetic SEDs of low-mass PMS stars with disks (§§4.4–4.5) in order to (a) ascertain whether dusty disks are present around these stars, and (b) if so, determine quantitatively whether the inner edges of those disks are sufficiently close to the stellar surface to interact with the large flaring loops observed by Favata et al. (2005). The results (§4.6) indicate that more than half of the sample stars lack significant disk material within reach of their flaring magnetic loops; evidently the extremely large flaring loops observed by Favata et al. (2005) are in most cases free-standing structures anchored only to the stellar surface. In §4.7 we discuss some implications of this finding.

4.2 Data

4.2.1 Study Sample, Loop Heights, and Stellar Data

The 32 stars for our study constitute a unique subset of the COUP (Getman et al., 2005b) observations, identified by Favata et al. (2005) as exhibiting the brightest $\sim 1\%$ of all flares observed by COUP. These 32 flares had sufficient photon statistics with which a uniform cooling loop (UCL) analysis could be performed.

The UCL model is based on observations of solar flares. The occurrence of reconnection events on the Sun has been used to benchmark relationships between X-ray flare decay slopes and the magnetic field structure confining the emitting plasma. After a magnetic reconnection event occurs, heated plasma evaporates from the chromosphere into the confining loop. The material then emits soft X-rays as it cools (Priest & Forbes, 2002), and the X-ray light curve's decay time as well as its slope in density-temperature space is related to the magnetic loop length (Reale et al., 1997). This method was developed using hydrodynamic simulations which were calibrated against spatially resolved imaging observations of solar flaring loops (for further detail, see §B).

Favata et al. (2005) applied the UCL analysis to their sample of 32 stars and thus derived the lengths of the magnetic loops confining the flare events observed by COUP. A reanalysis by Getman et al. (2008a) includes these 32 objects. The derived loop lengths in both studies are consistent within uncertainties, so we adopt the former for consistency throughout. For simplicity, we estimate the loop height from the stellar surface as the loop length divided by 2. This is an overestimate of what the actual loop height may be; for example, in a circular or semi-circular loop geometry, the actual loop height would be the loop length divided by π. These loop heights (half loop lengths) and their uncertainties are summarized in Table IV.1. Uncertainties in the loop lengths are generally fairly large, and arise from uncertainty in the measurement of the flare's peak temperature, decay time, and decay slope. For a detailed discussion of the quoted uncertainties in the loop lengths, see Favata et al. (2005, cf. their §3.2).

To narrow the range of acceptable best-fit spectral energy distributions (§4.4), we require basic stellar parameters including effective temperatures (T_{eff}), and radii (R_{star}). These are taken primarily from Hillenbrand (1997) and are summarized in Table IV.1. In cases where stellar parameters were not available from the literature, we adopt the temperatures and radii of the best-fit SED model (see §4.4). Table IV.1 also contains Ca II equivalent widths (as measured by Hillenbrand, 1997) and our newly reported ΔK_{S} and $\Delta(U-V)$ excess measurements (see §4.3). We use ΔK_{S} excess as a supplemental indicator of close-in, hot disk material, and the Ca II equivalent widths in combination with $\Delta(U - V)$ excess to indicate ongoing accretion onto the stellar surface.

4.2.2 Photometric Data

Fluxes for each of the 32 stars in our study sample were assembled over the wavelength range 0.34 μm (U band) to 24 μm (*Spitzer* Multiband Imaging Photometer, MIPS). With these data, we probe the stellar photosphere and circumstellar dust content. These measurements are summarized in Tables IV.2 and IV.3.

Optical fluxes were taken from the ground-based observations of the Orion Nebula Cluster (ONC) by Da Rio et al. (2009) in the $UBVI_C$ passbands (0.36, 0.44, 0.55, and 0.83 μm, respectively), obtained with the ESO Wide Field Imager (WFI). We supplemented these with fluxes from *Hubble* Space Telescope Advanced Camera for Surveys (ACS) data (Robberto et al., 2005), providing broadband fluxes at 0.43, 0.54, 0.77, and 0.91 μm, as well as V and I_C magnitudes from the ground-based observations of Hillenbrand (1997).

The 2 Micron All Sky Survey (2MASS; Skrutskie et al., 2006) provides near-infrared JHK_S magnitudes. Of critical importance to our analysis, infrared photometry from the *Spitzer* Infrared Array Camera (IRAC) and MIPS instruments provide the clearest probes of warm circumstellar dust in the 3.6, 4.5, 5.8 and 8 μm bandpasses (IRAC) and at 24 μm (MIPS). We measured these fluxes using pipeline-processed, archival data, and found our values to agree within a few mJy of the unpublished measurements of the *Spitzer* GTO team (S. T. Megeath, private communication). The MIPS fluxes were measured by us from the *Spitzer* archive using the pipeline reduced 24 μm images. Unfortunately, the MIPS image of the ONC is saturated over most of the region of interest, and we were thus unable to recover more than a few upper limits (see Table IV.3).

Where magnitudes were originally reported, these have been converted to fluxes using published zero points for each instrument (see final rows in Table IV.2 and IV.3). In addition, we have in general adopted larger uncertainties on the fluxes than the formal measurement errors in order to account for typical variability levels in the optical and near-infrared of ~ 0.1 mag (e.g., Herbst et al., 1994; Carpenter, 2001). Specifically, we adopt an uncertainty of at least 10% on the fluxes, unless the formal measurement error is larger.

4.3 Preliminary Disk Diagnostics: Color Excess and Accretion Indicators

Traditionally, the presence of warm circumstellar dust around low-mass PMS stars has been traced using near-IR "color excesses," such as $\Delta(H-K)$, defined as the difference between the observed (de-reddened) color and the color expected from a bare stellar photosphere (e.g., Strom et al., 1989; Lada & Adams, 1992; Edwards et al., 1993; Meyer et al., 1997). The use of a single color excess of course does not permit a detailed, quantitative determination of disk structure (such as the size of the inner truncation radius, which is our primary interest here) because a given color excess depends in complex ways upon multiple disk and stellar parameters (see also §4.4 below). Moreover, near-IR colors may cause the observer to miss the presence of some disks, particularly those with large inner holes or around very cool stars whose photospheres peak in the near-IR. For example, the overall disk frequency in the Orion Nebula Cluster has been estimated at ~65% on the basis of excess emission in the K band (Hillenbrand et al. 1998), but increases to ~85% simply by adding an L-band measurement (Lada et al. 2000). In other words, the addition of mid-IR measurements can be very important for the detection of disks (for a discussion of disk-detection efficiency using near-IR colors, see Hillenbrand et al., 1998; Lada et al., 2000; Ercolano et al., 2009). This is particularly relevant to our sample, in which many of the stars have cool photospheric temperatures, and where even disks with relatively large inner holes could be within reach of the observed very large magnetic flaring loops (see Table IV.1).

Still, color excesses have the advantage of being easy to collect and analyze for large numbers of stars—especially prior to the advent of the wide and deep longer-wavelength surveys made possible by *Spitzer*—and of providing a relatively straightforward "yes/no" criterion for the presence of a disk. For example, Hillenbrand et al. (1998) used the $\Delta(I-K)$ color excess to conduct a census of disks among ~ 1000 low-mass stars in the ONC. In that approach, the observed $V-I$ color was used to measure the extinction, A_V, which was used in turn to deredden the observed $I-K$ color. Any excess $\Delta(I-K)$ was then attributed to the presence of a disk. This approach has the advantage of requiring for each star only three flux measurements (VIK) and a spectral type (with which to establish the expected photospheric colors). It assumes that (a) the observed I-band flux is purely photospheric in origin, and (b) the observed V-band flux is only affected by reddening (i.e., does not include any "blue excess" due to veiling emission from accretion).

Using our compiled fluxes in Tables IV.2 and IV.3 for our study sample, we have calculated ΔK_{S} in a manner similar to Hillenbrand et al. (1998). However, rather than use only the observed $V - I$ color to determine A_V, and rather than normalize the stellar flux to the observed I-band flux, we have performed a two-parameter fit to each star's observed SED. To isolate the stellar flux from the disk and/or accretion flux, we use fluxes which appear to be photospheric in origin only, excluding the bluest wavelength fluxes which could be affected by accretion flux or scattered light (Whitney et al., 2003a) as well as the reddest wavelength fluxes which could contain flux from a disk. In general we used the fluxes from 0.5 to 1.0 μm (total of 8 flux measurements, see Tables IV.2 and IV.3) for this fitting, which should be a substantial improvement over the two-band (V and I_C) approach described above. To the observed fluxes, we fit a NextGen model atmosphere (Hauschildt et al., 1999) at the spectroscopically determined T_{eff} from the literature (Table IV.1). The two free parameters of the fit are the A_V and the overall normalization of the stellar flux. For comparison, previously published A_V values (Hillenbrand, 1997) are listed in Table IV.1, and our newly determined A_V values are also reported along with their corresponding errors (99% confidence limits) as determined from the two-parameter SED fit. For 10 stars in our study sample, A_V values are reported here for the first time. In many of these cases we find large A_V values ($A_V \gtrsim 10$). These stars were likely absent from the optical study of Hillenbrand (1997) due to the high reddening/extinction.

For about half of the stars in our sample, our newly measured A_V values agree within 99% confidence with those previously reported. For the remaining stars, the A_V values differ significantly; the reason for this difference is illustrated in Fig. 4.1 for the case of star COUP

262. The red model SED represents the previously reported fit of a $T_{\rm eff} = 4395$ K photosphere to just the V and I_C band fluxes from Hillenbrand (1997). The extinction that results is $A_V = 3.77$ (see Table IV.1 and Hillenbrand, 1997), and as a consequence the K-band flux appears to be highly in excess of the photosphere with $\Delta(I - K) = 2.21$ (Hillenbrand et al., 1998). However it is evident from visual inspection of the complete set of observed fluxes that this model fit is a poor representation of the additional measurements included here. As shown in the figure, our new fit to the entire set of fluxes gives $A_V = 7.91^{+0.70}_{-0.53}$ and $\Delta K_{\rm S}$ $= 0.14 \pm 0.11$. For this particular case, evidently the previously reported V-band flux was anomalously high by $\sim 5\sigma$ (perhaps due to the ubiquitous optical variability of PMS stars), and so fitting for A_V to just the V and I_C fluxes resulted in a distorted model SED. The difference between the two SED fits is very important in the context of our study: e.g., the previously reported value of $\Delta(I - K)$ for COUP 262 implies a massive, warm circumstellar disk close to the star, whereas our newly determined best-fit SED model is in fact consistent with no close-in disk. We revisit the SED fit of COUP 262 in the context of the entire study sample below (§§ 4.4 and 4.6).

Hillenbrand (1997) adopted photospheric colors of main-sequence dwarfs (i.e., for dwarfs, $\log g \sim 4.5$) in the calculation of near-IR excesses. However, low-mass PMS stars at the young age of the ONC (~ 1 Myr) are expected to have somewhat lower $\log g$ values due to their large radii. Thus we have also considered the extent to which the assumed $\log g$ affects the predicted stellar colors and thus the inferred near-IR excesses. In Fig. 4.2, we compare the SEDs of NextGen stellar atmosphere models as a function of $\log g$ for several representative

$T_{\rm eff}$ appropriate for our study sample (all models shown are solar metallicity). We see that the choice of $\log g$ is not important for stars warmer than $T_{\rm eff} \gtrsim 4200$ K. However, we find that for cooler objects the predicted $I-K$ colors become increasingly redder with decreasing $\log g$, which could lead to over-estimated near-IR excesses for the coolest stars. Therefore in this study we have opted to use model atmospheres with $\log g$ appropriate to each object ($\log g$ calculated from previously reported stellar masses and radii; see Table IV.1).

Newly determined $\Delta K_{\rm S}$ values following the procedure described above are reported in Table IV.1. Several previous studies (e.g., Stassun et al., 1999; Rebull, 2001; Herbst et al., 2002; Lamm et al., 2004; Makidon et al., 2004), adopted a threshold value of $\Delta K_{\rm S} > 0.3$ (i.e., $\sim 3\sigma$ excess given typical $\sigma_K = 0.1$ mag; see Sec. 4.2.2) for identifying stars with close-in circumstellar disks. By this criterion alone, five of the stars in our sample (COUP 141, 223, 1246, 1343, 1608) show large near-IR excesses indicative of the presence of warm circumstellar dust [1]. The remaining stars in our sample show very weak or no evidence for near-IR excess emission (i.e., $\Delta K_{\rm S} < 0.3$).

In the context of the principal aims of the present study—where we seek to determine whether the large magnetic loops observed in the sample stars are linked to circumstellar disks—one might anticipate that $\Delta K_{\rm S}$ could be used as a quantitative tracer of circumstellar dust located within reach of the observed magnetic loops. For example, if the presence of substantial $\Delta K_{\rm S}$ excess correlates with the location of the disk truncation radius ($R_{\rm trunc}$, the distance from the inner edge of the disk to the star), then we might simply take stars with

---

[1] As described below, the large $\Delta K_{\rm S}$ in COUP 1246 is likely the result of an underestimated A_V, and we consider its near-IR excess to be not significant for the remainder of our analyses.

$\Delta K_{\rm S} > 0.3$ as those whose inner disks are likely to be magnetically linked to the star. This is similar to the approach of Getman et al. (2008b).

The combination of factors discussed above, however—relatively cool stellar photospheres which peak in the near-IR, magnetic flaring loops that are large enough to interact with disks at relatively large heights above the stellar surface, etc.—makes the near-IR excess an inefficient tracer of the types of disks we seek to characterize. Table IV.4 categorizes the sample stars according to whether or not they display significant near-IR excess emission (i.e., $\Delta K_{\rm S} > 0.3$ vs. $\Delta K_{\rm S} < 0.3$) and whether the inner-disk truncation radius is larger or smaller than the dust destruction radius (i.e., $R_{\rm trunc} > R_{\rm dust}$ vs. $R_{\rm trunc} \lesssim R_{\rm dust}$, where $R_{\rm dust}$ is the distance from the star within which dust is warm enough to sublimate). Here $R_{\rm trunc}$ is determined from our detailed SED model fitting as described below (§4.4). The off-diagonal elements of Table IV.4 represent cases contradicting the assumption that $\Delta K_{\rm S}$ excess correctly and quantitatively predicts the location of the inner-disk edge. For only one of the sample stars (COUP 1246) do we find a relatively large inner-disk hole ($R_{\rm trunc} > R_{\rm dust}$) but a large $\Delta K_{\rm S} > 0.3$. This one case appears unusual because the best-known explanation for a strong near-IR excess is the presence of warm dust close to the star. Upon closer inspection of this case (COUP 1246), we found that the fitted A_V was underestimated because of the presence of a moderate blue excess, likely due to chromospheric activity, as suggested by the observed filled-in Ca II emission (Table IV.1), and which is not included in the photosphere model. If we manually adjust the A_V value upward by $\sim 3\sigma$ from the fit value of $A_V = 1.52^{+0.70}_{-0.60}$ (see Table IV.1) to $A_V = 2.22$, the value of $\Delta K_{\rm S}$ becomes 0.17.

Indeed, our final best fit SED model (see §4.4) has an A_V of 3.04, and thus an even lower ΔK_{S}. Therefore, for the following analysis and discussion, we assume that the calculated excess ΔK_{S} in COUP 1246 is not significant (i.e., ΔK_{S} is consistent with being less than 0.3).

Several stars in our sample exhibit a meager $\Delta K_{\mathrm{S}} < 0.3$, and by this criterion alone would be classified as "diskless." However, for eight of these stars (in the lower left quadrant of Table 4), our SED fitting found these to in fact have disks that reach relatively close to the star ($R_{\mathrm{trunc}} \lesssim R_{\mathrm{dust}}$), and in some cases (shown below, §4.6), the disk reaches sufficiently close to the star to interact with the observed large flaring loops. In summary, Table 4 indicates that while $\Delta K_{\mathrm{S}} \geq 0.3$ appears to be an accurate indicator of dusty material close to the star, the lack of significant ΔK_{S} does not rule out the presence of dusty material close to the star. Thus, for the purposes of the present study where we seek to establish quantitatively the location of the inner-disk edge in relation to the observed large magnetic flaring loops, we cannot rely solely on traditional near-IR excesses.

In addition to ΔK_{S} measurements, from our new SED fits we calculate blueward color excesses, $\Delta(U - V)$ which can be used as a tracer of accretion at the stellar surface ("hot spots") and/or chromospheric activity and can help in our interpretation of some SEDs (see §4.5; these are reported in Table IV.1.). Table IV.5 categorizes the sample stars in a manner similar to Table IV.4, but now using $\Delta(U - V)$. We identify objects with $\Delta(U - V) < -0.3$ as those likely possessing hot accretion spots on their surfaces (see Rebull et al., 2000) and thus likely to be undergoing active accretion (but see Findeisen & Hillenbrand, 2010, for a discussion of other phenomena that may cause blue excesses in PMS stars). Five of the sample stars show evidence for active accretion, and all but one of these have $R_{\text{trunc}} \lesssim R_{\text{dust}}$ as expected for a disk that extends close enough to the star for accretion to occur. Furthermore for two of these stars the Ca II measurements of Hillenbrand (1997, see Table IV.1) also indicate active accretion. Only one star (COUP 1568) fails to show $\Delta(U-V)$ excess despite possessing a close-in disk edge. Thus, while $\Delta(U-V)$ cannot provide a quantitative measure of the location of the inner disk for non-accretors [$\Delta(U-V) > -0.3$], it is, as expected, a relatively reliable indicator of $R_{\text{trunc}} \lesssim R_{\text{dust}}$ for active accretors [$\Delta(U-V) < -0.3$].

In the analysis that follows, we use detailed SED fits over the full range of available photometric data (Tables IV.2 and IV.3). Where applicable, we use the ΔK_{S} and $\Delta(U-V)$ excesses and Ca II equivalent widths in Table IV.1 as secondary information to aid our classifications in order to characterize in detail the presence and structure of circumstellar disks in our sample.

4.4 Synthetic Spectral Energy Distribution Models

To compare the observed SEDs of our sample with the SEDs expected from young stars with disks within reach of the observed flaring loops, we employed the Monte Carlo radiative transfer code of Whitney et al. (2003a,b), TTSRE (T Tauri Star radiative equilibrium), to generate synthetic SEDs. Our aim is to quantitatively constrain the structure of any circumstellar material around each of the 32 stars in our sample so that we may determine, in detail for each star, whether there is in fact disk material within reach of the magnetic loops observed by Favata et al. (2005). Thus for each of the stars in our sample, we wish to determine the range of disk parameters—the most important of these being the location of the inner edge of the disk—that are able to reproduce the observed SEDs (§4.2).

The TTSRE code models randomly emitted photons from the central illuminating source and follows the photons as they interact with (i.e., are absorbed or scattered by) any circumstellar material. The circumstellar material is modeled as an optically thick dust disk extending from an inner truncation radius, $R_{\rm trunc}$, to an outer radius of typically a few hundred AU. The disk in general may be "flared" such that its scale-height increases with increasing distance from the star, or it may be flat. Surrounding the star and disk may be a spherically distributed infalling envelope with bipolar cavities; such an envelope is generally required for reproducing the scattered-light properties of embedded objects (generally seen as moderate excesses in the blue; e.g., Stark et al., 2006). The code also self-consistently solves for thermal equilibrium in the disk as absorbed photons heat the disk and are re-radiated. Sublimation of dust is also included (for details of the dust properties used by the code, see Table 3 of Whitney et al., 2003b). The code models the central illuminating source using the NextGen atmosphere models of Hauschildt et al. (1999). We adopted the solar-metallicity atmosphere models, with $\log g$ and $T_{\rm eff}$ chosen according to each star's observationally determined $M_{\rm star}$, $R_{\rm star}$, and $T_{\rm eff}$ (Table IV.1).

Because of the very large number of permutations on the possible star/disk/envelope parameters included in the TTSRE model (i.e., disk mass, disk inner and outer radius, disk flaring profile, disk accretion rate, disk inclination angle, etc.), there is in general not a simple one-to-one correspondence between a given observed SED and, say, $R_{\rm trunc}$. Thus, to fully explore the range of disk parameters that could possibly reproduce the observed SEDs of our sample, we made use of the very large grid of TTSRE models constructed by Robitaille et al. (2006). The grid includes some 200,000 models representing 14 star/disk/envelope parameters (see Table 1 of Robitaille et al., 2006) that were independently varied to encompass virtually all possible combinations for young stellar objects with masses 0.1–50 $M_\odot$ in the Class 0–III stages of evolution. The parameter space for this grid was specifically set to be very finely sampled for T Tauri stars (i.e., $T_{\rm eff}$ <5200 K); at higher temperatures, $\gtrsim$5200 K, the grid is more sparsely sampled. Whereas at $T_{\rm eff}$ <5200 K the grid is sampled in $R_{\rm trunc}$ by ∼5%, at $T_{\rm eff} > 5200$ K it is sampled much more sparsely at ∼50%. This issue affected only the hottest object in our sample, COUP 597 (see §4.5.1). Additionally, by construction, the models in this grid are set to only include non-zero accretion rates and to always include emission from a hot accretion spot on the star. As a result, in some cases the blueward excess due to the hot accretion spots is seen in the best-fit model SEDs, which we disregard when we lack U or B band fluxes to constrain the blue side of the SED.

With the added free parameter of extinction, A_V, we searched the grid via χ^2 minimization for all synthetic SEDs that fit the observed SED of a given star within the 99% confidence level (that is, we rejected those models that yielded a $\Delta\chi^2$ goodness-of-fit likelihood of 1% or less relative to the best-fit model; Press et al., 1995). For stars with spectral-type determinations from the literature (see Table IV.1), we furthermore require the model fits to have stellar $T_{\rm eff}$ within 500 K of the literature value except for a few cases where we found it necessary to relax the $T_{\rm eff}$ constraint in order to achieve an acceptable SED fit; these exceptions are noted when we discuss each object individually below.

In addition to temperature, we also filter the best-fit models by disk mass. In fitting the SEDs of the sample stars, particularly in cases with little or no IR excess emission in the observed SED, we found that a number of the best-fit models nonetheless had disks with small $\rm R_{trunc}$, but only if the disk also had a very low mass. The extensive model grid of Robitaille et al. (2006) allows for disks with masses as low as 10^{-10} $\rm M_{\odot}$. Such low disk masses, however, may be well below what is physically realistic, and certainly below what is observable, for young T Tauri stars. Recent detailed studies of PMS stars with so-called "transitional" and "pre-transitional" circumstellar disks (e.g., Espaillat et al., 2007)—disks that are undergoing the rapid disk-clearing process from the inside out (e.g., Barsony et al., 2005)—show that even at this late stage the circumstellar disks are in fact quite massive. For example, Espaillat et al. (2007) derive $M_{\rm disk} \approx 10^{-1}$ $\rm M_{\odot}$ for the pre-transitional disk of LkCa 15 with $R_{\rm trunc} \sim 45$ AU, and $M_{\rm disk} \approx 10^{-2}$ $\rm M_{\odot}$ for the slightly more evolved disk of UX Tau A, with $R_{\rm trunc} \sim 60$ AU. A more extreme case is that of CoKu/Tau 4, for which D'Alessio et al. (2005) find an extremely low $M_{\rm disk} \approx 10^{-3}$ $\rm M_{\odot}$. In what follows, we will thus restrict our analysis to include only model SEDs with $M_{\rm disk} > 10^{-3}$ $\rm M_{\odot}$ as more accurately representing the empirical disks of young, low-mass stars. For illustrative purposes, however, we display all models with disk masses greater than 10^{-4} $\rm M_{\odot}$.

In addition, for the purpose of interpreting the resulting best-fit model SEDs, we found it useful for each star to generate an additional TTSRE synthetic SED as a fiducial reference model. For the cases where there is an apparent IR excess in the data indicating the presence of a disk, we generate a fiducial model identical to the best-fit SED model, except that we impose an inner disk boundary, setting R_{trunc} equal to the magnetic loop height, R_{loop} (Table IV.1). In the cases for which the data show no IR evidence for dusty disks, the fluxes of the best fit SED model are essentially arbitrary beyond the longest wavelength data point. For simplicity in these cases our fiducial model is a simple star+disk SED, adopting stellar properties from the literature. The modeled structure is that of an optically thick, geometrically thin, slightly flared disk with no envelope and no accretion. The disk mass in these cases is set to 0.01 $M_{\odot}$, and its inner truncation radius is again set equal to the magnetic loop height. Thus, in all cases, the fiducial model allows a direct, visual comparison of the observed and best-fit SEDs against that expected if the inner disk is within reach of the magnetic flaring loop. It is important to note that in cases where the magnetic loop height is within the dust destruction radius, the disk is truncated at dust destruction by default (i.e., the TTSRE models require $R_{\text{trunc}} \geq R_{\text{dust}}$).

We present in Figs. 4.3–4.6 and C.1–C.28 the SEDs of the 32 stars in our study sample. Flux measurements and upper limits (Tables IV.2–IV.3) are represented by diamond symbols with error bars (which are in most cases smaller than the symbols) and blue triangles, respectively. The SED of the underlying stellar photosphere (NextGen atmosphere) is shown for comparison as a dashed line. Superposed on the observed SEDs, the best-fitting SED models from the grid of Robitaille et al. (2006) discussed above are shown as dash-dotted curves. The fiducial TTSRE model that we calculated is shown as a solid, blue curve.

Figures 4.3–4.6 are included in this chapter for illustrative purposes below (see §4.5), with the remaining figures appearing in Appendix C.

4.5 Interpreting the Spectral Energy Distributions

With observed and model SEDs in hand for all 32 stars in our study sample (Figs. 4.3–4.6, C.1–C.28), we can now attempt to answer the central question of this paper: Are the large flaring loops observed on these stars likely due to a magnetic star-disk interaction, or do they represent primarily stellar phenomena unrelated to disks? To answer this question, in this section we discuss the specific criteria by which we determine, from examination of each star's SED, the likelihood that it possesses a disk whose inner edge is within reach of the observed flaring magnetic loop.

4.5.1 SED Categorization Criteria

As discussed above, in general we found that $R_{\rm trunc}$ correlates with $M_{\rm disk}$ in the model SEDs, e.g., a small $R_{\rm trunc}$ can fit even a bare photosphere SED if $M_{\rm disk}$ is made sufficiently small (see §4.4). Thus we found it helpful to visualize $R_{\rm trunc}$ versus $M_{\rm disk}$, as shown in the lower panel of Figs. 4.3–4.6 in order to better interpret the SED model fits. A vertical line at 10^{-3} $M_\odot$ indicates our disk mass threshold (see §4.4). In orange, we show the stellar photosphere for reference. In each figure, the $M_{\rm disk}$ and $R_{\rm disk}$ values corresponding to each model SED from the upper panel are shown as diamonds. For comparison, the magnetic loop height ($R_{\rm loop}$) and its uncertainty (see §4.2.1) are shown as a cartoon parabola and a hatched region, respectively.

From these plots, we can thus begin to assess the degree of spatial correspondence between $R_{\rm trunc}$ and $R_{\rm loop}$ for each star. Cases for which $R_{\rm trunc} \leq R_{\rm loop}$ can be interpreted as representing disks that are within reach of the observed flaring loops. Cases for which $R_{\rm trunc} > R_{\rm loop}$ are somewhat less straightforward to interpret because we must first account for the effects of dust sublimation. The location of dust destruction, or the sublimation radius, is calculated using each model's stellar temperature and radius as follows (Whitney et al., 2004):

$$R_{\rm dust} = R_{\rm star} \times \left(\frac{1600 \text{ K}}{T_{\rm star}} \right)^{-2.1} \tag{4.1}$$

where 1600 K is the dust sublimation temperature. This relationship was empirically determined by running radiative transfer code iteratively and tracing the radius at which disk temperature rises above $\rm T_{sub}$. Uncertainties in $R_{\rm star}$ and $T_{\rm star}$ create a range of possible values for $R_{\rm dust}$. We adopt 5% uncertainty in $T_{\rm star}$ and 20% uncertainty in $R_{\rm star}$ in this calculation (see e.g., Hillenbrand, 1997). In each of Figs. 4.3–4.6 (and C.1–C.28), filled (red) diamonds represent models effectively truncated at the dust destruction radius, $R_{\rm dust}$, while unfilled points have vertical bars in the $-y$ direction to show where that particular model's dust destruction radius is located. For the model uncertainty in $R_{\rm trunc}$, we adopt 5% and 50% for stars with $T_{\rm eff}$ <5200 K and $T_{\rm eff}$ >5200 K, respectively (see §4.4). Thus, when we say the disk is truncated "effectively" at the dust destruction radius, the intended meaning is that $R_{\rm trunc}$ and $R_{\rm dust}$ are equivalent within their uncertainties. We also report fiducial $R_{\rm dust}$ values for our sample stars in Table IV.1; these are calculated using Eq. 4.1 and the $R_{\rm star}$

and $T_{\rm star}$ data in that same table.

The broadband fluxes used here trace the spatial extent of a disk's dust; in principle the inner edge of the *gas* in the disk could extend even closer to the stellar surface. For the cases in which we find that an observed dust disk is truncated at the dust destruction radius, the dust disk is likely truncated by sublimation, a process which would not remove gas. Indeed, some systems have been observed to be accreting even though the dust disk is truncated far from the star (Eisner et al., 2005, 2007). For dust disks truncated near the sublimation radius, but not within reach of the magnetic loop, it is possible that a gas disk extends closer to the star and is truncated within the loop height (this has been observed by Najita et al., 2003; Eisner et al., 2005). Conversely, if the dust disk is truncated outside the dust destruction radius, some other process may be responsible for clearing out the inner portion of the disk, and therefore we assume that the inner gas is cleared out as well (e.g., Isella et al., 2009).

Finally, for a few stars we lack sufficient photometric data to adequately constrain the location of $R_{\rm trunc}$. In most cases, this is due to a lack of *Spitzer* photometry and thus the longest wavelength measurement is the 2MASS 2.2 μm flux. Consequently, the model SEDs in these cases are largely unconstrained and result in a wide variety of possible star-disk configurations which can fit the observed SED.

Based on these considerations, in what follows we categorize our sample stars into four groups, based on the degree to which the SEDs indicate that the inner disk edge is within reach of the flare loop height:

Category 1: $R_{\mathrm{trunc}} \leq R_{\mathrm{loop}}$: The inner disk edge is clearly within reach of the magnetic flaring loop.

Category 2: $R_{\mathrm{trunc}} > R_{\mathrm{loop}}$ but $R_{\mathrm{trunc}} \approx R_{\mathrm{dust}}$: The dusty inner disk edge is beyond the flaring loop height, however the dust disk is truncated at the dust-destruction distance and thus a gas disk may extend inward to R_{loop} (i.e., $R_{\mathrm{trunc}} \lesssim R_{\mathrm{dust}}$).

Category 3: $R_{\mathrm{trunc}} > R_{\mathrm{loop}}$ and $R_{\mathrm{trunc}} > R_{\mathrm{dust}}$: The inner edge of the dust diskis clearly beyond reach of the magnetic flaring loop.

Category 4: Indeterminate: More than one category above is permitted by the available data (generally due to lack of *Spitzer* data).

In general, for a given star there are multiple SED models that are good fits to the observed SED, and in some cases the multiple best-fitting model SEDs yield a mixed verdict regarding the placement of R_{trunc} with respect to R_{loop}. Thus if one of categories 1–3 above is favored by more than $\frac{2}{3}$ of the best-fit SED models, we assign the star to that category, and we assign "indeterminate" (category 4) otherwise.

4.5.2 Example Cases

As an example of our approach to interpreting the SEDs of our study sample, we show in Fig. 4.3 (upper panel) the SED of COUP 1410. The fiducial SED model in Fig. 4.3, corresponding to a disk with $R_{\mathrm{trunc}} = R_{\mathrm{loop}}$, predicts an excess of IR flux at wavelengths as short as 3 μm, unlike the data and best-fit model SEDs which follow the profile of a bare stellar photosphere to 4.5 μm. Intuitively, this implies that the best-fit model SEDs must therefore correspond to disks with moderately large inner holes. Indeed, the lower panel of Fig. 4.3 shows that nearly all of the best-fit model SEDs, representing disks with $10^{-4} \lesssim M_{\rm disk}/{\rm M}_{\odot} \lesssim 10^{-2}$, have $R_{\rm trunc} > 1$ AU. Furthermore, the majority of these models are truncated well outside their respective dust destruction radii (i.e. $R_{\rm trunc} > R_{\rm dust}$); only one fit model has $R_{\rm trunc} \lesssim R_{\rm dust}$, and this model has very low $M_{\rm disk}$, below our threshold of 10^{-3} ${\rm M}_{\odot}$

Note that the observed SED for this star does not in fact *require* any disk at all; the fact that many of the SED models shown in Fig. 4.3 exhibit large excesses longward of 4.5 μm implies only that these hypothetical disks with very large inner holes are formally *permitted* by the available data. These models thus provide a lower limit to the size of $R_{\rm trunc}$ that any as-yet undetected disk could possibly have. Since this lower limit is in this case much larger than $R_{\rm loop}$, we conclude that no disk is present that could interact with the observed magnetic flaring loop, and we assign COUP 1410 to category 3 (§4.5.1).

COUP 141 (Fig. 4.4) is a case in which the observed SED is reasonably well matched by the fiducial SED model, for which $R_{\rm trunc} = R_{\rm loop}$. The best-fit SEDs have inner truncation radii well beyond reach of the magnetic loop. However, these models' inner disk radii are also equal to their dust destruction radii, and thus it is likely that sublimation is responsible for the apparent clearing of the inner disk. In cases like COUP 141, while the magnetic loop may not intersect the dust disk, it could nonetheless intersect a gas disk that extends inward of the dust to within reach of $R_{\rm loop}$. Indeed, both Ca II and $\Delta(U - V)$ strongly indicate active accretion (Table IV.1). Thus we assign COUP 141 to category 2.

As another example, consider COUP 720 (Fig. 4.5). In this case, all of the best-fit model SEDs with $M_{\rm disk}$ above our adopted threshold of 10^{-3} $\rm M_{\odot}$ have similar $R_{\rm trunc} \sim 0.1$ AU, which overlaps $R_{\rm loop}$ within its uncertainty. Many of these best-fit models, moreover, have $R_{\rm trunc} \approx R_{\rm dust}$, and thus may possess gas disks that extend even closer to the star. COUP 720 thus represents a good example of an SED that is consistent with $R_{\rm trunc} \approx R_{\rm loop}$, and for which the large magnetic loops observed by COUP may facilitate the magnetic star-disk interaction envisaged in magnetospheric accretion models. COUP 720 is assigned to category 1.

Finally, consider COUP 997 (Fig. 4.6). The observed SED data (0.34–4.5 μm) show excess IR flux. About half of the best-fit models are truncated at their dust destruction radii (category 2), while the other half are truncated beyond 1 AU (category 3). We also do not have Ca II or $\Delta(U-V)$ measurements to help disambiguate the two possibilities, and thus it is not possible to say which set of models correctly describes the observed star-disk system. Requiring additional data (particularly longward of $\sim 10\mu$m) to discriminate between the category 2 and 3 model fits, we assign this object to category 4.

4.6 Results

In Table IV.6, we present a summary of the results for the 32 stars in our sample. Following the procedure described in §4.5, we have identified which stars' SEDs have massive (i.e., greater than our $10^{-3}\rm M_{\odot}$ cutoff) disks that are consistent with being within reach of the observed magnetic loops. Notes about each star relevant to its classification are provided in the figure captions.

We find six stars that clearly appear to have SEDs consistent with $R_{\rm trunc} \leq R_{\rm loop}$ (category 1). Another four stars do not show direct evidence of disks within reach of the magnetic loops, but could potentially have gas that extends interior to the observed dusty inner edge of the disk (category 2). Fourteen stars either have disks whose inner edges are situated beyond the reach of the magnetic loops, or are simply devoid of detected disk material entirely (category 3). For eight stars, we could not assign a definitive category as additional data are necessary to support or eliminate different classes of best-fit SED models (category 4).

4.7 Discussion and Conclusions

Of the 24 stars in our 32-star sample for which we have enough optical–infrared data to strongly constrain the location of the disk inner edge (i.e., excluding stars in category 4; §4.5.1 and Table IV.6), for about 58% we are able to rule out close-in disks within reach of the observed large flaring loops (category 3). For these stars, the energetic flares discovered by Favata et al. (2005) are evidently intrinsically stellar phenomena. This gives added justification *a posteriori* for the application of the solar-flare cooling loop model to these stars (§4.2.1), and suggests that it may be possible by further extension of the solar analogy to infer other flare-related properties for these flares, such as coronal heating rates and coronal mass ejections. The latter in particular may be important for furthering our understanding of mass and angular momentum loss in these low-mass PMS stars (for an example of this, see §D).

Our samplealso includes six cases for which the SED clearly indicates a dusty disk that extends close enough to the star to permit interaction with the flaring loop (category 1; Table IV.6). In four additional cases, the dust disk appears to be truncated beyond the reach of the flaring loop, but at or close to the predicted dust destruction radius (category 2). In these cases, the dust disk may in fact be truncated by dust sublimation, a process which does not remove gas. Thus, in these 10 cases, it seems likely that a gas disk (undetected in the broadband flux measurements used in our SED models) extends closer to the star and may be within reach of the observed flaring loops. One of the four category 2 objects has a Ca II measurement from the literature (COUP 141), and two have $\Delta(U-V)$ measurements (COUP 141 and COUP 1568). COUP 141 is, interestingly, the most strongly accreting object in the sample as probed by its Ca II equivalent width (see Table IV.1) and it also has a very negative $\Delta(U-V)$; the combination of these indicators is strong evidence for ongoing accretion. For COUP 141 the ΔK_S near-IR excess also indicates a disk very close to the star (see Sec. 4.3 and Table IV.4). These examples further strengthen the interpretation of the category 2 stars as likely having gas accretion disks within reach of the stellar magnetosphere.

Several studies clearly find a high frequency of close-in, dusty disks in the ONC population as a whole. For example, Hillenbrand et al. (1998) find a disk fraction in the ONC of ∼70% on the basis of excess emission at 2.2μm. Thus, the ∼25% (category 1) or ∼38% (categories 1 and 2) frequency of close-in disks in our 32-star sample, representing the ∼1% of ONC stars with the most powerful X-ray flares observed by COUP, is evidently not representative of the disk characteristics of the ONC as a whole.

The six cases with close-in, dusty disks which intersect the magnetic loops (category 1) are interesting candidates for further study. Specifically, it would be informative to determine if the flares in these cases are in some way different than the category 3 cases. Three of these objects have $\Delta(U-V)$ measurements, all of them ≤ -0.3 (Table IV.1), strongly indicating active accretion. Temporally linking accretion as seen in optical variability to the X-ray flare events (e.g., Stassun et al., 2006) could solidify whether a magnetic star-disk interaction has taken place. Geometric information would be necessary to determine where the magnetic loop is on the stellar surface—for example, a given flaring loop could extend in a direction perpendicular to the disk and thus not interact, even if the dust (or gas) disk is within the appropriate distance from the stellar surface.

The question of how the large magnetic structures are stabilized (prior to the flaring event) was posed in the discovery publication of these objects (Favata et al., 2005). It was proposed that the loops may be anchored to corotating disk material and thereby not subject to shear which could disrupt the loops. In this work we have found such disk-anchoring to indeed be a possibility for 10 objects (categories 1 and 2), but further analysis is needed to determine how massive and ionized a disk must be to enable interaction. For fourteen objects (category 3), disk-supported loops are unlikely, as these stars lack disks within reach of the loops. We speculate that as long as the confining magnetic field at the upper end of the loop is sufficiently strong and the confined material corotating, stability is feasible even without a disk. For example, Cranmer (2009) describes a loop geometry in which the pressure of the confined gas decreases with increasing loop length, implying that in fact the largest coronal loops may be most stable against rupture. Additionally, our findings may imply that the largest flaring loops cannot readily form in the presence of a disk, given that they appear in our sample to preferentially occur on stars lacking close-in disk material.

Alternate scenarios to explain the long X-ray decay timescales include observations of corotating, embedded structures in coronae (e.g., Collier Cameron & Robinson, 1989a,b), and prominences and stellar winds (Skelly et al., 2008; Massi et al., 2008). The observed coronal structures from those studies lend additional support to the idea of these large magnetic structures remaining stable in hot coronae or within the stellar wind over multiple rotation periods as the X-ray flare decays, even if no disk is present to anchor the magnetic loop (Jardine & van Ballegooijen, 2005).

In summary, the 32 most powerful flares observed by the COUP survey were found to have magnetic structures multiple stellar radii in arc length confining the X-ray emitting, heated plasma (Favata et al., 2005). With the goal of understanding the nature of these large X-ray emitting flare structures, we have modeled the optical–infrared SEDs of these objects, finding 58% to be lacking close-in circumstellar disks to which these loops could anchor. It is evident that in at least these cases the large-scale flares are phenomena of purely stellar origin, neither triggered nor stabilized by star-disk interactions.

Table IV.1: Stellar Parameters

Object Name	$T_{\rm eff}^1$ [K]	Mass^1 [$M_\odot$]	Radius^1 [$R_\odot$]	Magnetic Loop Height [$R_\odot$]^2	Dust Destruction Radius^3 [$R_\odot$]	Ca 2 EW^1 [Å]	Literature A_V^1 [mag]	Re-calculated A_V^3 [mag]	$\Delta(K_S)^3$ [mag]	$\Delta(U-V)^3$ [mag]
COUP 7	4581	2.12	6.23	0.65	56.8	···	0.75	0.67 (-0.58, +0.54)	0.12	0.03
COUP 28	3802	0.53	2.3	7.91±5.46	14.2	1.6	0.63	0.30 (-0.30, +0.54)	0.20	0.24
COUP 43	3606	0.4	2.92	16.1 (+3.16,-5.32)	16.0	1.4	1.36	1.18 (-0.60, +0.56)	0.012	0.64
COUP 90	3802	0.52	2.51	1.04 (+4.86,-1.04)	15.5	1.6	4.97	3.97 (-1.13, +1.13)	0.053	···
COUP 141	5236	2.11	3.3	1.97	39.2	-17.8	1.83	2.17 (-0.63, +0.60)	0.37	-0.67
COUP 223	4395	1.19	2.79	6.95	23.3	1.7	4.66	5.81 (-0.75, +0.88)	0.31	···
COUP 262	4395	1.13	1.58	28.5 (+16.8,-22.3)	13.2	2.3	3.77	7.89 (-1.20, +1.24)	0.14	···
COUP 332	3111†	0.5‡	2‡	105±38.4	8.09	···	···	12.8 (-1.67, +2.14)	0.032	···
COUP 342	4729†	0.5‡	2‡	20.3 (+21.4,-20.3)	19.5	···	···	7.89 (-0.78, +0.85)	0.085	···
COUP 454	4775	2.35	4.58	46.4 (+14.8,-9.20)	45.5	2.1	5.85	6.39 (-0.85, +0.87)	0.077	···
COUP 597	5662	1.49	2.01	3.16 (+7.62,-3.16)	28.6	4.5	2.69	3.32 (-1.35, +1.39)	0.27	-0.26
COUP 649	3589	0.4	2.17	9.20	11.8	0	4.11	3.82 (-0.73, +0.83)	0.17	···
COUP 669	4581	1.52	2.59	13.2 (+2.73,-3.31)	23.6	···	1.96	2.33 (-1.10, +1.20)	0.049	···
COUP 720	4452†	0.5‡	2‡	19.0 (+69.3,-19.0)	17.2	···	···	11.8 (-1.33, +1.66)	-0.23	···
COUP 752	3802	0.54	1.67	9.35 (+1.29,-9.35)	10.3	1.1	0.07	0.64 (-0.64, +1.10)	0.047	-0.70
COUP 848	3342	0.29	1.98	23.3 (+4.03,-3.31)	9.31	0	1.72	1.35 (-1.34, +1.46)	0.093	···
COUP 891	4775	2.43	4.85	24.9 (+3.88,-3.31)	48.8	1.8	8.00	10.7 (-1.02, +1.12)	0.13	···
COUP 915	4613†	0.5‡	2‡	11.2 (+3.88,-2.59)	18.4	···	···	15.8 (-1.76, +2.56)	-0.065	···
COUP 960	3177	0.24	2.16	0.53 (+1.48,-0.53)	9.27	0	2.72	1.29 (-0.41, +0.43)	-0.013	···
COUP 971	3999	0.69	3.28	5.03 (+0.72,-0.43)	22.5	1.8	0.	0.00 (-0.00, +0.15)	-0.24	-0.80
COUP 976	3177	0.18	0.91	10.9	3.85	0	0.	2.88 (-0.69, +1.13)	0.28	···
COUP 997	3856†	0.5‡	2‡	4.89 (+4.03,-3.88)	12.7	···	···	1.82 (-1.14, +1.13)	0.060	···
COUP 1040	4281†	0.5‡	2‡	1.25 (+1.91,-1.25)	15.8	···	···	16.5 (-2.03, +3.53)	-0.10	···
COUP 1083	4698†	0.5‡	2‡	33.8 (+9.63,-7.05)	19.2	···	···	4.16 (-0.56, +0.61)	-0.0072	···
COUP 1114	4903†	0.5‡	2‡	9.78 (+2.30,-9.78)	21.0	-1.5	···	6.08 (-0.71, +0.74)	0.086	···
COUP 1246	3177	0.23	1.62	5.75 (+1.01,-1.15)	6.95	0	0.92	1.52 (-0.60, +0.70)	0.45	···
COUP 1343	3649†	0.5‡	2‡	13.8 (+2.45,-2.44)	11.6	···	···	3.04 (-0.83, +3.66)	0.60	···
COUP 1384	3802	0.52	2.46	7.33±4.46	15.1	1.9	0.	0.67 (-0.67, +0.82)	-0.095	-0.35
COUP 1410	3606	0.36	0.51	15.8 (+12.9,-15.8)	2.80	0	0.57	4.98 (-0.98, +0.97)	0.053	···
COUP 1443	5528†	0.5‡	2‡	3.74 (+4.17,-0.57)	13.6	···	···	0.26 (-0.26, +0.55)	0.18	0.14
COUP 1568	5236	2.55	3.99	0.53 (+1.62,-0.53)	48.1	···	0.59	1.06 (-0.56, +0.60)	-0.040	-0.22
COUP 1608	3724	0.48	1.76	11.8 (+2.44,-11.8)	10.8	-1.3	0.93	0.25 (-0.25, +0.41)	0.43	-1.2

---

[0] Note- † Assigned $T_{\rm eff}$ from best fit SED model. Fiducial masses and radii of 0.5 $M_\odot$ and 2 $R_\odot$ taken when literature values unavailable.

[1] Taken from Hillenbrand (1997), unless otherwise noted.

[2] Taken from Favata et al. (2005). Uncertainty not quoted if only two points used in fitting the flare $\log(T)$-$\log(n_e)$ decay slope.

[3] Derived in this work.

Table IV.2: *Hubble* ACS and WFI Fluxes

Object Name	4317Å Flux [mJy]	5359Å Flux [mJy]	6584Å^1 Flux [mJy]	7693Å Flux [mJy]	9055Å Flux [mJy]	0.36μm Flux [mJy]	0.44μm Flux [mJy]	0.55μm Flux [mJy]	0.83μm Flux [mJy]
COUP 7	· · ·	· · ·	170	· · ·	· · ·	3.9±0.36	40.±3.7	83.0±7.6	290±27
COUP 28	0.89±0.082	2.9±0.27	7.3	· · ·	· · ·	0.099±0.0091	1.1±0.10	2.7±0.25	16±1.5
COUP 43	0.40±0.037	1.6±0.15	5.2	10.±0.95	20.±1.9	0.033±0.0031	0.42±0.039	1.2±0.11	15±1.4
COUP 90	0.028±0.0026	0.15±0.014	0.69	1.7±0.15	4.0±0.37	· · ·	0.038±0.0035	0.13±0.012	2.9±0.26
COUP 141	7.9±0.73	16±1.4	· · ·	· · ·	· · ·	1.3±0.12	· · ·	· · ·	66±6.1
COUP 223	0.074±0.0068	0.32±0.029	1.6	· · ·	· · ·	· · ·	0.095±0.0088	· · ·	6.2±0.57
COUP 262	0.011±0.0010	0.095±0.0088	0.57	2.0±0.18	6.7±0.61	· · ·	· · ·	0.11±0.010	4.4±0.41
COUP 332	· · ·	· · ·	· · ·	0.049±0.0045	0.33±0.030	· · ·	· · ·	· · ·	· · ·
COUP 342	0.008±0.00072	0.078±0.0072	0.52	1.9±0.17	6.3±0.58	· · ·	· · ·	0.099±0.0091	4.4±0.41
COUP 454	0.11±0.010	0.64±0.059	2.6	6.8±0.62	16±1.5	· · ·	0.16±0.014	0.63±0.058	13±1.2
COUP 597	2.0±0.18	5.8±0.54	· · ·	· · ·	26±2.4	0.34±0.032	2.3±0.22	5.3±0.48	23±2.1
COUP 649	0.019±0.0017	0.10±0.0093	0.38	1.5±0.14	3.4±0.31	· · ·	· · ·	· · ·	2.7±0.25
COUP 669	1.8±0.17	6.6±0.61	15	· · ·	· · ·	· · ·	2.4±0.22	5.6±0.52	31±2.8
COUP 720	· · ·	· · ·	0.070	0.31±0.029	1.5±0.14	· · ·	· · ·	· · ·	0.99±0.091
COUP 752	0.85±0.078	2.6±0.24	7.1	10.±0.92	16±1.4	0.18±0.016	1.3±0.12	3.0±0.27	16±1.5
COUP 848	0.097±0.0089	0.37±0.034	1.5	3.3±0.30	6.9±0.63	· · ·	· · ·	0.46±0.042	5.4±0.50
COUP 891	0.002±0.00022	0.046±0.0043	0.40	2.1±0.20	9.1±0.84	· · ·	· · ·	0.046±0.0042	5.7±0.53
COUP 915	· · ·	· · ·	· · ·	· · ·	· · ·	· · ·	· · ·	· · ·	0.17±0.015
COUP 960	0.022±0.0020	0.082±0.0075	0.40	1.6±0.14	4.3±0.40	· · ·	0.029±0.0027	0.076±0.0070	3.1±0.28
COUP 971	10.±0.96	21±2.0	43	· · ·	· · ·	1.6±0.15	11±1.0	· · ·	64±5.9
COUP 976	0.016±0.0015	0.080±0.0074	0.51	1.4±0.13	3.8±0.35	· · ·	· · ·	· · ·	2.7±0.25
COUP 997	0.60±0.055	2.1±0.19	5.9	11±0.98	18±1.7	· · ·	0.77±0.071	2.0±0.18	14±1.3
COUP 1040	· · ·	· · ·	· · ·	· · ·	· · ·	· · ·	· · ·	· · ·	0.10±0.0093
COUP 1083	0.43±0.040	1.8±0.17	6.2	14±1.3	26±2.4	· · ·	0.55±0.051	1.7±0.16	18±1.7
COUP 1114	0.23±0.021	1.6±0.15	7.0	· · ·	· · ·	· · ·	0.38±0.035	1.6±0.14	37±3.4
COUP 1246	0.046±0.0043	0.22±0.020	1.2	1.3±0.12	5.2±0.48	· · ·	0.059±0.0055	0.19±0.017	3.9±0.36
COUP 1343	0.058±0.0054	0.31±0.028	1.7	2.8±0.26	6.7±0.62	· · ·	0.082±0.0075	0.27±0.025	5.0±0.46
COUP 1384	2.8±0.26	7.9±0.73	17	· · ·	· · ·	0.39±0.036	3.3±0.30	6.9±0.64	30.±2.7
COUP 1410	0.0040±0.00037	0.022±0.0020	0.13	0.48±0.045	1.4±0.13	· · ·	· · ·	0.021±0.0019	1.0±0.093
COUP 1440	1.9±0.18	6.2±0.57	15	· · ·	24±2.2	0.21±0.019	2.5±0.23	6.0±0.56	31±2.8
COUP 1568	· · ·	85±7.8	· · ·	· · ·	· · ·	8.4±0.77	50.±4.6	· · ·	202±19
COUP 1608	· · ·	1.4±0.13	· · ·	· · ·	· · ·	0.20±0.018	0.73±0.068	· · ·	11±1.02
Zero points	25.793$^{(2)}$	25.744$^{(2)}$	22.393$^{(2)}$	25.291$^{(2)}$	24.347$^{(2)}$	1823 Jy$^{(3)}$	4130 Jy$^{(3)}$	3640 Jy$^{(3)}$	2430 Jy$^{(3)}$

---

[0] The first five data columns report *HST* fluxes, the last four columns report WFI fluxes. Zeropoint fluxes used are reported in the final row of the table.

[1] For the purposes of fitting, the Hα fluxes were given a wide (99%) error in order to allow for variability commonly observed T Tauri stars.

[2] The ACS data utilized were in the Vegamag system; these values were used in the conversion to the ABmag system, for which flux calculation is straightforward as outlined in the online ACS documentation found here: `http://www.stsci.edu/hst/acs/analysis/zeropoints/`

[3] Johnson-Cousins zero points; UBVI$_C$.

Table IV.3: V, I, 2MASS, and *Spitzer* Fluxes

Object Name	0.55μm Flux [mJy]	0.79μm Flux [mJy]	1.235 μm Flux [mJy]	1.662 μm Flux [mJy]	2.159 μm Flux [mJy]	3.6 μm Flux [mJy]	4.5 μm Flux [mJy]	5.8 μm Flux [mJy]	8.0 μm Flux [mJy]	23.6 μm Flux[1] [mJy]
COUP 7	102±9.4	280±25	460±42	590±54	440±41	200±18	130±12	84±7.8	50.±4.6	10
COUP 28	3.8±0.35	17±1.6	39±3.6	47±4.4	41±3.8	20.±1.8	13±1.2	8.9±0.82	6.5±0.60	14
COUP 43	2.2±0.20	15±1.4	51±4.7	72±6.6	62±5.7	33±3.0	23±2.1	16±1.4	11±0.98	···
COUP 90	0.084±0.0078	1.8±0.16	14±1.2	27±2.5	27±2.5	16±1.5	11±1.0	6.6±0.60	···	···
COUP 141	24±2.2	71±6.6	130±12	180±16	170±16	150±14	140±13	120±11	160±15	···
COUP 223	0.42±0.038	5.1±0.47	39±3.6	93±8.6	120±11	140±13	130±12	110±10.	91±8.4	···
COUP 262	0.31±0.028	2.7±0.25	35±3.2	96±8.8	130±12	98±9.0	68±6.3	39±3.6	···	···
COUP 332	···	···	4.8±0.44	22±2.0	40.±3.7	64±5.9	69±6.3	87±8.0	150±14	···
COUP 342	···	···	32±3.0	81±7.5	95±8.7	72±6.6	50.±4.6	63±5.8	···	···
COUP 454	0.66±0.061	10.±0.93	74±6.8	150±14	150±14	150±14	130±12	120±11	150±14	···
COUP 597	6.1±0.56	21±1.9	41±3.8	58±5.4	63±5.8	71±6.5	62±5.7	···	···	···
COUP 649	0.082±0.0075	1.6±0.15	14±1.3	29±2.6	31±2.8	···	···	···	···	···
COUP 669	5.8±0.54	24±2.2	68±6.3	97±8.9	83±7.7	110±9.9	···	···	···	···
COUP 720	···	···	13±1.2	43±4.0	65±6.0	83±7.7	70±6.5	58±5.4	57±5.2	···
COUP 752	3.4±0.31	12±1.1	31±2.8	40±3.7	34±3.1	20.±1.9	21±1.9	15±1.4	20.±1.8	11
COUP 848	0.36±0.033	4.1±0.37	17±1.6	22±2.0	20.±1.9	···	···	···	···	···
COUP 891	0.10±0.0094	3.4±0.31	69±6.3	240±22	350±32	240±22	170±15	120±11	79±7.3	90
COUP 915	···	···	5.6±0.52	34±3.1	68±6.3	78±7.2	67±6.2	56±5.1	···	···
COUP 960	0.093±0.0086	2.1±0.19	11±1.0	13±1.2	11±1.0	6.6±0.61	4.7±0.43	···	···	36
COUP 971	26±2.4	62±5.7	102±9.4	140±13	82±7.6	44±4.1	···	···	···	···
COUP 976	···	···	13±1.2	24±2.2	26±2.4	24±2.2	20.±1.8	···	···	···
COUP 997	2.0±0.19	11±0.98	36±3.3	55±5.0	50.±4.6	39±3.6	27±2.5	···	···	···
COUP 1040	···	···	4.0±0.37	26±2.4	58±5.3	75±6.9	76±7.0	60.±5.6	56±5.2	···
COUP 1083	3.2±0.29	16±1.5	57±5.2	95±8.8	86±7.9	54±5.0	36±3.3	···	···	···
COUP 1114	1.9±0.17	26±2.4	190±18	380±35	410±37	250±23	190±18	130±12	86±7.9	···
COUP 1246	0.28±0.025	3.2±0.29	15±1.3	24±2.2	28±2.5	18±1.7	17±1.5	21±1.9	42±3.9	···
COUP 1343	0.32±0.029	3.5±0.32	25±2.3	58±5.4	82±7.5	70±6.5	62±5.7	35±3.2	···	···
COUP 1384	8.2±0.75	28±2.6	66±6.1	87±8.0	69±6.4	34±3.1	23±2.1	18±1.6	···	···
COUP 1410	0.14±0.013	0.72±0.067	5.8±0.53	12±1.1	12±1.1	7.2±0.67	4.8±0.44	···	···	···
COUP 1443	6.5±0.60	25±2.3	57±5.3	77±7.1	62±5.7	32±3.0	20.±1.9	18±1.7	···	···
COUP 1568	109±10.	207±19	290±26	300±27	240±22	130±12	100.±9.6	97±8.9	130±11	156±14
COUP 1608	···	···	26±2.4	39±3.6	46±4.2	45±4.1	46±4.3	34±3.2	43±3.9	119±16
Zero points [Jy]	3640[1]	2490[2]	1594[3]	1024[3]	666.7[3]	280.9[4]	179.7[4]	115.[4]	64.13[4]	7.17[5]

---

[0] Note- *Fluxes reported without error are 3σ upper limits.

[1] Bessell (1979).

[2] Cousins (1976).

[3] Cohen et al. (2003).

[4] `http://ssc.spitzer.caltech.edu/documents/cookbook/html/cookbook-node208.html`

[5] Engelbracht et al. (2007).

Table IV.4: Reliability of Near-IR Excess as Tracer of Inner Disk Edge

⋯	$\mathrm{R_{trunc}} \lesssim \mathrm{R_{dust}}$	$\mathrm{R_{trunc}} > \mathrm{R_{dust}}$
$\Delta(K_S) \geq 0.3$	141[a], 223, 1608[a]	1246[b]
$\Delta(K_S) < 0.3$	332, 454, 720, 752, 976, 1040, 1384, 1568	7, 28, 43, 90, 262, 597, 669, 891, 960, 971, 1083, 1114, 1410, 1443

---

[a] Object possesses Ca 2 in emission (Table IV.1) a spectroscopic indicator of active accretion.

[b] We consider the ΔK_{S} measurement for COUP 1246 to be statistically insignificant (see discussion of this specific case in §4.3), so this object actually belongs in the lower right corner of the Table.

Note. — Category 4 objects have been omitted, as a clear determination of R_{trunc} could not be made; see §4.5.1.

Table IV.5: Reliability of Near-UV Excess as Tracer of Inner Disk Edge

⋯	$\mathrm{R_{trunc}} \lesssim \mathrm{R_{dust}}$	$\mathrm{R_{trunc}} > \mathrm{R_{dust}}$
$\Delta(U-V) \leq -0.3$	141[a], 752, 1384, 1608[a]	971
$\Delta(U-V) > -0.3$	1568	7, 28, 43, 597, 1443

---

[a] Object possesses Ca 2 in emission (Table IV.1) a spectroscopic indicator of active accretion.

Note. — Category 4 objects have been omitted, as a clear determination of R_{trunc} could not be made; see §4.5.1.

Table IV.6. Spectral Energy Distribution Result Summary

Category 1	Category 2	Category 3	Category 4
332	141	7	223
454	1040	28	342
720	1568	43	649
752	···	90	848
1384	···	262	915
1608	···	597	976
···	···	669	997
···	···	891	1343
···	···	960	···
···	···	971	···
···	···	1083	···
···	···	1114	···
···	···	1246	···
···	···	1410	···
···	···	1443	···

Note. — Categories as described in §4.5.1 for all COUP sample objects.

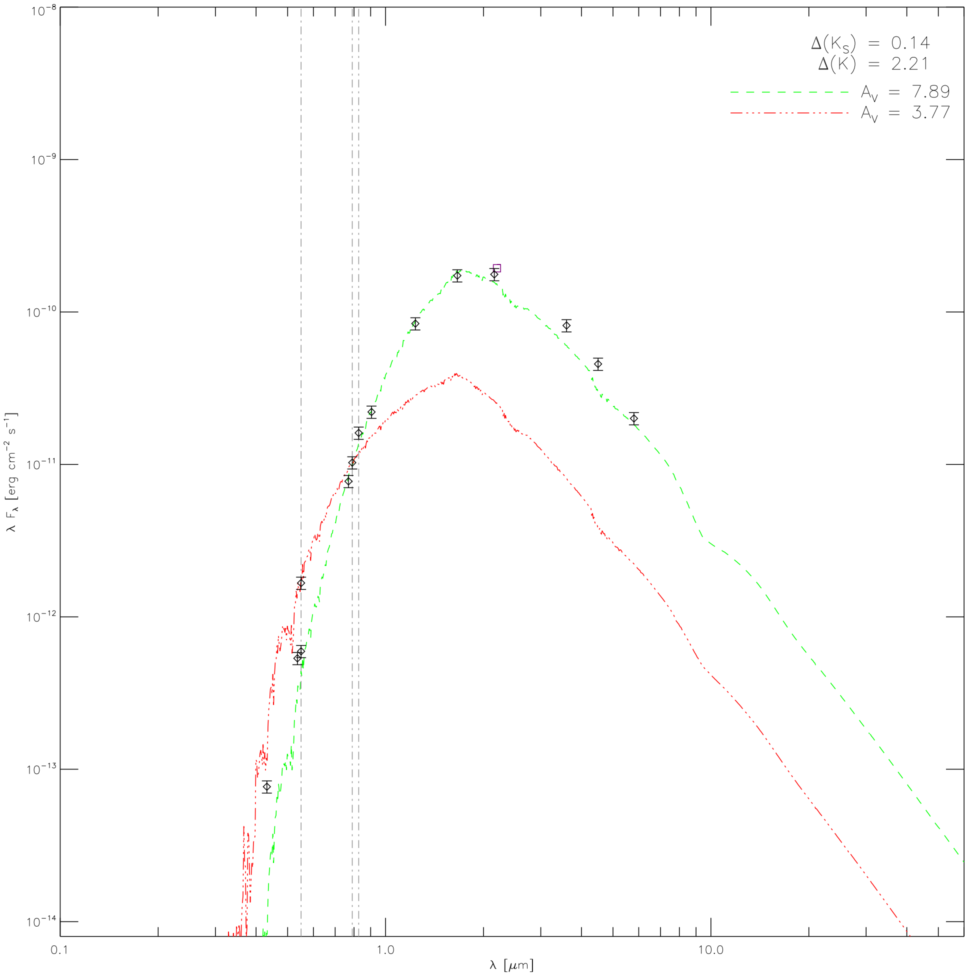

Figure 4.1: SED for COUP 262. Diamonds are photometric data from Tables IV.2–IV.3 (see §4.2.2). The purple square is the K-band flux from (Hillenbrand et al., 1998) used to calculate ΔK_S for the red atmosphere model. The green curve is the best fitting NextGen stellar atmosphere model with T_{eff} set to the literature value (Table IV.1). The best-fit extinction, A_V, is reported upper right. The red curve represents the same stellar atmosphere model but with A_V as previously determined by Hillenbrand (1997) based on a fit to the V and I fluxes only. Vertical lines indicate the wavelengths of the (from left to right) V and I_C bands used by Hillenbrand (1997) and the WFI I-band newly reported here. The resulting ΔK_S color excesses for both model atmosphere fits are reported at upper right (see also Table IV.1). It is clear that the new fit to the full set of available photometric fluxes results in a more accurate representation of the stellar SED. Whereas this star was previously identified as possessing a very large near-IR excess, the new SED fit here clearly indicates no significant excess.

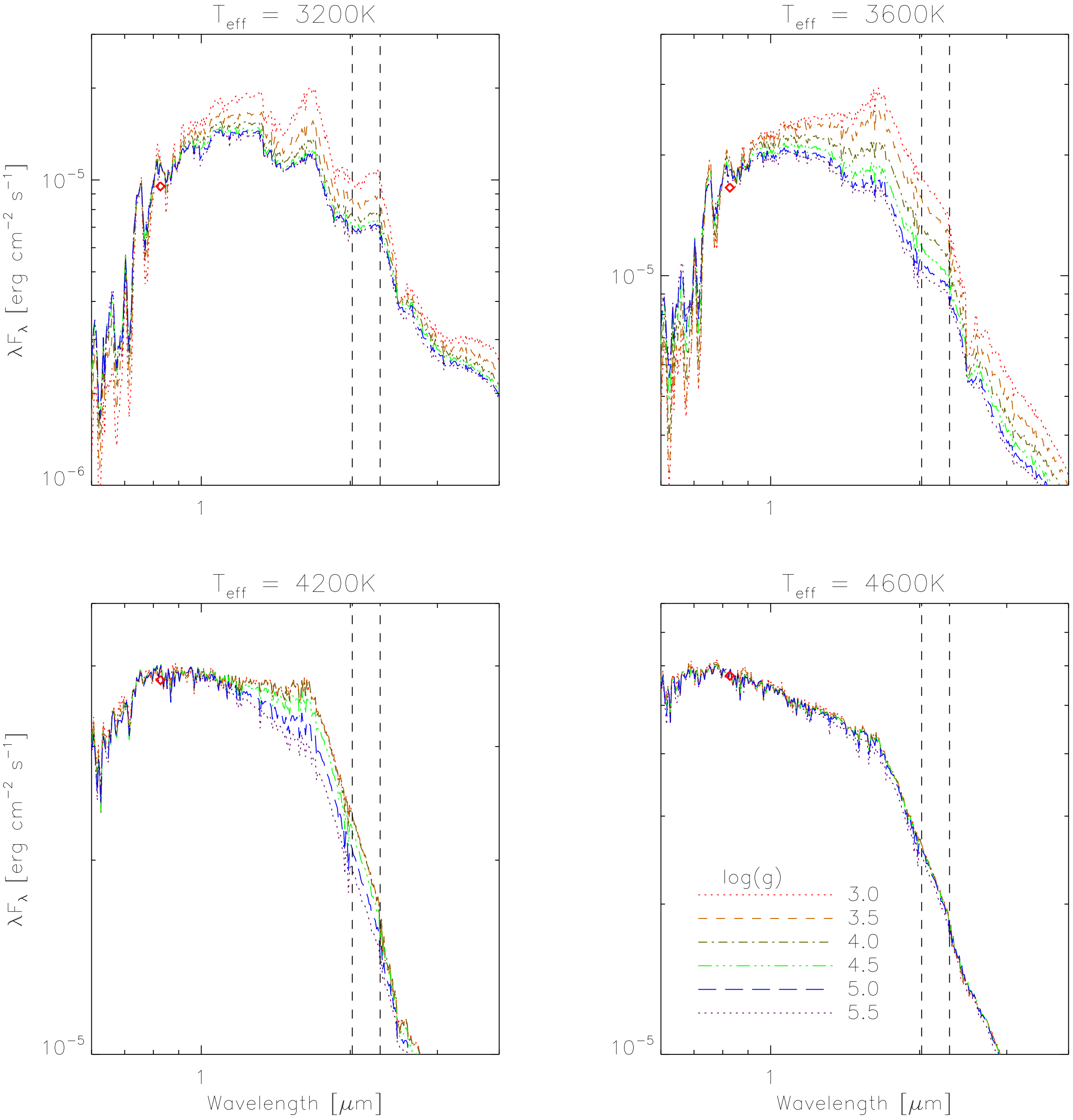

Figure 4.2: Effects of changing surface gravity ($\log g$) on flux in the K_S passband (represented by vertical dashed lines) as a function of stellar temperature. Each panel represents a different temperature within the expected range for young, low-mass stars in our study sample. In each plot, solar-metallicity NextGen stellar atmospheres are plotted with six different $\log g$ values. Each atmosphere is normalized to the I_{WFI} bandpass at 0.83 μm, indicated by red diamonds. For cooler stars, i.e. the atmospheres in the upper panels, K_S flux varies by a factor of three depending on $\log g$; the effect is most pronounced at $T_{\mathrm{eff}} \lesssim 4000$ K.

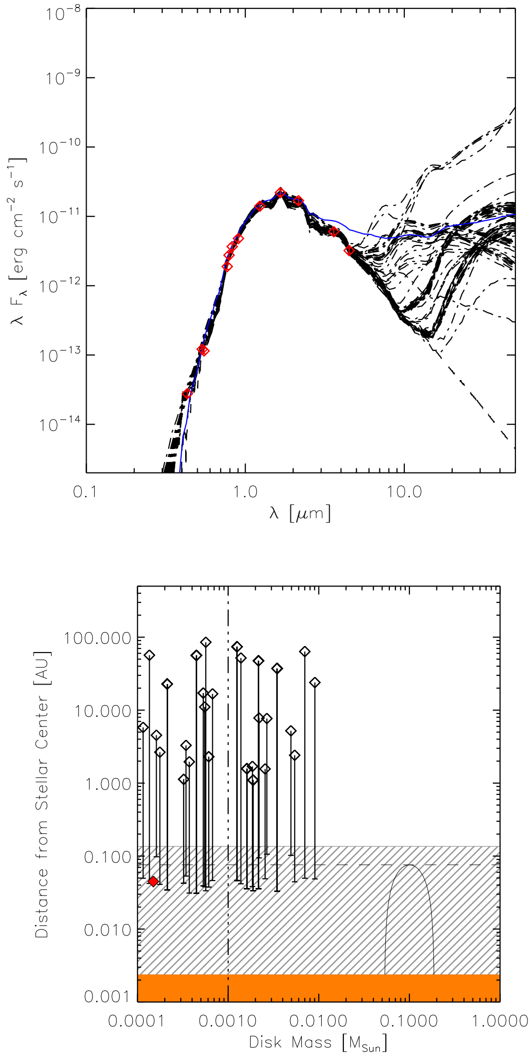

Figure 4.3: SED of COUP 1410, category 3. This object is discussed in greater detail in §4.5.2. *Upper panel:* Best fit model SEDs from the model grid of Robitaille et al. (2007, black dash-dotted curves). The fiducial TTSRE model with $R_{\text{trunc}} = R_{\text{loop}}$ (see §4.4), shown as a solid blue line and normalized to the peak near-IR flux (J, H, or K_S band), is meant to illustrate approximately how the SED would appear if there were a disk within reach of the flaring magnetic loop. The dashed curve is a solar-metallicity NextGen atmosphere model representing the stellar photosphere. Red diamonds are measured fluxes (Tables IV.2–IV.3) as detailed in §4.2.2. *Lower panel:* Comparison of R_{loop} and R_{trunc} for best-fit SED models. The parabola, plotted arbitrarily at 0.1 on the x-axis, is a cartoon illustration of a magnetic loop anchored to the stellar surface (orange), extending to the loop height (dashed line). Uncertainty in the loop height is shown as a gray, hatched region. Open diamonds represent the R_{trunc} values of the best-fit SED models from the upper panel. For each model, a vertical bar indicates the location of R_{dust} for that model (according to Eq. 4.1). Filled red diamonds indicate models which have $R_{\text{trunc}} \approx R_{\text{dust}}$ (see §4.5 for more detail). Finally, the vertical dash-dotted line indicates our disk mass threshold value, 10^{-3} $M_\odot$; less massive disks do not represent the disks typical of T Tauri stars (see §4.4).

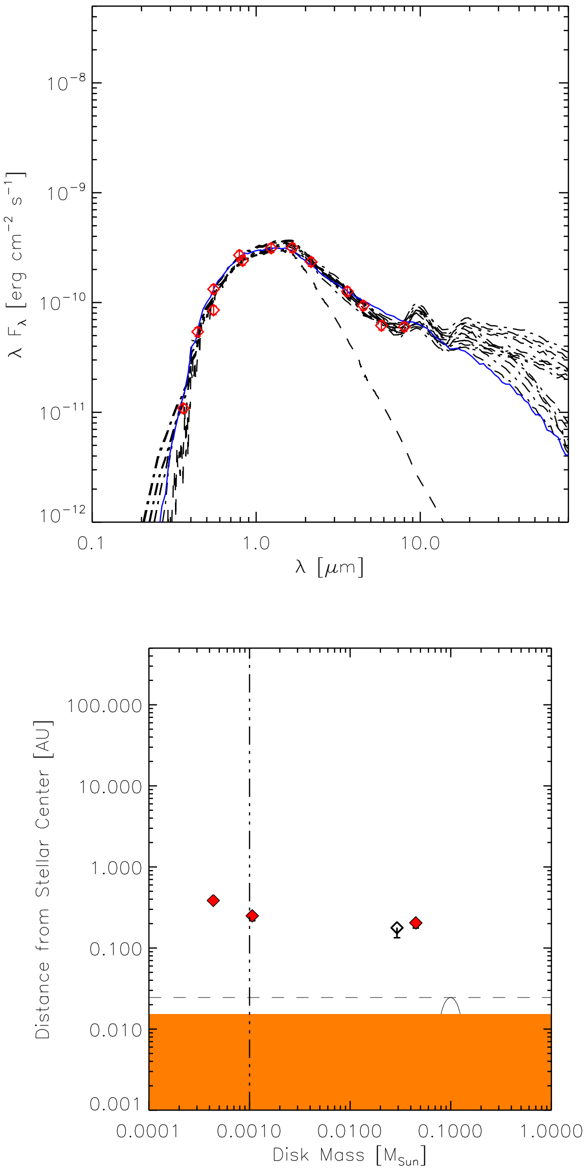

Figure 4.4: SED of COUP 141, category 2. All symbols are as in Fig. 4.3. Excess flux in the IRAC bands indicates a dusty disk. Fourteen best-fit SEDs are plotted, but three of these are degenerate in $M_{\rm disk}$ or $R_{\rm trunc}$, representing four inclinations of the same star–disk configuration. Three sets of model SEDs have $M_{\rm disk} > 10^{-3}$ M$_\odot$, and more than 2/3 of these are truncated at their respective dust destruction radii (red points in lower panel). Thus these disks may possess gas that extends inward of $R_{\rm dust}$ to $R_{\rm loop}$. This object is very likely accreting, based on its strong Ca II emission (−17.8Å) and $\Delta(U-V)$ excess of −1.26. For further discussion of this object, see §4.5.2.

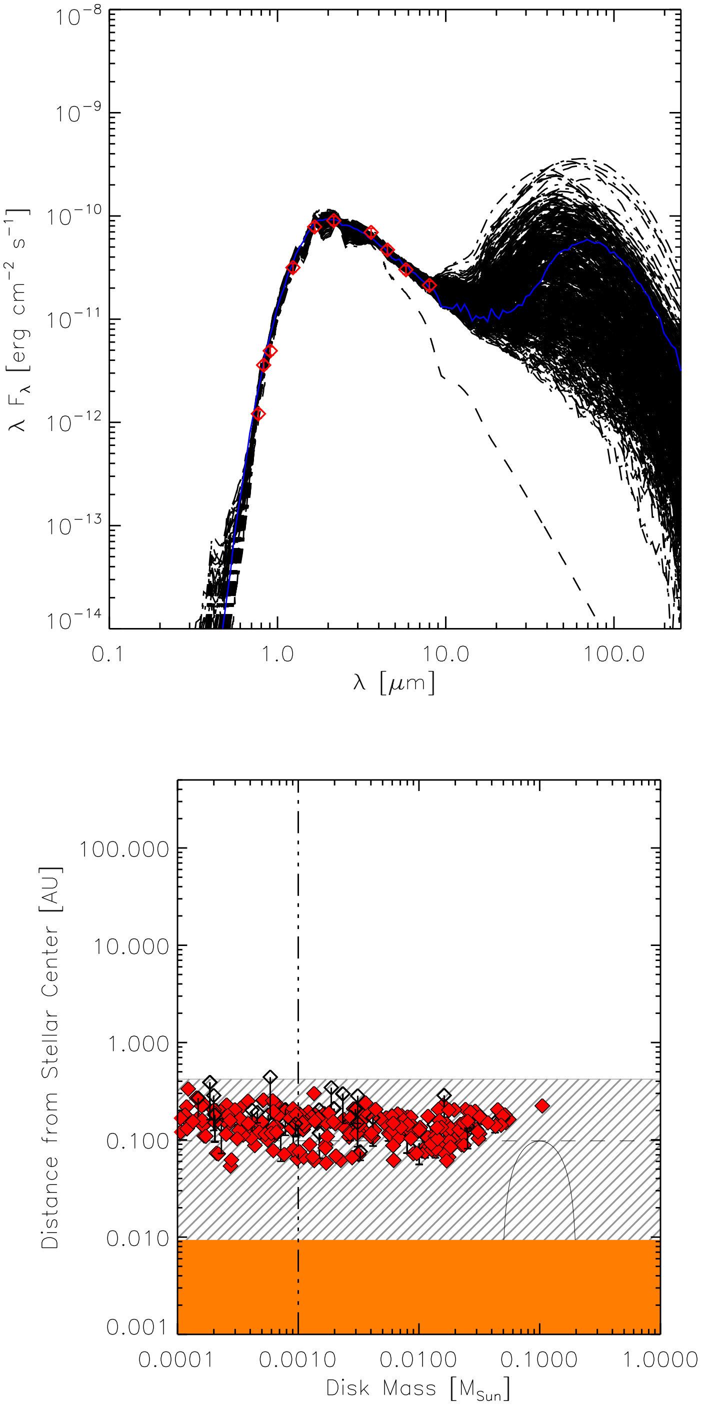

Figure 4.5: SED of COUP 720, category 1. All symbols are as in Fig. 4.3. This object is discussed in detail in §4.5.2.

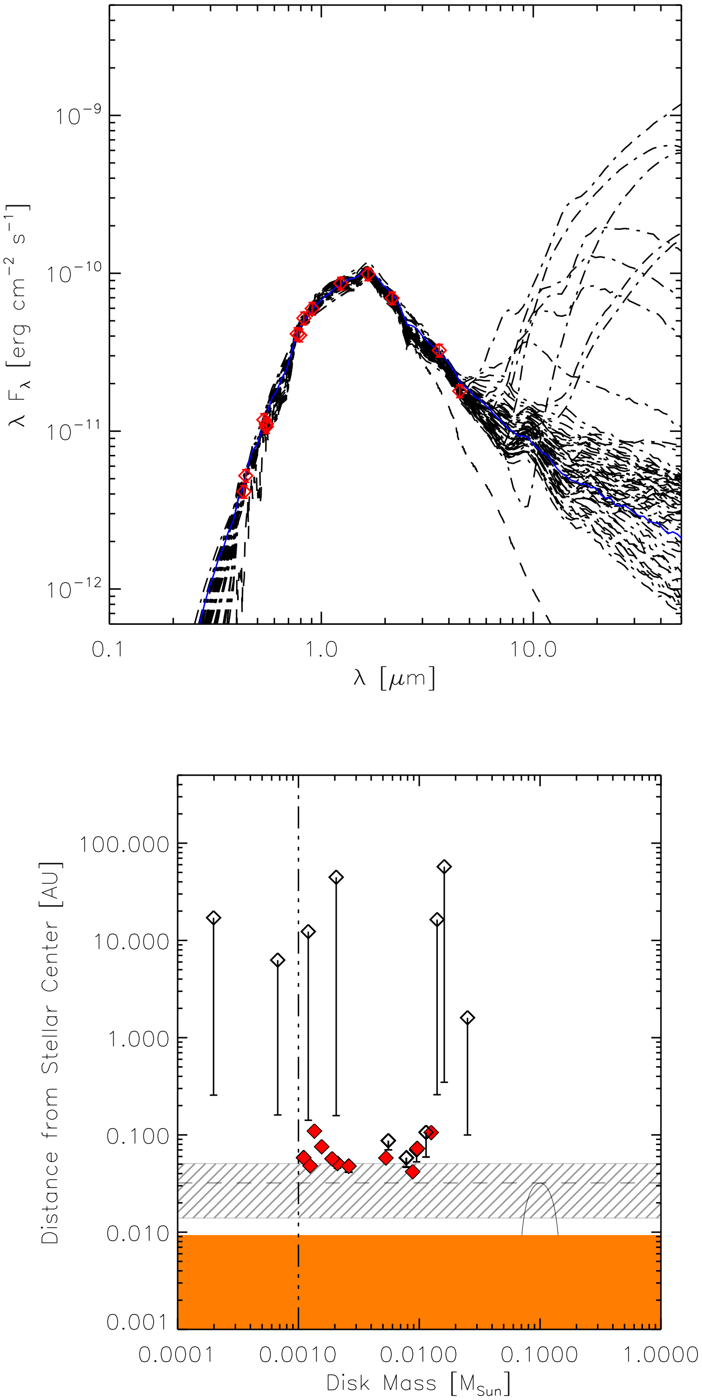

Figure 4.6: SED of COUP 997, category 4. All symbols are as in Fig. 4.3. This object is discussed in detail in §4.5.2.

CHAPTER V

SOLAR FLARES AND CORONAL MASS EJECTIONS: A STATISTICALLY DETERMINED FLARE FLUX-CME MASS CORRELATION

Long-term observations of the Sun have provided an abundance of archival data documenting flares, coronal mass ejections (CMEs), and their properties. Using extensive databases from LASCO and GOES, we temporally and spatially correlate X-ray flare and CME occurrence from 1996 to 2006 in an effort to examine the relationship between flare flux and corresponding CME mass. We cross-reference 6,733 CMEs having well-measured masses against 12,050 X-ray flares having position information as determined from their optical counterparts. For a given flare, we search in time for CMEs that occur 10 to 80 minutes afterward, and we further require the flare and CME to occur within $\pm 45^\circ$ in position angle on the solar disk. There are 826 CME/flare pairs which fit these criteria, indicating that $\sim$90% of CMEs occur without flares, while $\gtrsim$90% of flares occur without CMEs. Comparing the flare fluxes with CME masses of the 826 paired events, we find CME mass increases with flare flux, following an approximately log-linear, broken relationship: in the limit of lower flare fluxes, $\log(\text{CME mass}) \propto 0.68 \times \log(\text{flare flux})$, and in the limit of higher flare fluxes, $\log(\text{CME mass}) \propto 0.21 \times \log(\text{flare flux})$. The functions describe the relationship between CME mass and flare flux over at least 3 dex in flare flux, from $\sim 10^{-7}$ to 10^{-4} W m^{-2}.

5.1 Solar and Stellar Flares and CMEs

For decades, flares and coronal mass ejections have been observed on the Sun. Based on solar studies, we understand that when a flare occurs, magnetically heated plasma evaporates from the solar surface into a confining magnetic loop. The plasma then emits soft X-rays and cools (Priest & Forbes, 2002); this sudden rise in X-ray flux and its subsequent decay is the definition of a flare. The physical connection between solar flares and coronal mass ejections has long been a topic of debate and ongoing research in solar physics. CMEs have been observed to occur in conjunction with flares and eruptive prominences (Munro et al., 1979; Webb & Hundhausen, 1987) and with helmet streamer disruptions (Dryer, 1996). While these phenomena have not yet been causally related, it can be definitively said that both X-ray flares and CMEs arise from regions of complex magnetic topology. Indeed, Švestka (2001) asserted that CMEs all share the same cause –magnetic field lines opening– and the deciding factor in the properties of the resulting CME is the magnetic field strength in the region whence the CME originates. Nindos & Andrews (2004) proposed that the helicity of magnetic structures may be the link between flares and CMEs. CMEs have been observed to facilitate helicity loss, "carrying" high helicity magnetic flux from the Sun (Chen et al., 1997; Wood et al., 1999; Vourlidas et al., 2000); LaBonte et al. (2007) observed that active regions producing X-class flares generate enough helicity to match that lost via CME within hours to days after the flare.

Efforts have been made to identify a physical link between the two phenomena by correlating properties of cospatial, contemporaneous flares and CMEs. Although flares themselves do not appear to be the cause of CMEs, their properties could serve as prediction tools for imminent CMEs and particle events, which are of much concern in the field of space weather. Statistical relationships between solar flares and CMEs are of interest to astronomers as large scale time-series X-ray observations have found solar-like X-ray activity on TTS. Haisch et al. (1995) noted that stellar X-ray flare light curves behave similarly to solar X-ray flares, that is, the structure of the light curve –impulsive initial rise followed by exponential decay– is effectively identical, save flux normalization. Based on these observations, theory and modeling of stellar flares has been guided by the premise that the physics behind both solar and stellar X-ray flares is the same (e.g., Reale et al., 1997). Peres et al. (2001) demonstrated that stellar coronal X-ray emission could be reproduced by modifying solar observations to include greater fractional coverage of active regions and solar coronal structures. Further underscoring the similarities in solar/stellar coronae, features similar to helmet streamers and slingshot prominences have indeed been found on TTS (e.g., Massi et al., 2008; Skelly et al., 2008).

In the stellar case, the observable phenomenon is the X-ray flare, but the desired quantity is the mass loss. While solar CMEs do not shed large quantities of mass, young (∼1 Myr) solar analogs exhibit ∼3 orders of magnitude more energetic flares at a higher frequency, and the problem of how substantial angular momentum vis-à-vis mass is shed in these stars remains unresolved. Additionally, CME -like events on young stars could aid in understanding circumstellar disk evolution and planet formation: for example, could CMEs on young stars be a mechanism for "flash-heated" chondrule formation (Miura & Nakamoto, 2007)? To be clear, the motivation for this work is not to establish a solar flare-CME causal relationship. We seek to quantify a relationship between solar flare fluxes and CME masses under the general premise that in some cases, flares and CMEs arise from common regions of complex magnetic topology and high field strength and thus may have correlated properties. Specifically, we aim to calibrate a relationship between solar flare flux and CME mass to apply to early stellar evolution of T Tauri Stars, TTS.

5.2 Archival Data

The LASCO CME database (Gopalswamy et al., 2009)[1] catalogs observations of the Large Angle and Spectrometric Coronagraph dating back to January, 1996. LASCO observations were complete for ∼83% of the decade analyzed in this work. The catalog documents 13,862 manually identified CMEs and their measured parameters. Of particular interest in this work, 6733 CMEs with well-measured masses (see Fig. 5.1) are reported, along with their linear speeds, accelerations, and position angles. The CME start time reported is when the CME first crosses the C2 telescope field of view; C2 images the circumsolar environment from 2.0 to 6.0 $R_\odot$.

Spanning more than two decades, the Geostationary Operational and Environmental Satellite (GOES) flare database[2] reports the 1 to 8 Å band full-disk X-ray flux at Earth; flare classifications are then applied based upon the peak flux in that bandpass. From 1996-2006,

---

[1] This CME catalog is generated and maintained at the CDAW Data Center by NASA and The Catholic University of America in cooperation with the Naval Research Laboratory. SOHO is a project of international cooperation between ESA and NASA.

[2] `http://www.ngdc.noaa.gov/stp/SOLAR/ftpsolarflares.html` maintained by `Edward.H.Erwin@noaa.gov`

the database contains information for 22,674 flares. Of these, positions for optical counterparts are documented for approximately half of the flares in the database (see Fig. 5.2). For flares with positions, 1 A, 3,638 B, 7,248 C, 1,056 M, and 107 X class flares are recorded.

5.3 Determining Flare-CME Association

The subset of data reported in the LASCO CME database utilized here consists of the 6,733 CMEs with well measured masses (i.e., sufficient signal in the C2 field of view, no halo events). Likewise, the GOES flare database has been cropped to include only the 12,050 flares with reports of optical counterpart positions.

In determining whether a given flare and CME are associated, we use spatial and temporal data, requiring that both the flare and CME occur within a set time window and angular separation. We first set the time window to select CMEs which occur within ±2 hours of a flare's start time. Converting Stonyhurst system flare positions (Cartesian) on the disk to spherical coordinates, we further require that the CME central position angle (CPA) is equal to the flare's position angle within a certain angular separation.

After applying a ±2 hour temporal cut, in the resulting flare-CME pairs' time separations (CME start time - flare start time), there appears to be a significant peak (see Fig. 5.3) between 10 to 80 minutes. Other time separations surrounding this peak appear to represent a "background" level at N∼180 pairs per 10 minute time bin; these time offsets could represent randomly matched flare-CME pairs which are not truly associated. Interpreting this peak as a time offset region in which there is a higher probability of finding associated flares and

CMEs, we conservatively narrow the time correlation window to accept CMEs which occur 10 to 80 minutes after a flare. This is consistent with the findings of Andrews & Howard (2001) and Mahrous et al. (2009); in the latter work, the analysis included using flare peak flux times and end times.

We also check the time offset distributions when using flare peak and end times (Fig. 5.4) and find that events appear to be the most strongly correlated when using the flare start time; this is to say that the number of events in the 10 to 80 minute bins of Fig. 5.3 are greater in number and there is less "background" variation than is seen for the other flare time choices (dashed, red and dot-dashed, gray histograms in Fig. 5.4). This choice in temporal separation could potentially eliminate true flare-CME pairs – previous studies (for example, Harrison, 1991, 1995) have shown instances in which CMEs precede flares – but we do not consider these cases due to the absence of a distinct peak in the range of negative time offsets. Potentially these cases only represent a minority of flare-associated CMEs.

In Fig. 5.5, we show the angular separations of flares and CMEs paired based solely upon the 10 to 80 minute flare-CME time separation criterion. About 0° is a very clear peak; Yashiro et al. (2008) also observed this relationship using a very similar time selection method as well as visual verification of flare-CME association. Based upon Fig. 2 in Yashiro et al. (2008) and our Fig. 5.5, we adopt an angular separation criterion of ±45°, e.g., both events occur in the same quadrant of the disk with respect to the CPA of the CME. 45° is a value intermediate to the ±30° distribution of Yashiro et al. (2008) and our apparent ±75° distribution. Our choice errs toward potentially excluding flare-CME pairs of high separation.

Interestingly, but beyond the scope of this work, we note that there is a significant peak for flares which occur ∼180° in separation from the CME CPA, potentially indicative of large-scale correlated disruptions.

5.4 Results

Presented below are comparisons of four different flare and CME parameters: flare flux, and CME linear speed, acceleration, and mass. Primarily, we seek to define a flare flux-CME mass relationship, but perform the other correlations with our flare-CME pair sample in order to compare with previous work.

With each constraint applied, the total number of flare-CME pairs in the sample decreases as illustrated in Fig. 5.6. The final sample contains 826 flare-CME pairs, 737 of these are unique. As performed, the correlation allows for the selection of multiple CMEs per flare. This is because with the data available, there is no way to distinguish which CME may actually be associated with the flare, or if all results are indeed associated. Unable to eliminate any superfluous matches, we use all 826 pairs when comparing flare and CME properties. When analyzing properties of flare-associated CMEs vs CMEs occurring without flares, we use only the 737 unique CMEs' properties (Figs. 5.7, 5.8, 5.9).

We have checked with previously reported literature findings to assess whether our method returns similar numbers of associated flares and CMEs. Surprisingly, we find that in the application of our time and angular separation constraints, most of the 107 X class flares are lost from the sample: only 7 of the 826 pairs have X class flares. This contradicts the results of Andrews (2003), who found an almost 100% X class flare-CME association. To investigate this further, we loosened our time constraint as suggested by the helicity analysis of LaBonte et al. (2007); instead of searching for CMEs which occur within hours to days of an X class flare, though, we simply select the closest CME in time following the flare. Referring to the spatial correlation study of Yashiro et al. (2008), in which the majority of X-class flares were found to be within ±30° of the CME CPA, we did not relax or tighten our angular separation criterion. Even with these very loose constraints, forcing 100% retention after the time cut and a applying a generous spatial coincidence requirement, only 52 X class flares are found to be paired with CMEs. We found that 18 X class flares were lost from the sample due to a gap in LASCO coverage at the time of the flare, the rest were beyond the bounds of the spatial requirement. Data gaps, in fact, could partially resolve this apparent discrepancy: the Andrews (2003) study was affected by data gaps as well. Their sample contained a total of 44 X class flares, but only 24 of those occurred outside of LASCO data gaps. 100% flare-CME association simply reflects that for every X class flare for which there were LASCO data, a CME was found correlated to that X class flare. If one assumed that the flares occurring during LASCO data gaps are not associated with CMEs, this would imply that of the 44 flare sample, Andrews (2003) could safely say that ∼64% of the time, X class flares are associated with CMEs. Including the 18 X class flares our study loses to data gaps, we can say that at most, our method predicts that 23% of X class flares will be associated with CMEs. Without a more detailed analysis of simultaneous flare and CME movies, we cannot resolve this discrepancy; potentially we are either observing a weakness of small-number sample statistics, or the flare-CME pairing methodology we use has the limitation that it over-constrains temporal and spatial parameters. Either way, we believe the requisite time and position conditions applied here are sound in reasoning and represent a conservative approach which may only under-count flare-CME pairs.

Also of interest are the total number of CMEs which are not apparently associated with flares. Of the ~7,000 CMEs in our study, we find only 826 CMEs associated with flares, or 12%. This number, however, is subject to some bias: the LASCO data gaps (83% complete coverage from 1996-2006) in addition to the manual nature of CME selection mean that our 12% could be either an over- or underestimate. For comparison, previous estimates of CMEs associated with flares are 40% (Munro et al., 1979) and 34% (St. Cyr & Webb, 1991).

5.4.1 CME Linear Speed and Flare Flux

Previous studies have found a correlation between flare flux and associated CME linear speed. Flare and eruptive prominence-associated CMEs generally have higher linear speeds than CMEs that are not associated with flares (Gosling et al., 1976; Moon et al., 2003). To check whether our flare-CME pairs reflect this observed relationship, we show in Fig. 5.7 the two distributions of CME linear speeds. A t-test (Press et al., 1995) assesses the probability that two distributions have significantly different means. The mean linear speed for CMEs associated with flares is 494.7±8.3 km s^{-1}; in the converse case, CMEs not associated with flares have an average speed of 421.7±2.8 km s^{-1}. The t statistic for these distributions is 8.5, and the corresponding probability (the likelihood that one distribution will have a mean less than that of the other) is $\ll 10^{-6}$, a highly statistically significant difference.

Because of the asymmetric skew of the data, we also perform a non-parametric version of the t-test, the Wilcoxon-Mann-Whitney test (also known as a U test). The statistic is Z, and the corresponding probability assesses the likelihood, when sampling two distributions, of preferentially finding a higher value in one distribution than another. The results of the U test corroborate those of the t test: the Z statistic is -9.0, and the probability of Z being larger is $\ll 10^{-6}$. These two distributions have statistically significantly different means, consistent with observations that flare-associated CMEs have higher linear speeds than CMEs not associated with flares.

5.4.2 CME Mass and Acceleration

In Fig. 5.8, CME acceleration is shown as a function of CME mass for both CMEs with and without associated flares. The mean acceleration of the CME -flare pair distribution is -1.8 ± 0.1 m s^{-2} (deceleration), while the mean acceleration of the unimodal distribution of CMEs without flares is 0.07 ± 0.25 m s^{-2}. Similar to §5.4.1, we apply a t test to determine whether the acceleration distributions have significantly different means. The t statistic is -2.5, the corresponding probability 0.01. This low probability indicates these distributions do indeed have significantly different means. A non-parametric U test was also performed, the Z statistic found to be 4.6, and the probability of finding Z to be larger is 1.9×10^{-6}. The CME -flare pairs having CMEs which tend to decelerate on average, while the CMEs not associated with flares are centered about 0; these CMEs accelerate very little, if at all. A bimodal distribution of accelerations for CMEs with and without associated flares has been supported by some studies (MacQueen & Fisher, 1983; Andrews & Howard, 2001), while others assert that it is more likely that there exists a continuous spectrum of CME accelerations, depending upon the strength of the magnetic field where the CME was formed (Švestka, 2001). Our results do not show any indication of a bimodal distribution and thus appear to support the former of these ideas, with very large number statistics.

Examining closer the potential effect of CME mass on acceleration for CMEs associated with flares, we separate by mass and analyze the resulting acceleration distributions (Fig. 5.9). The highest mass division includes CME masses $\geq 10^{15}$ g, while the middle and lowest mass subsets span the ranges of 10^{14} g $\leq$ CME mass $< 10^{15}$ g and CME mass $< 10^{14}$ g, respectively. Again using the U test, we find that all three distributions have statistically similar means. We find a difference in mean acceleration of CMEs with and without flares, but there doesn't appear to be a dependence on mass.

5.4.3 CME Mass, Flare Flux

For the associated flares and CMEs, the relationship between CME mass and flare flux is shown in Figs. 5.10 and 5.11. Dividing the pairs by flare flux into four groups, we fit the resulting distributions with Gaussian functions. The Gaussian centroids clearly progress to higher CME mass as the flare flux sampled increases (Fig. 5.10). In Figure 5.11, the 826 flare-CME pairs are binned into fourteen equal sets of N=59 pairs each of similar flare fluxes. Again it is apparent that the mean CME mass in each bin increases with flare flux. There is an apparent "knee" to the function around log(flare flux) $\sim$ -3, so we use two linear regression fits to describe the functional relationship on both sides of this "knee." The first function is fit to bins 0-8, and the second to bins 7-13. There is slight in these two fits because precisely where the "knee" of the function occurs is unclear. The first linear fit is of the form:

$$\log(\text{cme mass}) = (18.5 \pm 0.57) + (0.68 \pm 0.10) \times \log(\text{Flareflux}) \tag{5.1}$$

The second linear fit follows the form:

$$\log(\text{cme mass}) = (16.7 \pm 2.77) + (0.21 \pm 0.67) \times \log(\text{Flareflux}) \tag{5.2}$$

To assess whether a broken fit is indeed necessary, we fit the correlated flux and mass bins of Fig. 5.11 with a single linear fit. The χ^2 value of this fit is 10.98, almost triple the χ^2 values for each of the fits above (χ^2 = 4.47 and 3.03, respectively). We also determine the robustness of the "knee" by re-binning the data and fitting again. The data divided this time into seven bins of N=118, we fit a single line (Fig. 5.12; fit parameters are in the figure caption). This fit has a χ^2 of 3.47. For comparison, we apply another broken log-linear fit to the data with the "knee" placed at the same point, log(Flare flux)$\sim$-5.5 (Fig. 5.13). Each of the functions better fits the data (χ^2 values of 0.16 and 0.07, respectively). Thus in both cases, we find that fitting the CME mass-flare flux relationship with a broken linear function indeed produces a better fit than simply fitting all of the data points with a single linear function.

We utilize a τ test to assess the correlation of flare flux and CME mass, finding the τ coefficient to be 0.27 with a significance of $\ll 10^{-6}$: these are significantly correlated properties.

5.5 Conclusions and Discussion

For flares and CMEs arising from the same active regions, one might anticipate some of their properties to be correlated. For example, a less magnetically complex active region may produce lower flux flares and lower mass CMEs. Conversely, a highly magnetically complex active region may produce both higher energy flares and more massive CMEs. Our method for pairing flares and CMEs reproduces previously observed correlations, specifically, CMEs with higher linear speeds tend to be flare-associated and also decelerate. While we do find that CMEs associated with flares generally decelerate, or do not show signs of acceleration, there does not appear to be a clear relationship between the mass of the CME and its acceleration. Finally, we indeed find that for flare-associated CMEs, flare flux and CME mass are strongly correlated.

In § 5.4.3 we show an apparently broken log-linear function best describes the relationship between CME mass and flare flux. Beyond the “knee” of the broken function, the rate of increase in CME mass lessens with increasing flare flux. Future work will serve to elucidate whether a physical mechanism could be causing this change in slope. Potentially, this could represent a saturation point, approaching a set limit of possible CME mass. In young stars, it would be interesting to see whether this saturation point has any correlation with the saturation point in X-ray activity (see § 2.2.2).

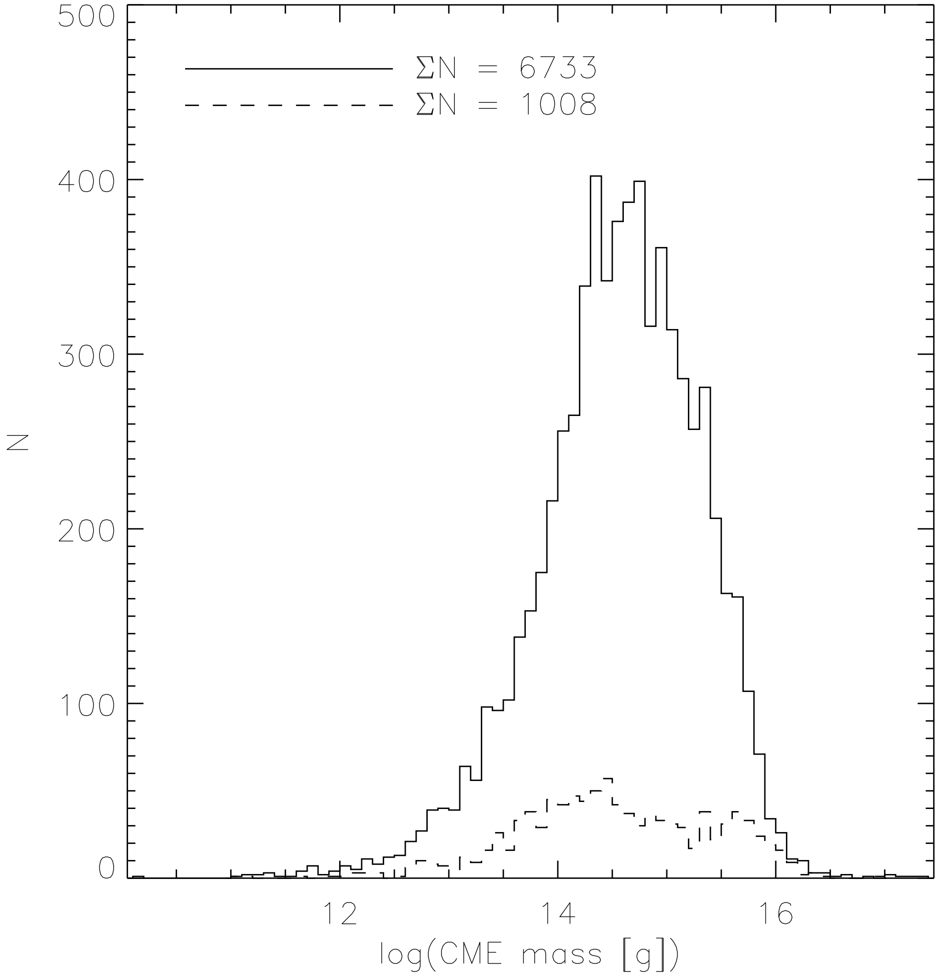

Figure 5.1: Summary of the LASCO CME database. From 1996 to 2006, there were 7741 CME mas measurements; 6,733 were well-constrained, and 1,008 were poorly constrained. We use the distribution of 6,733 events and subsets thereof in all analyses presented here.

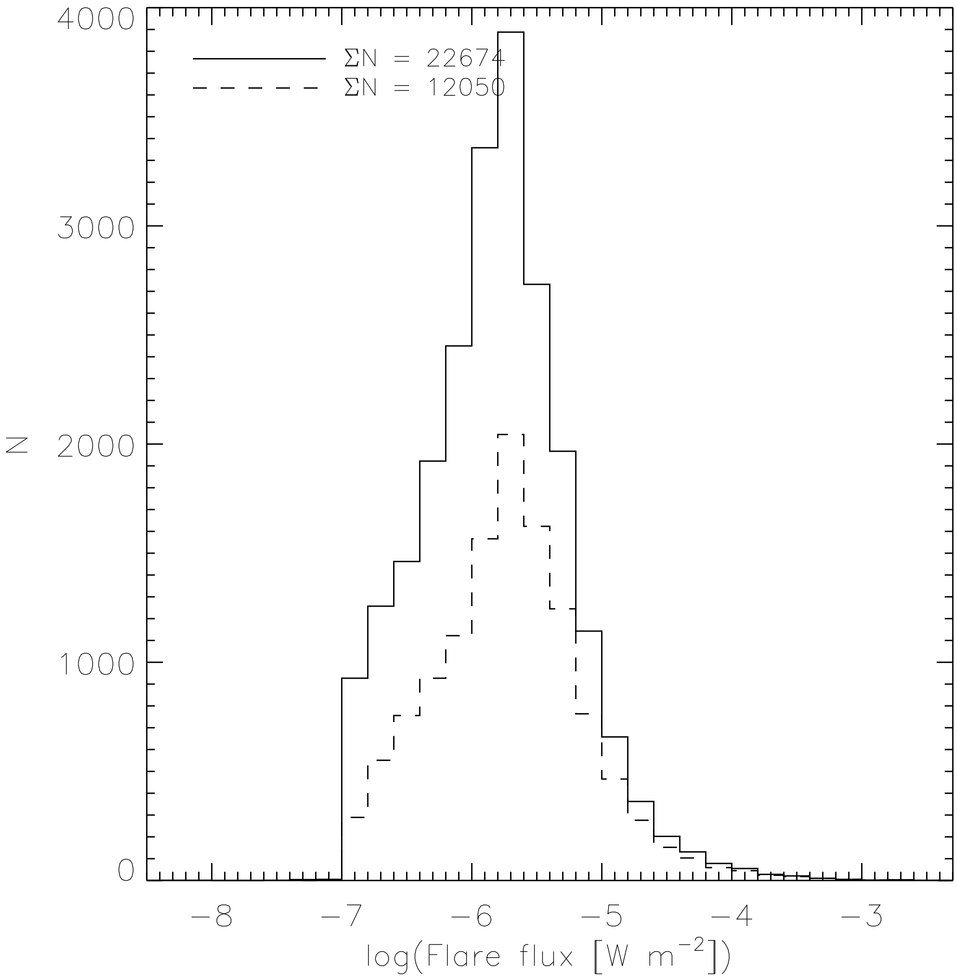

Figure 5.2: Summary of flare fluxes recorded in the GOES X-ray flare database from 1996-2006. 22,674 flares in total were recorded, 12,050 of which had measured positions of optical counterparts to the X-ray flare. For correlation with CMEs, we use only the subset of flares with known positions.

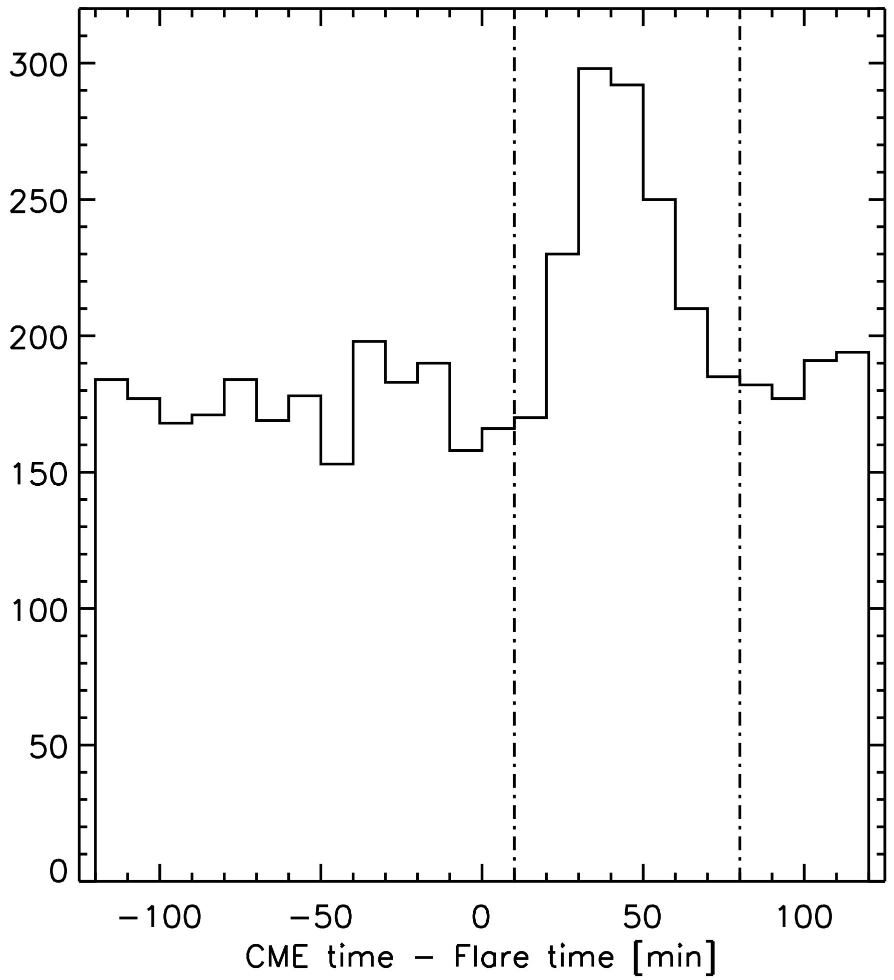

Figure 5.3: Temporal separation of flares and CMEs paired within the ±2 hour time window. Vertical dot-dashed lines denote a new time correlation window (see §5.3).

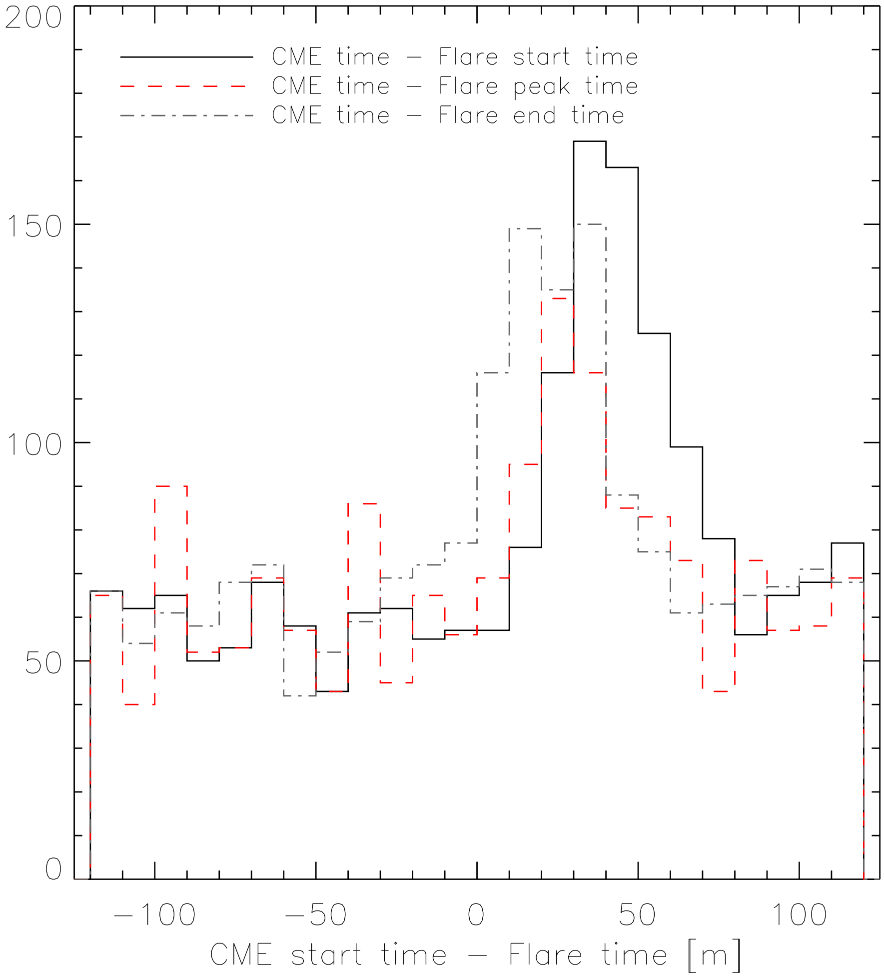

Figure 5.4: Assessment of which flare time to use. Previous studies found that the degree of parameter correlation depends on the flare start, peak, or end time is used in flare-CME pairing. Time offsets are shown here of flare start (solid, black), peak (dashed, red), and end times (dot-dashed, gray) minus CME start time. In time offset space, we observe the strongest peak in the number of pairs when using the flare start time. The peak of the black histogram is an order of magnitude above the "noise" and well-defined in shape.

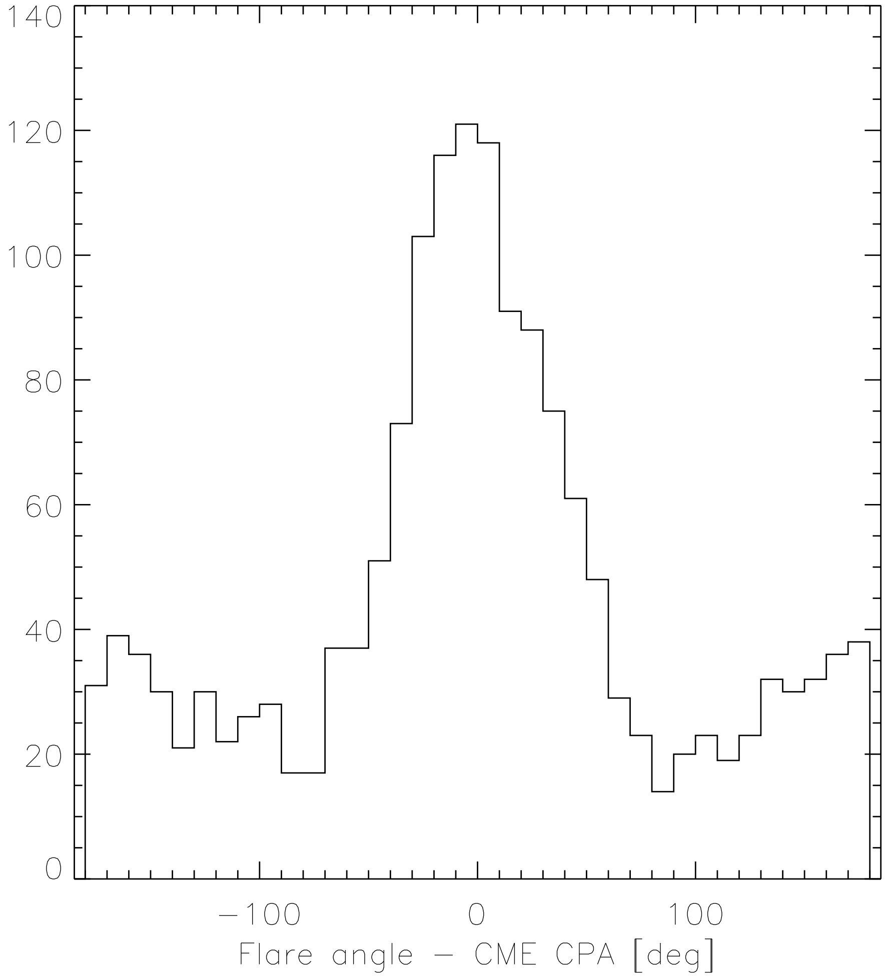

Figure 5.5: For flares and CMEs matched within the 10 to 80 minute time window (see Fig. 5.3), we show the angular separation of flares and CME central position angle. There is a clear peak about 0°This figure, in concert with Fig. 2 of Yashiro et al. (2008), guides the choice of ±45° as our angular separation criterion.

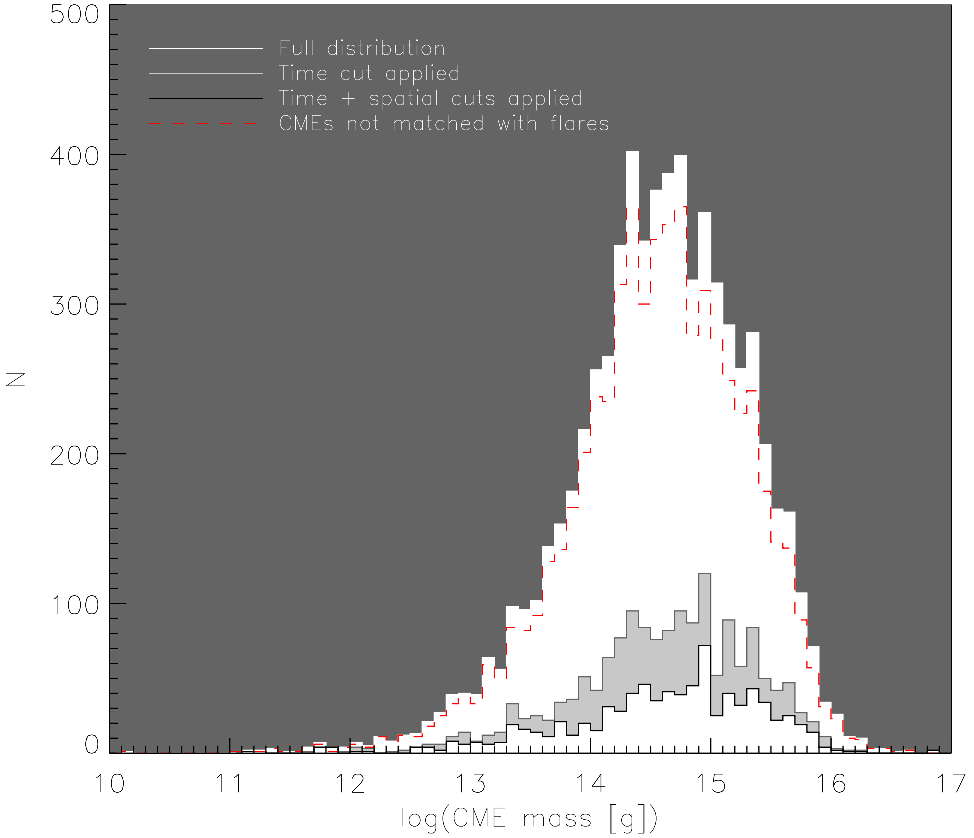

Figure 5.6: Change in the distribution of CME masses as flare-CME pairs are correlated. The white histogram bounded by dark gray shows the full initial distribution of well constrained CME mass measurements. Pairing flares with CMEs occurring 10 to 80 minutes after the flare start time, the data set is greatly reduced in number (filled, light gray histogram). The position criterion, CME and flare position angle equality within ±45°, leaves 826 flare-CME pairs (solid black line, white filled histogram). In red, we show CMEs not associated with flares by these criteria.

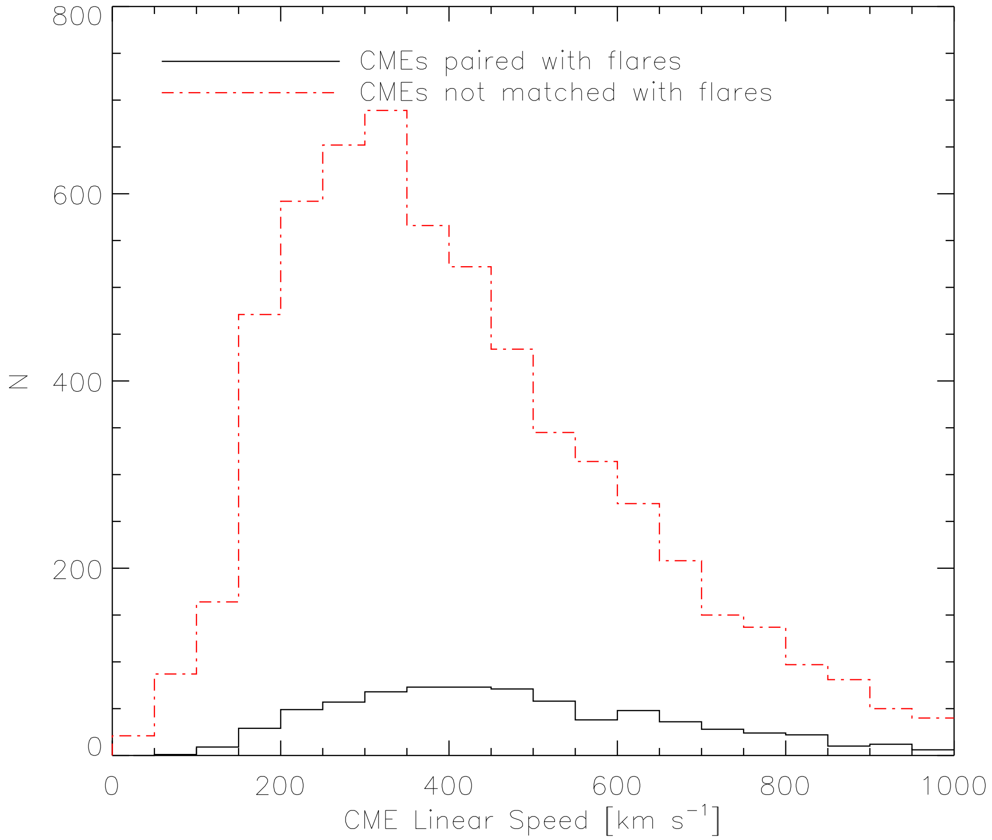

Figure 5.7: As in Fig. 5.6, the red and black distributions show CMEs not matched with flares and CME/flare pairs, respectively. We find that CMEs associated with flares have faster linear speeds (see §5.4.1).

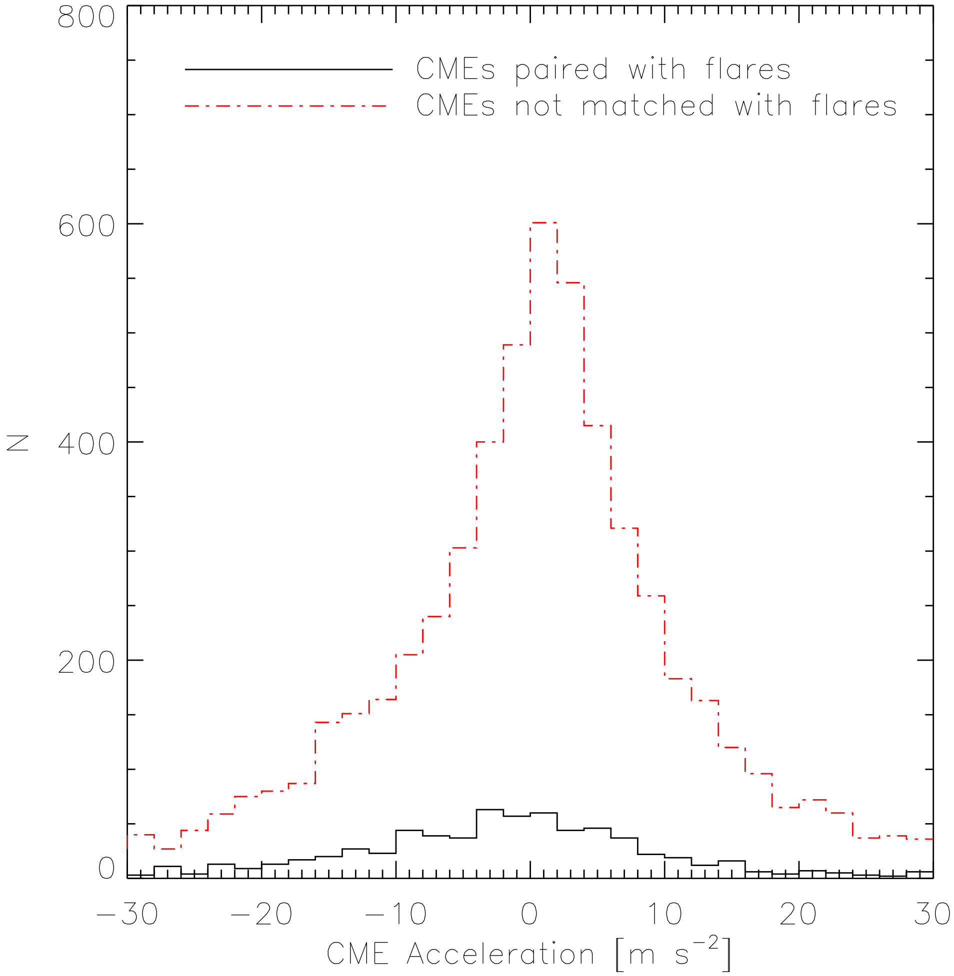

Figure 5.8: CME accelerations: CME/flare pairs (solid, black distribution) and CMEs without associated flares (dot-dashed, red).

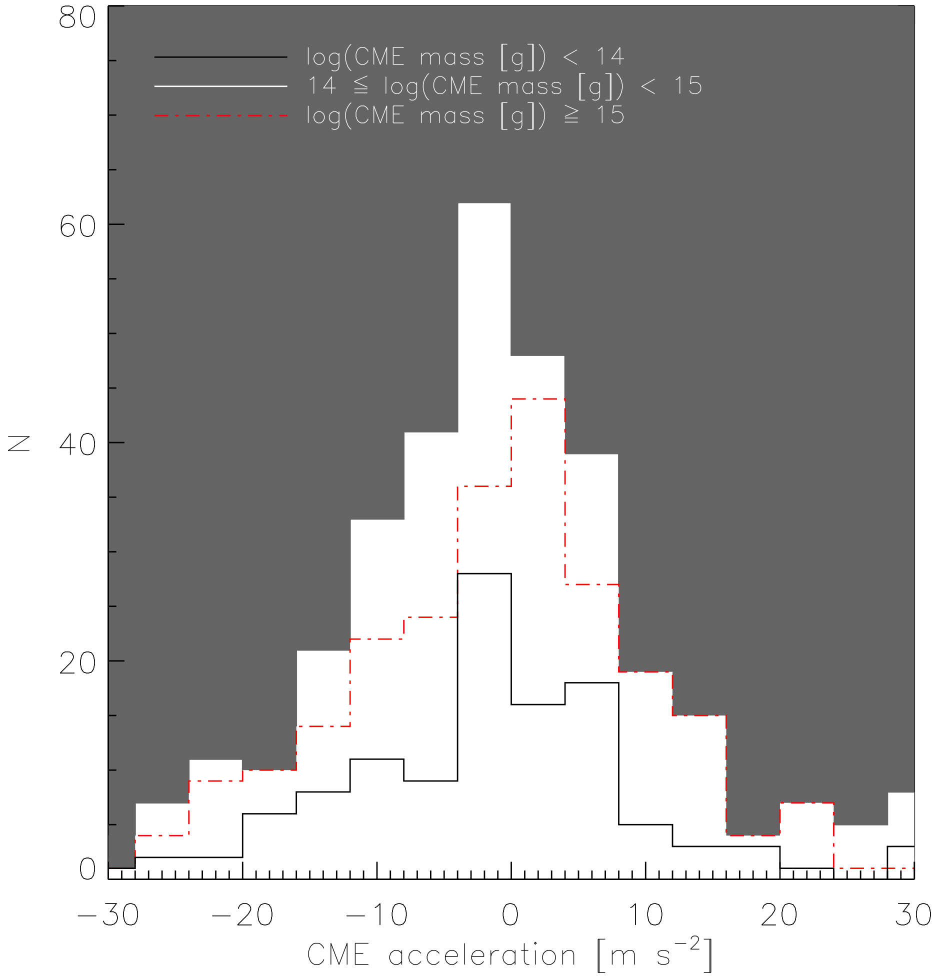

Figure 5.9: Relationship between CME mass and CME acceleration. The dot-dashed (red) histogram represents accelerations for the highest mass CMEs, with log(CME mass [g]) $\geq$ 15. The white histogram bounded by dark gray shows accelerations for CMEs with masses $\geq 10^{14}$ g and $<10^{15}$ g. The lowest masses shown, $<10^{14}$ g, are represented by the solid (black) outlined histogram.

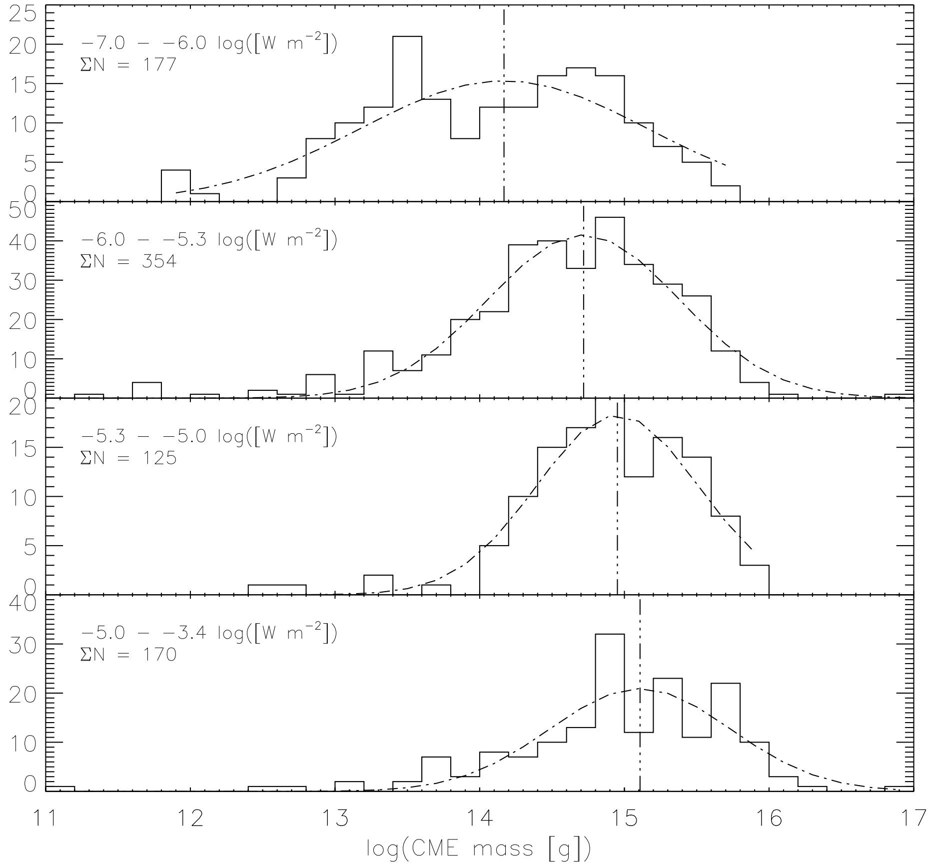

Figure 5.10: Grouping flare-CME pairs by flare flux, ascending flux from top to bottom, we see a clear increase in the centroid value of CME mass.

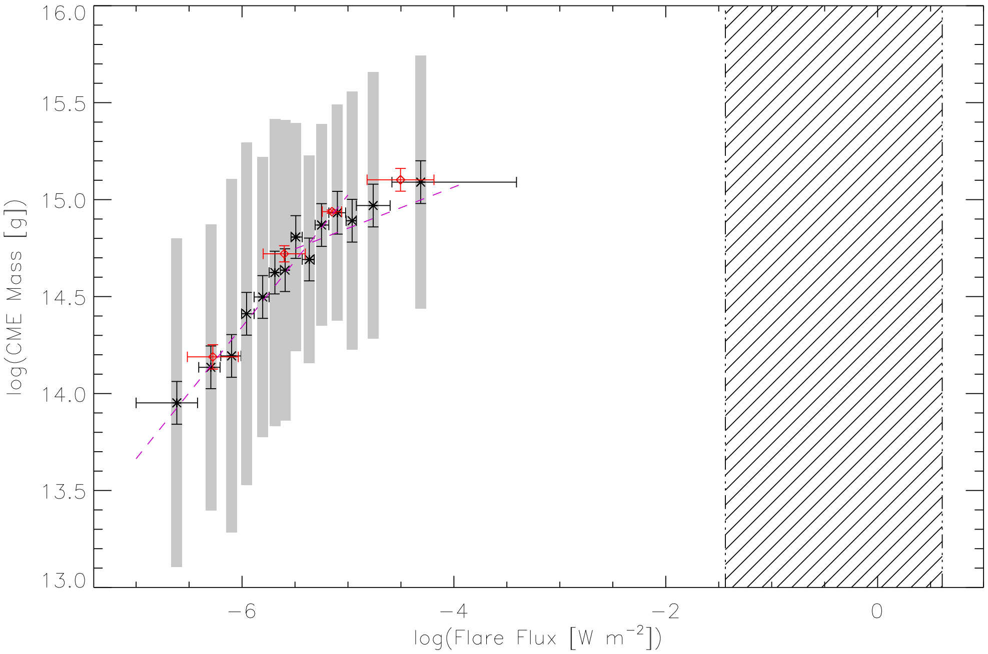

Figure 5.11: Relationship between CME mass and flare flux. Black X: the 826 flare-CME pairs are binned into equivalent boxes of N=59. Each asterisk point is centered on the mean flux and mass per 59 pair bin. The flux error bars show the minimum/maximum flare flux values spanned by that bin, and the mass error bars are the error on the mean (i.e., $\sigma/\sqrt{N}$). Four red diamonds: abscissae are the mean flux values for each of the groups as set in Fig. 5.10; ±x error is the standard deviation of that mean. The ordinates are the mass values corresponding to the peaks of the Gaussian fits in Fig. 5.10; their errors are the fit errors of the centroid. The light gray shaded boxes in the background are of arbitrary width, but show the standard deviation of the mean mass plotted in the foreground. For comparison, the hatched region represents the highest flux flares observed on young stars (see § 5.1). Two linear functions are fit to the data, the first to bins 0-8, and the second to bins 7-13. There is slight overlap in that precisely where the "knee" of the function occurs is unclear. The first linear fit yields log(CME mass) $\propto$ 0.68×log(Flare flux), while the second linear fit shows log(CME mass) $\propto$ 0.21×log(Flare flux).

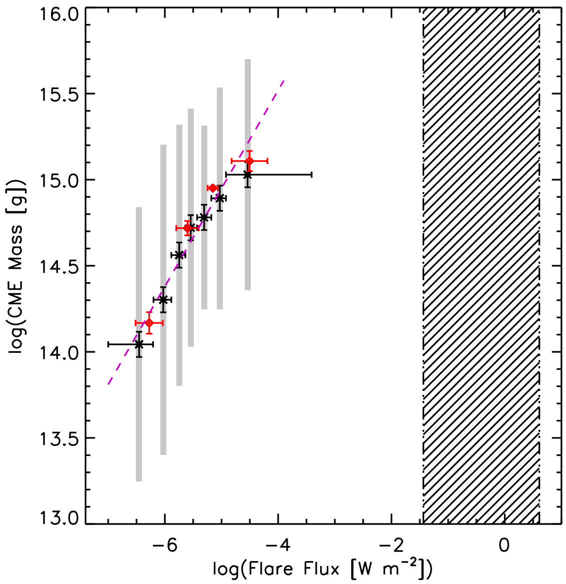

Figure 5.12: Re-binned data of Fig. 5.11 with a single linear fit. Linear equation is: log(CME mass)=(0.57±0.10)×log(Flare flux) + (17.8±0.45).

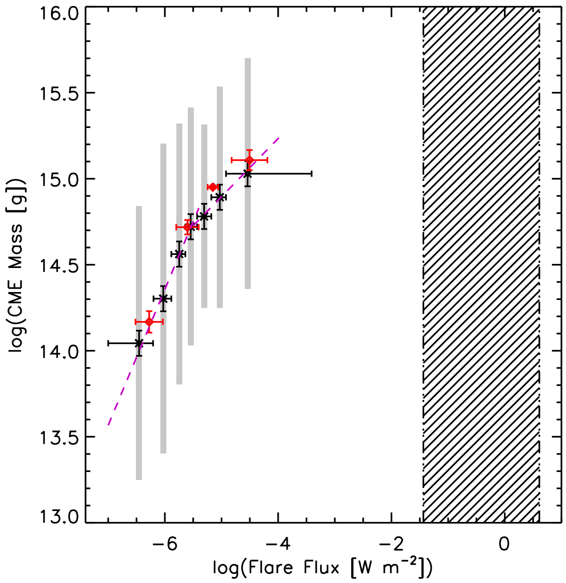

Figure 5.13: Re-binned data of Fig. 5.11 with a broken linear fit. The lower flare flux portion of the relationship is described by the function: log(CME mass)=(0.79±0.19)×log(Flare flux) + (19.1±1.2). The second function is of the form: log(CME mass)=(0.34±0.19) + (16.6±0.98).

CHAPTER VI

T TAURI ANGULAR MOMENTUM LOSS EXAMPLE CALCULATION

Proceeding as outlined in Section D, we demonstrate here how to proceed with calculating a stellar CME angular momentum loss rate utilizing the solar and stellar calibrated flare and CME distributions defined above.

6.1 Data and procedure

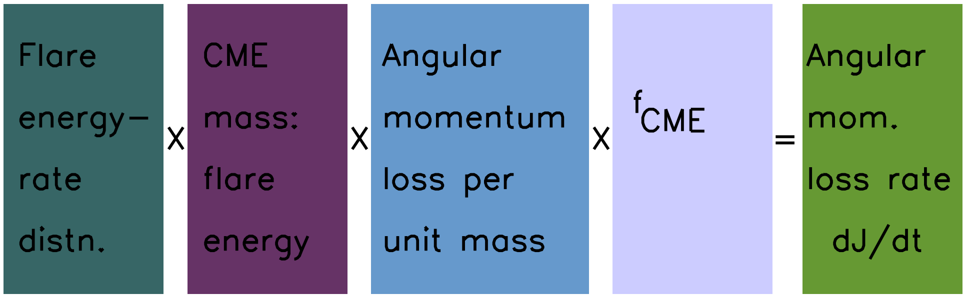

Figure 6.1: Our procedure for determining a stellar angular momentum loss rate via CMEs. The flare energy-rate distribution is available in the literature for the ONC (∼1 Myr). A CME mass/flare energy distribution as determined by us (Chapter V) will be used, as well as f_{CME} from that same work. The third term, how much angular momentum is lost per CME, remains to be defined.

In Fig. 6.1, we outline the basic procedure for determining an angular momentum loss rate. To relate our solar flare flux/CME mass relationship (see Chapter V) to stellar flares, we first need to know how frequently flares of a given energy occur on young stars. For comparison, we convert solar flare flux into energy, and re-frame the CME mass/flare flux relationship into a CME mass/flare energy relationship. To determine solar flare energy, we integrate the X-ray flux of the light curve from flare start to end time (lacking the actual solar X-ray light curves, we approximate this shape to be a right triangle). We then convert the resulting flux (× time) to a luminosity, scaling by the distance to the Sun. Our final CME mass/flare energy distribution is shown in Fig. 6.2, with the stellar flare energy/event distribution (inset, bottom panel).

As a first effort in determining the masses of CMEs on young stars, we extend the second of the linear fits to the solar data into the regime of energies occupied by TTS flares (Fig. 6.2, lower panel, gray dot-dashed line). Interpolating this function at energies defined by the stellar flare energy distribution (Fig. 6.2, teal inset), we obtain a stellar CME mass/flare energy distribution (Fig. 6.3).

Converting the stellar flare energy-event rate distribution from the ONC to describe the number of flares of a given energy per Myr, we determine then how many corresponding CMEs occur in 1 Myr (Fig. 6.4).

The sum of all mass in the distribution shown in Fig. 6.4 is 1.3×10^{25}g, or 6.3×10^{-9} $M_\odot$. This is to say, in 1 Myr, a TTS could shed $\sim10^{-9}$ $M_\odot$ via CMEs. When calculating an angular momentum loss, the angle of the lever arm (the position from which mass is "launched" from the system) is necessary. For this purpose, we can utilize a result from Chapter V: the distribution of central position angles of flare-associated CMEs (Fig. 6.5).

The greatest torque is applied against the star's rotation when the lever arm is perpendicular to the rotation axis. In Fig. 6.5, this angle is 90°; thus a $\sin(i)$ factor will be included in the angular momentum loss calculation (where $\sin(i)$ is maximum, the angular momentum loss is maximum, with less angular momentum loss for material ejected almost parallel to the stellar rotation axis). To simplify the distribution of CME CPAs, we fold on 90° (Fig. 6.6).

At this point, three of four factors from Fig. 6.1 are defined (a discussion of f_{CME} appears in section 5.4), with only the angular momentum loss per unit mass left to be defined. Unfortunately, this quantity is very difficult to define, as the radius from which the material is launched is unknown, and angular momentum loss depends on this quantity squared (see eqn. 6.1). With this quantity, we would proceed to calculate angular momentum loss as follows:

$$\frac{dJ}{dt} = N_{CME} M_{CME} \omega r_{launch}^2 sin(CPA) \tag{6.1}$$

Where N_{CME} is the number of CMEs per unit time, M_{CME} is the mass ejected, ω the stellar angular rotation frequency, and r_{launch} the length of the effective lever arm. This calculation assumes that all the mass contained in the CME is lost from one specific radius, and effectively simultaneously. Informing the determination of this radius with the results of Favata et al. (2005), we could take as an extremum the largest loop length determined as an effective lever arm length. Assuming this as well as a typical TTS radius of 2 $R_\odot$, we have $r_{launch} \simeq 107$ $R_\odot$. Table VI.1 summarizes the calculation and results.

Table VI.1: Angular Momentum Loss Parameters

N_{CME} [Myr^{-1}]	$Mass_{CME}$ [log([g])]	CPA [°]	CPA probability	$\frac{dJ}{dt}$ [Myr^{-1} $M_\odot$ $R_\odot^2$ Hz]
22325766	15.5475	2	0.0048	5.627e-12
21817582	15.5584	7	0.012	5.639e-12
21320942	15.5694	12	0.011	5.652e-12
20361342	15.5804	17	0.016	5.535e-12
19897874	15.5913	22	0.016	5.547e-12
19444932	15.6023	27	0.011	5.560e-12
18569768	15.6132	32	0.015	5.445e-12
17330326	15.6242	37	0.031	5.212e-12
15805446	15.6351	42	0.028	4.875e-12
14921300	15.6461	47	0.062	4.720e-12
13765970	15.6571	52	0.054	4.465e-12
12554701	15.6680	57	0.069	4.177e-12
11189397	15.6790	62	0.088	3.817e-12
9972556	15.6899	67	0.096	3.489e-12
9306936	15.7009	72	0.115	3.340e-12
7921484	15.7119	77	0.119	2.915e-12
6292260	15.7228	82	0.127	2.375e-12

Continued on Next Page…

Table VI.1 – Continued

N_{CME} [Myr^{-1}]	$Mass_{CME}$ [log([g])]	CPA [°]	CPA probability	$\frac{dJ}{dt}$ [Myr^{-1} $M_\odot$ $R_\odot^2$ Hz]
5738610	15.7338	87	0.126	2.221e-12
4998121	15.7447	···	···	1.984e-12
3970145	15.7557	···	···	1.616e-12
3153599	15.7666	···	···	1.317e-12
2504993	15.7776	···	···	1.072e-12
2156783	15.7886	···	···	9.470e-13
1580542	15.7995	···	···	7.117e-13
1044254	15.8105	···	···	4.822e-13
792148	15.8214	···	···	3.752e-13
499811	15.8324	···	···	2.428e-13
281064	15.8433	···	···	1.400e-13
198978	15.8543	···	···	1.016e-13
137659	15.8653	···	···	7.212e-14
111893	15.8762	···	···	6.012e-14
90950	15.8872	···	···	5.012e-14
68993	15.8981	···	···	3.899e-14
68993	15.9091	···	···	3.998e-14

Continued on Next Page…

Table VI.1 – Continued

N_{CME} [Myr^{-1}]	Mass_{CME} [log([g])]	CPA [°]	CPA probability	$\frac{dJ}{dt}$ [Myr^{-1} $M_\odot$ $R_\odot^2$ Hz]
46645	15.9201	⋯	⋯	2.772e-14
			Σ	8.99e-11

6.2 Results

The calculation of $\frac{dJ}{dt}$ proceeds by taking the product of the columns of Table VI.1. For example, the first element of column one is how many CMEs of log(mass) 15.5475 occur in 1 Myr. Columns three and four (from the distribution illustrated in Fig. 6.6) indicate the probability one of the $\sim 2\times 10^7$ CMEs will occur at a given angle. From these, we find how many CMEs of the $\sim 2\times 10^7$ occur at each angle given, and sum $\frac{dJ}{dt}$ (calculated as shown in Equation 6.1) over all angles. We have assumed a rotation period of 5 days, the median period for the ONC.

Our final result for total angular momentum loss rate in 10 Myr is 8.99×10^{-10} [$M_\odot$ $R_\odot^2$ Hz]. The angular momentum content of a 1 $M_\odot$, 2 $R_\odot$ star with a 5 day rotation period is 2.33×10^{-5} [$M_\odot$ $R_\odot^2$ Hz], assuming solid-body rotation. Even over 10 Myr, our angular momentum loss rate via CMEs would not noticeably affect stellar rotation. There are, however, many caveats to this calculation and assumptions made which need to be refined.

6.3 Discussion

One of the most pivotal parts of this calculation is the extrapolation of the CME mass/flare energy relationship. If the second part of the broken log-linear relationship used (Fig. 6.2) should indeed have a steeper slope like the first part of the relationship (i.e., simply slide the solar relationship over and up a few dex), it would indicate we had underestimated the total mass lost. Additionally, in Section 5.4, we note that according to our flare-CME pairing, only 12% of CMEs are flare-associated. We could be underestimating the mass lost via CME by 88% right away by only using the events associated with flares. Assuming this to be the case, and that our angular momentum loss is only 12% of what is actually shed via CMEs, we would gain an order of magnitude, but still find that CMEs only shed 0.01% of a the star's total angular momentum content.

Interestingly, we see from Table VI.1 that the lowest mass CMEs occur the most often by orders of magnitude and supply the majority of the angular momentum loss. Albacete Colombo et al. (2007) note that in determining the flare energy-rate distribution stellar flare events were potentially excluded from the sample based upon the bayesian block light curve binning process. Larger bins (greater width in time) exclude lower energy flares from the sample, while smaller bins fail to detect the higher energy flares. The lowest energy flares are completely lost to detection due to low to no signal. Solar data could be used to fill this gap, potentially creating an energy distribution that spans the entire flare energy range from solar flares to stellar flares (i.e., the X-axis of Fig. 6.2).

A simplification adopted in performing this calculation was that of a single lever arm length; we assumed that all mass was lost from a fixed position at the greatest loop height observed by Favata et al. (2005). Combining solar flare height observations (akin to those of Warwick, 1955; Pallavicini & Peres, 1983) and stellar loop heights, we could create a flare energy/loop height relationship to root this assumption firmly in observations. There would be a firm lower limit to loop heights that would need be included in this calculation, as at some distance close to the rotation axis, shed material would not apply a substantial torque against rotation.

In conclusion, this represents a first attempt at performing this calculation. Many factors going into this procedure need to be refined and re-evaluated. A more detailed approach would include modeling a time-variable activity rate tied to the stellar rotation period and including a flare energy-magnetic loop height relationship to improve estimates of launch radii. In the future, we hope to have high-resolution spectroscopic data of the innermost regions of circumstellar disks, potentially confirming the presence of stellar CMEs , measuring their frequency of occurrence, and assessing whether they are analogous to solar CMEs.

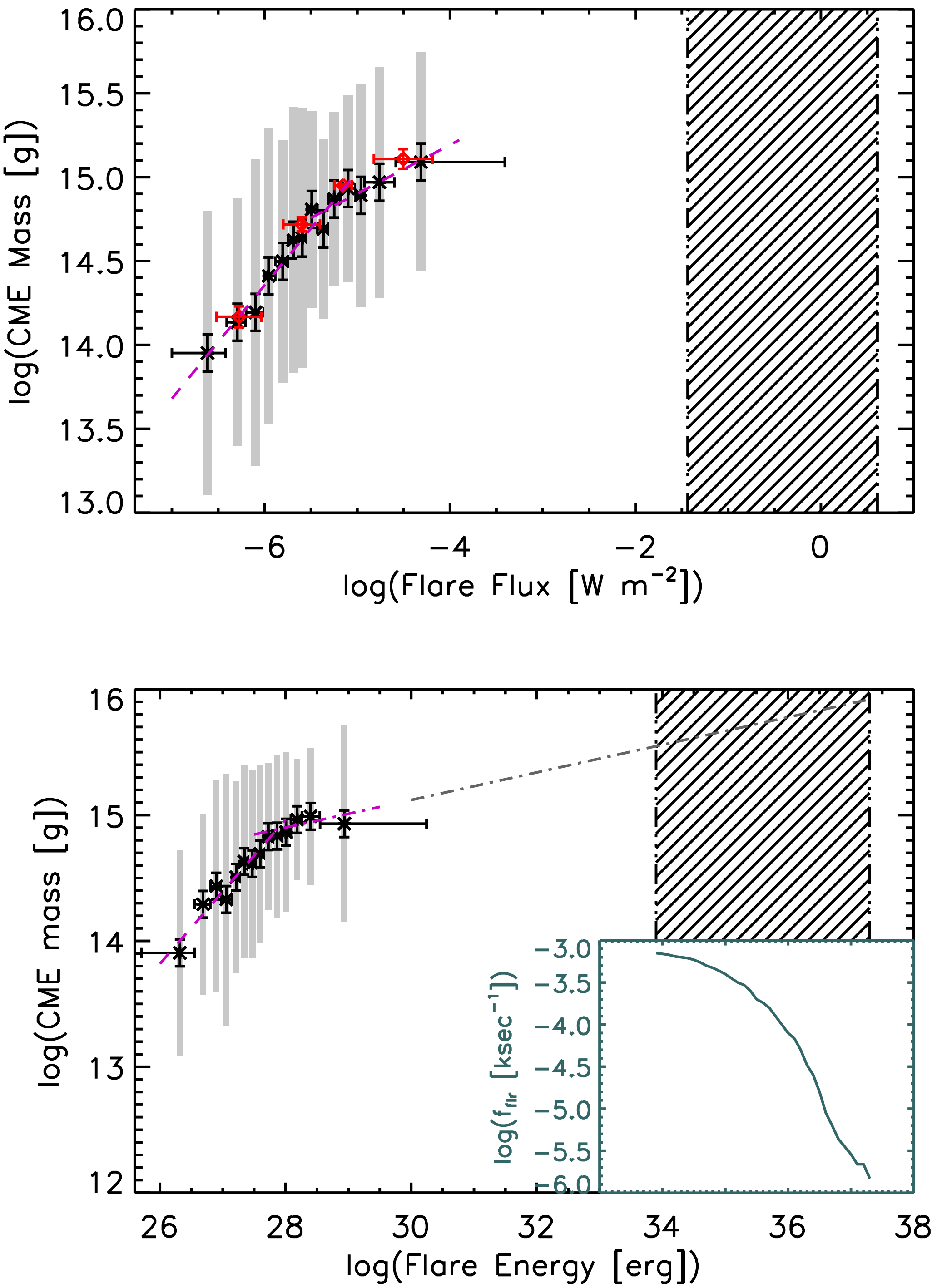

Figure 6.2: Solar CME mass/flare flux relationship converted to CME mass/flare energy. Also shown, lower panel, teal inset, is the stellar flare energy/event rate distribution of Albacete Colombo et al. (2007).

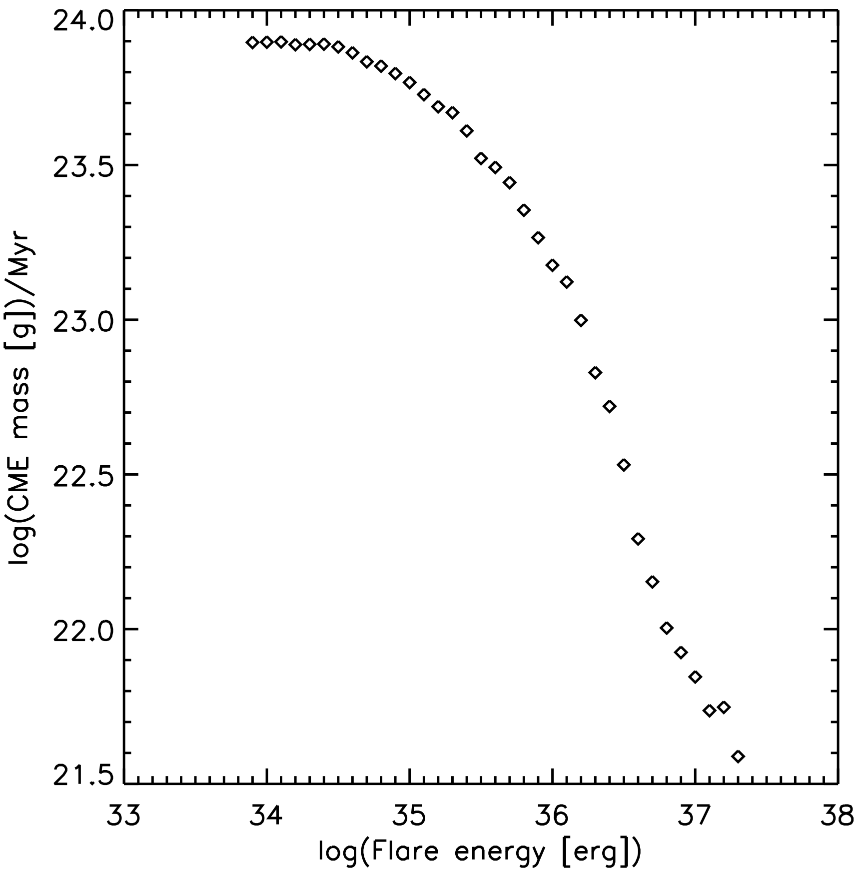

Figure 6.3: Stellar CME mass/flare energy distribution, obtained by interpolating over the extrapolated solar CME mass/flare energy relationship (Fig. 6.2, lower panel).

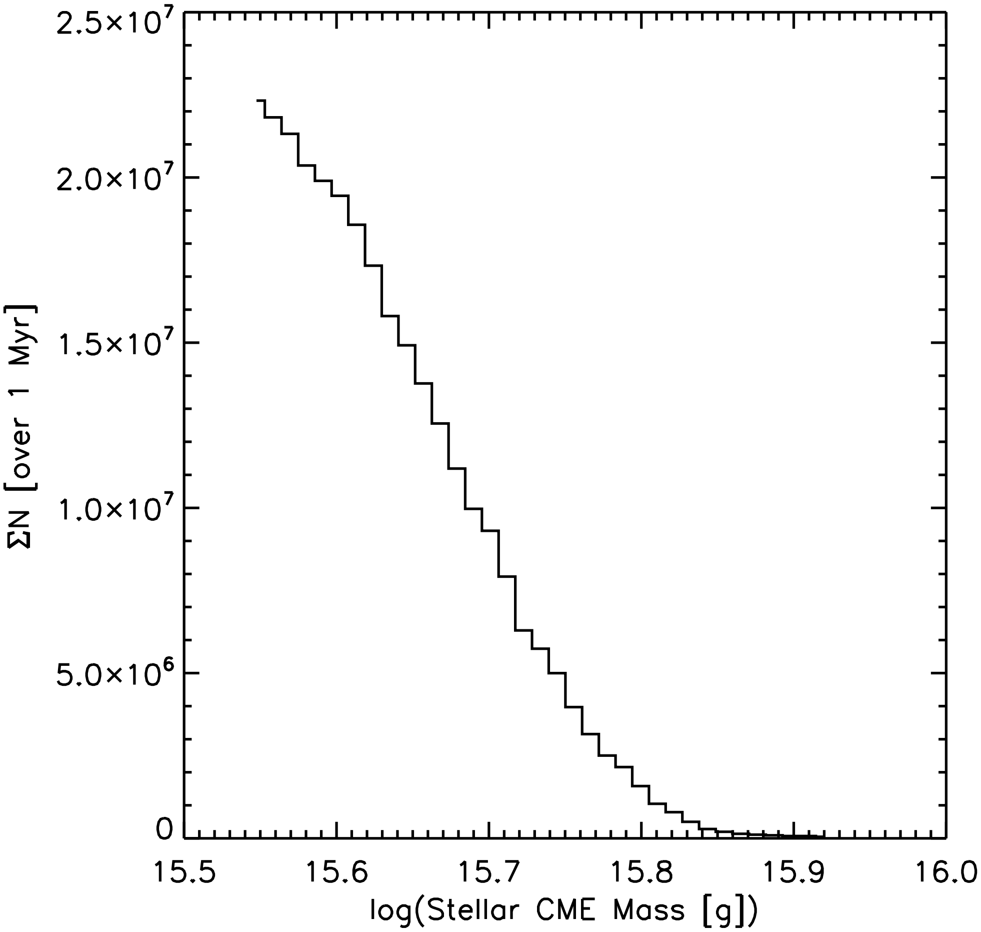

Figure 6.4: Stellar CME frequency over 1 Myr.

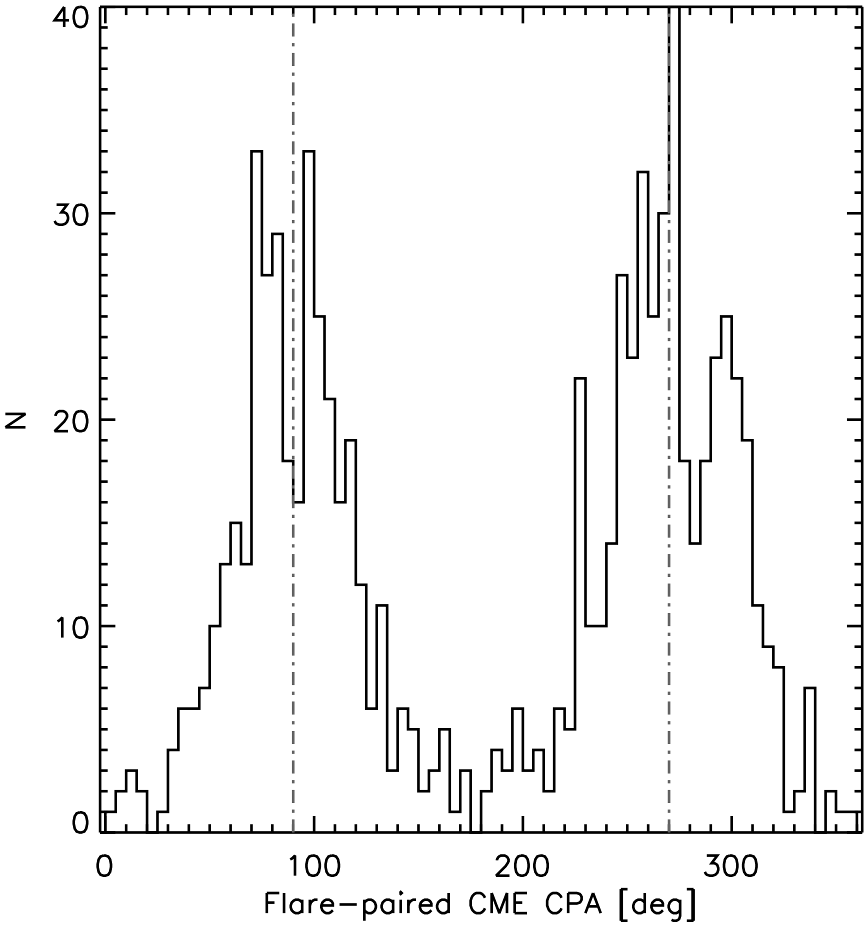

Figure 6.5: Central position angles of our sample of 826 flare-associated CMEs . In this figure, 0° and 360° represent the North Solar Pole; 90° and 270° are approximately the East and West equatorial latitudes.

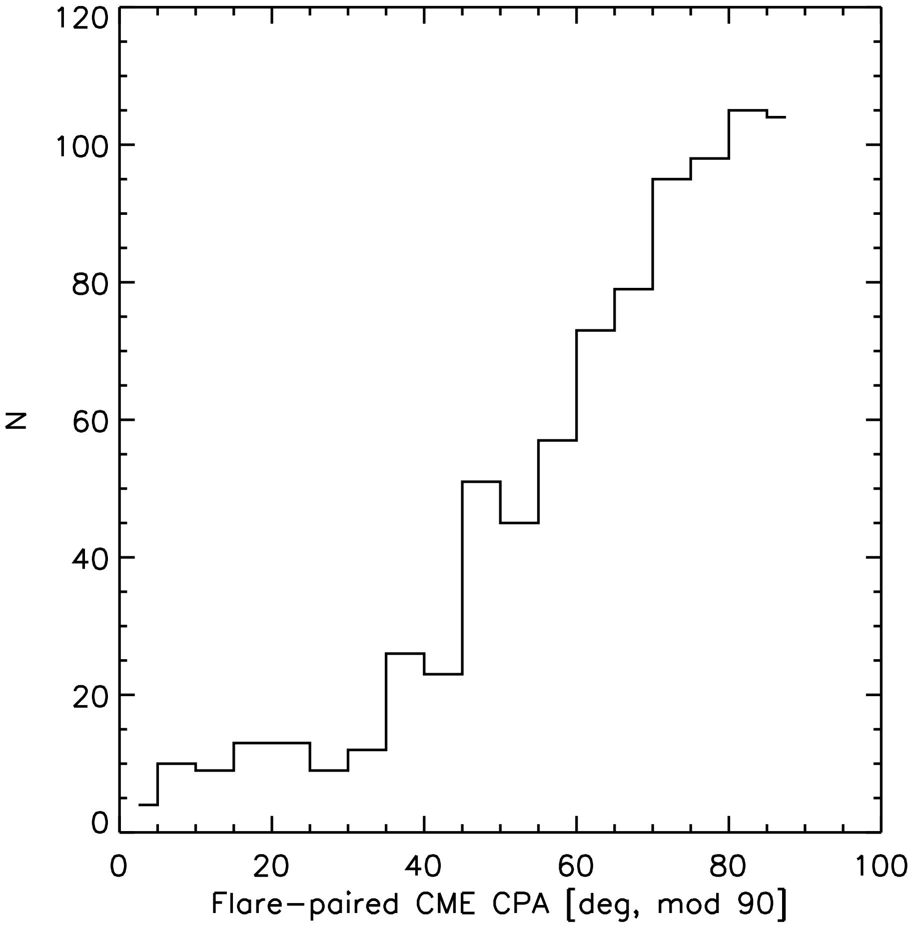

Figure 6.6: Here, we have folded the CME central position angles (from Fig. 6.5) about 90°; as anticipated, the distribution peaks closer to the equator than the poles, reflecting the position of sunspots during the solar cycle. A nuance absent from this is the actual position of the solar equator: due to the misalignment of the Earth and solar spin axes as well as so-called solar "back-tilt," the apparent position of a feature on the disk does not always map to its true heliographic position.

APPENDIX A

STELLAR ASSOCIATION: SUPPLEMENTAL TABLES

Table A.1: Observing Log

Object Name	Observation Time [UT]	Integration Time [s]	S/N[1]	Comment(s)
2001-06-18 : UCO / Lick				
Alpha Boo	04:17:13.0	1	200	K2III v_r Standard
HD 137396	04:28:35.0	720	127	···
RHS 48	04:52:38.0	1500	158	···
HD 138969	05:25:23.0	720	105	···
HD 140574	05:45:22.0	720	132	···
HD 141612	06:05:08.0	1500	178	···
HD 141693	06:37:21.0	360	105	···
HD 142987	06:50:42.0	1800	75	···
TYC 6191-0552	07:30:24.0	2400	31	···
HD 143332	08:17:18.0	600	126	···
HIP 79354	08:34:18.0	1000	97	···
HD 145551	08:58:01.0	600	98	···
BD -06 4414	09:15:34.0	600	72	···
HD 143810	09:32:25.0	600	72	···
HD 144726	09:49:16.0	600	145	···
HD 145169	10:06:16.0	450	95	···
HD 177178	10:20:40.0	300	175	A4V v_r Standard
HD 187691	10:33:26.0	240	184	F8V v_r Standard
16 Cyg/HD186427	10:45:50.0	240	197	G2V v_r Standard
HD 184467	10:59:00.0	300	139	K2V v_r Standard
2002-04-17 : LCO				
HD 80170	01:07:53.4	30	107	K5III v_r Standard
HD 102870	01:16:31.1	20	131	F9V v_r Standard
TYC 6141-0525-1	03:17:19.9	1080	81	···
TYC 0909-0125-1	03:43:18.4	1080	79	···
TYC 7312-0236-1	00:00:00.0	1500	89	···
TYC 7327-0689-1	04:37:09.7	1500	77	···
TYC 5003-0138-1	05:09:45.3	1500	112	···
TYC 0937-0754-1	05:41:42.1	1500	75	···
TYC 6781-0415-1	06:16:54.2	900	86	···
TYC 6790-1227-1	06:40:12.4	1500	101	···
HD 142016	07:26:45.0	255	58	···
TYC 0376-0769-1	07:42:44.8	1200	85	···
TYC 7346-1182-1	08:12:47.3	1200	117	···
HD 153439	08:37:23.9	750	136	···
TYC 6815-0084-1	08:57:16.9	900	150	···
TYC 6817-1757-1	09:18:32.5	1350	80	···
HD 188376	09:47:46.4	65	109	G5V v_r Standard
HD 165341	09:58:15.0	45	206	K0V Spectral Type Standard
HD 209290	10:06:48.1	750	52	M0.5V Spectral Type Standard
2002-04-18 : LCO				
TYC 5022-0263-1	06:22:52.4	1500	116	···
HD 143358	06:54:12.0	900	117	···
TYC 6784-0717-1	07:14:23.6	900	153	···
HD 144732	07:34:59.7	1200	105	···
TYC 6806-0888-1	07:59:41.7	1800	100	···
TYC 6803-0897-1	08:35:31.7	1800	99	···
HD 148982	09:11:17.0	1200	115	···
HD 157310	09:38:10.9	1200	99	Double star - brighter component
HD 157310B	09:59:37.2	1200	60	Double star - fainter component
2002-04-19 : LCO				
HD 141813	05:41:33.5	900	120	···
HD 148396	06:06:32.7	1500	119	Cataloged Double star
TYC 0976-1617-1	06:40:26.6	2400	100	SB (2)
HD 154922	07:27:02.2	450	107	···
TYC 6242-0104-1	08:03:30.1	3600	52	Double star - brighter component
TYC 6242-0104-1B	09:09:59.6	3600	71	Double star - fainter component
2002-04-20 : LCO				

Continued on Next Page...

Table A.1 – Continued

Object Name	Observation Time [UT]	Integration Time [s]	S/N[1]	Comment(s)
HD 109524	04:11:22.8	750	238	K2V v_r Standard
HIP 75685	05:43:37.4	900	122	···
TYC 6234-1287-1	06:06:12.0	1800	118	···
TYC 7334-0429-1	06:43:18.0	1500	110	···
TYC 5668-0365-1	07:14:42.1	2400	134	···
HD 144393	08:01:37.6	360	109	···
TYC 6214-2384-1	08:59:30.1	1800	99	···
TYC 6215-0184-1	09:35:25.5	2400	129	SB (2)
HD 177178	10:24:04.7	150	109	A4V v_r Standard

---

[0] The two doubles observed in this survey have components identified here as A and B: HD 157310B also goes by the identifier BD +04 3405B, and TYC 6242-0104B is also known as 2MASS J17215666-2010498.

[1] Approximated using *Splot* at ∼6500Åand ∼6700Å.

[2] Suspected spectroscopic binary based upon broadened troughs of spectral features.

Table A.2: Stellar Parameters

Plot ID[0]	Object Name	J[2]	H[2]	K_S[2]	PM R.A[3] [mas yr^{-1}]	PM Dec[3] [mas yr^{-1}]	Parallax[4] [mas]
A	HD 141569	6.872±0.027	6.861±0.040	6.281±0.026	-18.3±1.1	-20.5±1.1	8.63±0.59
1	TYC 6242-0104-1B[1]	8.150±0.023	7.187±0.047	6.840±0.023	···	···	···
2	TYC 6191-0552	9.261±0.022	8.535±0.042	8.325±0.024	-15.0±3.3	-20.2±3.7	···
3	TYC 6234-1287-1	8.659±0.025	8.012±0.024	7.829±0.020	-10.1±2.6	-39.0±2.7	···
4	TYC 7312-0236-1	9.601±0.024	9.079±0.024	8.919±0.019	-20.5±3.3	-20.5±3.2	···
5	TYC 7327-0689-1	9.300±0.024	8.755±0.036	8.563±0.019	-19.7±3.2	-27.5±3.1	···
6	TYC 6781-0415-1	7.974±0.030	7.367±0.033	7.241±0.024	-19.5±2.7	-30.1±2.4	···
7	TYC 6803-0897-1	9.275±0.024	8.743±0.049	8.648±0.025	-15.6±2.5	-28.6±2.5	···
8	TYC 6214-2384-1	9.230±0.019	8.659±0.036	8.509±0.019	-18.7±3.5	-26.2±3.8	···
9	HD 148396	8.420±0.023	8.095±0.019	8.100±0.020	-6.9±2.4	-15.4±2.4	···
10	TYC 6806-0888-1	9.216±0.025	8.785±0.027	8.659±0.026	-13.4±3.0	-27.5±2.7	···
11	HD 157310B	9.759±0.022	9.413±0.031	9.262±0.019	-5.3±1.5*	-14.9±1.8*	···
12	TYC 6784-0717-1	7.847±0.021	7.538±0.034	7.431±0.020	-11.7±1.7	-20.7±1.6	···
13	HD 153439	8.073±0.020	7.852±0.049	7.729±0.047	-6.7±1.6	-28.6±1.6	···
14	TYC 7334-0429-1	9.168±0.018	8.690±0.049	8.565±0.021	-17.5±2.2	-25.5±2.2	···
15	TYC 6817-1757-1	8.815±0.021	8.350±0.042	8.179±0.031	-10.1±2.8	-7.4±2.5	···
16	HD 157310	9.160±0.022	9.088±0.047	9.006±0.021	-5.4±1.5	-12.0±1.5	···
17	HD 142016	6.785±0.020	6.707±0.034	6.622±0.018	-26.4±1.2	-38.8±1.3	···
18	TYC 6815-0084-1	8.099±0.020	7.661±0.029	7.525±0.038	-9.8±2.0	-28.2±1.8	···
19	TYC 6242-0104-1	9.963±0.027	9.305±0.026	9.151±0.024	-11.7±3.6	-13.7±4.0	···
20	TYC 6790-1227-1	9.212±0.023	8.719±0.026	8.624±0.023	-20.4±2.8	-26.0±2.3	···
21	TYC 7346-1182-1	9.018±0.027	8.663±0.053	8.530±0.019	-14.3±2.3	-27.0±2.2	···

Continued on Next Page...

Table A.2 – Continued

Plot ID[0]	Object Name	J[2]	H[2]	K_S[2]	PM R.A[3] [mas yr^{-1}]	PM Dec[3] [mas yr^{-1}]	Parallax[4] [mas]
E	HD 142987	8.279±0.035	7.774±0.063	7.614±0.021	-15.4±2.1	-22.3±2.2	···
E	HD 143358	8.470±0.023	8.164±0.036	8.074±0.020	-18.3±1.4	-29.6±1.5	···
E	BD-06 4414	8.359±0.027	8.043±0.038	7.936±0.033	-27.0±2.1	-33.7±2.2	···
E	HD 137396	7.632±0.023	7.493±0.033	7.419±0.027	-14.9±1.4	-12.0±1.0	···
E	HD 138969	7.946±0.027	7.693±0.040	7.666±0.017	-11.3±1.4	-8.5±1.0	10.69±1.4
E	HD 140574	7.623±0.018	7.495±0.036	7.459±0.029	-27.2±1.3	-30.2±0.9	10.8±1.15
E	HD 141612	8.808±0.024	8.497±0.057	8.398±0.031	-17.7±2.4	-10.7±1.8	9.62±1.74
E	HD 141693	6.886±0.020	6.888±0.034	6.828±0.023	-29.7±1.2	-26.5±0.7	8.96±0.96
E	HD 141813	8.232±0.023	7.963±0.036	7.862±0.020	-22.7±1.7	-38.1±1.9	···
E	HD 143332	6.987±0.024	6.783±0.044	6.680±0.023	-10.6±1.3	-24.9±1.3	9.96±1.36
E	HD 143810	8.953±0.030	8.766±0.061	8.643±0.019	-24.8±1.5	-13.7±1.5	9.26±1.51
E	HD 144393	7.323±0.027	7.099±0.046	6.980±0.021	-6.3±1.2	-23.9±1.1	10.97±1.14
E	HD 144726	7.527±0.027	7.322±0.036	7.244±0.026	-16.7±1.4	-19.4±1.3	8.49±1.20
E	HD 144732	8.531±0.023	8.231±0.051	8.147±0.026	-15.2±2.1	-33.2±1.9	···
E	HD 145169	7.159±0.039	6.912±0.040	6.876±0.023	-20.2±1.1	-30.5±1.1	12.75±1.78
E	HD 145551	7.906±0.029	7.677±0.042	7.600±0.018	-20.3±1.3	-19.4±1.3	9.48±1.51
E	HD 148982	8.669±0.026	8.381±0.036	8.308±0.023	-15.8±2.0	-25.4±1.7	···
E	HD 154922	7.742±0.023	7.540±0.042	7.456±0.021	-7.4±1.3	-13.1±1.2	···
E	HIP 75685	9.186±0.024	8.870±0.042	8.810±0.024	-28.8±1.5	-19.4±1.4	8.92±1.72
E	HIP 79354	8.090±0.023	7.752±0.031	7.649±0.021	-12.1±1.0	-29.8±1.0	9.18±1.99
E	RHS 48	8.465±0.029	7.830±0.053	7.624±0.024	-15.1±1.6	-10.6±1.7	···
E	TYC 0376-0769-1	8.196±0.024	7.649±0.031	7.496±0.036	-18.8±1.8	-4.4±1.7	···
E	TYC 0909-0125-1	9.433±0.026	8.987±0.022	8.896±0.023	-16.2±2.7	-17.6±2.6	···
E	TYC 0937-0754-1	9.016±0.029	8.525±0.040	8.404±0.023	-13.1±2.0	-1.4±2.0	···
E	TYC 0976-1617-1	10.158±0.026	9.798±0.026	9.664±0.021	-11.0±3.0	-15.1±3.1	···
E	TYC 5003-0138-1	9.084±0.023	8.492±0.027	8.317±0.026	-27.3±1.6	-13.1±1.5	···
E	TYC 5022-0263-1	8.855±0.029	8.401±0.047	8.244±0.031	-6.7±3.2	-24.5±3.4	···
E	TYC 5668-0365-1	9.564±0.024	9.033±0.026	8.840±0.025	-2.8±2.2	-18.7±2.3	···
E	TYC 6141-0525-1	9.335±0.027	8.957±0.024	8.872±0.024	-15.2±2.3	-35.9±2.4	···
E	TYC 6215-0184-1	8.677±0.026	8.003±0.036	7.756±0.024	-3.6±2.9	-21.8±3.1	···

---

[0] Star IDs of "E" denote objects exluded from analysis due to low Li I content.

[1] Note- For star #1, we adopt proper motions of its companion. * Proper motions from UCAC2.

[2] From 2MASS Catalog.

[3] Tycho-2 proper motions.

[4] Hipparcos parallaxes.

Table A.3: Effective Temperatures and Lithium Equivalent Widths

Plot ID[1]	Object Name	Li I EW [mÅ] Integ.	Li I EW [mÅ] GFit	Ctmn. [mÅ]	Hα Flag[2]	Spectral Type	Type Source[3]	T_{eff} [K]	λ6200/λ6210 Line Ratio	Spectral Type	T_{eff} [K]	Adopted T_{eff} [K]
1	TYC 6242-0104-1B	491	487	25	e*	···	···	···	0.58	K7.5	4060	4060
2	TYC 6191-0552	481	492	15	e*	K2	1	4900	1.91	K2	4900	4900
3	TYC 6234-1287-1	464	452	18	e*	K4 Ve	2	4590	2.65	K1.5	4990	4590
4	TYC 7312-0236-1	434	433	15	e*	K2 Ve	2	4900	2.30	K2	4900	4900
5	TYC 7327-0689-1	416	414	15	e*	K2 Ve	2	4900	2.52	K2	4900	4900
6	TYC 6781-0415-1	409	426	13	e*	G9 IVe	2	5410	4.69	G9.5	5330	5410
7	TYC 6803-0897-1	408	413	14	a	···	···	···	3.62	K0.5	5165	5165
8	TYC 6214-2384-1	397	398	14	a	K1 IV	2	5080	2.48	K2	4900	5080
9	HD 148396	197	216	14	a	K1/2 + F	3	5080	8.09	G8.5	5465	5080
10	TYC 6806-0888-1	320	345	12	a	G8 IV	2	5520	11.3	G3	5830	5520
11	HD 157310B	233	242	5	a	···	···	···	‡	···	···	6600*
12	TYC 6784-0717-1	164	193	5	a	F4	5	6590	‡	···	···	6590
13	HD 153439	180	198	5	a	F5 V	3	6440	‡	···	···	6440
14	TYC 7334-0429-1	368	378	15	a	K2e	2	4900	3.99	K0	5250	4900
15	TYC 6817-1757-1	274	244	13	e*	K0 Ve	2	5250	6.03	G9	5410	5250
16	HD 157310	52	76	1	a	A7 II/III	5	7850	‡	···	···	7850
17	HD 142016	20	57	0	a	A4 IV/V	3	8460	‡	···	···	8460
18	TYC 6815-0084-1	307	324	13	a	K0 IV	2	5250	8.72	G8.5	···	5250
19	TYC 6242-0104-1	223	226	20	e*	K5 Ve	2	4350	1.07	K5	4350	4350
20	TYC 6790-1227-1	324	344	13	a	G9 IV	2	5410	4.53	G9.5	5330	5410
21	TYC 7346-1182-1	256	262	12	a	G8 V	2	5520	5.94	G9	5410	5520

Continued on Next Page...

Table A.3 – Continued

Plot ID[1]	Object Name	Li I EW [mÅ] Integ.	Li I EW [mÅ] GFit	Ctmn. [mÅ]	Hα Flag[2]	Spectral Type	Type Source[3]	$T_{\rm eff}$ [K]	λ6200/λ6210 Line Ratio	Spectral Type	$T_{\rm eff}$ [K]	Adopted $T_{\rm eff}$ [K]
E	BD -06 4414	···	···	10	c	G5	1	5770	‡	···	···	5770
E	HD 137396	47	77	4	a	F2/3 IV/V	5	6890 / 6740	‡	···	···	6815
E	HD 138969	113	109	9	c	G1 V	4	5945	4.68	K9.5	3955	5945
E	HD 140574	···	···	1	a	A9 V / A3	5 / 1	7390 / 8720	‡	···	···	8055
E	HD 141612	128	120	10	a	G5 V	5	5770	4.25	K0	5250	5770
E	HD 141693	···	···	···	a	A0	1	9520	‡	···	···	9520
E	HD 141813	201	187	14	a	G8/K2 III + F/G	3	5520 / 4900	31.4	>G2	>5860	5210
E	HD 142987	150	216	10	e*	G3/6 / G5	4 / 6	5830-5700/5770	‡	···	···	5770
E	HD 143332	···	···	5	a	F5 V	5	6440	4.01	K0	5250	6440
E	HD 143358	196	215	9	a	G1 / G2V	3	5945 / 5860	‡	···	···	5900
E	HD 143810	66	67	6	a	F5/6 V	5	6440 / 6360	9.25	G8	5520	6400
E	HD 144393	···	···	7	a	F7/8 V	4	6280 / 6200	13.8	>G2	>5860	6240
E	HD 144726	29	36	5	a	F5 V	5	6440	‡	···	···	6440
E	HD 144732	178	195	9	a	G0 V / G0	3 / 6	6030	27.1	>G2	>5860	6030
E	HD 145169	51	46	10	a	G3 V	5	5830	13.5	>G2	>5945	5830
E	HD 145551	26	25	6	a	F5/6 V	5	6440 / 6360	9.17	G8.5	5465	6400
E	HD 148982	181	216	8	a	F8 / G0	3	6200 / 6030	‡	···	···	6115
E	HD 154922	···	12†	1	a	A7 III	4	7850	‡	···	···	7850
E	HIP 75685	99	99	11	a	G6	1	5700	9.05	G8.5	5465	5700
E	HIP 79354	38	41	8	a	F8	1	6200	2.87	K1	5080	6200
E	RHS 48	157	153	15	e*	K2	1	4900	1.77	K2	4900	4900
E	TYC 0376-0769-1	12	21	···	a	···	···	···	‡	···	···	···
E	TYC 0909-0125-1	53	54	14	a	···	···	···	4.19	K0.5	5165	5165
E	TYC 0937-0754-1	99	97	16	c	···	···	···	1.89	K2.5	4815	4815
E	TYC 0976-1617-1	···	···	3	a	A9 V	5	7390	‡	···	···	7390
E	TYC 5003-0138-1	79	79	16	e*,p	···	···	···	1.85	K2.5	4815	4815
E	TYC 5022-0263-1	···	···	···	o	···	···	···	‡	···	···	···
E	TYC 5668-0365-1	61	70	···	e	···	···	···	‡	···	···	···
E	TYC 6141-0525-1	···	···	···	a	···	···	···	‡	···	···	···
E	TYC 6215-0184-1	49	52	15	e*	K2IVe	2	4900	‡	···	···	4900

---

[0] Note- We report here two Li λ6707 measurements- "Integ." in column 3 refers to direct integration over the line profile, and "Gfit" in column 4 indicates the result of fitting a Gaussian to the absorption feature. In column 5, we also report contamination (denoted "Ctmn.") of the Li I line; see § 3.3.2 for description of its derivation. #9 appears here in the high Li sample as it is a binary; we double the plotted EW as line dilution may have occurred, seeing was $1\farcs5$, thus contribution from the companion is possible. † Blended line; result indicates Gaussian feature fit to Li I in deblending. ‡ denotes cases in which the line ratio could not be measured from the spectrum either due to extreme rotational broadening or the lack of presence of either or both lines in question. * Effective temperature determined via interpolation of dereddened $H-K$ color over the color-effective temperature relationship of Kenyon & Hartmann (1995), see Fig. 3.2.

[1] Star IDs of "E" denote objects exluded from analysis due to low Li I content.

[2] Indicator flags are defined as follows: Absorption, a; core filling observed, c; double peaked emission, e*; P-Cygni like feature, p; emission with overlaid absorption, o.

[3] Spectral types drawn from the following sources: typed by A.J. Weinberger using KAST low-resolution spectrograph, 1; Torres et al. (SACY, 2006), 2; Michigan spectral atlas (Houk, 1982; Houk & Smith-Moore, 1988; Houk & Swift, 1999), 3, 4, and 5, respectively; HD Catalog spectral type, 6.

APPENDIX B

UNIFORM COOLING LOOP MODEL

Using spatially resolved solar magnetic loop images and X-ray light curves, Reale et al. (1997) developed a method for assessing the sizes of magnetic structures confining X-ray emitting plasma on stars. The authors compare a model of plasma evolution for heated gas inside a closed coronal loop to the observed loop sizes. The 1-D hydrodynamic model used is of a compressible, viscous fluid in a gravitational field; all bulk fluid motion is restricted to occur along the magnetic field lines. The model takes into account radiative and conductive energy losses. The plasma's evolution begins from a quasi-static condition, at the temporal boundary between the impulsive rise phase–so deemed due to the brevity of the period of initial rise in X-ray flux–of the X-ray flare and the exponential decay phase. An assumption folded into the model then is that sustained heating is not present in the system. The model is then time-evolved over various combinations of loop length, density, temperature, and velocity to well-sample the parameter space occupied by observed flares. Finally, the model results are then adjusted to produce synthetic "observations" dependent on the response of the desired comparison instrument.

For application to X-ray flares observed on stars, Reale et al. (1997) found the following relationships (as summarized in Favata et al., 2005) describing the dependence of decay timescale on the geometry of the confining magnetic loop:

$$\tau_{\rm cond} \simeq \frac{3nkT}{\kappa T^{\frac{7}{2}}/L^2}, \tag{2.1}$$

where $\tau_{\rm cond}$ is the conductive decay timescale. The radiative decay timescale is:

$$\tau_{\rm rad} \simeq \frac{3nkT}{n^2 P(T)}. \tag{2.2}$$

The effective cooling timescale, $\tau_{\rm th}$ is a combination of these:

$$\frac{1}{\tau_{\rm th}} \simeq \frac{1}{\tau_{\rm cond}} + \frac{1}{\tau_{\rm rad}}. \tag{2.3}$$

The observable parameter is the decay timescale, $\tau_{\rm lc}$, which is equivalent to $\tau_{\rm th}$ within an instrument-dependent function. F(ζ) is the ratio of the observed light curve decay time to $\tau_{\rm th}$, the intrinsic decay time, where ζ is the slope of the flare decay in temperature-density space. ζ can serve as a diagnostic of sustained heating (i.e., shallow slope, or a slower decline in temperature, indicates heating continues to be provided during the flare). F(ζ), then, depends on the bandpass observed in and the spectral response, as these factors provide the limitations on measurements of temperature and density. The final relationship used by Favata et al. (2005) with flares observed by the ACIS instrument on *Chandra* determines the confining loop length as follows:

$$L = \frac{\tau_{\rm lc}\sqrt{T_{\rm pk}}}{3.7 \times 10^{-4} F(\zeta)}. \tag{2.4}$$

Note that this is actually half the full loop length, as the material begins at the loop apex and gradually falls as it radiates and conducts away the energy initially gained from the impulsive reconnection event.

APPENDIX C

SPECTRAL ENERGY DISTRIBUTIONS

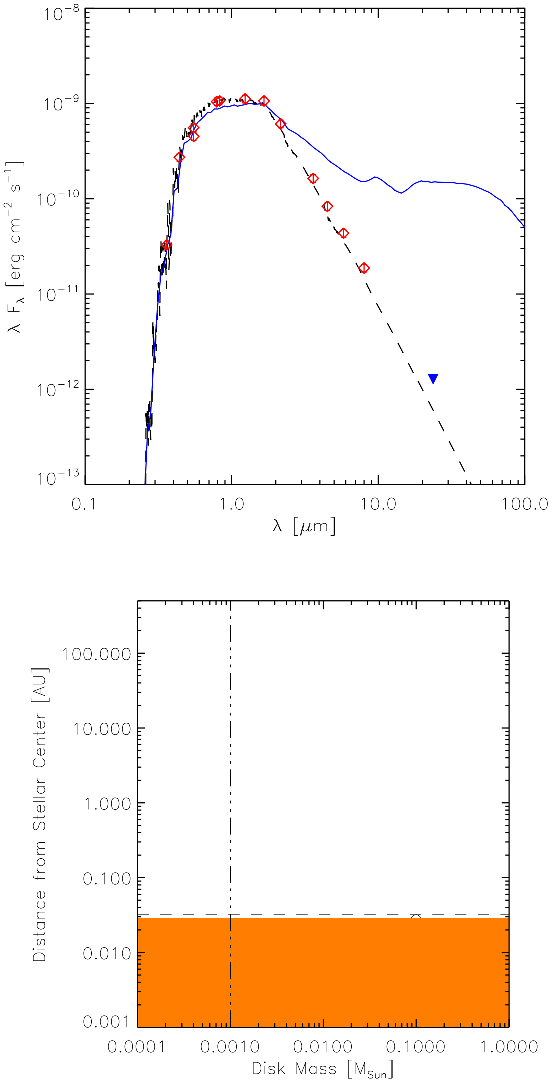

Figure C.1: SED of COUP 7, category 3. All symbols are as in Fig. 4.3; the blue triangle is an upper limit. The comprehensive set of observed fluxes for this object are most consistent with a bare photosphere, and thus none of the star+disk model SEDs from the extensive grid of Robitaille et al. (2007) are able to fit the data.

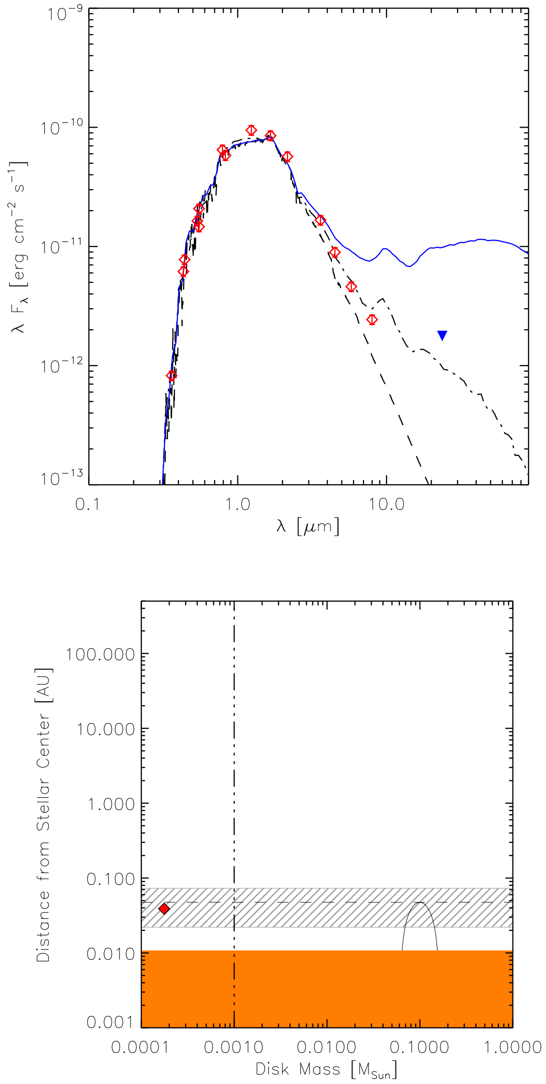

Figure C.2: SED of COUP 28, category 3. All symbols are as in Fig. 4.3; the blue triangle is an upper limit. This SED is most consistent with a bare photosphere.

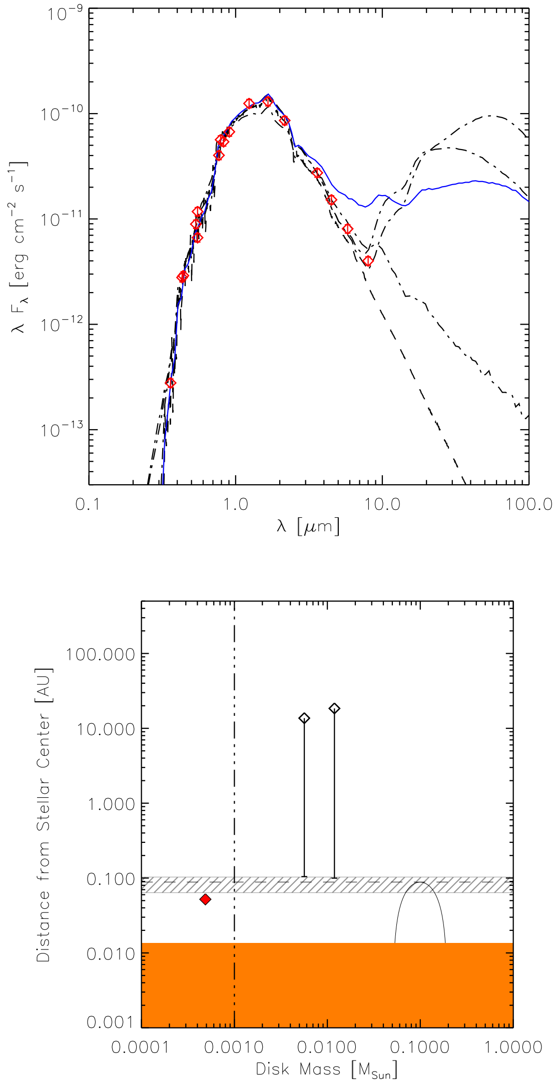

Figure C.3: COUP 43, category 3. All symbols are as in Fig. 4.3. The observed SED is consistent with a bare photosphere, and the available $\Delta(U-V)$ indicates no accretion. All best-fit models above the $M_{\rm disk}$ threshold have inner disk truncation radii beyond 10 AU.

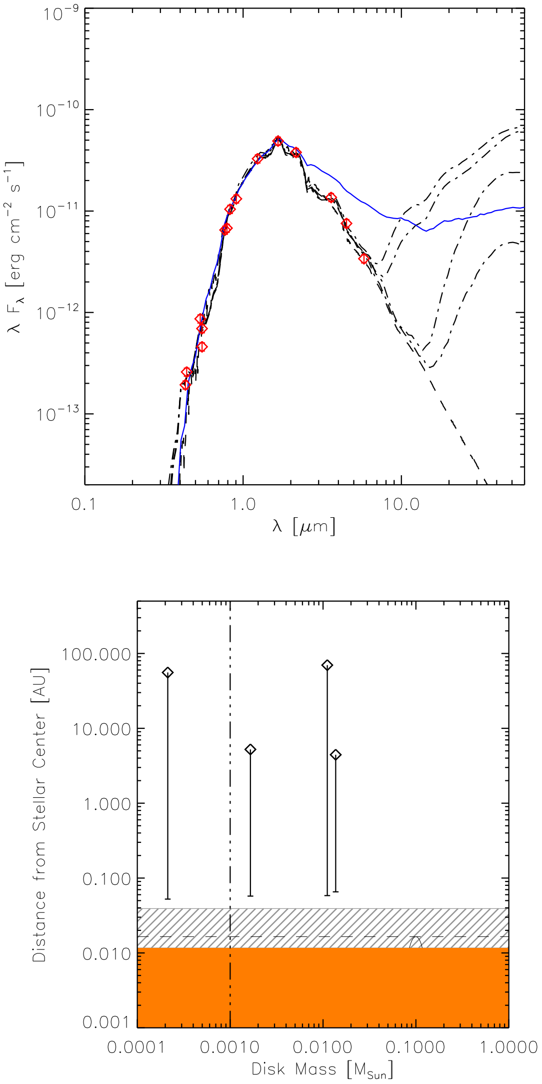

Figure C.4: COUP 90, category 3. All symbols are as in Fig. 4.3. The observed SED is consistent with a bare photosphere. All best-fit models above the $M_{\rm disk}$ threshold have inner disk truncation radii beyond 1 AU.

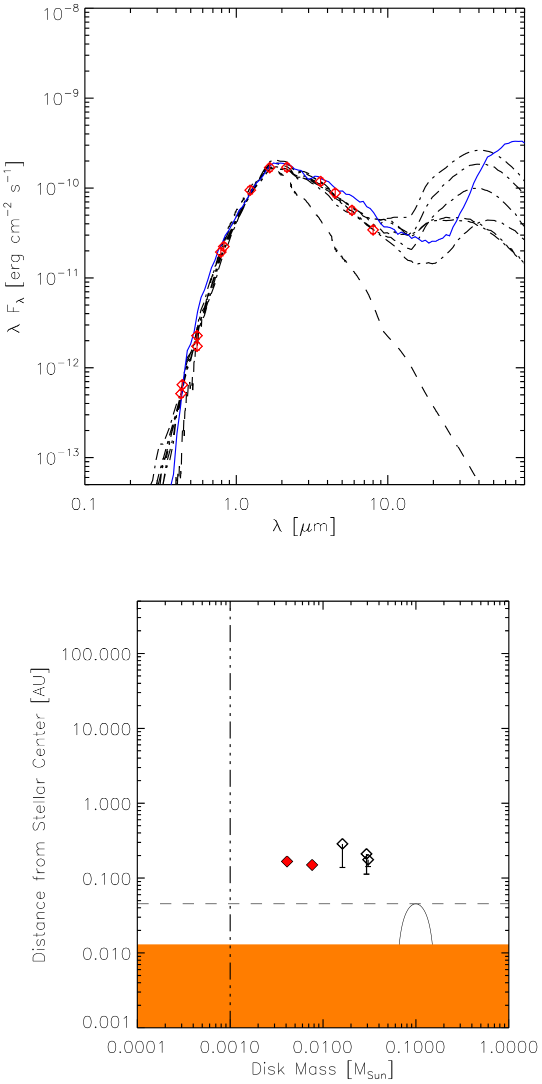

Figure C.5: COUP 223, category 4. All symbols are as in Fig. 4.3. The model SED fits are roughly evenly divided between those with $R_{\rm trunc} \lesssim R_{\rm dust}$ and those with $R_{\rm trunc} > R_{\rm dust}$.

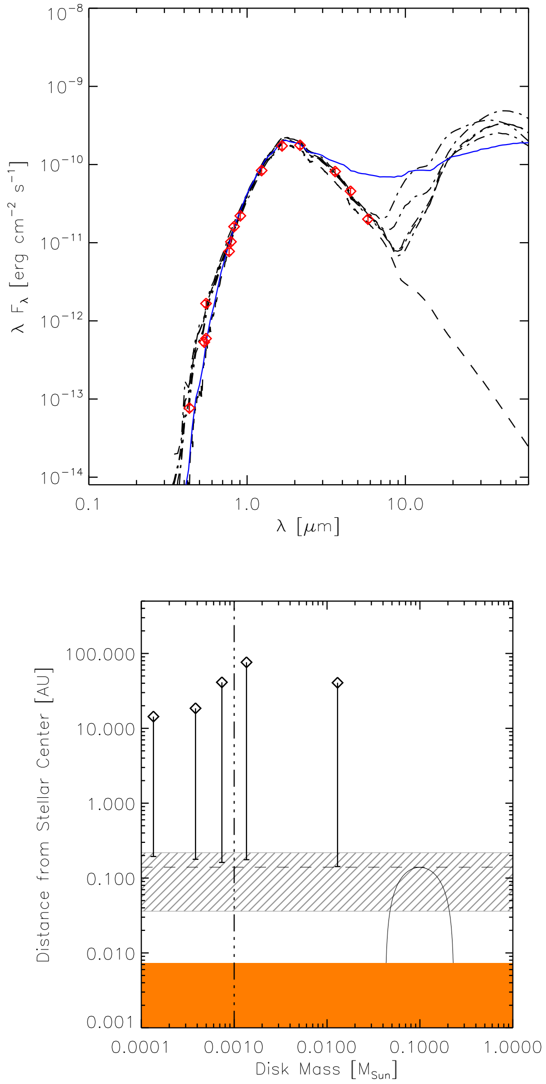

Figure C.6: COUP 262, category 3. All symbols are as in Fig. 4.3. The observed SED is consistent with a bare photosphere. All best-fit models above the $M_{\rm disk}$ threshold have inner disk truncation radii beyond 30 AU.

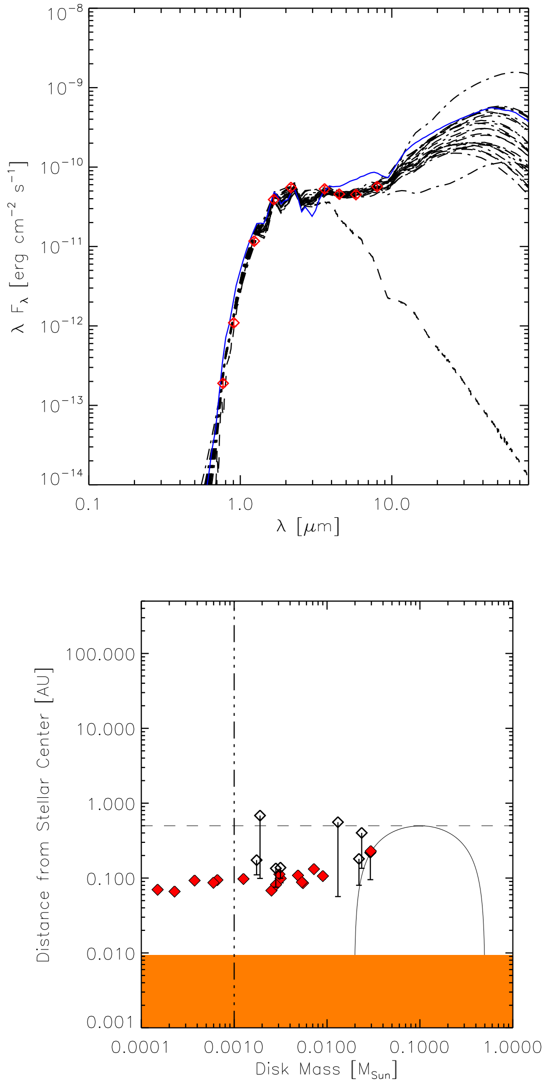

Figure C.7: COUP 332, category 1. All symbols are as in Fig. 4.3. More than 2/3 of best-fit model disks are truncated within reach of the magnetic loop height.

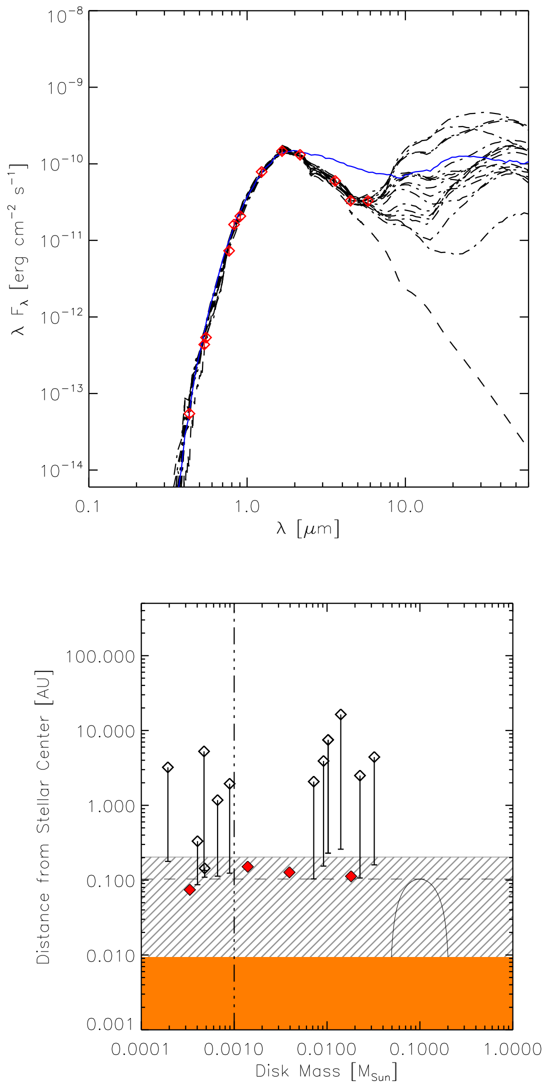

Figure C.8: COUP 342, category 4. Three of the best-fit models have disks within reach of the magnetic loop, six models do not. The fiducial model suggests that a flux measurement at 10μm could resolve which set of models best describe the system.

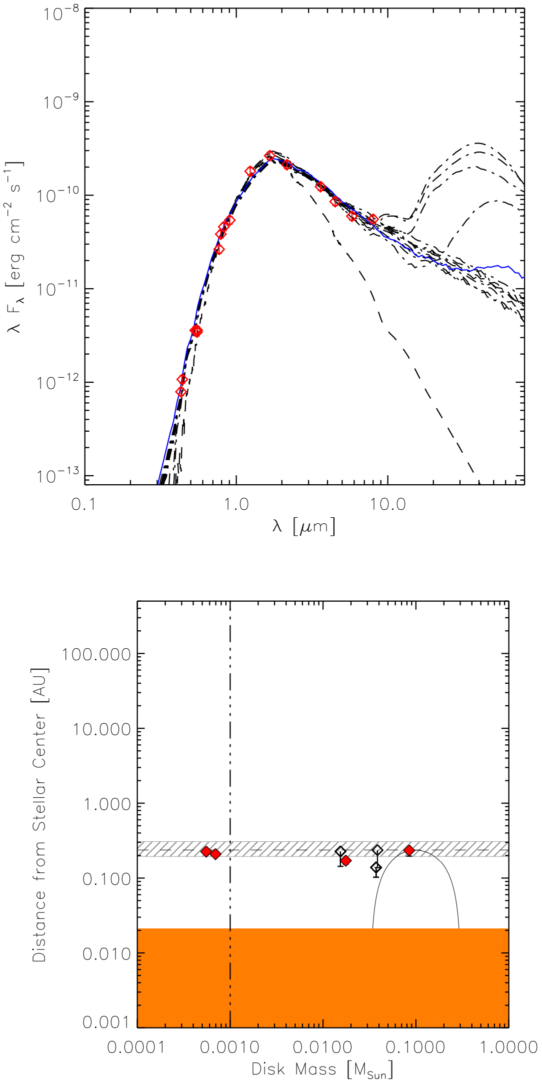

Figure C.9: COUP 454, category 1. All symbols are as in Fig. 4.3. Excess in the IRAC bands indicates close-in disk material, and all of the best fit models are well within reach of the well-constrained magnetic loop height.

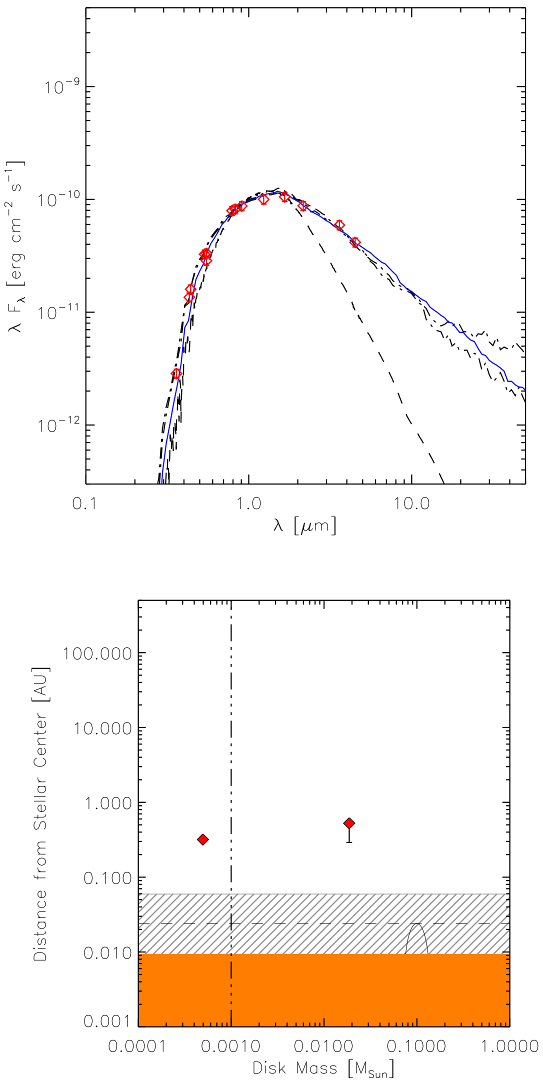

Figure C.10: COUP 597, category 2. All symbols are as in Fig. 4.3.

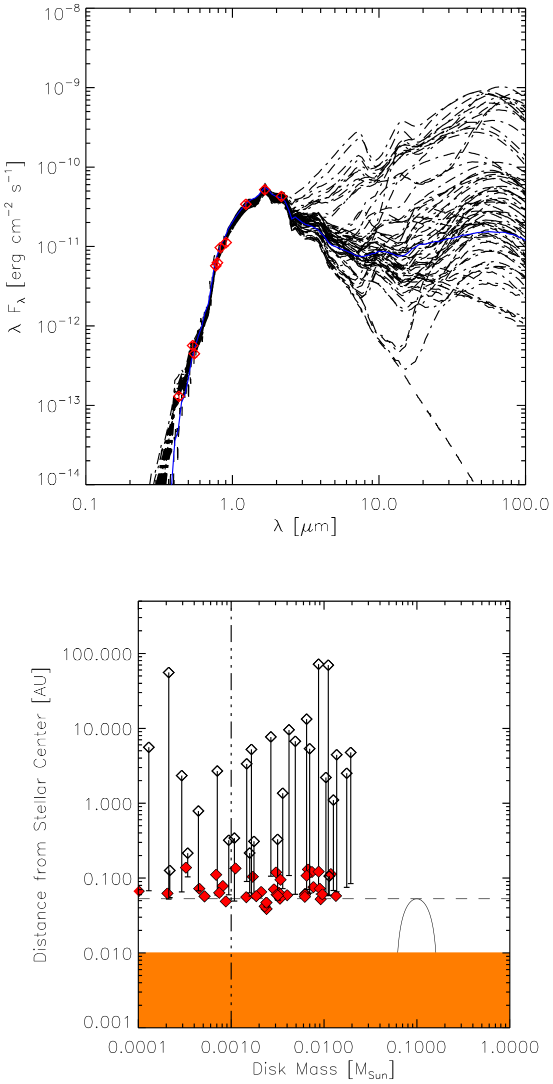

Figure C.11: COUP 649, category 4. All symbols are as in Fig. 4.3. With fluxes out only to the K_S band, the SED is not well enough constrained to discriminate between the many best-fit models.

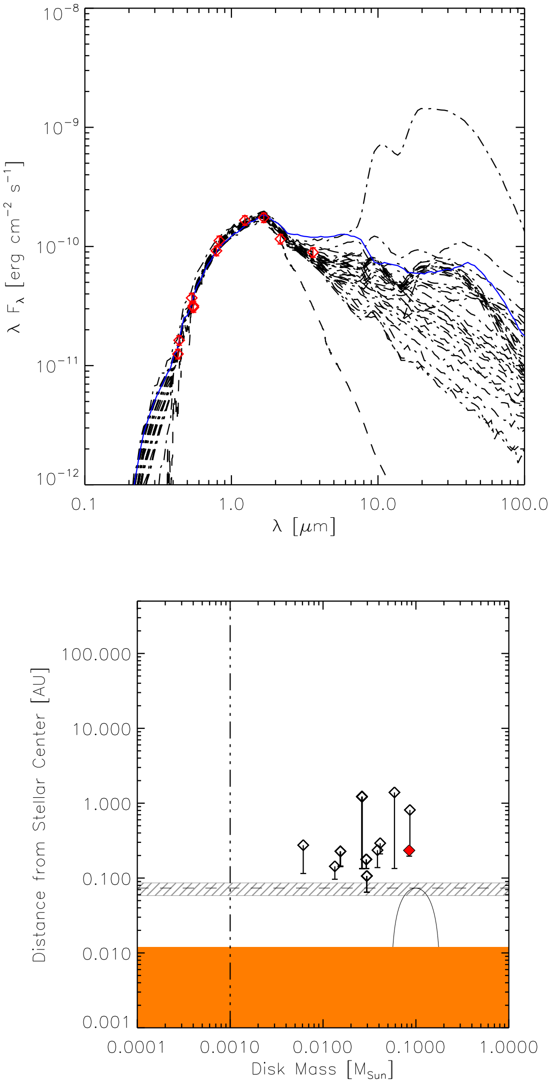

Figure C.12: COUP 669, category 3. All symbols are as in Fig. 4.3. All but one of the best-fit SEDs represent massive disks truncated both beyond reach of the magnetic loop and beyond dust destruction.

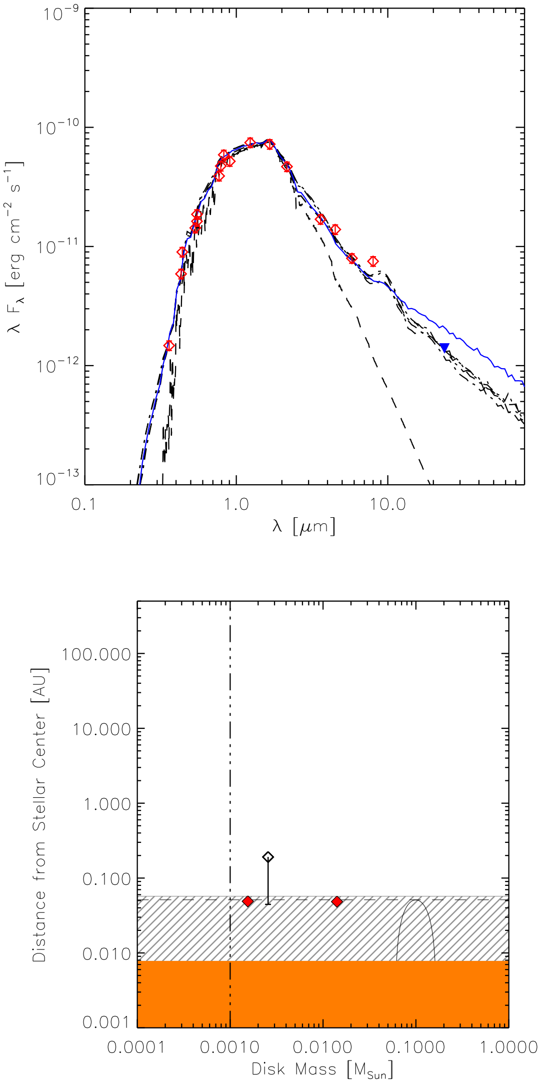

Figure C.13: COUP 752, category 1. All symbols are as in Fig. 4.3; the blue triangle is an upper limit. More than two-thirds of the best-fit models have $R_{\rm trunc} \lesssim R_{\rm loop}$. In addition to excess in the IRAC bandpasses, this object shows $\Delta(U-V) = -0.7$ indicative of active accretion (Table IV.1), which is consistent with a gas disk extending inward of $R_{\rm trunc}$.

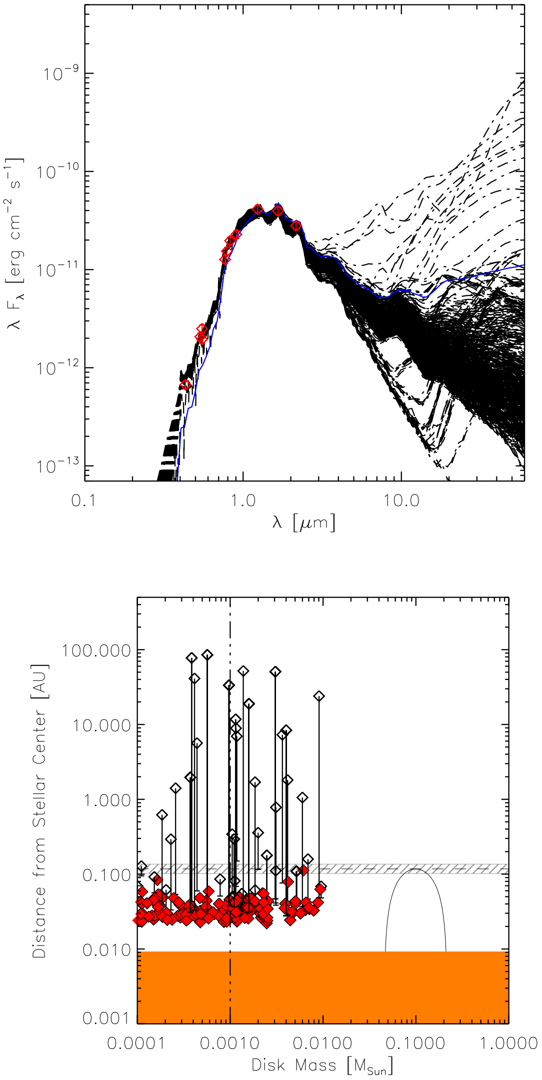

Figure C.14: COUP 848, category 4. All symbols are as in Fig. 4.3. The ensemble of best fit models is unconstrained beyond 2.2μm. The models are divided between categories 1 and 3, and the available Ca 2 measurement is consistent with either interpretation.

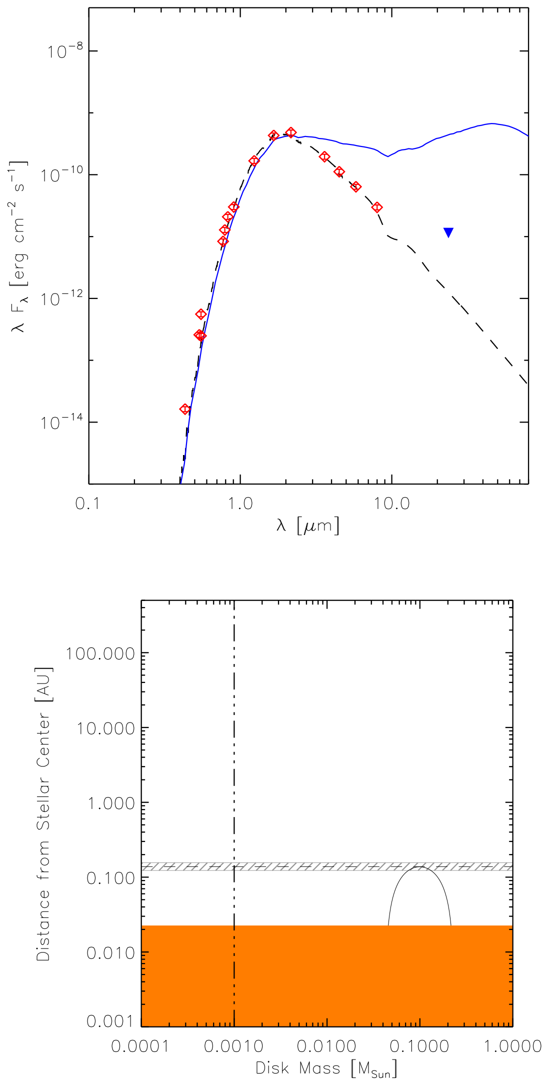

Figure C.15: COUP 891, category 3. All symbols are as in Fig. 4.3; the blue triangle is an upper limit. The observed fluxes for this object are most consistent with a bare photosphere, and thus none of the star+disk model SEDs from the extensive grid of Robitaille et al. (2007) are able to fit the data.

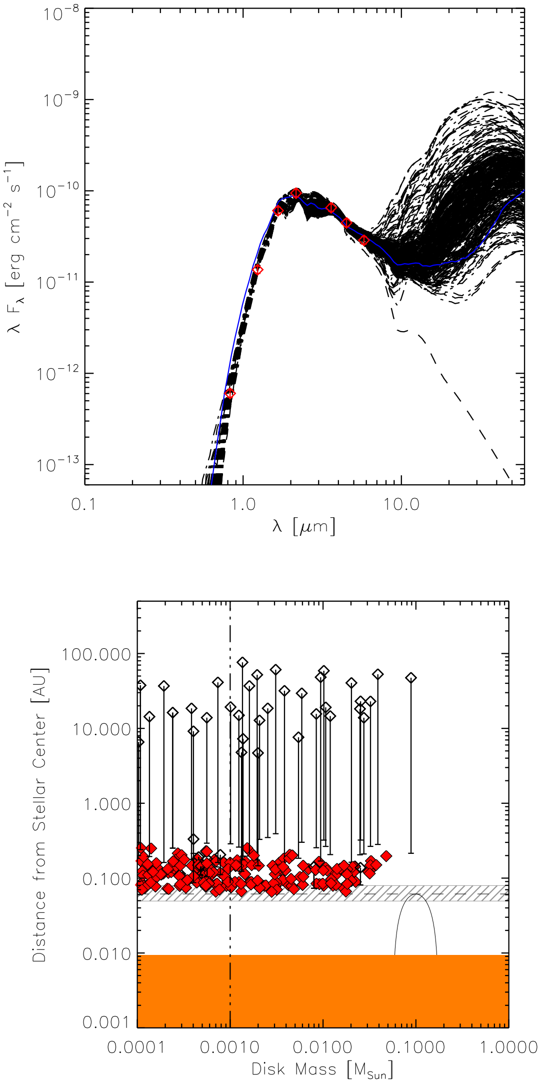

Figure C.16: COUP 915, category 4. All symbols are as in Fig. 4.3. The model fits are unconstrained beyond 5.8μm. Approximately half of the models are truncated at their respective dust destruction radii, but the remaining models have truncation radii $\gtrsim$ 10 AU. The fiducial model suggests that a flux measurement at 10μm could allow a definitive category assignment.

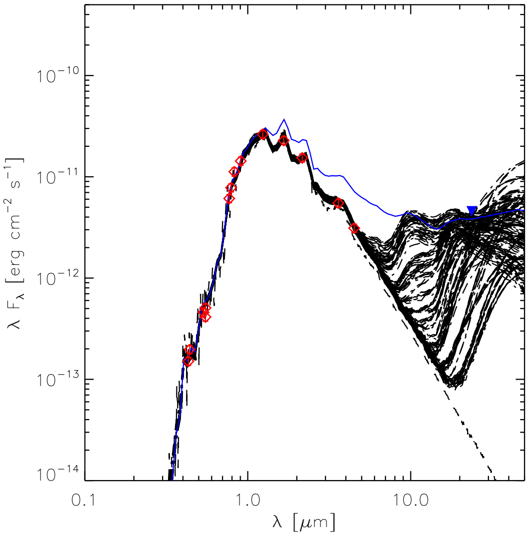

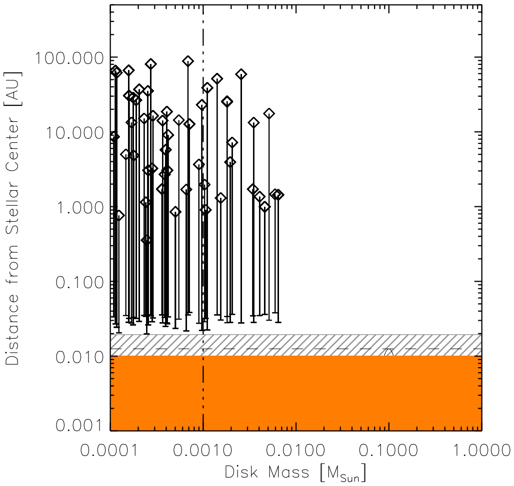

Figure C.17: COUP 960, category 3. All symbols are as in Fig. 4.3; the blue triangle is an upper limit. The available flux measurements are consistent with a bare photosphere. All best fit models are truncated at 1 AU and beyond, well beyond the magnetic loop extent.

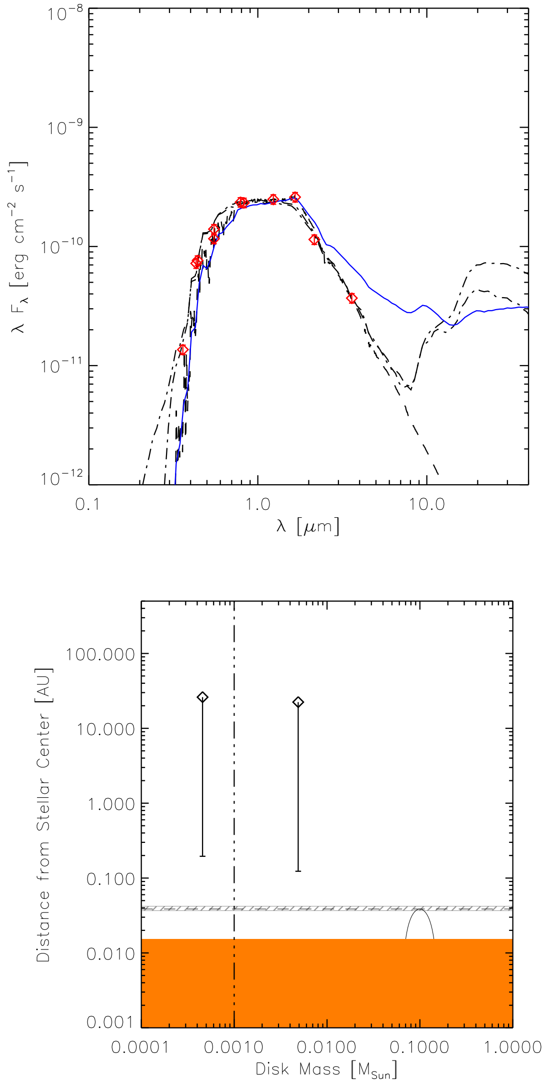

Figure C.18: COUP 971, category 3. All symbols are as in Fig. 4.3. The available flux measurements are consistent with a bare photosphere. The mild $\Delta(U - V)$ excess in this object is consistent with chromospheric activity (e.g. Rebull et al., 2000). The best-fit models are truncated well beyond the magnetic loop height.

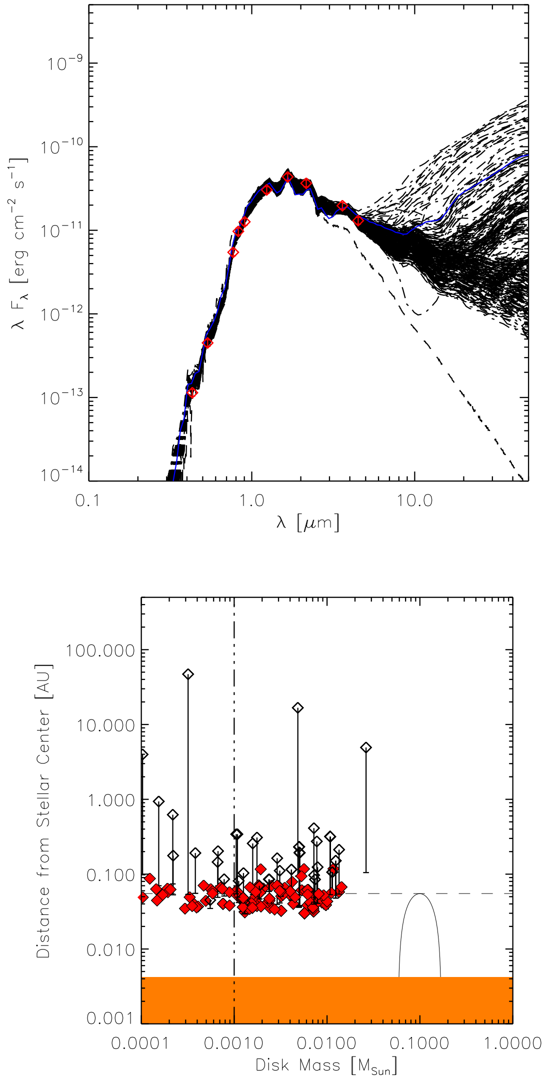

Figure C.19: COUP 976, category 4. All symbols are as in Fig. 4.3. The array of best fitting models are divided almost evenly between categories 1 and 3.

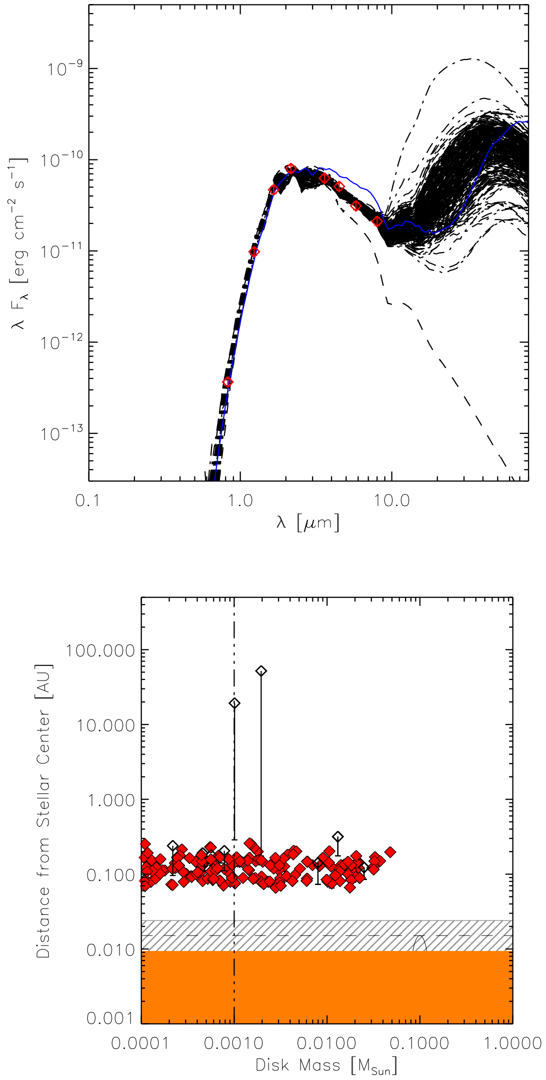

Figure C.20: COUP 1040, category 2. All symbols are as in Fig. 4.3. The vast majority of models have their inner disks truncated at their respective dust destruction radii.

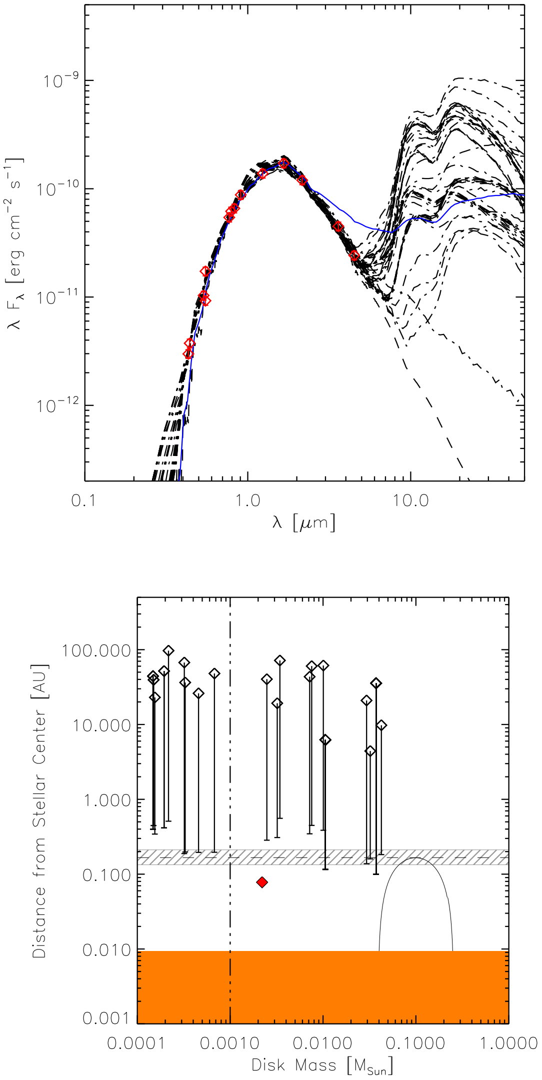

Figure C.21: COUP 1083, category 3. All symbols are as in Fig. 4.3. The measured fluxes are consistent with a bare photosphere. The overwhelming majority of best fit models for COUP 1083 are truncated at $\gtrsim$ 10 AU, well beyond reach of the magnetic loop.

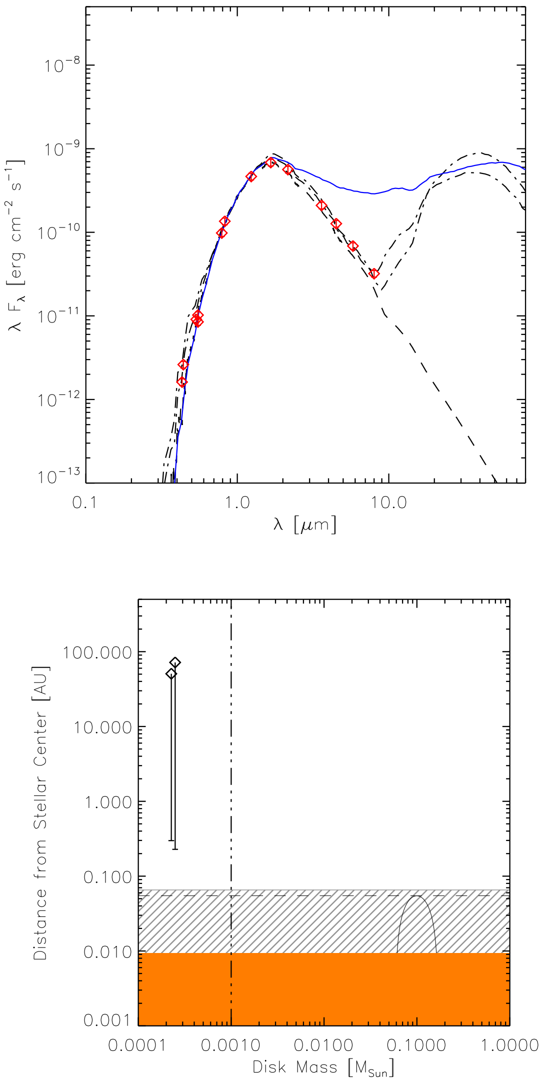

Figure C.22: COUP 1114, category 3. All symbols are as in Fig. 4.3. The flux measurements are consistent with a bare photosphere. Accordingly, the only best-fit star+disk SED models have extremely low disk masses and in any case have extremely large inner-disk holes.

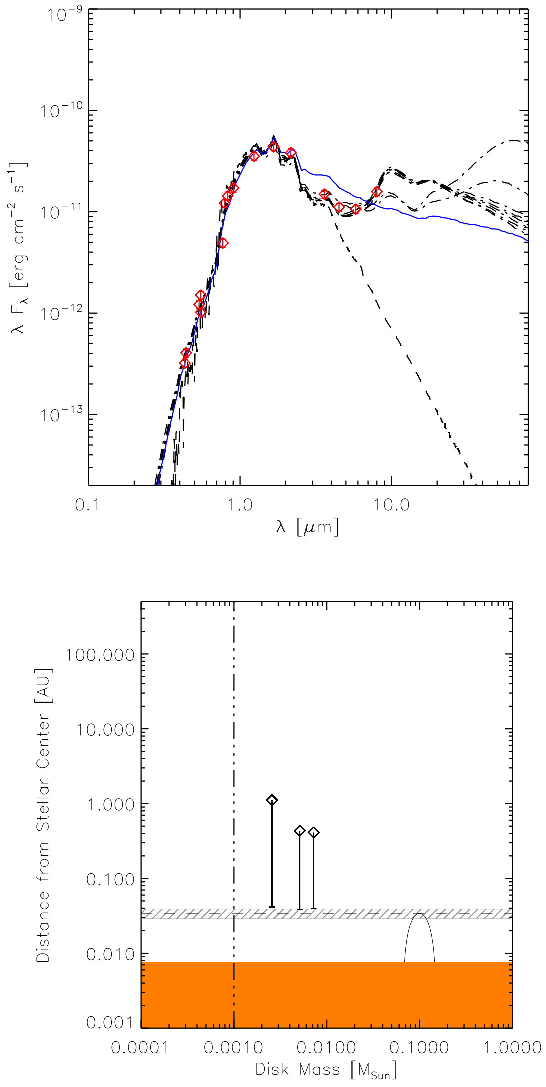

Figure C.23: COUP 1246, category 3. All symbols are as in Fig. 4.3. COUP 1246 represents the sole case in which we initially measured a large $\Delta K_{\rm S} > 0.3$, suggestive of a close-in, warm dusty disk, but for which our detailed modeling clearly indicates a large inner-disk hole (see Table IV.4). Adjusting the best-fit A_V of this star upward by $\sim 3\sigma$ removes the apparent near-IR excess, as shown here (see § 4.3). A modest blue excess is likely due to chromospheric activity as indicated by filled-in Ca 2 emission (Table IV.1).

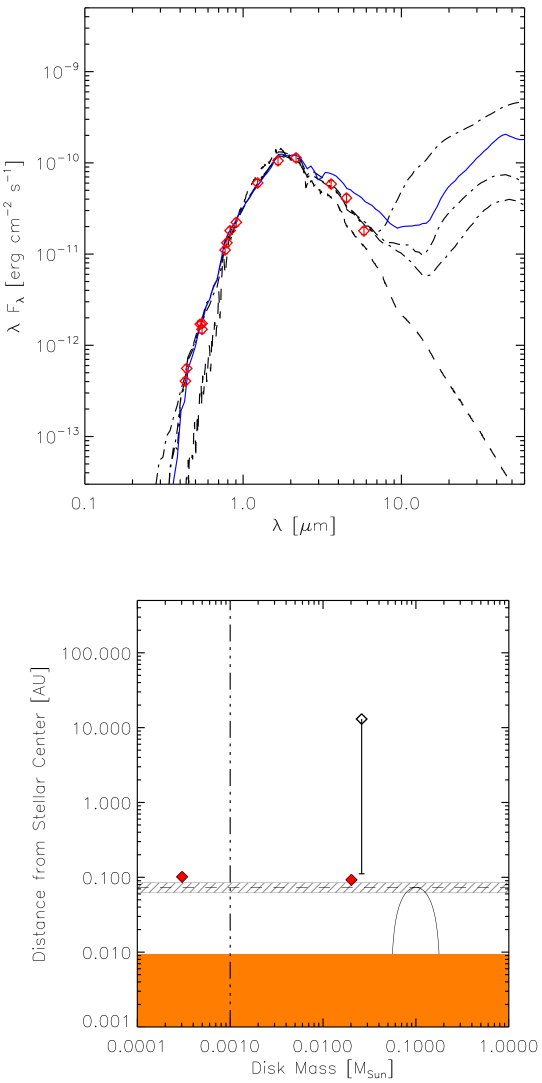

Figure C.24: COUP 1343, category 4. All symbols are as in Fig. 4.3. The best fit models with disk mass $> 10^{-3}$ M$_\odot$ are evenly divided between categories 2 and 3. COUP 1343 proved to be a particularly difficult object to classify definitively. It does not have a published $T_{\rm eff}$, and consequently there is a strong degeneracy in our fits between $T_{\rm eff}$, A_V, $\Delta K_{\rm S}$ and a possible blue excess. On the whole, the evidence slightly favors a category 2 interpretation, however we have conservatively kept this object in category 4 until either a spectroscopic $T_{\rm eff}$ determination, a U-band measurement, or longer wavelength fluxes become available to definitively distinguish the category 2 and 3 solutions.

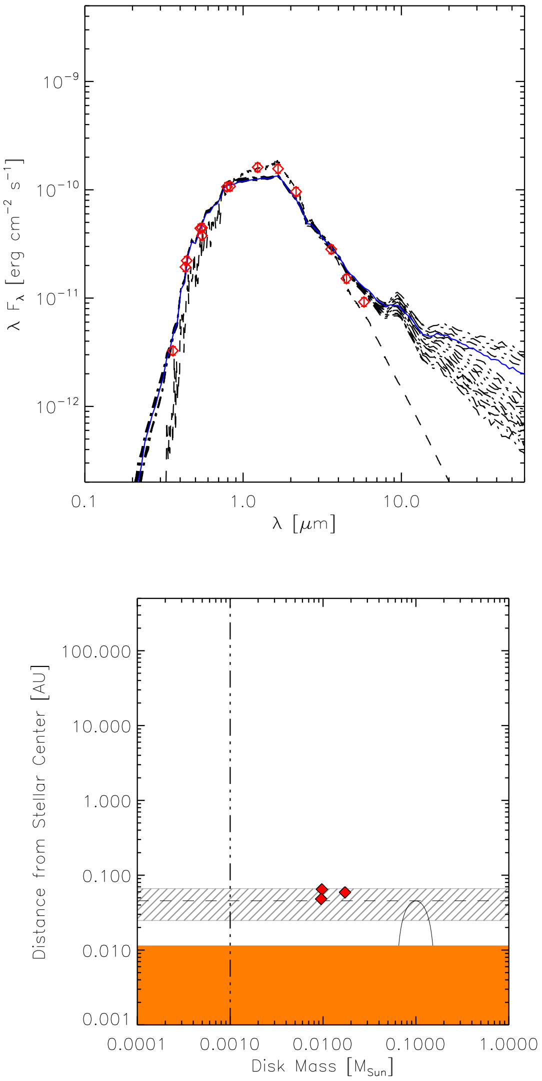

Figure C.25: COUP 1384, category 1. All symbols are as in Fig. 4.3. Despite having only mild excess at the longest wavelengths, all best-fit models have $R_{\rm trunc} \approx R_{\rm dust}$ as well as $R_{\rm trunc}$ within the range of possible magnetic loop heights. Additionally, the best fit models are consistent with the fiducial model, and the object shows a $\Delta(U - V)$ excess suggesting active accretion.

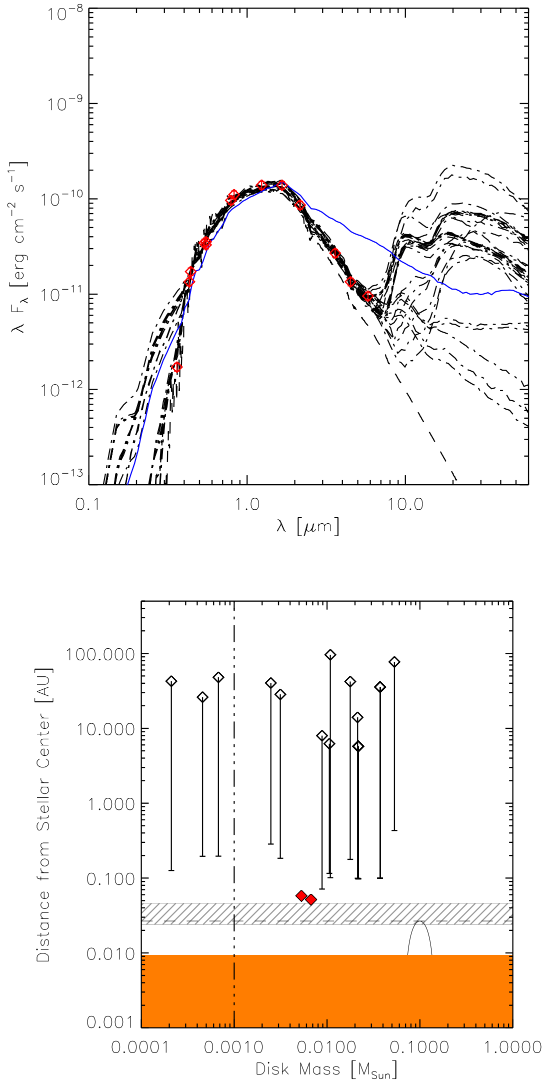

Figure C.26: COUP 1443, category 3. All symbols are as in Fig. 4.3. More than 2/3 of best-fit model disks are truncated beyond ∼10 AU, well beyond reach of the magnetic loop height.

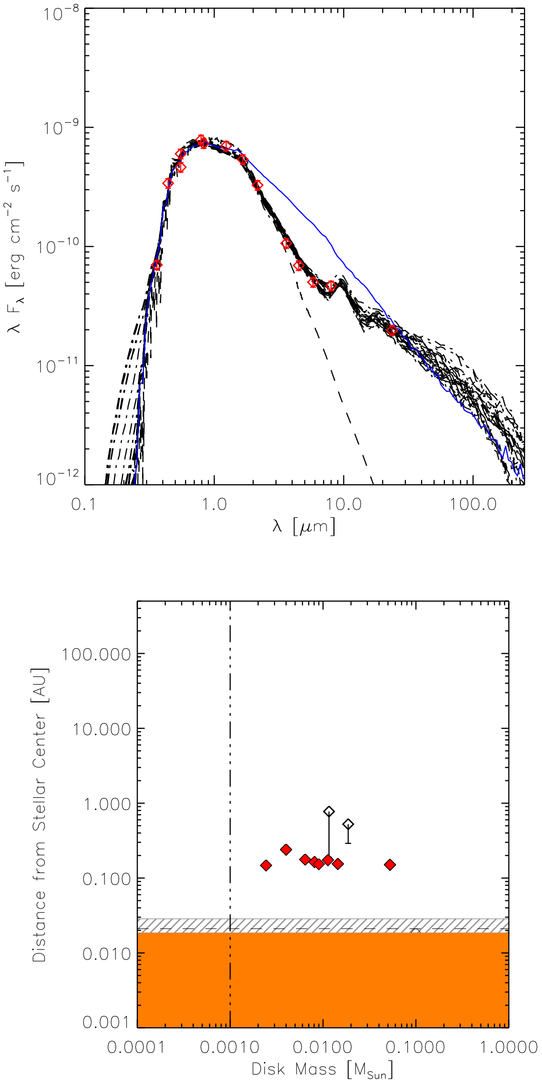

Figure C.27: COUP 1568, category 2. All symbols are as in Fig. 4.3. More than 2/3 of the best-fit model disks are truncated at their respective dust destruction radii.

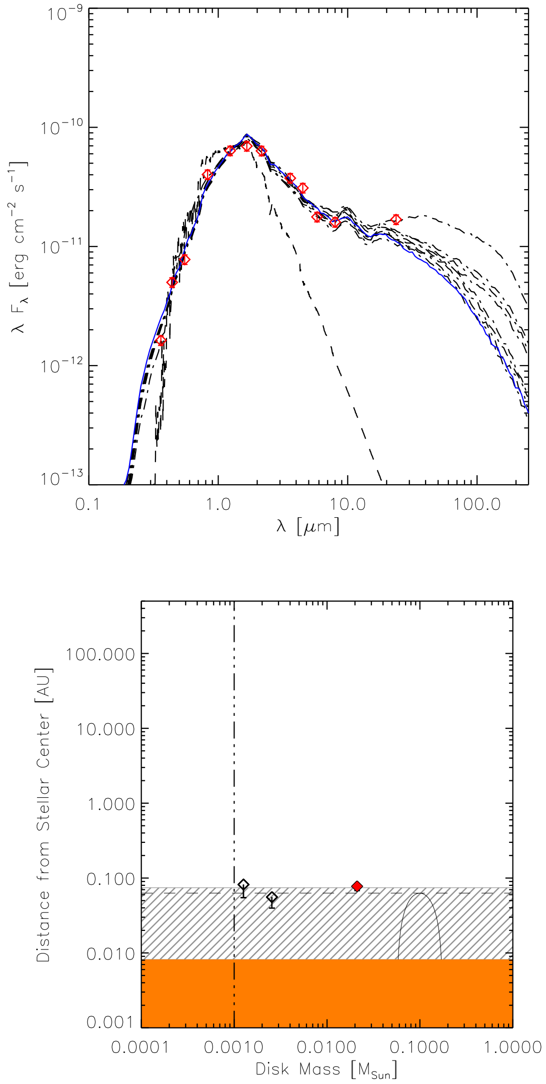

Figure C.28: COUP 1608, category 1. All symbols are as in Fig. 4.3. All of the best-fit model SEDs show $R_{\text{trunc}} \lesssim R_{\text{loop}}$. COUP 1608 also has Ca 2 in emission and a strong $\Delta(U-V)$ excess, both suggesting active accretion.

APPENDIX D

ANGULAR MOMENTUM LOSS: AN ORDER-OF-MAGNITUDE APPROXIMATION

We begin by defining the density within the flaring loop based on X-ray light curve-derived parameter, n_e, and assuming a plasma of ionized H with negligible mass electrons:

$$\rho = n_e m_p. \tag{4.1}$$

As per Favata et al. (2005), a loop volume is defined as:

$$V_{loop} = 2\pi\beta^2 l^3, \tag{4.2}$$

where β is defined as $\frac{r}{l}$, the ratio of loop radius to arc length. Typically in solar flares, $\beta = 0.1$. The mass within the loop is then:

$$M_{loop} = \rho\ V_{loop}. \tag{4.3}$$

The angular momentum content of the loop is defined:

$$J_{CME} = M_{loop}\ \omega\ r_A^2, \tag{4.4}$$

where r_A is the Alfvén radius, where material in the loop is effectively corotating with the star (Weber & Davis, 1967). It is typically twice the loop height (Mestel & Spruit, 1987; Matt & Balick, 2004) which we take to be half its length:

$$r_A = R_{star} \ + \ 2\frac{l}{2} \ = R_{star} + l. \tag{4.5}$$

The rates of mass loss and thus angular momentum loss can be expressed as:

$$\dot{M}_{loop} = M_{loop} \ N_{events}. \tag{4.6}$$

This expression ultimately depends on the number of large scale flaring events occurring over time. The rate of angular momentum loss can then be related to the rate of mass lost from loop-related ejections:

$$\dot{J}_{CME} = \dot{M}_{loop} \ \omega \ r_A^2. \tag{4.7}$$

For comparison purposes,

$$\dot{M}_{\odot} \sim 10^{-14} \ \mathrm{M}_{\odot} \ \mathrm{yr}^{-1}, \tag{4.8}$$

which is much less than typical mass loss rates of young stars. The corresponding solar angular momentum loss rate via this wind is:

$$\dot{J}_{\odot} \sim 10^{30} \ \mathrm{dyn\ cm} = 4,468 \ \mathrm{g\ AU}^2 \ \mathrm{s}^{-2}, \tag{4.9}$$

as per Li (1999).

For a star accreting 10^{-8} $M_{\odot}$ yr^{-1}, the spin up torque would be 10^{36} dyn cm = 4.468×10^{9} g AU^{2} s^{-2} (Matt & Pudritz, 2007). For demonstrative purposes, we have applied this analysis to the star COUP 1410, the star with the largest loop length to stellar radius ratio (55) in our 32 star sample. We find that even for a modest event rate, one large scale event per year (dot-dashed, red line in Fig. 2.7), we can account for ∼10% of the star's angular momentum loss in 10 Myr, roughly the disk dissipation timescale. See Chapter VI for a more detailed application of this calcuation.

REFERENCES

Aarnio, A., Stassun, K. G., & Matt, S. P. 2007, in American Astronomical Society Meeting Abstracts, Vol. 211, American Astronomical Society Meeting Abstracts, 62.18

Aarnio, A. N., Weinberger, A. J., Stassun, K. G., Mamajek, E. E., & James, D. J. 2008, AJ, 136, 2483

Albacete Colombo, J. F., Caramazza, M., Flaccomio, E., Micela, G., & Sciortino, S. 2007, A&A, 474, 495

Andrews, M. D. 2003, Sol. Phys., 218, 261

Andrews, M. D. & Howard, R. A. 2001, Space Science Reviews, 95, 147

Audard, M., Briggs, K. R., Grosso, N., Güdel, M., Scelsi, L., Bouvier, J., & Telleschi, A. 2007, A&A, 468, 379

Baraffe, I., Chabrier, G., Allard, F., & Hauschildt, P. H. 1998, A&A, 337, 403

Barsony, M., Ressler, M. E., & Marsh, K. A. 2005, in Protostars and Planets V, 8622–+

Basri, G. & Batalha, C. 1990, ApJ, 363, 654

Basri, G., Marcy, G. W., & Valenti, J. A. 1992, ApJ, 390, 622

Bertout, C., Siess, L., & Cabrit, S. 2007, A&A, 473, L21

Bessell, M. S. 1979, PASP, 91, 589

—. 1991, AJ, 101, 662

Bessell, M. S. & Brett, J. M. 1988, PASP, 100, 1134

Bondi, H. 1952, MNRAS, 112, 195

Browning, M. K. & Basri, G. 2007, in American Institute of Physics Conference Series, Vol. 948, American Institute of Physics Conference Series, 157–164

Camenzind, M. 1990, in Reviews in Modern Astronomy, Vol. 3, Reviews in Modern Astronomy, ed. G. Klare, 234–265

Carpenter, J. M. 2001, AJ, 121, 2851

Chabrier, G. & Baraffe, I. 1997, A&A, 327, 1039

Chen, J., Howard, R. A., Brueckner, G. E., Santoro, R., Krall, J., Paswaters, S. E., St. Cyr, O. C., Schwenn, R., Lamy, P., & Simnett, G. M. 1997, ApJ, 490, L191+

Christlein, D. & Zabludoff, A. I. 2005, ApJ, 621, 201

Cohen, M., Wheaton, W. A., & Megeath, S. T. 2003, AJ, 126, 1090

Collier Cameron, A. & Campbell, C. G. 1993, A&A, 274, 309

Collier Cameron, A. & Robinson, R. D. 1989a, MNRAS, 236, 57

—. 1989b, MNRAS, 238, 657

Cousins, A. W. J. 1976, Monthly Notes of the Astronomical Society of South Africa, 35, 70

Cox, A. N. 2000, Allen's astrophysical quantities (Allen's astrophysical quantities, 4th ed. Publisher: New York: AIP Press; Springer, 2000. Editedy by Arthur N. Cox. ISBN: 0387987460)

Cranmer, S. R. 2009, ApJ, 706, 824

Da Rio, N., Robberto, M., Soderblom, D. R., Panagia, N., Hillenbrand, L. A., Palla, F., & Stassun, K. 2009, ApJS, 183, 261

D'Alessio, P., Hartmann, L., Calvet, N., Franco-Hernández, R., Forrest, W. J., Sargent, B., Furlan, E., Uchida, K., Green, J. D., Watson, D. M., Chen, C. H., Kemper, F., Sloan, G. C., & Najita, J. 2005, ApJ, 621, 461

Dame, T. M., Ungerechts, H., Cohen, R. S., de Geus, E. J., Grenier, I. A., May, J., Murphy, D. C., Nyman, L.-A., & Thaddeus, P. 1987, ApJ, 322, 706

D'Antona, F. & Mazzitelli, I. 1997, Memorie della Societa Astronomica Italiana, 68, 807

Daou, A. G., Johns-Krull, C. M., & Valenti, J. A. 2006, AJ, 131, 520

de Bruijne, J. H. J. 1999, MNRAS, 306, 381

de Bruijne, J. H. J., Hoogerwerf, R., & de Zeeuw, P. T. 2001, A&A, 367, 111

de Zeeuw, P. T., Hoogerwerf, R., de Bruijne, J. H. J., Brown, A. G. A., & Blaauw, A. 1999, AJ, 117, 354

Dobashi, K., Uehara, H., Kandori, R., Sakurai, T., Kaiden, M., Umemoto, T., & Sato, F. 2005, PASJ, 57, 1

Dryer, M. 1996, Sol. Phys., 169, 421

Edwards, S., Hartigan, P., Ghandour, L., & Andrulis, C. 1994, AJ, 108, 1056

Edwards, S., Strom, S. E., Hartigan, P., Strom, K. M., Hillenbrand, L. A., Herbst, W., Attridge, J., Merrill, K. M., Probst, R., & Gatley, I. 1993, AJ, 106, 372

Eisner, J. A., Hillenbrand, L. A., White, R. J., Akeson, R. L., & Sargent, A. I. 2005, ApJ, 623, 952

Eisner, J. A., Hillenbrand, L. A., White, R. J., Bloom, J. S., Akeson, R. L., & Blake, C. H. 2007, ApJ, 669, 1072

Engelbracht, C. W., Blaylock, M., Su, K. Y. L., Rho, J., Rieke, G. H., Muzerolle, J., Padgett, D. L., Hines, D. C., Gordon, K. D., Fadda, D., Noriega-Crespo, A., Kelly, D. M., Latter, W. B., Hinz, J. L., Misselt, K. A., Morrison, J. E., Stansberry, J. A., Shupe, D. L., Stolovy, S., Wheaton, W. A., Young, E. T., Neugebauer, G., Wachter, S., Pérez-González, P. G., Frayer, D. T., & Marleau, F. R. 2007, PASP, 119, 994

Ercolano, B., Clarke, C. J., & Robitaille, T. P. 2009, MNRAS, 394, L141

Espaillat, C., Calvet, N., D'Alessio, P., Hernández, J., Qi, C., Hartmann, L., Furlan, E., & Watson, D. M. 2007, ApJ, 670, L135

Favata, F., Flaccomio, E., Reale, F., Micela, G., Sciortino, S., Shang, H., Stassun, K. G., & Feigelson, E. D. 2005, ApJS, 160, 469

Favata, F. & Micela, G. 2003, Space Science Reviews, 108, 577

Feigelson, E. D., Broos, P., Gaffney, III, J. A., Garmire, G., Hillenbrand, L. A., Pravdo, S. H., Townsley, L., & Tsuboi, Y. 2002, ApJ, 574, 258

Feigelson, E. D. & Montmerle, T. 1999, ARA&A, 37, 363

Findeisen, K. & Hillenbrand, L. 2010, ArXiv e-prints

Flaccomio, E., Micela, G., Sciortino, S., Feigelson, E. D., Herbst, W., Favata, F., Harnden, Jr., F. R., & Vrtilek, S. D. 2005, ApJS, 160, 450

Getman, K. V., Feigelson, E. D., Broos, P. S., Micela, G., & Garmire, G. P. 2008a, ArXiv e-prints, 807

Getman, K. V., Feigelson, E. D., Grosso, N., McCaughrean, M. J., Micela, G., Broos, P., Garmire, G., & Townsley, L. 2005a, ApJS, 160, 353

Getman, K. V., Feigelson, E. D., Micela, G., Jardine, M. M., Gregory, S. G., & Garmire, G. P. 2008b, ArXiv e-prints, 807

Getman, K. V., Flaccomio, E., Broos, P. S., Grosso, N., Tsujimoto, M., Townsley, L., Garmire, G. P., Kastner, J., Li, J., Harnden, Jr., F. R., Wolk, S., Murray, S. S., Lada, C. J., Muench, A. A., McCaughrean, M. J., Meeus, G., Damiani, F., Micela, G., Sciortino, S., Bally, J., Hillenbrand, L. A., Herbst, W., Preibisch, T., & Feigelson, E. D. 2005b, ApJS, 160, 319

Gómez de Castro, A. I. 2002, MNRAS, 332, 409

Gopalswamy, N., Yashiro, S., Michalek, G., Stenborg, G., Vourlidas, A., Freeland, S., & Howard, R. 2009, Earth Moon and Planets, 104, 295

Gosling, J. T., Hildner, E., MacQueen, R. M., Munro, R. H., Poland, A. I., & Ross, C. L. 1976, Sol. Phys., 48, 389

Gregory, S. G., Wood, K., & Jardine, M. 2007, MNRAS, 379, L35

Güdel, M. 2004, A&A Rev., 12, 71

Güdel, M., Briggs, K. R., Arzner, K., Audard, M., Bouvier, J., Feigelson, E. D., Franciosini, E., Glauser, A., Grosso, N., Micela, G., Monin, J.-L., Montmerle, T., Padgett, D. L., Palla, F., Pillitteri, I., Rebull, L., Scelsi, L., Silva, B., Skinner, S. L., Stelzer, B., & Telleschi, A. 2007, A&A, 468, 353

Haisch, B., Antunes, A., & Schmitt, J. H. M. M. 1995, Science, 268, 1327

Harrison, R. A. 1991, Advances in Space Research, 11, 25

—. 1995, A&A, 304, 585

Hartmann, L. 1994, in NATO ASIC Proc. 417: Theory of Accretion Disks - 2, ed. W. J. Duschl, J. Frank, F. Meyer, E. Meyer-Hofmeister, & W. M. Tscharnuter, 19–+

Hauschildt, P. H., Allard, F., & Baron, E. 1999, ApJ, 512, 377

Hayashi, M. R., Shibata, K., & Matsumoto, R. 1996, ApJ, 468, L37+

Herbst, W., Bailer-Jones, C. A. L., Mundt, R., Meisenheimer, K., & Wackermann, R. 2002, A&A, 396, 513

Herbst, W., Herbst, D. K., Grossman, E. J., & Weinstein, D. 1994, AJ, 108, 1906

Hillenbrand, L. A. 1997, AJ, 113, 1733

Hillenbrand, L. A., Strom, S. E., Calvet, N., Merrill, K. M., Gatley, I., Makidon, R. B., Meyer, M. R., & Skrutskie, M. F. 1998, AJ, 116, 1816

Høg, E., Fabricius, C., Makarov, V. V., Urban, S., Corbin, T., Wycoff, G., Bastian, U., Schwekendiek, P., & Wicenec, A. 2000, A&A, 355, L27

Houk, N. 1982, in Michigan Spectral Survey, Ann Arbor, Dep. Astron., Univ. Michigan, 3 (1982) (Ann Arbor : Dept. of Astronomy, University of Michigan), 0–+

Houk, N. & Smith-Moore, M. 1988, in Michigan Spectral Survey, Ann Arbor, Dept. of Astronomy, Univ. Michigan (Vol. 4) (1988) (Ann Arbor : Dept. of Astronomy, University of Michigan), 0–+

Houk, N. & Swift, C. 1999, Michigan catalogue of two-dimensional spectral types for the HD Stars ; vol. 5 (Ann Arbor : Dept. of Astronomy, University of Michigan)

Hoyle, F. & Lyttleton, R. A. 1941, MNRAS, 101, 227

Hussain, G. A. J., Jardine, M., Donati, J.-F., Brickhouse, N. S., Dunstone, N. J., Wood, K., Dupree, A. K., Collier Cameron, A., & Favata, F. 2007, MNRAS, 377, 1488

Isella, A., Carpenter, J. M., & Sargent, A. I. 2009, ApJ, 701, 260

Jardine, M., Cameron, A. C., Donati, J.-F., Gregory, S. G., & Wood, K. 2006, MNRAS, 367, 917

Jardine, M. & van Ballegooijen, A. A. 2005, MNRAS, 361, 1173

Jardine, M., Wood, K., Collier Cameron, A., Donati, J.-F., & Mackay, D. H. 2002, MNRAS, 336, 1364

Jeffries, R. D. 1999, in Astronomical Society of the Pacific Conference Series, Vol. 158, Solar and Stellar Activity: Similarities and Differences, ed. C. J. Butler & J. G. Doyle, 75–+

Jeffries, R. D., Evans, P. A., Pye, J. P., & Briggs, K. R. 2006, MNRAS, 367, 781

Johns-Krull, C. M., Valenti, J. A., & Koresko, C. 1999, ApJ, 516, 900

Johnson, D. R. H. & Soderblom, D. R. 1987, AJ, 93, 864

Kalberla, P. M. W., Burton, W. B., Hartmann, D., Arnal, E. M., Bajaja, E., Morras, R., & Pöppel, W. G. L. 2005, A&A, 440, 775

Kawaler, S. D. 1988, ApJ, 333, 236

Kenyon, S. J. & Hartmann, L. 1995, ApJS, 101, 117

Kereš, D., Katz, N., Weinberg, D. H., & Davé, R. 2005, MNRAS, 363, 2

Koenigl, A. 1991, ApJ, 370, L39

Kurosawa, R., Harries, T. J., & Symington, N. H. 2006, MNRAS, 370, 580

LaBonte, B. J., Georgoulis, M. K., & Rust, D. M. 2007, ApJ, 671, 955

Lada, C. J. & Adams, F. C. 1992, ApJ, 393, 278

Lada, C. J., Muench, A. A., Haisch, Jr., K. E., Lada, E. A., Alves, J. F., Tollestrup, E. V., & Willner, S. P. 2000, AJ, 120, 3162

Lamm, M. H., Bailer-Jones, C. A. L., Mundt, R., Herbst, W., & Scholz, A. 2004, A&A, 417, 557

Li, J. 1999, MNRAS, 302, 203

Li, J. Z. 2005, Ap&SS, 298, 525

MacQueen, R. M. & Fisher, R. R. 1983, Sol. Phys., 89, 89

Madsen, S., Dravins, D., & Lindegren, L. 2002, A&A, 381, 446

Mahrous, A., Shaltout, M., Beheary, M. M., Mawad, R., & Youssef, M. 2009, Advances in Space Research, 43, 1032

Makidon, R. B., Rebull, L. M., Strom, S. E., Adams, M. T., & Patten, B. M. 2004, AJ, 127, 2228

Mamajek, E. E. 2005, ApJ, 634, 1385

—. 2008, Astronomische Nachrichten, 329, 10

Mamajek, E. E., Meyer, M. R., & Liebert, J. 2002, AJ, 124, 1670

Massi, M., Ros, E., Menten, K. M., Kaufman Bernadó, M., Torricelli-Ciamponi, G., Neidhöfer, J., Boden, A., Boboltz, D., Sargent, A., & Torres, G. 2008, A&A, 480, 489

Matt, S. & Balick, B. 2004, ApJ, 615, 921

Matt, S. & Pudritz, R. E. 2005a, ApJ, 632, L135

—. 2005b, MNRAS, 356, 167

Matt, S. & Pudritz, R. E. 2007, in IAU Symposium, Vol. 243, IAU Symposium, ed. J. Bouvier & I. Appenzeller, 299–306

McKee, C. F. & Ostriker, E. C. 2007, ARA&A, 45, 565

Merín, B., Montesinos, B., Eiroa, C., Solano, E., Mora, A., D'Alessio, P., Calvet, N., Oudmaijer, R. D., de Winter, D., Davies, J. K., Harris, A. W., Cameron, A., Deeg, H. J., Ferlet, R., Garzón, F., Grady, C. A., Horne, K., Miranda, L. F., Palacios, J., Penny, A., Quirrenbach, A., Rauer, H., Schneider, J., & Wesselius, P. R. 2004, A&A, 419, 301

Mestel, L. & Spruit, H. C. 1987, MNRAS, 226, 57

Meyer, M. R., Calvet, N., & Hillenbrand, L. A. 1997, AJ, 114, 288

Meyer, M. R., Carpenter, J. M., Mamajek, E. E., Hillenbrand, L. A., Hollenbach, D., Moro-Martin, A., Kim, J. S., Silverstone, M. D., Najita, J., Hines, D. C., Pascucci, I., Stauffer, J. R., Bouwman, J., & Backman, D. E. 2008, ApJ, 673, L181

Miura, H. & Nakamoto, T. 2007, Icarus, 188, 246

Moon, Y.-J., Choe, G. S., Wang, H., Park, Y. D., & Cheng, C. Z. 2003, Journal of Korean Astronomical Society, 36, 61

Morin, J., Donati, J.-F., Forveille, T., Delfosse, X., Dobler, W., Petit, P., Jardine, M. M., Cameron, A. C., Albert, L., Manset, N., Dintrans, B., Chabrier, G., & Valenti, J. A. 2008, MNRAS, 384, 77

Mouschovias, T. C., Tassis, K., & Kunz, M. W. 2006, ApJ, 646, 1043

Munro, R. H., Gosling, J. T., Hildner, E., MacQueen, R. M., Poland, A. I., & Ross, C. L. 1979, Sol. Phys., 61, 201

Najita, J., Carr, J. S., & Mathieu, R. D. 2003, ApJ, 589, 931

Nindos, A. & Andrews, M. D. 2004, ApJ, 616, L175

Ostriker, E. C. & Shu, F. H. 1995, ApJ, 447, 813

Paerels, F. B. S. & Kahn, S. M. 2003, ARA&A, 41, 291

Pallavicini, R., Golub, L., Rosner, R., Vaiana, G. S., Ayres, T., & Linsky, J. L. 1981, ApJ, 248, 279

Pallavicini, R. & Peres, G. 1983, Sol. Phys., 86, 147

Parker, E. N. 1955, ApJ, 122, 293

—. 1975, ApJ, 198, 205

Pelupessy, F. I. & Papadopoulos, P. P. 2009, ApJ, 707, 954

Peres, G., Orlando, S., Reale, F., & Rosner, R. 2001, ApJ, 563, 1045

Perryman, M. A. C. & ESA, eds. 1997, ESA Special Publication, Vol. 1200, The HIPPARCOS and TYCHO catalogues. Astrometric and photometric star catalogues derived from the ESA HIPPARCOS Space Astrometry Mission

Preibisch, T., Brown, A. G. A., Bridges, T., Guenther, E., & Zinnecker, H. 2002, AJ, 124, 404

Preibisch, T., Kim, Y.-C., Favata, F., Feigelson, E. D., Flaccomio, E., Getman, K., Micela, G., Sciortino, S., Stassun, K., Stelzer, B., & Zinnecker, H. 2005, ApJS, 160, 401

Press, W. H., Flannery, B. P., Teukolsky, S. A., & Vetterling, W. T. 1995, Numerical Recipes in FORTRAN Example Book: The Art of Scientific Computing (Cambridge University Press)

Priest, E. R. & Forbes, T. G. 2002, A&A Rev., 10, 313

Randich, S. 2000, in Astronomical Society of the Pacific Conference Series, Vol. 198, Stellar Clusters and Associations: Convection, Rotation, and Dynamos, ed. R. Pallavicini, G. Micela, & S. Sciortino, 401–+

Randich, S., Aharpour, N., Pallavicini, R., Prosser, C. F., & Stauffer, J. R. 1997, A&A, 323, 86

Randich, S., Pallavicini, R., Meola, G., Stauffer, J., & Balachandran, S. C. 2001, A&A, 372, 862

Reale, F., Betta, R., Peres, G., Serio, S., & McTiernan, J. 1997, A&A, 325, 782

Rebull, L. M. 2001, AJ, 121, 1676

Rebull, L. M., Hillenbrand, L. A., Strom, S. E., Duncan, D. K., Patten, B. M., Pavlovsky, C. M., Makidon, R., & Adams, M. T. 2000, AJ, 119, 3026

Robberto, M., Soderblom, D. R., O'Dell, C. R., Stassun, K. G., Hillenbrand, L. A., Simon, M., Feigelson, E. D., Najita, J., Stauffer, J., Meyer, M., Panagia, N., Romaniello, M., Palla, F., Krist, J., Reid, I. N., McCullough, P., Makidon, R., Bergeron, E., McMaster, M., Kozhurina-Platais, V., Smith, K., & Sherry, W. 2005, in Protostars and Planets V, 8441–+

Robichon, N., Arenou, F., Mermilliod, J.-C., & Turon, C. 1999, VizieR Online Data Catalog, 334, 50471

Robitaille, T. P., Whitney, B. A., Indebetouw, R., & Wood, K. 2007, ApJS, 169, 328

Robitaille, T. P., Whitney, B. A., Indebetouw, R., Wood, K., & Denzmore, P. 2006, ApJS, 167, 256

Rossiter, R. A. 1943, Publications of Michigan Observatory, 8, 133

Schatzman, E. 1962, Annales d'Astrophysique, 25, 18

Schrijver, C. J. & Zwaan, C. 2000, Solar and Stellar Magnetic Activity (Solar and stellar magnetic activity / Carolus J. Schrijver, Cornelius Zwaan. New York : Cambridge University Press, 2000. (Cambridge astrophysics series ; 34))

Shu, F., Najita, J., Ostriker, E., Wilkin, F., Ruden, S., & Lizano, S. 1994, ApJ, 429, 781

Simon, M., Dutrey, A., & Guilloteau, S. 2000, ApJ, 545, 1034

Skelly, M. B., Unruh, Y. C., Cameron, A. C., Barnes, J. R., Donati, J.-F., Lawson, W. A., & Carter, B. D. 2008, MNRAS, 385, 708

Skrutskie, M. F., Cutri, R. M., Stiening, R., Weinberg, M. D., Schneider, S., Carpenter, J. M., Beichman, C., Capps, R., Chester, T., Elias, J., Huchra, J., Liebert, J., Lonsdale, C., Monet, D. G., Price, S., Seitzer, P., Jarrett, T., Kirkpatrick, J. D., Gizis, J. E., Howard, E., Evans, T., Fowler, J., Fullmer, L., Hurt, R., Light, R., Kopan, E. L., Marsh, K. A., McCallon, H. L., Tam, R., Van Dyk, S., & Wheelock, S. 2006, AJ, 131, 1163

Soderblom, D. R., Jones, B. F., Balachandran, S., Stauffer, J. R., Duncan, D. K., Fedele, S. B., & Hudon, J. D. 1993, AJ, 106, 1059

St. Cyr, O. C. & Webb, D. F. 1991, Sol. Phys., 136, 379

Stahler, S. W. & Palla, F. 2005, The Formation of Stars (The Formation of Stars, by Steven W. Stahler, Francesco Palla, pp. 865. ISBN 3-527-40559-3. Wiley-VCH , January 2005.)

Stark, D. P., Whitney, B. A., Stassun, K., & Wood, K. 2006, ApJ, 649, 900

Stassun, K. G., Ardila, D. R., Barsony, M., Basri, G., & Mathieu, R. D. 2004a, AJ, 127, 3537

Stassun, K. G., Mathieu, R. D., Mazeh, T., & Vrba, F. J. 1999, AJ, 117, 2941

Stassun, K. G., Mathieu, R. D., Vaz, L. P. R., Stroud, N., & Vrba, F. J. 2004b, ApJS, 151, 357

Stassun, K. G., Mathieu, R. D., Vrba, F. J., Mazeh, T., & Henden, A. 2001, AJ, 121, 1003

Stassun, K. G., van den Berg, M., Feigelson, E., & Flaccomio, E. 2006, ApJ, 649, 914

Steffen, A. T., Mathieu, R. D., Lattanzi, M. G., Latham, D. W., Mazeh, T., Prato, L., Simon, M., Zinnecker, H., & Loreggia, D. 2001, AJ, 122, 997

Strom, K. M., Strom, S. E., Edwards, S., Cabrit, S., & Skrutskie, M. F. 1989, AJ, 97, 1451

Sylwester, J., Sylwester, B., Jakimiec, J., Garcia, H. A., Serio, S., & Reale, F. 1993, Advances in Space Research, 13, 307

Tayler, R. J. 1997, The Sun as a star (Cambridge ; New York, NY, USA : Cambridge University Press, 1997.)

Telleschi, A., Güdel, M., Briggs, K. R., Audard, M., & Palla, F. 2007, A&A, 468, 425

Torres, C. A. O., Quast, G. R., da Silva, L., de La, R. R., Melo, C. H. F., & Sterzik, M. 2006, VizieR Online Data Catalog, 346, 695

Uzdensky, D. A., Königl, A., & Litwin, C. 2002, ApJ, 565, 1191

Švestka, Z. 2001, Space Science Reviews, 95, 135

van Leeuwen, F. 2007, Hipparcos, the New Reduction of the Raw Data, Vol. 20 (Cambridge University, Cambridge, UK Series: Astrophysics and Space Science Library)

Voges, W., Aschenbach, B., Boller, T., Bräuninger, H., Briel, U., Burkert, W., Dennerl, K., Englhauser, J., Gruber, R., Haberl, F., Hartner, G., Hasinger, G., Kürster, M., Pfeffermann, E., Pietsch, W., Predehl, P., Rosso, C., Schmitt, J. H. M. M., Trümper, J., & Zimmermann, H. U. 1999, A&A, 349, 389

Voges, W., Aschenbach, B., Boller, T., Brauninger, H., Briel, U., Burkert, W., Dennerl, K., Englhauser, J., Gruber, R., Haberl, F., Hartner, G., Hasinger, G., Pfeffermann, E., Pietsch, W., Predehl, P., Schmitt, J., Trumper, J., & Zimmermann, U. 2000, IAU Circ., 7432, 1

Vourlidas, A., Subramanian, P., Dere, K. P., & Howard, R. A. 2000, ApJ, 534, 456

Warwick, J. W. 1955, ApJ, 121, 376

Webb, D. F. & Hundhausen, A. J. 1987, Sol. Phys., 108, 383

Webb, R. A., Zuckerman, B., Platais, I., Patience, J., White, R. J., Schwartz, M. J., & McCarthy, C. 1999, ApJ, 512, L63

Weber, E. J. & Davis, L. J. 1967, ApJ, 148, 217

Weinberger, A. J., Becklin, E. E., Schneider, G., Smith, B. A., Lowrance, P. J., Silverstone, M. D., Zuckerman, B., & Terrile, R. J. 1999, ApJ, 525, L53

Weinberger, A. J., Rich, R. M., Becklin, E. E., Zuckerman, B., & Matthews, K. 2000, ApJ, 544, 937

Weintraub, D. A., Kastner, J. H., & Bary, J. S. 2000, ApJ, 541, 767

Whitney, B. A., Indebetouw, R., Bjorkman, J. E., & Wood, K. 2004, ApJ, 617, 1177

Whitney, B. A., Wood, K., Bjorkman, J. E., & Cohen, M. 2003a, ApJ, 598, 1079

Whitney, B. A., Wood, K., Bjorkman, J. E., & Wolff, M. J. 2003b, ApJ, 591, 1049

Wood, B. E., Karovska, M., Chen, J., Brueckner, G. E., Cook, J. W., & Howard, R. A. 1999, ApJ, 512, 484

Yashiro, S., Michalek, G., Akiyama, S., Gopalswamy, N., & Howard, R. A. 2008, ApJ, 673, 1174

Zacharias, N., Urban, S. E., Zacharias, M. I., Wycoff, G. L., Hall, D. M., Monet, D. G., & Rafferty, T. J. 2004, AJ, 127, 3043

Zuckerman, B. & Song, I. 2004, ARA&A, 42, 685

Zuckerman, B., Song, I., Bessell, M. S., & Webb, R. A. 2001, ApJ, 562, L87